Acoustic Resonance in a Cavity under a Subsonic Flow

by

José Oliverio Alvarez Sierra

A Dissertation Submitted to the Faculty of the

Graduate Interdisciplinary Program
in Applied Mathematics

In Partial Fulfillment of the Requirements
For the Degree of

Doctor of Philosophy

In the Graduate College

The University of Arizona

2005

THE UNIVERSITY OF ARIZONA
GRADUATE COLLEGE

As members of the Dissertation Committee, we certify that we have read the dissertation prepared by José Oliverio Alvarez Sierra

entitled: Acoustic Resonance in a Cavity under a Subsonic Flow

and recommend that it be accepted as fulfilling the dissertation requirement for the Degree of Doctor of Philosophy

Edward J. Kerschen Date: 04/08/2005

Michael Tabor Date: 04/08/2005

Bruce Bayly Date: 04/08/2005

Anatoli Tumin Date: 04/08/2005

Thomas Balsa Date: 04/08/2005

Final approval and acceptance of this dissertation is contingent upon the candidate's submission of the final copies of the dissertation to the Graduate College.

I hereby certify that I have read this dissertation prepared under my direction and recommend that it be accepted as fulfilling the dissertation requirement.

Edward J. Kerschen 04/08/2005

Dissertation Director Date

STATEMENT BY AUTHOR

This dissertation has been submitted in partial fulfillment of requirements for an advanced degree at The University of Arizona and is deposited in the University Library to be made available to borrowers under rules of the Library.

Brief quotations from this dissertation are allowable without special permission, provided that accurate acknowledgment of source is made. Requests for permission for extended quotation from or reproduction of this manuscript in whole or in part may be granted by the head of the major department or the Dean of the Graduate College when in his or her judgment the proposed use of the material is in the interests of scholarship. In all other instances, however, permission must be obtained from the author.

SIGNED: José Oliverio Alvarez

Acknowledgements

I am very grateful to my father, Hernán Alvarez for his love and support throughout my PhD studies. I recognize that it was hard for him to see me leave my country and the plan a father has for a son. Gracias papá.

I am also grateful to my mother, Carmen Cecilia Sierra for her love and moral support. My life through graduate school would not have been the same without her enthusiasm in our weekly phone conversations. Also, I am very thankful to the Murga Arroyave family for their support and unconditional love. My heart is in debt to my uncle Roberto Murga and my aunt Lucrecia de Murga.

I want to thank my brother Rodrigo Alvarez for his unconditional love and for the regular phone calls. Also, I want to thank my sister Maria Cecilia and my brother Juan Ignacio for their love and moral support.

My gratitude is immense to my advisor, Professor Edward Kerschen, who not only was my academic advisor, but a life mentor and a good friend. It was through his enthusiasm, passion and guidance that I discovered the beauty and fascinating problems of aeroacoustics.

I am indebted with my committee members, Professors Anatoli Tumin, Bruce Bayly, Michael Tabor and Thomas Balsa for their valuable advice, insightful comments and moral support. In particular I want to thank Professor Tumin for all his advice and recomendations. I also want to thank Professor Werner Koch for taking the time to be the external reviewer for this dissertation.

My life in graduate school would not have been so joyful and fullfilling if it was not for the love, patience, understanding and encouragement that I received from my fiancee Clare Perpich. I am also thankful to Clare for taking the time to check this dissertation and making it more readable.

Life in Tucson would have been sad and boring if it was not for all my friends. I take with me fund memories from all them and the hope that we can see each other again.

Dedication

In memory of my beloved grandmother,
Carmen Arroyave de Sierra,
to whom I owe so much of who I am.

Table of Contents

List of Tables **9**

List of Figures **13**

Abstract **16**

1. INTRODUCTION **17**

2. GLOBAL MODEL **23**

2.1 Global Model 23

2.2 Simplified Global Model 27

3. SCATTERING PROCESS AT THE UPSTREAM END OF THE CAVITY **31**

3.1 General Formulation at the Upstream End of the Cavity 32

3.2 Analysis for a Semi-infinite Overhanging Lip 38

3.2.1 Impingement of the Upstream Cavity Mode $\mathcal{U}$ 40

3.2.2 Impingement of a Downstream Duct Mode 54

3.3 Analysis for a Finite-length Overhanging Lip or a Square Corner . . . 60

4. NUMERICAL RESULTS AND DISCUSSION FOR THE SCATTERING PROBLEM AT THE UPSTREAM END **67**

4.1 Mode Wavenumbers 67

4.2 Mode Shapes 70

4.3 Results for a Semi-infinite Overhanging Lip 77

4.3.1 Impingement of the Upstream Cavity Mode $\mathcal{U}$ 77

4.3.2 Impingement of a Downstream Duct Mode 82

4.4 Results for a Finite-length Overhanging Lip or a Square Corner . . . 90

4.4.1 Duct Mode Coefficients 91

Table of Contents—*Continued*

4.4.2 Receptivity Coefficients 93
4.4.3 Other Coefficients 94

5. SCATTERING PROCESS AT THE DOWNSTREAM END OF THE CAVITY 97
5.1 General Formulation at the Downstream End of the Cavity 99
5.2 Analysis for a Semi-infinite Overhanging Lip 100
5.2.1 Impingement of an Upstream Duct Mode 100
5.2.2 Impingement of a Shear-layer Instability Wave 109
5.2.3 Impingement of a Downstream Cavity Mode 115
5.3 Analysis for a Finite-length Overhanging Lip or a Square Corner . . . 121

6. NUMERICAL RESULTS AND DISCUSSION FOR THE SCATTERING PROBLEM AT THE DOWNSTREAM END 127
6.1 Results for a Semi-infinite Overhanging Lip 127
6.1.1 Impingement of an Instability Wave 127
6.1.2 Impingement of an Upstream Duct Mode 132
6.1.3 Impingement of a Downstream Cavity Mode 137
6.2 Results for a Finite-length Overhanging Lip or a Square Corner . . . 143
6.2.1 Duct Mode Coefficients 144
6.2.2 Cavity Mode Coefficients 146
6.2.3 Other Interactions 148

7. RESULTS FOR GLOBAL MODEL 151

8. CONCLUSIONS AND FUTURE WORK 161
8.1 Conclusions 161
8.2 Future Work 161

Table of Contents—*Continued*

APPENDIX A WIENER-HOPF KERNEL FUNCTION 163

APPENDIX B PROPAGATION ACROSS CAVITY LENGTH . . 167

APPENDIX C CALCULATION OF THE EXTERNAL FIELDS . 169

APPENDIX D STEEPEST DESCENT AND CHOICE OF BRANCH CUTS 171

REFERENCES 176

List of Tables

4.1 *Wavenumbers of the upstream and downstream cavity modes and duct modes, for* $M = 0.35$. 68

4.2 *Wavenumbers of the upstream and downstream cavity modes and duct modes, for* $M = 0.85$. 68

4.3 *Amplitudes and phases of the upstream duct modes and downstream cavity modes generated by the interaction of the upstream cavity mode* $\mathcal{U}$ *with a semi-infinite overhanging lip, for* $M = 0.35$ *and* $d = 1.5$. 80

4.4 *Amplitudes and phases of the upstream duct modes and downstream cavity modes generated by the interaction of the upstream cavity mode* $\mathcal{U}$ *with a semi-infinite overhanging lip, for* $M = 0.85$ *and* $d = 1.5$. 80

4.5 *Receptivity coefficients for the interaction of the* $k = 0$ *downstream duct mode, with a semi-infinite overhanging lip, for* $M = 0.35$. 84

4.6 *Receptivity coefficients for the interaction of the* $k = 0$ *downstream duct mode, with a semi-infinite overhanging lip, for* $M = 0.85$. 84

4.7 *Amplitudes,* $|C_j^{d,k}|$*, of the downstream cavity modes generated by the interaction of the k-th downstream duct mode with a semi-infinite overhanging lip, for Mach number 0.35* 84

4.8 *Phases,* $\arg[C_j^{d,k}]$*, of the downstream cavity modes generated by the interaction of the k-th downstream duct mode with a semi-infinite overhanging lip, for* $M = 0.35$ 85

4.9 *Amplitudes,* $|D_j^{d,k}|$*, of the upstream duct modes generated by the interaction of the k-th downstream duct mode with a semi-infinite overhanging lip, for* $M = 0.35$ 86

4.10 *Phases,* $\arg[D_j^{d,k}]$*, of the upstream cavity modes generated by the interaction of the k-th downstream duct mode with a semi-infinite overhanging lip, for* $M = 0.35$ 87

List of Tables—*Continued*

4.11 *Magnitudes* $|A_{j,k}|$ *of the entries of the matrix* $\widetilde{A}$ *for a square* (90°) *corner* ($b = 0$), *for* $M = 0.35$ 91

4.12 *Amplitudes and phases of the downstream duct modes obtained as the solution of the matrix equation (3.108) for a square* (90°) *corner* ($b = 0$). *Results for an eight-mode truncation and a four-mode truncation, for* $M = 0.35$, *are listed.* 92

4.13 *Amplitudes and phases of the receptivity coefficients obtained from the matrix equation (3.110) for a square* (90°) *corner* ($b = 0$), *for* $M = 0.35$. *Results for an eight-mode truncation and a two-mode truncation are listed.* 94

4.14 *Amplitudes and phases of the scattering coefficients for the downstream cavity modes; for a square* (90°) *corner* ($b = 0$), *for* $M = 0.35$. *Results for an eight-mode truncation and a four-mode truncation are listed.* . . . 95

6.1 *Amplitudes and phases of the upstream cavity modes and downstream duct modes generated by the interaction of a shear-layer instability wave with a semi-infinite overhanging lip, for* $M = 0.35$ 129

6.2 *Amplitudes* $|C_j^{u,k}|$ *of the upstream cavity modes generated by the interaction of the k-th upstream duct mode with a semi-infinite overhanging lip, for* $M = 0.35$ 133

6.3 *Phases* $\arg[C_j^{u,k}]$ *of the upstream cavity modes generated by the interaction of the k-th upstream duct mode with a semi-infinite overhanging lip, for* $M = 0.35$ 133

6.4 *Amplitudes* $|D_j^{u,k}|$ *of the downstream duct modes generated by the interaction of the k-th upstream duct mode with a semi-infinite overhanging lip, for* $M = 0.35$ 134

List of Tables—*Continued*

6.5 *Phases* $\arg[D_j^{u,k}]$ *of the downstream duct modes generated by the interaction of the k-th upstream duct mode with a semi-infinite overhanging lip, for* $M = 0.35$ 135

6.6 *Amplitudes* $|C_j^{\mathcal{D}k}|$ *of the upstream cavity modes generated by the interaction of the k-th downstream cavity mode with a semi-infinite overhanging lip, for* $M = 0.35$ 138

6.7 *Phases* $\arg[C_j^{\mathcal{D}k}]$ *of the upstream cavity modes generated by the interaction of the k-th downstream cavity mode with a semi-infinite overhanging lip, for* $M = 0.35$ 139

6.8 *Amplitudes* $|D_j^{\mathcal{D}k}|$ *of the downstream duct modes generated by the interaction of the k-th downstream cavity mode with a semi-infinite overhanging lip, for* $M = 0.35$ 140

6.9 *Phases* $\arg[D_j^{\mathcal{D}k}]$ *of the downstream duct modes generated by the interaction of the k-th downstream cavity mode with a semi-infinite overhanging lip, for* $M = 0.35$ 140

6.10 *Magnitudes* $|A_{j,k}|$ *of the entries of the matrix* $\widetilde{A}$ *for a square (*$90°$*) corner (*$b = 0$*), for* $M = 0.35$ 144

6.11 *Amplitudes and phases of the downstream duct modes obtained as the solution of the matrix equation (5.97) for a square (*$90°$*) corner (*$b = 0$*). Results for an eight-mode truncation and a four-mode truncation, for* $M = 0.35$*,are listed.* 145

6.12 *Amplitudes and phases of the scattering coefficients for the upstream cavity modes; for a square (*$90°$*) corner (*$b = 0$*). Results for an eight-mode truncation and a four-mode truncation, for* $M = 0.35$*, are listed.* 147

List of Tables—*Continued*

6.13 *Amplitudes and phases of the scattering coefficients for the upstream cavity modes, for the impingement of the downstream cavity mode $\mathcal{D}$; for a square (90°) corner ($b = 0$). Results for an eight-mode truncation and a four-mode truncation, for $M = 0.35$, are listed.* 149

7.1 *Comparison of the first five resonant frequencies (fL'/U) for $\eta = 0$ and $\eta = 0.1$. Results for $M = 0.85$.* 160

List of Figures

1.1 *Rectangular cavity under a subsonic uniform flow U.* 17

1.2 *Analytical predictions of the resonant frequencies made by Heller & Bliss (1975), using their improved Rossiter formula* 19

2.1 *Global model for subsonic flow* 23

3.1 *Sketch of geometries for the interactions at the upstream end of the cavity: (a) square corner, (b) thin overhanging lip of finite length b, (c) semi-infinite overhanging lip.* 33

3.2 *Singularities in the Complex Plane* 39

4.1 *Mode shape for the shear-layer instability wave, for* $M = 0.35$. 71

4.2 *Mode shapes for the first three upstream cavity modes for* $M = 0.35$. 72

4.3 *Mode shapes for the first three upstream cavity modes for* $M = 0.85$. 72

4.4 *Mode shapes for the first three downstream cavity modes for Mach number 0.35.* 74

4.5 *Mode shapes for the first three downstream cavity modes for Mach number 0.85.* 74

4.6 *Mode shape for the upstream external acoustic field, for* $M = 0.35$. 76

4.7 *Mode shape for the downstream external acoustic field, for* $M = 0.35$. 77

4.8 *Amplitude and phase of the pressure field on the cavity bottom for the interaction of the upstream cavity mode* $\mathcal{U}$ *with an overhanging lip, for* $M = 0.35$. . . 82

4.9 *Amplitude and phase of the pressure field on the cavity bottom for the interaction of the* $k = 0$ *downstream duct mode with an overhanging lip, for* $M = 0.35$. 88

5.1 *Sketch of geometries for the interactions at the downstream end of the cavity: (a) square corner, (b) thin overhanging lip of finite length b, (c) semi-infinite overhanging lip.* 98

6.1 *Amplitude and phase of the pressure field on the cavity bottom for the interaction of a shear-layer instability wave with a semi-infinite overhanging lip, for* $M = 0.35$. 130

List of Figures—*Continued*

6.2 *Amplitude and phase of the pressure field on the cavity bottom for the interaction of the $k = 0$ upstream duct mode with a semi-infinite overhanging lip, for $M = 0.35$.* 137

6.3 *Amplitude and phase of the pressure field on the cavity bottom for the interaction of the $k = 0$ downstream cavity mode with a semi-infinite overhanging lip, for $M = 0.35$.* 142

7.1 *Magnitude and phase of the scattering coefficient $C_{\mathcal{SU}}$ for the upstream end of the cavity, as a function of Mach number. (a) $|C_{\mathcal{SU}}|$; (b) $\arg[C_{\mathcal{SU}}]$. $d = 1$, long dashes; $d = 1.5$, medium dashes; $d = 2$, short dashes; $d = 2.5$, solid; $d = 3$, solid thick.* 152

7.2 *Magnitude and phase of the scattering coefficient $C_{\mathcal{US}}$ for the downstream end of the cavity, as a function of Mach number. (a) $|C_{\mathcal{US}}|$; (b) $\arg[C_{\mathcal{US}}]$. $d = 1$, long dashes; $d = 1.5$, medium dashes; $d = 2$, short dashes; $d = 2.5$, solid; $d = 3$, solid thick.* 152

7.3 *Magnitude and phase of the scattering coefficient $C_{\mathcal{DU}}$ for the upstream end of the cavity, as a function of Mach number. (a) $|C_{\mathcal{DU}}|$; (b) $\arg[C_{\mathcal{DU}}]$. $d = 1$, long dashes; $d = 1.5$, medium dashes; $d = 2$, short dashes; $d = 2.5$, solid; $d = 3$, solid thick.* 153

7.4 *Magnitude $|\mathcal{S}/\widehat{\mathcal{S}}|$ and phase $\arg[\mathcal{S}/\widehat{\mathcal{S}}]$ of the transfer functions for the instability wave for $M = 0.35$, results by Yang & Tumin (2002). Rossiter's empirical prediction for $\arg[\mathcal{S}/\widehat{\mathcal{S}}]$ is shown as a dotted line.* 156

7.5 *Magnitude $|\mathcal{S}/\widehat{\mathcal{S}}|$ and phase $\arg[\mathcal{S}/\widehat{\mathcal{S}}]$ of the transfer function for the instability wave for $M = 0.35$, results by Yang & Tumin (2002). Rossiter's empirical prediction for $\arg[\mathcal{S}/\widehat{\mathcal{S}}]$ is shown as a dashed line.* 156

List of Figures—*Continued*

7.6 *Magnitude* $|\widehat{\mathcal{U}}/\mathcal{U}|$ *and phase* $\arg[\widehat{\mathcal{U}}/\mathcal{U}]$ *of the transfer function for the upstream cavity mode, for M=0.35. Rossiter's empirical prediction for* $\arg[\widehat{\mathcal{U}}/\mathcal{U}]$ *is shown as a dashed line.* 157

7.7 *Magnitude* $|\widehat{\mathcal{U}}/\mathcal{U}|$ *and phase* $\arg[\widehat{\mathcal{U}}/\mathcal{U}]$ *of the transfer function for the upstream cavity mode, for M=0.85. Rossiter's empirical prediction for* $\arg[\widehat{\mathcal{U}}/\mathcal{U}]$ *is shown as a dashed line.* 157

7.8 *Comparison of the predicted resonant frequencies with experimental data presented by Heller & Bliss (1975).* 158

D.1 *Path of steepest descents for different angles of observation* 173

D.2 *Other possible choices of branch cuts.* 175

Abstract

Acoustic resonances leading to high unsteady pressure levels may occur in flow past cavities. The resonance involves a coupling between the downstream-propagating instability wave on the shear layer spanning the open face of the cavity, and acoustic waves propagating within and external to the cavity. These elements of the disturbance field are coupled by the scattering processes that occur at the upstream and downstream ends of the cavity. We develop a theoretical prediction method that combines propagation models in the central region of the cavity with scattering models for the end regions. In our analyses of the scattering processes at the cavity ends, the square-corner geometry is treated exactly, by a method employing the Wiener–Hopf technique. The shear layer is approximated as a vortex sheet in the edge scattering analyses, but finite shear-layer thickness is accounted for in analyzing the propagation of the waves along the length of the cavity. The global analysis leads to a prediction for the resonant frequencies which has a form similar to the Rossiter formula, but contains no empirical constants. In addition to prediction of the frequency, our theory determines the temporal growth or decay rate of each mode. Finally, our theory also predicts the influence of secondary feedback loops involving other components of the unsteady field. Comparisons of the predictions with existing experimental data are made.

1. INTRODUCTION

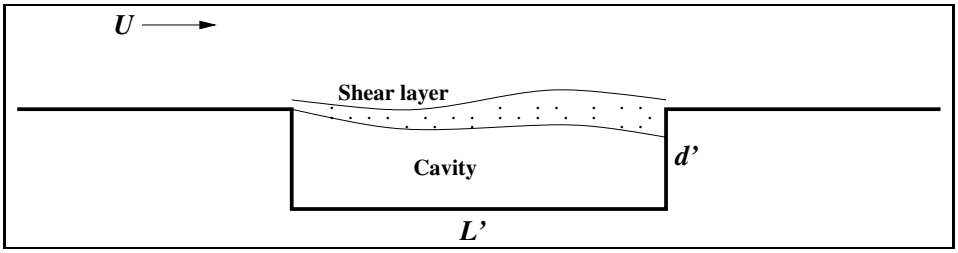

Figure 1.1 *Rectangular cavity under a subsonic uniform flow U.*

Flow-acoustic resonances may occur in flow past cavities, leading to very high unsteady pressure levels. These are of concern in a variety of applications, including military aircraft weapons bays. This dissertation addresses relatively shallow cavities that are representative of weapons bays. For shallow cavities, wave propagation along the length of the cavity (parallel to the flow direction) is a crucial feature of the resonance phenomenon.

The geometry of the problem that is studied in this dissertation is shown in figure 1.1. The basic problem consists of a cavity of length L' and depth d', a uniform subsonic flow U, a shear layer spanning the face of the cavity, and acoustic fields in the cavity. In the present work we focus on shallow cavities ($3 \leq L'/d' \leq 8$).

The cavity acoustic resonance contains four main elements: (1) an instability wave in the free shear layer, which amplifies as it propagates downstream across the face of the cavity, (2) an acoustic field that is generated by the impingement of the instability wave on the downstream edge of the cavity, (3) propagation of this acoustic field back upstream, and (4) the regeneration of the instability wave by the impingement of the acoustic field on the upstream edge of the cavity (other elements make secondary contributions to the resonance, as discussed later). The resonant frequencies are determined by a phase relationship around the feedback loop that leads to constructive reinforcement. The resultant amplitude of the resonant field

is controlled by a subsequent nonlinear saturation, often associated with nonlinear effects in the development of the shear-layer instability wave as it propagates across the face of the cavity.

A seminal contribution to the understanding and prediction of cavity resonances was made by Rossiter (1964), who performed an extensive experimental study of cavity resonances for free-stream Mach numbers in the range $0.5 \leq M \leq 1.2$, and also proposed the semi-empirical formula for the resonant frequencies

$$\frac{fL'}{U} = \frac{m - \alpha}{M + 1/\kappa}, \tag{1.1}$$

where f is the frequency, L' is the dimensional length of the cavity, U is the free-stream velocity and $M = U/c$ is the Mach number (here c is the speed of sound, assumed to be the same inside and outside the cavity). Also, α and κ are empirical constants chosen by Rossiter to best match the experimental data, and m is a positive integer. The empirical constant α accounts for the change in phase due to the scattering at the cavity ends and κ is a fraction of the speed of the free-stream at which the shear-layer instability wave is assumed to travel. Despite its limitations, Rossiter's formula still is widely used today.

Rossiter's formula (1.1) is based on the four-element description of the resonant loop presented in the preceding paragraph. Rossiter introduced an empirical constant to account for the phase shifts associated with the scattering processes at the two ends of the cavity (elements 2 and 4), the constant being chosen to best fit the experimental data.

Heller & Bliss (1975) presented experimental results over an extended Mach number range $0.3 \leq M \leq 3.0$. They proposed a modified Rossiter formula, in which the static temperature in the cavity is assumed to be the stagnation temperature of the stream, thereby increasing the acoustic propagation speed in the cavity. This factor is relatively unimportant for subsonic Mach numbers, but becomes increasingly

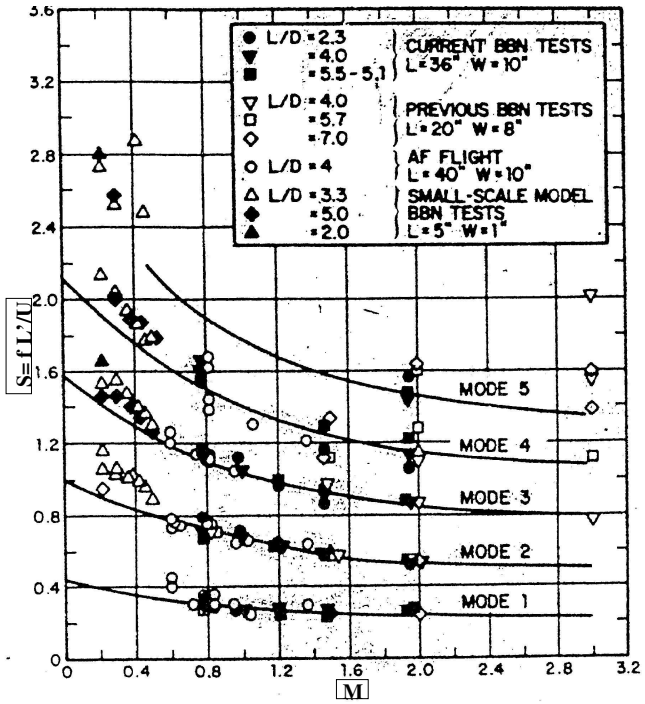

Figure 1.2 *Analytical predictions of the resonant frequencies made by Heller & Bliss (1975), using their improved Rossiter formula*

important for supersonic Mach numbers.

Figure 1.2 shows in solid lines the analytical predictions made by Heller & Bliss (1975). They compared their predictions with results from several different experiments. Note that the resonant frequencies decay with Mach number. Also, for the Mach number range $0 < M < 0.6$, no first mode is found and the predictions for the higher-order modes lie below the experimental data. For Mach number 0.85, the first three Rossiter modes are predicted accurately, but the predictions for fourth and fifth modes have what appear to be scattered data around them. In Chapter 7, it will be shown that these points above and below the fourth mode are independent modes and not scattered data.

Tam & Block (1978) carried out an extensive experimental investigation at low Mach numbers. They also developed a theoretical model which involved excitation of the shear layer instability wave by the acoustic field generated at the downstream

end of the cavity. The scattering process at the downstream end was represented in a simplified fashion, by introducing a concentrated acoustic monopole source at the downstream corner of the cavity. The phase of the source relative to the local instability wave motion was chosen heuristically. The excitation of the shear layer instability wave was then calculated through a 'distributed receptivity' model, which ignored details of the interaction at the upstream end of the cavity. The amplitude of the monopole source was not determined. Therefore, the theory produced an expression for the resonance frequencies, but did not determine whether a particular resonant mode corresponded to a globally stable or unstable disturbance.

Recent contributions to the cavity acoustics literature include, among others, the experiments and active control studies by Cattafestta *et al.* (1999), Raman *et al.* (1999), Stanek *et al.* (2000), Williams *et al.* (2002), Rowley *et al.* (2002*a*), Kegerise *et al.* (2002) and Ukeiley *et al.* (2003), and numerical simulations by Cain *et al.* (2000), Rowley *et al.* (2002*b*) and Larcheveque *et al.* (2003).

Previous theoretical models for cavity resonances have generally provided only incomplete representations of the phenomenon. In particular, the scattering processes at the cavity ends have generally not been analyzed, or have been treated heuristically. A key element in the present work is the analysis of the scattering processes at the cavity ends. The phases of the scattering coefficients at the two ends of the cavity are required for a first-principles prediction of the resonant frequency, while the amplitudes of the scattering coefficients are required in order to determine the temporal growth (or decay) rate of the mode, and the instability boundaries of the mode in parameter space. Prediction of the amplitude at which a resonant mode saturates is also dependent upon accurate determination of the amplitudes of the scattering coefficients.

For the case of supersonic flow, Kerschen & Tumin (2003) presented a model for cavity resonances that incorporates theoretical predictions for the scattering coefficients at the two ends of the cavity. In their analysis, the scattering coefficients are

determined by using a method employing the Wiener-Hopf technique (Noble, 1988), which treats the square-corner geometry exactly. The scattering coefficients are then combined with theoretical predictions for the propagation of the shear-layer instability wave and the acoustic waves along the length of the cavity. The combined system takes the form of a matrix eigenvalue problem, which determines the complex frequencies of the modes. The real part of the frequency determines the temporal oscillation of the unsteady field, while the imaginary part of the frequency determines the temporal growth (or decay) rate of the mode. Predictions of the model were found to be in good agreement with experimental data.

In this dissertation, we study flow-acoustic resonance in a cavity under a subsonic stream, in an unbounded stream. We extend the approach by Kerschen & Tumin (2003) to the case of a subsonic flow. While the general approach remains the same to that for the supersonic case, there are significant differences in the analysis related to the fact that external acoustic waves (with cylindrical spreading and algebraic decay) can propagate upstream in a subsonic flow.

The common description of cavity resonance is that of a free response of an unstable system, also known as self-sustained oscillations (feedback loop). These oscillations are caused by the four elements discussed at the begining of this chapter, and in the absence of external forcing, the oscillations will keep going. The final amplitudes of the oscillations are determined by nonlinear saturation. A remarkable result by Rowley *et al.* (2002*b*) proposes that for many parameter ranges in which resonance occurs, the oscillations are the forced response of a stable system and the final amplitude is determined by the amplitude of the forcing disturbances. In other words, if the external forcing (for example mixing layer turbulence) is taken away, the resonances would disappear. Our theory will examine this issue.

Experiments performed by Williams *et al.* (2000) and Ukeiley *et al.* (2003) showed the existence of a dominant mode for certain conditions, like Mach number and cavity length to depth ratio. Debiasi *et al.* (2004) performed experiments for a cavity in

a wind tunnel for Mach numbers $0.25 < M < 0.5$. Acoustic treatment was not introduced within the wind tunnel. In their experiments, dominant mode behavior is observed over much of the Mach number range they examined.

Another important issue related to dominant mode behavior was raised by Rowley *et al.* (2002*b*). They found dominant mode behavior for $M = 0.34$, a Mach number sweep showed no dominant mode behavior at other Mach numbers in the range $0.1 \leq M \leq 0.45$. By examining the probability density function (PDF) and phase portrait, they showed that the dominant mode response at $M = 0.34$ had a limit cycle behavior, as expected for the nonlinear saturation of a linearly unstable mode. However, at all other Mach numbers, the PDF and the phase portrait showed that the resonance was the forced response of a stable system.

Koch (2004) performed numerical computations for the prediction of the resonant frequencies and their decaying rates for the case of an unconfined cavity, with no mean flow. Recent investigations by Alvarez & Kerschen (2005) suggest that extending the current theory to a wind tunnel setting may give a physical and mathematical explanation of the dominant mode behavior.

2. GLOBAL MODEL

In this chapter we present the different disturbance elements that have an effect in cavity acoustic resonances, for the cavities of interest. In section 2.1 we present a global model with all the elements that are important for shallow cavities ($3 \leq L'/d' \leq 8$), representative of aircraft weapon bays. The model obtained involves different feedback loops. Section 2.2 presents a reasonable simplification of this model that allows us to predict the resonant frequencies and their stability characteristics.

2.1 Global Model

The global model for subsonic flow contains a shear-layer instability wave ($\mathcal{S}$), upstream and downstream-propagating acoustic modes in the cavity ($\mathcal{U}$ and $\mathcal{D}$), and upstream- and downstream-propagating external acoustic fields ($\mathcal{E}_u$ and $\mathcal{E}_d$) as illustrated in figure 2.1.

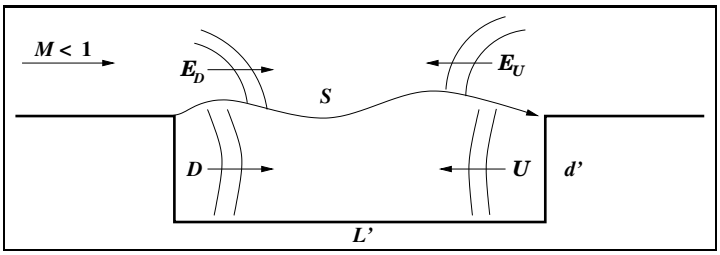

Figure 2.1 *Global model for subsonic flow*

A cavity mode is a disturbance dominated by the physics of wave propagation in the cavity region, which produces a deflection of the instability wave, producing a disturbance (a 'tail') in the stream. An external field is an outward propagating cylindrical wave field in the stream which produces a deflection of the instability wave, producing a disturbance in the cavity.

The total disturbance field actually contains an infinite number of upstream and downstream cavity modes, but for reasons that will become clear in Chapter 3, only

the lowest order modes exhibit weak exponential decay while traveling across the length of the cavity, while the higher-order modes exhibit rapid exponential decay that increases with mode order. This and the fact that we are considering cavities with length to depth aspect ratios $3 \leq L'/d' \leq 8$, allows us to do the present simplification.

First consider the scattering process at the upstream end of the cavity. The local amplitudes of all quantities at the upstream end of the cavity ($x' = 0$) are denoted by the decoration ($\hat{}$). The scattering process at the upstream end involves the impingement of the upstream-propagating acoustic cavity mode of amplitude $\hat{\mathcal{U}}$ and the upstream-propagating external field of amplitude $\hat{\mathcal{E}}_u$, which produce the three downstream-propagating components. The (complex) amplitudes of the downstream-propagating components generated by this scattering process are given by

$$\begin{bmatrix} \hat{\mathcal{S}} \\ \hat{\mathcal{D}} \\ \hat{\mathcal{E}}_d \end{bmatrix} = \begin{bmatrix} C_{\mathcal{S}\mathcal{U}} & C_{\mathcal{S}\mathcal{E}_u} \\ C_{\mathcal{D}\mathcal{U}} & C_{\mathcal{D}\mathcal{E}_u} \\ C_{\mathcal{E}_d\mathcal{U}} & C_{\mathcal{E}_d\mathcal{E}_u} \end{bmatrix} \begin{bmatrix} \hat{\mathcal{U}} \\ \hat{\mathcal{E}}_u \end{bmatrix}, \tag{2.1}$$

where the six scattering coefficients for the upstream end, $C_{\mathcal{S}\mathcal{U}}$, $C_{\mathcal{D}\mathcal{U}}$, $C_{\mathcal{E}_d\mathcal{U}}$, $C_{\mathcal{S}\mathcal{E}_u}$, $C_{\mathcal{D}\mathcal{E}_u}$ and $C_{\mathcal{E}_d\mathcal{E}_u}$, are determined by the procedure discussed in chapter 3.

Next consider the scattering process at the downstream end of the cavity. Quantities without decoration denote the local amplitudes at the downstream end of the cavity ($x' = L'$). The scattering process at the downstream end involves the impingement of the three downstream-propagating components, each of which makes a contribution to the amplitude of the upstream-propagating acoustic cavity mode $\mathcal{U}$ and external field $\mathcal{E}_u$,

$$\begin{bmatrix} \mathcal{U} \\ \mathcal{E}_u \end{bmatrix} = \begin{bmatrix} C_{\mathcal{U}\mathcal{S}} & C_{\mathcal{U}\mathcal{D}} & C_{\mathcal{U}\mathcal{E}_d} \\ C_{\mathcal{E}_u\mathcal{S}} & C_{\mathcal{E}_u\mathcal{D}} & C_{\mathcal{E}_u\mathcal{E}_d} \end{bmatrix} \begin{bmatrix} \mathcal{S} \\ \mathcal{D} \\ \mathcal{E}_d \end{bmatrix}, \tag{2.2}$$

where the six scattering coefficients for the downstream end, $C_{\mathcal{U}\mathcal{S}}$, $C_{\mathcal{U}\mathcal{D}}$, $C_{\mathcal{U}\mathcal{E}_d}$, $C_{\mathcal{E}_u\mathcal{S}}$, $C_{\mathcal{E}_u\mathcal{D}}$ and $C_{\mathcal{E}_u\mathcal{E}_d}$, are determined by the procedure discussed in Chapter 5.

Since the instability wave is the only disturbance element that grows both in

space (as it travels downstream) and time, it is useful to introduce the nondimensional length scale U/ω and time scale $1/\omega$, where ω is the real part of the complex frequency $\omega_c = \omega(1 + \mathrm{i}\eta)$ of the instability wave.

Finally, consider the evolution of all components as they propagate from one end of the cavity to the other. For the sake of convenience in formulating the analysis, we consider the case where the propagation characteristics are not a function of x. However, the streamwise dependence of the propagation characteristics is accounted for in the actual calculations, as discussed in appendix B. For the downstream-propagating components, the changes in the complex amplitudes of the components in propagating from the upstream end of the cavity to the downstream end are given by

$$\mathcal{S} = \hat{\mathcal{S}}\mathrm{e}^{\mathrm{i}\alpha L}, \quad \mathcal{D} = \hat{\mathcal{D}}\mathrm{e}^{\mathrm{i}\tau_d L}, \quad \mathcal{E}_d = \hat{\mathcal{E}}_d \mathrm{e}^{\mathrm{i}M_d L}/L^{3/2}. \tag{2.3}$$

Here, $L = \frac{\omega L'}{d}$ is the dimensionless length of the cavity and α and τ_d are the wavenumbers of the instability wave and the downstream-propagating acoustic cavity mode. The wavenumber for the downstream propagating wave in the external stream is given by $M_d = M(1 + \mathrm{i}\eta)/(1 + M)$, where $M = U/c$ is the Mach number. Note that the external field exhibits an algebraic decay of $x^{-3/2}$ along the cavity, in contrast to the $r^{-1/2}$ decay for directions away from the cavity boundary ($r = \sqrt{x^2 + y^2}$) (see Appendix C). This behavior differs from the case of an external field generated by a two dimensional point source, in which the external field exhibits an $r^{-1/2}$ in all directions.

Similarly, for the upstream-propagating components, the changes in the complex amplitudes in propagating from the downstream end of the cavity to the upstream end are given by

$$\hat{\mathcal{U}} = \mathcal{U}\mathrm{e}^{\mathrm{i}\tau_u L}, \quad \hat{\mathcal{E}}_u = \mathcal{E}_u \mathrm{e}^{\mathrm{i}M_u L}/L^{3/2}. \tag{2.4}$$

Here τ_u is the wavenumber of the upstream-propagating cavity mode, while the wavenumber for the upstream-propagating wave in the external stream is given by

$M_u = M(1+\mathrm{i}\eta)/(1-M)$.

The global eigenrelation is obtained by combining the above scattering and propagation relations. Consider the unknown amplitude vector

$$X = \begin{bmatrix} \mathcal{U} \\ \mathcal{E}_u \\ \hat{\mathcal{S}} \\ \hat{\mathcal{D}} \\ \hat{\mathcal{E}}_d \end{bmatrix}. \tag{2.5}$$

Substituting (2.3) into (2.2), and (2.4) into (2.1), we can form the matrix equation $AX = 0$, where

$$A = \begin{bmatrix} -1 & 0 & C_{\mathcal{US}}\mathrm{e}^{\mathrm{i}\alpha L} & C_{\mathcal{UD}}\mathrm{e}^{\mathrm{i}\tau_d L} & L^{-3/2}C_{\mathcal{U}\mathcal{E}_d}\mathrm{e}^{\mathrm{i}M_d L} \\ 0 & -1 & C_{\mathcal{E}_u\mathcal{S}}\mathrm{e}^{\mathrm{i}\alpha L} & C_{\mathcal{E}_u\mathcal{D}}\mathrm{e}^{\mathrm{i}\tau_d L} & L^{-3/2}C_{\mathcal{E}_u\mathcal{E}_d}\mathrm{e}^{\mathrm{i}M_d L} \\ C_{\mathcal{SU}}\mathrm{e}^{\mathrm{i}\tau_u L} & L^{-3/2}C_{\mathcal{S}\mathcal{E}_u}\mathrm{e}^{\mathrm{i}M_u L} & -1 & 0 & 0 \\ C_{\mathcal{DU}}\mathrm{e}^{\mathrm{i}\tau_u L} & L^{-3/2}C_{\mathcal{D}\mathcal{E}_u}\mathrm{e}^{\mathrm{i}M_u L} & 0 & -1 & 0 \\ C_{\mathcal{E}_d\mathcal{U}}\mathrm{e}^{\mathrm{i}\tau_u L} & L^{-3/2}C_{\mathcal{E}_d\mathcal{E}_u}\mathrm{e}^{\mathrm{i}M_u L} & 0 & 0 & -1 \end{bmatrix}. \tag{2.6}$$

Calculating the determinant, we obtain the eigenvalue relation

$$\begin{aligned}
&\mathrm{e}^{\mathrm{i}L(\alpha+\tau_u)}C_{\mathcal{SU}}C_{\mathcal{US}} + \mathrm{e}^{\mathrm{i}L(\tau_d+\tau_u)}C_{\mathcal{DU}}C_{\mathcal{UD}} + L^{-3/2}\mathrm{e}^{\mathrm{i}L(\alpha+M_u)}C_{\mathcal{S}\mathcal{E}_u}C_{\mathcal{E}_u\mathcal{S}} \\
&+L^{-3/2}\mathrm{e}^{\mathrm{i}L(\tau_d+M_u)}C_{\mathcal{D}\mathcal{E}_u}C_{\mathcal{E}_u\mathcal{D}} + L^{-3/2}\mathrm{e}^{\mathrm{i}L(M_d+\tau_u)}C_{\mathcal{E}_d\mathcal{U}}C_{\mathcal{U}\mathcal{E}_d} + L^{-3}\mathrm{e}^{\mathrm{i}L(M_d+M_u)}C_{\mathcal{E}_d\mathcal{E}_u}C_{\mathcal{E}_u\mathcal{E}_d} \\
&+L^{-3/2}\mathrm{e}^{\mathrm{i}L(\alpha+\tau_d+M_u+\tau_u)}[C_{\mathcal{SU}}C_{\mathcal{E}_u\mathcal{S}}C_{\mathcal{D}\mathcal{E}_u}C_{\mathcal{UD}} + C_{\mathcal{DU}}C_{\mathcal{E}_u\mathcal{D}}C_{\mathcal{S}\mathcal{E}_u}C_{\mathcal{US}} \\
&-C_{\mathcal{DU}}C_{\mathcal{UD}}C_{\mathcal{S}\mathcal{E}_u}C_{\mathcal{E}_u\mathcal{S}} - C_{\mathcal{SU}}C_{\mathcal{US}}C_{\mathcal{D}\mathcal{E}_u}C_{\mathcal{E}_u\mathcal{D}}] \\
&+L^{-3}\mathrm{e}^{\mathrm{i}L(\alpha+M_d+M_u+\tau_u)}[C_{\mathcal{SU}}C_{\mathcal{E}_u\mathcal{S}}C_{\mathcal{E}_d\mathcal{E}_u}C_{\mathcal{U}\mathcal{E}_d} + C_{\mathcal{E}_d\mathcal{U}}C_{\mathcal{E}_u\mathcal{E}_d}C_{\mathcal{S}\mathcal{E}_u}C_{\mathcal{US}} \\
&-C_{\mathcal{E}_d\mathcal{U}}C_{\mathcal{U}\mathcal{E}_d}C_{\mathcal{S}\mathcal{E}_u}C_{\mathcal{E}_u\mathcal{S}} - C_{\mathcal{SU}}C_{\mathcal{US}}C_{\mathcal{E}_d\mathcal{E}_u}C_{\mathcal{E}_u\mathcal{E}_d}] \\
&+L^{-3}\mathrm{e}^{\mathrm{i}L(M_d+\tau_d+M_u+\tau_u)}[C_{\mathcal{E}_d\mathcal{U}}C_{\mathcal{E}_u\mathcal{E}_d}C_{\mathcal{D}\mathcal{E}_u}C_{\mathcal{UD}} + C_{\mathcal{DU}}C_{\mathcal{E}_u\mathcal{D}}C_{\mathcal{E}_d\mathcal{E}_u}C_{\mathcal{U}\mathcal{E}_d} \\
&-C_{\mathcal{DU}}C_{\mathcal{UD}}C_{\mathcal{E}_d\mathcal{E}_u}C_{\mathcal{E}_u\mathcal{E}_d} - C_{\mathcal{E}_d\mathcal{U}}C_{\mathcal{U}\mathcal{E}_d}C_{\mathcal{D}\mathcal{E}_u}C_{\mathcal{E}_u\mathcal{D}}] = 1
\end{aligned} \tag{2.7}$$

The complex frequency enters implicitly in the propagation wavenumbers (τ_u, M_u, α, τ_d and M_d) for the components of the disturbance field ($\mathcal{U}$, $\mathcal{E}_u$, $\mathcal{S}$, $\mathcal{D}$ and $\mathcal{E}_d$), and in the various scattering coefficients ($C_{\mathcal{SU}}$, etc.). This eigenvalue relation contains all possible feedback paths involving the two upstream-propagating components ($\mathcal{U}$ and

$\mathcal{E}_u$) and the three downstream-propagating components ($\mathcal{S}$, $\mathcal{D}$ and $\mathcal{E}_d$). Our theoretical model incorporates non-parallel mean flow effects, so that the simple propagation factors in (2.7) are replaced by integrals along the length of the cavity.

2.2 Simplified Global Model

The relative importance of the various feedback loops in the eigenrelation (2.7), depends on the propagation factors or the scattering coefficients. When looking at the propagation factors in (2.7), the only component of the disturbance field that exhibits exponential growth is the instability wave ($\mathrm{Im}[\alpha] < 0$). The amplitude of the instability wave can increase by a factor of ten when propagating across the length of the cavity. In contrast, the wavenumbers τ_d and M_d of the other two downstream-propagating disturbances (the downstream mode $\mathcal{D}$ and the external field $\mathcal{E}_d$) are real when $\eta = 0$. The upstream-propagating cavity mode $\mathcal{U}$ exhibits weak exponential decay at a rate set by $\mathrm{Im}[\tau_u] > 0$. The wavenumber of the upstream external field $\mathcal{E}_u$ is real for $\eta = 0$, but decays algebraically as $x^{-3/2}$. Furthermore, the amplitude of scattering coefficient $C_{\mathcal{E}_u\mathcal{S}}$ is small compared to that of $C_{\mathcal{U}\mathcal{S}}$. Thus, for shallow cavities of interest ($3 < L/d < 8$), it is clear that the main loop involves the instability wave and the upstream-propagating cavity mode. Hence the eigenrelation (2.7) simplifies to

$$\left(C_{\mathcal{S}\mathcal{U}}\mathrm{e}^{\mathrm{i}\alpha L}\right)\left(C_{\mathcal{U}\mathcal{S}}\mathrm{e}^{\mathrm{i}\tau_u L}\right) = 1. \tag{2.8}$$

The first factor in parentheses involves the scattering of an upstream cavity mode of amplitude unity into a downstream-propagating shear-layer instability wave of amplitude $C_{\mathcal{S}\mathcal{U}}$, which is then amplified and phase shifted by the factor $\mathrm{e}^{\mathrm{i}\alpha L}$ in propagating the length of the cavity. The impingement of the shear-layer instability wave on the downstream end of the cavity then generates an upstream-propagating acoustic cavity mode of relative amplitude $C_{\mathcal{U}\mathcal{S}}$, which suffers a decay and phase shift given by $\mathrm{e}^{\mathrm{i}\tau_u L}$

in propagating the length of the cavity. For the eigenvalue relation to be satisfied, the argument on the left-hand side of (2.8) must be a multiple of 2π, while its magnitude must be equal to one. These two conditions are a coupled set of equations for ω and η, but the coupling is relatively weak. The frequency ω of the resonant mode ($\mathrm{Re}[\omega_c]$) is primarily set by the phase condition; while the growth rate ($\mathrm{Im}[\omega_c] = \omega\eta$) is primarily set by the amplitude condition. This behavior is easily seen by introducing a complex version of the non-dimensional frequency $L_c = \omega_c L'/U$ and modified forms of the disturbances wavenumbers $\bar{\alpha} = \alpha/(1 + \mathrm{i}\eta)$ and $\bar{\tau_u} = \tau_u/(1 + \mathrm{i}\eta)$. The modified wave numbers exhibit only weak dependence on η. Now, equation (2.8) can be solved for

$$L_c = \omega_c L'/U = L_r + \mathrm{i}L_i.$$

We obtain

$$L_r = 2\pi \frac{m - (\mathrm{Arg}[C_{US}] + \mathrm{Arg}[C_{SU}] + \epsilon \log(|C_{US}||C_{SU}|)/2\pi}{\mathrm{Re}[\bar{\alpha} + \bar{\tau_u}](1 + \epsilon^2)} \tag{2.9}$$

and

$$L_i = \frac{\log(|C_{US}||C_{SU}|) - \mathrm{Im}[\bar{\alpha} + \bar{\tau_u}]L_r}{\mathrm{Re}[\bar{\alpha} + \bar{\tau_u}]}, \tag{2.10}$$

where

$$\epsilon = \frac{\mathrm{Im}[\bar{\alpha} + \bar{\tau_u}]}{\mathrm{Re}[\bar{\alpha} + \bar{\tau_u}]}.$$

The formula (2.9) for the non-dimensional resonance frequency has much in common with Rossiter's semi-empirical formula. In order to obtain Rossiter's formula from (2.9), we would set ϵ to zero, replace $\mathrm{Re}[\bar{\tau_u}]$ by propagation of $\mathcal{U}$ at the speed of sound, replace $\mathrm{Re}[\bar{\alpha}]$ by propagation of $\mathcal{S}$ at some fraction of the flow speed U, and replace $(\mathrm{Arg}[C_{US}] + \mathrm{Arg}[C_{SU}])/2\pi$ by an additional empirical constant. In our theoretical model, all quantities are obtained from solutions to the governing equations—our result contains no empirical constants. Note also that the 'constants' in Rossiter's formula are actually functions of the various geometric and flow parameters. The

success of Rossiter's semi-empirical prediction for the resonant frequencies is largely due to the fact that these various 'constants' do not change rapidly as a function of the parameters.

In addition to prediction of the resonant frequency, our theory also provides an expression for L_i, the growth (or decay) rate of each mode. Rossiter's semi-empirical formula provides no information for this important quantity. Values $L_i > 0$ correspond to unstable modes. Our expression for L_i has a clear physical interpretation. We see that the growth (or decay) rate of the mode depends on both amplitude gains (or losses) due to scattering at the cavity ends, and amplification (or decay) of the components $\mathcal{S}$ and $\mathcal{U}$ in propagating the length of the cavity. To account for the shear-layer thickness across the length of the cavity, the dependece of the wavenumber α of the instability wave on x, must be taken into account. Our prediction method for the instability wave propagation is a multiple-scale technique, used by Yang & Tumin (2002), that accounts for the streamwise variation of the mean flow. The method determines the complex gain across the length of the cavity $\mathcal{S}/\hat{\mathcal{S}}$ of the instability wave. Then the multiple-scales prediction is introduced in equations (2.9) and (2.10) by setting

$$\bar{\alpha} = \frac{\ln(|\mathcal{S}/\hat{\mathcal{S}}|) + \mathrm{i}\arg(\mathcal{S}/\hat{\mathcal{S}})}{\mathrm{i}L_c}, \tag{2.11}$$

which is obtained from equation (2.3). Note that no empirical constants are present in our expression for L_i.

Returning to the eigenvalue relation (2.7) for the more general case, we see that it contains many secondary loops involving other components of the total field. Some secondary loops involve only one downstream and one upstream pass (for example, $\mathrm{e}^{\mathrm{i}L(\tau_d+\tau_u)}C_{\mathcal{DU}}C_{\mathcal{UD}}$), while other secondary loops involve multiple upstream and downstream passes.

We found that the secondary feedback paths are relatively unimportant for the

case of a cavity under an unbounded subsonic stream. Recent results by Alvarez & Kerschen (2005) show that the situation is quite different for a cavity under a bounded stream, such as the case of cavity resonance experiments performed in a wind tunnel. In this situation the field external to the cavity may have a significant effect on the resonance behavior.

In the following chapters, we discuss the calculation of the various scattering and propagation coefficients which enter in the eigenrelation for the global modes. In general, the solution of the linear eigenvalue relation corresponds to a complex frequency $\omega_c = \omega(1 + \mathrm{i}\eta)$, for fixed geometry and mean flow conditions. The imaginary part of the frequency, $\omega\eta$, corresponds to a temporal growth rate for the cavity resonant mode. However, our eventual goal is the full prediction of saturated cavity resonances. In this case the temporal growth of the linear cavity resonance has been counteracted by dissipative nonlinear effects, so that the resonance has saturated at a finite amplitude and no longer exhibits temporal growth. In this situation, the scattering coefficients for real values of the frequency ($\eta = 0$) are relevant. One of most important sources of nonlinear saturation is the instability wave behavior. The nonlinear saturation of the instability wave will reduce the gain from this element of the resonant loop to a value significantly below $\mathrm{e}^{\mathrm{i}\alpha L}$.

3. SCATTERING PROCESS AT THE UPSTREAM END OF THE CAVITY

In this chapter results for the scattering processes at the upstream end of the cavity are presented. The cavity is assumed large enough that the effects of the downstream end can be neglected. We assume harmonic time dependence, linearize the governing equations, and approximate the shear-layer by a vortex sheet.

At the upstream end, the primary incident field is the lowest-order upstream-propagating acoustic cavity mode (the $\mathcal{U}$ mode discussed in section 2.1). In Section 3.1, we present the governing equations and boundary conditions with the afore mentioned simplifications.

The scattering problems are solved using the generalized Wiener-Hopf technique (Noble, 1988). To do this, the upstream end of the cavity is substituted by a semi-infinite overhanging lip of zero thickness. An acoustic duct mode is an acoustic field that propagates in the 'duct' formed by the cavity bottom and overhanging lip. It satisfies the no-penetration boundary conditions on the cavity bottom and inner surface of the overhanging lip.

Since both usptream-/downstream-propagating acoustic cavity and duct modes are acoustic in nature, we will omit the words acoustic and propagating when refering to these modes, throughout the rest of this work. Instead, we shall refer to them as upstream/downstream cavity modes and upstream/downstream duct modes, respectively.

In section 3.2.1, we consider the interaction of the upstream cavity mode $\mathcal{U}$ with the edge of the overhanging lip, and in section 3.2.2, the interaction of a downstream-propagating duct mode with the edge of the overhanging lip.

In section 3.3, a vertical end-wall is added under the overhanging lip, creating a finite-length overhanging lip of length b'. This problem is solved by solving a truncated

matrix problem and then $b' \to 0$ to solve for a square (90°) upstream corner.

3.1 General Formulation at the Upstream End of the Cavity

The geometries and non-dimensional coordinate system for analysis of the unsteady flow in the vicinity of the upstream edge of a cavity are illustrated in figure 3.1. Three model geometries are illustrated. The case of a square (90°) corner is illustrated in figure 3.1(a), the case of a thin overhanging lip of finite length b' is illustrated in figure 3.1(b), and a semi-infinite overhanging lip with no end wall is illustrated in figure 3.1(c). The origin of the coordinate system is placed at the edge of the cavity lip. In analyzing the interaction at the upstream edge of the cavity, the cavity is assumed long enough that the presence of the downstream edge can be neglected.

Since the shear layer instabilities, which form a crucial element of the cavity resonance phenomenon, are primarily two-dimensional in nature, we shall assume that the geometry and flow field are two dimensional. In order to simplify the local analyses for the scattering processes at the ends of the cavity, the shear layer will be represented by a vortex sheet. This approximation is quite realistic for the upstream interaction, since the upstream boundary layer which sets the initial thickness of the shear layer is usually quite thin. The vortex-sheet approximation is less realistic for the interactions at the downstream end.

We shall call 'stream region' the region where $y' > 0$ and $x' > 0$, and 'cavity region' where $y' < 0$ and $x' > 0$. The subscript $(\cdot)_1$ will denote a quantity in the stream region, while the subscript $(\cdot)_2$ a quantity in the cavity region. In general, the temperature in each region is different ($T_1 \neq T_2$), therefore we have different mean properties for both regions (ρ_{01}, ρ_{02}, c_{01}, c_{02}).

In the stream region $y' > 0$, a uniform flow of speed U and Mach Number $M = U/c < 1$ is present. There is no mean flow in the cavity region $y' < 0$. The shear layer spanning the open face of the cavity is represented by a vortex sheet. In the analysis

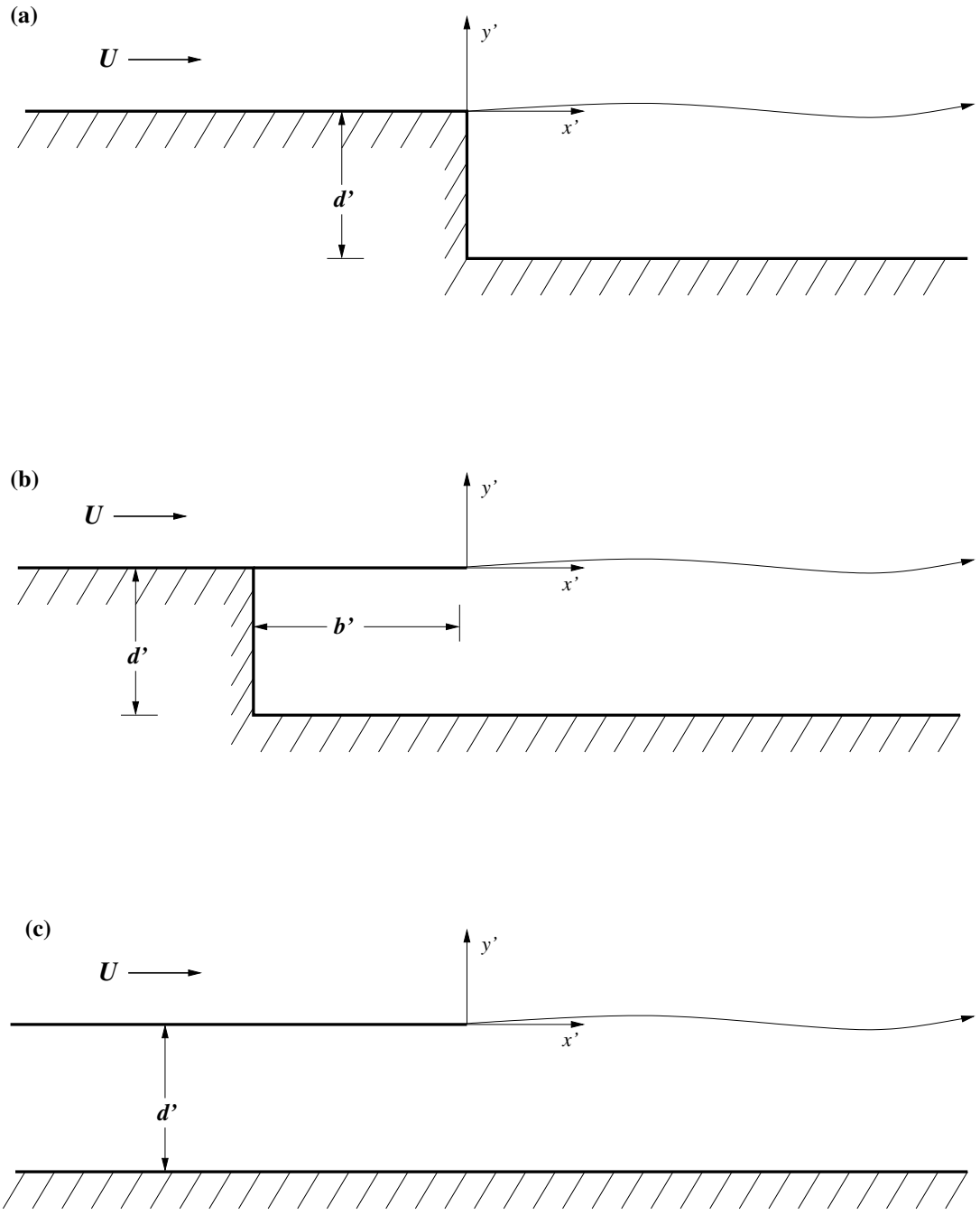

Figure 3.1 *Sketch of geometries for the interactions at the upstream end of the cavity: (a) square corner, (b) thin overhanging lip of finite length b, (c) semi-infinite overhanging lip.*

of the local interaction at the upstream edge of the cavity, the cavity geometry and the vortex sheet are assumed to extend to infinity in the downstream direction. The cavity bottom at $y' = -d'$ is assumed to be rigid and impermeable, and to have infinite extent in the case illustrated in figure 3.1(c).

Linearizing the governing equations about the base state, the flow perturbations $(p_1', \rho_1', \mathbf{u_1'})$ in the stream $(y' > 0)$ satisfy the dimensional equations

$$\frac{Dp_1'}{Dt'} + \rho_{01} c_1^2 \nabla \cdot \mathbf{u_1'} = \mathbf{0}, \tag{3.1}$$

$$\rho_{01} \frac{D\mathbf{u_1'}}{Dt'} = -\nabla p_1', \tag{3.2}$$

$$p_1' = c_1^2 \rho_1', \tag{3.3}$$

where $\mathbf{u_1'} = (u_1', v_1')$, t' is time, and $\frac{D}{Dt'} = \frac{\partial}{\partial t'} + U\frac{\partial}{\partial x'}$ is the substantial derivative with respect to the mean flow. The flow perturbations $(p_2', \rho_2', \mathbf{u_2'})$ within the cavity $(y' < 0)$ satisfy the above equations with the mean flow properties for region 2 and with U set to zero, namely

$$\frac{\partial p_2'}{\partial t'} + \rho_{02} c_2^2 \nabla \cdot \mathbf{u_2'} = \mathbf{0}, \tag{3.4}$$

$$\rho_{02} \frac{\partial \mathbf{u_2'}}{\partial t'} = -\nabla p_2', \tag{3.5}$$

$$p_2' = c_2^2 \rho_2'. \tag{3.6}$$

Across the vortex sheet, the perturbation field satisfies the vortex sheet matching conditions:

- Continuity of pressure:

$$p_1'|_{y'=0^+} = p_2'|_{y'=0^-}, \tag{3.7}$$

- Continuity of particle displacement:

$$v_1'|_{y'=0^+} = \frac{\partial h'}{\partial t'} + U\frac{\partial h'}{\partial x'} \quad \text{and} \quad v_2'|_{y'=0^-} = \frac{\partial h'}{\partial t'}, \tag{3.8}$$

where $h'(x',t')$ is the displacement of the vortex sheet and linearization has been utilized to transfer the conditions from the instantaneous position $y' = h'(x',t')$ to the mean surface $y' = 0_{\pm}$.

Within the cavity, the no-penetration condition applies at the cavity bottom,

$$v_2'|_{y'=-d'} = 0. \tag{3.9}$$

Outside the cavity, the perturbation field satisfies the no-penetration condition on the body surface,

$$v_1'|_{y'=0^+} = 0. \tag{3.10}$$

For the case of overhanging lips, as in figures 3.1(b,c), the perturbation field also satisfies the no-penetration condition on the inside surface of the overhanging lip,

$$v_2'|_{y'=0^-} = 0. \tag{3.11}$$

For the case of a finite length overhanging lip (figure 3.1(b)), the perturbation field satisfies the no-penetration boundary condition on the vertical end wall,

$$u_2'|_{x'=-b'} = 0. \tag{3.12}$$

In the case of a 90° corner (figure 3.1(a)), the above condition applies at $x' = 0$. The Sommerfeld radiation condition applies at large distances from the downstream edge.

Since the flow is irrotational outside of the vortex sheet, the flow perturbations can be expressed in terms of velocity potentials, say $\phi_1(x',y',t')$ and $\phi_2(x',y',t')$. Setting $\mathbf{u_1'} = \nabla\phi_1'$, (3.2) can be integrated to obtain

$$p_1' = -\rho_{01}\frac{D\phi_1'}{Dt'}. \tag{3.13}$$

Equation (3.1) can now be written in the form

$$\nabla^2\phi_1' - \frac{1}{c_1^2}\frac{D^2}{Dt'^2}\phi_1' = 0. \tag{3.14}$$

The corresponding flow perturbations within the cavity satisfy the two equations above with ϕ_1' and c_1 replaced by ϕ_2' and c_2, respectively, and U set to zero,

$$\nabla^2\phi_2' - \frac{1}{c_2^2}\frac{\partial^2}{\partial t'^2}\phi_2' = 0. \tag{3.15}$$

Since we want to consider growing instabilities, it is necessary for the frequency to be complex. The complex frequency is $\omega_c = \omega(1 + \mathrm{i}\eta)$, where ω and η are real. It is convenient to utilize the real part of the frequency, ω, and the length scale U/ω to form the non-dimensional variables

$$(x, y) = \frac{\omega}{U}(x', y'), \qquad t = \omega t', \qquad d = \frac{\omega}{U}d', \qquad b = \frac{\omega}{U}b' \tag{3.16}$$

Since the governing equations are linear, we represent the unsteady perturbation as the sum of an incident field and a scattered field. The scattered field is generated by the interaction of the incident field with the upstream edge of the cavity. (Two different incident fields are considered in the following sections) Extracting the harmonic time dependence and utilizing the quantity U^2/ω to non-dimensionalize the velocity potentials, we obtain

$$\phi_{1,2}' = \frac{U^2}{\omega}\left[\phi_{i1,2} + \phi_{1,2}\right] e^{-\mathrm{i}(1+\mathrm{i}\eta)t}, \tag{3.17}$$

where $\phi_{i1,2}$ are the non-dimensional time-reduced potentials for the incident field and $\phi_{1,2}$ the corresponding potential for the scattered field. The incident field is assumed known (expressions are presented later), while the scattered field must be solved for.

The incident fields considered in this dissertation satisfy the convected wave equation (3.14) in the flow stream and its corresponding form (3.15) in the cavity. Hence the scattered field also satisfies these wave equations. The non-dimensional wave

equations satisfied by the scattered field are

$$\frac{\partial^2}{\partial x^2}\phi_1 + \frac{\partial^2}{\partial y^2}\phi_1 + M_1^2\left((1+\mathrm{i}\eta) + \mathrm{i}\frac{\partial}{\partial x}\right)^2\phi_1 = 0, \tag{3.18}$$

$$\frac{\partial^2}{\partial x^2}\phi_2 + \frac{\partial^2}{\partial y^2}\phi_2 + M_2^2(1+\mathrm{i}\eta)^2\phi_2 = 0, \tag{3.19}$$

where $M_1 = \frac{U}{c_1}$ and $M_2 = \frac{U}{c_2}$, and c_1 and c_2 are the speeds of sound in the stream and cavity region, respectively.

The incident field satisfies the no-penetration condition (3.9) on the bottom of the cavity, so that the scattered fields also satisfy

$$\frac{\partial \phi_2}{\partial y}|_{y=-d} = 0. \tag{3.20}$$

Expressing the no-penetration boundary conditions on the outside and inside surfaces of an overhanging lip (figures 3.1(b,c)) in terms of the reduced potentials for the scattered field, we have

$$\frac{\partial \phi_1}{\partial y}|_{y=0^+} = 0, \tag{3.21}$$

$$\frac{\partial \phi_2}{\partial y}|_{y=0^-} = 0. \tag{3.22}$$

If the incident field satisfies the no-penetration boundary conditions (3.10) and (3.11), then the scattered field satisfies the homogeneous conditions (3.21) and (3.22); if the incident field does not satisfy the no-penetration boundary conditions (3.10) and (3.11), then the scattered field satisfies an inhomogeneous form of (3.21) and (3.22).

Expressing the vortex sheet matching conditions (3.7) and (3.8) in terms of the reduced potentials for the scattered fields, we obtain

$$\rho_{01}\left[(1+\mathrm{i}\eta) + \mathrm{i}\frac{\partial}{\partial x}\right]\phi_1|_{y=0^+} = \rho_{02}(1+\mathrm{i}\eta)\phi_2|_{y=0^-}, \tag{3.23}$$

$$(1+\mathrm{i}\eta)\frac{\partial\phi_1}{\partial y}|_{y=0^+} = \left[(1+\mathrm{i}\eta)+\mathrm{i}\frac{\partial}{\partial x}\right]\frac{\partial\phi_2}{\partial y}|_{y=0^-}. \tag{3.24}$$

If the incident field satisfies the vortex sheet matching conditions (3.7) and (3.8), then the scattered field satisfies the homogeneous conditions (3.23) and (3.24); if the incident field does not satisfy the vortex sheet matching conditions, then the scattered field satisfies an inhomogeneous form of (3.23) and (3.24).

For the case of a finite length overhanging lip (figure 3.1(b)), the no-penetration boundary condition on the vertical end wall (3.12) takes the form

$$\frac{\partial\phi_2}{\partial x}|_{x=-b} = 0, \tag{3.25}$$

when expressed in terms of the reduced potentials for the scattered field. The homogeneous condition (3.25) applies if the incident field satisfies the no-penetration condition (3.12) on the end wall, while a non-homogeneous form of (3.25) applies if the incident field does not satisfy (3.12). In the case of a square (90 °) corner (figure 3.1(a)), the condition (3.25) applies at $x = 0$.

3.2 Analysis for a Semi-infinite Overhanging Lip

In this section we analyze the scattering process at the upstream edge of a cavity for the case of a semi-infinite overhanging lip. The geometry is illustrated in figure 3.1(c). This case is interesting in itself, and also provides a building block for the analysis in section 3.3 of the upstream interaction for the case of a finite-length overhanging lip or a square (90°) corner. In the next sections we consider the impingement of two different incident fields. In section 3.2.1 we consider the impingement of an upstream-propagating cavity mode which has originated further downstream in the cavity ($x > 0$), while in section 3.2.2 we consider the impingement of a downstream-propagating duct mode which has originated further upstream in the duct ($x < 0$ and

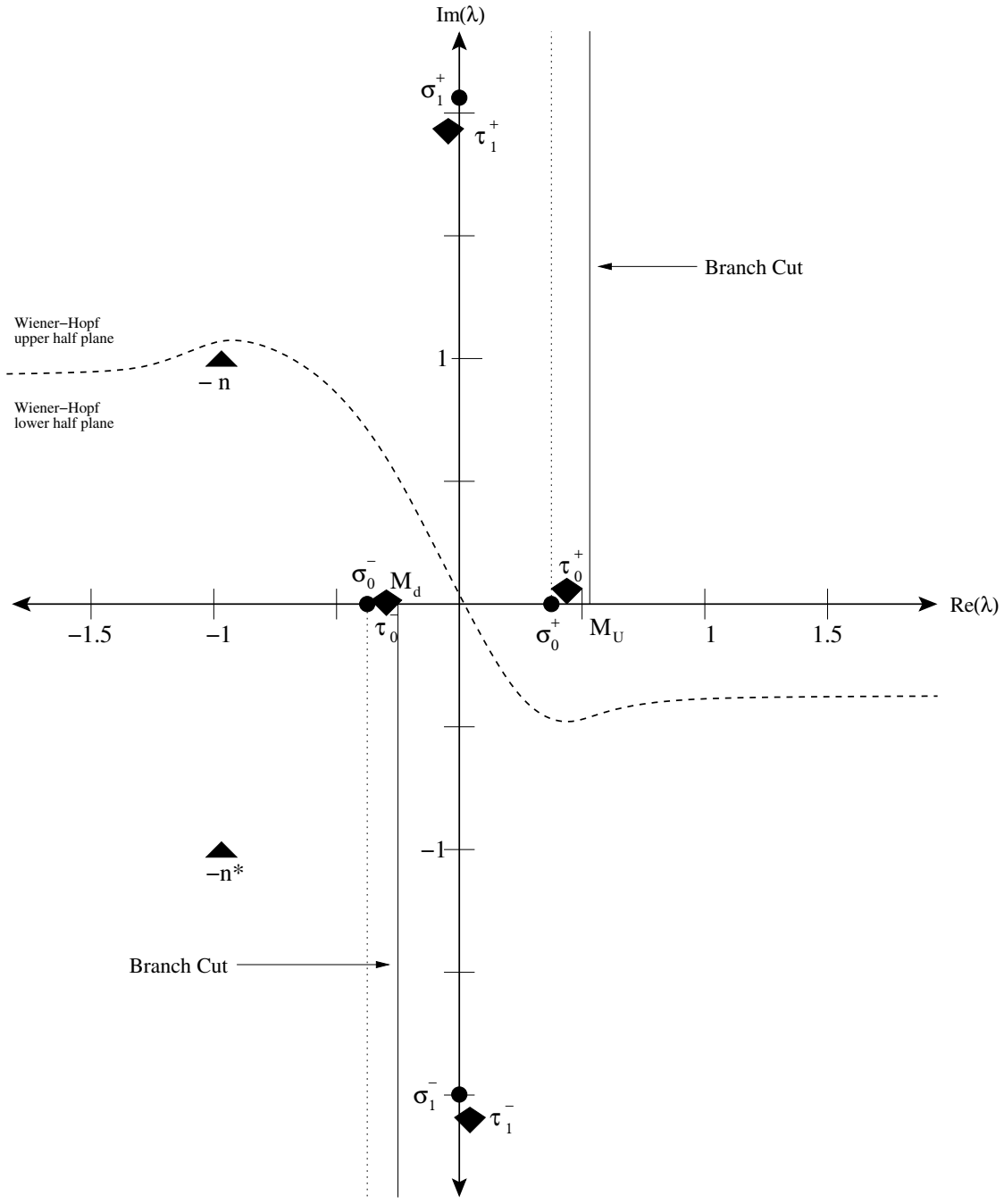

Figure 3.2 *Singularities in the Complex Plane*

$y < 0$). The results of these two sections will be used in section 3.3 to address the case of receptivity for a finite-length overhanging lip or a square (90°) corner.

A cavity mode is an acoustic field that satisfies the no-penetration boundary condition on the cavity bottom and the matching conditions of continuity of pressure and continuity of particle displacement across the vortex sheet. It is a disturbance dominated by physics of wave propagation in the cavity region. This field causes a deflection of the vortex sheet, which in turn produces a disturbance in the stream region ($y > 0$).

Both interactions in sections 3.2.1 and 3.2.2 will produce cavity modes, duct modes and external acoustic fields. An external acoustic field is basically an outward propagating, cylindrical wave field in the stream region ($y > 0$). Since this is also an acoustic disturbance, we will omit the word acoustic when refering to the external acoustic fields. An external field causes a deflection of the vortex sheet, producing a disturbance in the cavity. If this disturbance is produced by a downstream external field (same direction as the stream), the field in the cavity will be supersonic relative to the fluid in the cavity, similar to a Mach wave field. If the disturbance is produced by an upstream external field (opposite to the stream), the field in the cavity will be subsonic relative to the fluid in the cavity, producing an evanescent wave field.

3.2.1 Impingement of the Upstream Cavity Mode $\mathcal{U}$

In this section we analyze the unsteady field produced by the interaction of the upstream-propagating cavity mode $\mathcal{U}$ with a semi-infinite overhanging upstream lip. The cavity mode $\mathcal{U}$ is the first of an infinite set of eigenmodes for the cavity region. However, for the conditions of interest, all the higher-order modes exhibit strong exponential decay with upstream distance. Since the higher-order modes have decayed in amplitude to negligible levels, these modes do not contribute to the scattering process at the upstream end. Also, the wavenuber τ_u of the upstream cavity mode $\mathcal{U}$

introduced in the global model (see Chapter 2), is given by $\tau_u = \tau_0^+$, the wavenumber of the lowest order upstream cavity mode. The incident field for this case has the form

$$\phi_{i1}^{\mathcal{U}} = \frac{\rho_{02}(1+\mathrm{i}\eta)}{\rho_{01}[(1+\mathrm{i}\eta)+\tau_0^+]} \mathrm{e}^{-\mathrm{i}\tau_0^+ x} \mathrm{e}^{-\mu_1(\tau_0^+)y}, \tag{3.26}$$

$$\phi_{i2}^{\mathcal{U}} = \mathrm{e}^{-\mathrm{i}\tau_0^+ x} \frac{\cosh(\mu_2(\tau_0^+)(y+d))}{\cosh(\mu_2(\tau_0^+)d)}, \tag{3.27}$$

where $\mathcal{U}$ indicates that the incident field is the upstream-propagating cavity mode $\mathcal{U}$. The functions $\mu_1(\lambda)$ and $\mu_2(\lambda)$ are defined by (3.32) and (3.36), respectively. The incident field (3.26, 3.27) satisfies the reduced wave equations (3.18) and (3.19), the no-penetration condition on the cavity bottom (3.20) and the vortex sheet matching conditions (3.23) and (3.24). However, it does not satisfy the no-penetration conditions (3.21) and (3.22) on the inner and outer surfaces of the overhanging lip.

Thus, the scattered field also satisfies the reduced wave equations (3.18) and (3.19), the no-penetration condition on the cavity bottom (3.20), and the vortex sheet matching conditions (3.23) and (3.24) for $x > 0$. On the inner and outer surfaces of the overhanging lip ($x < 0$), it satisfies the inhomogeneous conditions

$$\frac{\partial \phi_1}{\partial y}|_{y=0^+} = \frac{\rho_{02}(1+\mathrm{i}\eta)}{\rho_{01}[(1+\mathrm{i}\eta)+\tau_0^+]} \mu_1(\tau_0^+) \mathrm{e}^{-\mathrm{i}\tau_0^+ x}, \tag{3.28}$$

$$\frac{\partial \phi_2}{\partial y}|_{y=0^-} = -\mathrm{e}^{-\mathrm{i}\tau_0^+ x} \mu_2(\tau_0^+) \tanh(\mu_2(\tau_0^+)d). \tag{3.29}$$

The equations governing the scattered field constitute a mixed boundary value problem, since the boundary conditions for $x < 0$ are different than those for $x > 0$. Due to the mixed boundary conditions, the solution cannot be obtained by a straight forward application of a Fourier transform. In this work, we use the Wiener-Hopf technique (Noble, 1988) to derive the solution. The Wiener-Hopf technique involves a combination of Fourier transform methods and analytic continuation in the complex plane of the transform variable λ.

The Fourier transform $\Phi(\lambda, y)$ and its inverse are defined as

$$\Phi(\lambda, y) = \int_{-\infty}^{\infty} \phi(x, y)\ \mathrm{e}^{\mathrm{i}\lambda x} dx, \qquad \phi(x, y) = \frac{1}{2\pi} \int_{-\infty}^{\infty} \Phi(\lambda, y)\ \mathrm{e}^{-\mathrm{i}\lambda x} d\lambda \tag{3.30}$$

Applying Fourier transform to (3.18), solving the resulting ordinary differential equation and noting that the solution must remain bounded as $y \to \infty$, we obtain the solution for $y > 0$,

$$\Phi_1 = B_1(\lambda) e^{-\mu_1(\lambda) y}, \tag{3.31}$$

where

$$\mu_1(\lambda) = \left[\lambda^2 - M_1^2(\lambda + (1 + \mathrm{i}\eta))^2\right]^{\frac{1}{2}} \tag{3.32}$$

$$= \beta \left[(\lambda - M_u)(\lambda - M_d)\right]^{\frac{1}{2}} \tag{3.33}$$

and

$$\beta = \left(1 - M_1^2\right)^{\frac{1}{2}}, \qquad M_u = \frac{M_1(1 + \mathrm{i}\eta)}{1 - M_1}, \qquad M_d = \frac{-M_1(1 + \mathrm{i}\eta)}{1 + M_1}, \tag{3.34}$$

where we have chosen the negative sign in the exponent in (3.31), so that for real λ, $\mu_1(\lambda) > 0$ as $\lambda \to \infty$. Notice also that the branch points M_u and M_d are the x-wavenumbers of the upstream and downstream external acoustic fields, respectively.

In order to satisfy the Sommerfeld radiation condition (solution must consist only of outward traveling waves), the branch points at $\lambda = M_u$ and $\lambda = M_d$ are assumed to lie just above and below the real λ axis, respectively. The branch cut from M_u extends up into the upper half-plane, while that from M_d extends down into the lower half-plane, as illustrated in figure 3.2. The function $\mu_1(\lambda)$ is real and positive for real values of λ in the ranges $\lambda < M_d$ and $\lambda > M_u$ and is negative imaginary for real values of λ in the range $M_d < \lambda < M_u$. The function $\mu_1(\lambda)$ changes sign when crossing the lines $M_d < \lambda < M_u$ and $\mathrm{Re}[\lambda] = \frac{M_u + M_d}{2}$. This allows some disturbances to grow in y, but as will be explained in Chapter 4, these disturbances will still decay as $r = \sqrt{x^2 + y^2} \to \infty$.

Similarly, applying the Fourier transform to (3.19) and utilizing the boundary condition (3.20) on the cavity bottom, we obtain the solution for $y < 0$,

$$\Phi_2 = B_2(\lambda)\frac{\cosh\left(\mu_2(\lambda)(y+d)\right)}{\cosh\left(\mu_2(\lambda)d\right)}, \tag{3.35}$$

where

$$\mu_2(\lambda) = \left(\lambda^2 - M_2^2(1+\mathrm{i}\eta)^2\right)^{\frac{1}{2}}. \tag{3.36}$$

The function $\mu_2(\lambda)$ corresponds to the branch of the square root that is real and positive as $\lambda \to \infty$ along the real λ axis, for the case $\eta = 0$. In order to satisfy the Sommerfeld radiation condition, the branch points of $\mu_2(\lambda)$ at $\lambda = \pm M_2(1+\mathrm{i}\eta)$ are assumed to lie just above and below the real λ axis, respectively, and the branch cuts are taken to infinity along the vertical lines in the corresponding half-planes. The function $\cosh(z)$ is an even function of z; hence the function $\Phi_2(\lambda, y)$ does not contain the branch cuts of $\mu_2(\lambda)$. Thus the branch cuts of $\mu_2(\lambda)$ are shown as dashed lines in figure 3.2.

Consider now the application of the Fourier transform to the boundary conditions on the cavity lip. Since the conditions (3.28) and (3.29) are related through (3.24), it suffices to apply the Fourier transform to (3.29). The boundary condition (3.29) applies only on the half-range $x < 0$, while the transform involves the full range $-\infty < x < \infty$. In applying the Wiener-Hopf technique, we introduce 'half known' functions $u(x)$ and $v(x)$ to extend the boundary conditions to the whole real line, as described by Carrier *et al.* (1983). The no-penetration boundary condition (3.29) applies only for $x < 0$. To extend the range to all x we set

$$\frac{\partial \phi_2}{\partial y}|_{y=0^-} = \begin{cases} -A\mathrm{e}^{-\mathrm{i}\tau_0^+ x} & x < 0, \\ v(x) & x > 0, \end{cases} \tag{3.37}$$

where $v(x) = 0$ for $x < 0$ and $A = \mu_2(\tau_0^+)\tanh(\mu_2(\tau_0^+)d)$. Applying the Fourier transform to the above equation we obtain

$$B_2(\lambda)\mu_2(\lambda)\tanh(\mu_2(\lambda)d) = \frac{\mathrm{i}A}{\lambda - \tau_0^+} + V^+(\lambda), \tag{3.38}$$

where $V^+(\lambda)$ is the Fourier transform of $v(x)$. The superscript $(\cdot)^+$ on $V(\lambda)$ denotes that this function is analytic in the upper half of the complex λ plane, a property which follows from the fact that $v(x) = 0$ for $x < 0$. In the Wiener-Hopf nomenclature, such functions are called 'plus' functions. An analytic continuation argument will be used to determine $V^+(\lambda)$.

Next consider the application of the Fourier transform (3.30) to the matching conditions across the vortex sheet. The pressure matching condition (3.23) applies only for $x > 0$. To extend the range to all x we set

$$\rho_{01}\left[(1+\mathrm{i}\eta)+\mathrm{i}\frac{\partial}{\partial x}\right]\phi_1|_{y=0^+} - \rho_{02}(1+\mathrm{i}\eta)\phi_2|_{y=0^-} = \begin{cases} u(x) & x<0, \\ 0 & x>0, \end{cases} \tag{3.39}$$

where $u(x) = 0$ for $x > 0$. In physical terms, the function $u(x)$ is related to the difference in perturbation pressure across the zero thickness plate that forms the upstream lip of the cavity. Applying the Fourier transform to (3.39), then using (3.31) and (3.35), we obtain

$$\rho_{01}\left[(1+\mathrm{i}\eta)+\lambda\right]B_1(\lambda) - \rho_{02}(1+\mathrm{i}\eta)B_2(\lambda) = U^-(\lambda), \tag{3.40}$$

where $U^-(\lambda)$ is the Fourier transform of $u(x)$. The superscript $(\cdot)^-$ on $U(\lambda)$ denotes that this function is analytic in the lower half of the complex λ plane, a property which follows from the fact that $u(x) = 0$ for $x > 0$. In the Wiener-Hopf nomenclature, such functions are called 'minus' functions. Subsequently, an analytic continuation argument will be used to determine $U^-(\lambda)$.

Finally, consider the continuity of particle displacement matching condition (3.24). Since the incident cavity mode (3.26, 3.27) satisfies this condition on the vortex sheet ($x > 0$), the scattered field also satisfies (3.24) for $x > 0$. But by (3.28) and (3.29), it is easy to see that the scattered field satisfies (3.24) on $x < 0$ as well. Therefore, the Fourier transform can be applied to (3.24) directly, leading to

$$-(1+\mathrm{i}\eta)\mu_1(\lambda)B_1(\lambda) = \left[(1+\mathrm{i}\eta)+\lambda\right]B_2(\lambda)\mu_2(\lambda)\tanh(\mu_2(\lambda)d). \tag{3.41}$$

Our next step is to obtain a single equation in which the only unknown quantities are the two half-analytic functions, $U^-(\lambda)$ and $V^+(\lambda)$. Solving for $B_2(\lambda)$ in (3.38) and substituting it in (3.40), we obtain

$$B_1(\lambda) = \frac{U^-(\lambda)}{\rho_{01}[(1+\mathrm{i}\eta)+\lambda]} + \frac{\rho_{02}(1+\mathrm{i}\eta)}{\rho_{01}[(1+\mathrm{i}\eta)+\lambda]} \frac{1}{\mu_2(\lambda)\tanh(\mu_2(\lambda)d)} \left[\frac{\mathrm{i}A}{\lambda-\tau_0^+} + V^+(\lambda)\right]. \tag{3.42}$$

Then, (3.41) can be written as

$$-U^-(\lambda) = \frac{\rho_{01}(\lambda+n)(\lambda+n^*)}{(1+\mathrm{i}\eta)\mu_1(\lambda)K(\lambda)} \left[\frac{\mathrm{i}A}{\lambda-\tau_0^+} + V^+(\lambda)\right] \tag{3.43}$$

where $-n$ and $-n^*$ are the x-wavenumbers of the vortex sheet instability wave and its exponentially decaying counterpart. The Wiener-Hopf kernel function $K(\lambda)$ is defined as

$$K(\lambda) = \frac{\rho_{01}(\lambda+n)(\lambda+n^*)\mu_2(\lambda)\sinh(\mu_2(\lambda)d)}{\Delta(\lambda)}, \tag{3.44}$$

where

$$\Delta(\lambda) = \rho_{01}\left[(1+\mathrm{i}\eta)+\lambda\right]^2 \mu_2(\lambda)\sinh(\mu_2(\lambda)d) + \rho_{02}(1+\mathrm{i}\eta)^2\mu_1(\lambda)\cosh(\mu_2(\lambda)d) \tag{3.45}$$

is the dispersion relationship for the vortex sheet in the presence of the bottom surface of the cavity. The function $\mu_2(\lambda)\sinh(\mu_2(\lambda)d)$ is the duct dispersion relationship, and its singularities are discussed below.

The definition of $K(\lambda)$ has been chosen for consistency with previous analyses by Cain *et al.* (2001). Details of this function are discussed in Appendix A. We note that $\Delta(\lambda)$ has two infinite and disjoint sets of zeros corresponding to the cavity modes. The first of these sets is formed by the points τ_j^+, which lie in the upper half-plane, while the second set is formed by the points τ_j^-, which lie in the lower half-plane. In addition, $\Delta(\lambda)$ has two additional zeros at $\lambda = -n$ and its complex conjugate $\lambda = -n^*$, corresponding to the shear layer instability wave and its exponentially decaying counterpart. The function $\mu_2(\lambda)\sinh(\mu_2(\lambda)d)$ has two infinite and disjoint sets of zeros corresponding to the wavenumbers of the duct modes. The first set

contains the points σ_j^+, which lie in the upper half-plane and are the wavenumbers of the upstream duct modes. The second set contains the points σ_j^-, which lie in the lower half-plane and are the wavenubers of the downstream duct modes. The function $K(\lambda)$ also contains the branch points of the function $\mu_1(\lambda)$, at $\lambda = M_u$ and $\lambda = M_d$. It is important to note that $\lambda = -n$ and $\lambda = -n^*$ are not poles of the kernel function $K(\lambda)$, since the factors $(\lambda + n)$ and $(\lambda + n^*)$ in the numerator cancel the zeros of $\Delta(\lambda)$ in the denominator. The locations of the zeros, branch points and branch cuts are illustrated in figure 3.2.

The Wiener-Hopf technique (Noble, 1988) involves a rearrangement of (3.43) such that one side is analytic in the 'upper' half of the complex λ plane, while the other side is analytic in the 'lower' half-plane. The appropriate definition of lower and upper half-planes for a particular wave-propagation problem depends on the stability (growth/decay) of the waves in the problem.

For wave-propagation problems not involving exponentially growing instabilities, like the present problem, the causal solution can be obtained by introducing weak damping into the governing equations. The waves then exhibit (mild) exponential decay at large distances from the source, so that the Fourier transform converges for real values of λ. The 'upper' and 'lower' half-planes for the Wiener-Hopf analysis can then be taken as the regions $\mathrm{Im}[\lambda] > -\alpha$ and $\mathrm{Im}[\lambda] < \alpha$ for some positive constant α related to the damping coefficient. The common region of analyticity is then $-\alpha < \mathrm{Im}[\lambda] < \alpha$ and the inversion contour can be taken as the real λ axis. The desired solution is then obtained by taking the limit $\alpha \to 0$.

For problems involving instability waves which grow exponentially with distance downstream, the Fourier transform does not exist in the usual sense, and a modified procedure is required. In the present case, in order to apply the causality condition, we use the procedure of Briggs (1964) and Bers (1975). Essentially, a sufficiently large positive imaginary component is introduced into the frequency ω so that the instability wave decays with downstream distance ($\mathrm{Im}[n] > 0$). The Fourier transform

then exists in the usual sense and the Fourier transform may be computed using the real λ axis. The solution for real ω is then obtained by analytic continuation, in which the imaginary part of the frequency approaches zero. In this process, the pole at $\lambda = -n$ moves across the real λ axis from the third quadrant into the second quadrant. But analytic continuation, with respect to frequency, then requires that the inversion contour be deformed so that it continues to pass above the pole $\lambda = -n$. In this process, the definition of 'upper' and 'lower' half-planes of analyticity for the Wiener-Hopf Analysis are modified, so that the $\lambda = -n$ remains in the 'lower' half-plane and the inversion contour lies in the region of overlap between the upper and lower half-planes. The causal inversion contour is shown in figure 3.2.

Now, in order to use analytic continuation, we need to rearrange (3.43) such that one side is analytic in the upper half-plane while the other side is analytic in the lower half-plane. The first step is to perform a multiplicative Factorization of $K(\lambda)$,

$$K(\lambda) = K^+(\lambda)K^-(\lambda), \tag{3.46}$$

where $K^+(\lambda)$ and $K^-(\lambda)$ are, respectively, analytic in the Wiener-Hopf upper and lower half-planes in the complex λ plane. Expressions for $K^+(\lambda)$ and $K^-(\lambda)$ are given in Appendix A. Substituting (3.46) in (3.43) and multiplying both sides by $\beta(1+\mathrm{i}\eta)K^-(\lambda)\sqrt{\lambda - M_u}$, we obtain

$$\begin{aligned} -\beta(1+\mathrm{i}\eta)K^-(\lambda)U^-(\lambda)\sqrt{\lambda - M_u} = &\frac{\mathrm{i}A\rho_{01}(\lambda+n)(\lambda+n^*)}{(\lambda-\tau_0^+)K^+(\lambda)\sqrt{\lambda - M_d}} \\ &+ \frac{\rho_{01}(\lambda+n)(\lambda+n^*)V^+(\lambda)}{K^+(\lambda)\sqrt{\lambda - M_d}}. \end{aligned} \tag{3.47}$$

The left-hand side of (3.47) is analytic in the lower half-plane, while the second term on the right-hand side is analytic in the upper half-plane. The first term on the right-hand side has singularities in both half-planes and is therefore a mixed function. However, since the only singularity of the mixed function in the upper half-plane is a pole at $\lambda = \tau_0^+$, an additive split of this mixed function is easily obtained by subtracting off the pole contribution,

$$\frac{\mathrm{i}A\rho_{01}(\lambda+n)(\lambda+n^*)}{(\lambda-\tau_0^+)K^+(\lambda)\sqrt{\lambda-M_d}} =$$
$$\mathrm{i}A\rho_{01}\left[\frac{(\lambda+n)(\lambda+n^*)}{(\lambda-\tau_0^+)K^+(\lambda)\sqrt{\lambda-M_d}} - \frac{(\tau_0^++n)(\tau_0^++n^*)}{(\lambda-\tau_0^+)K^+(\tau_0^+)\sqrt{\tau_0^+-M_d}}\right] + \frac{\mathrm{i}A\rho_{01}(\tau_0^++n)(\tau_0^++n^*)}{(\lambda-\tau_0^+)K^+(\tau_0^+)\sqrt{\tau_0^+-M_d}}. \tag{3.48}$$

Substituting the above equation into (3.47) and taking the minus function to the left-hand side of the equation, we obtain

$$-\beta(1+\mathrm{i}\eta)K^-(\lambda)U^-(\lambda)\sqrt{\lambda-M_u} - \frac{\mathrm{i}A\rho_{01}(\tau_0^++n)(\tau_0^++n^*)}{(\lambda-\tau_0^+)K^+(\tau_0^+)\sqrt{\tau_0^+-M_d}} =$$
$$\mathrm{i}A\left[\frac{\rho_{01}(\lambda+n)(\lambda+n^*)}{(\lambda-\tau_0^+)K^+(\lambda)\sqrt{\lambda-M_d}} - \frac{\rho_{01}(\tau_0^++n)(\tau_0^++n^*)}{(\lambda-\tau_0^+)K^+(\tau_0^+)\sqrt{\tau_0^+-M_d}}\right] + \frac{\rho_{01}(\lambda+n)(\lambda+n^*)V^+(\lambda)}{K^+(\lambda)\sqrt{\lambda-M_d}} = E(\lambda). \tag{3.49}$$

The left-hand side of (3.49) is analytic in the lower half-plane, while the right-hand side is analytic in the upper half-plane. Both sides of (3.49) are equal in the strip of overlap between the two regions of analyticity, and by analytic continuation define an entire function $E(\lambda)$, which is analytic in the whole complex λ plane. Thus, setting each side of (3.49) equal to $E(\lambda)$, expressions for $V^+(\lambda)$ and $U^-(\lambda)$ can now be obtained, namely,

$$V^+(\lambda) = \frac{K^+(\lambda)\sqrt{\lambda-M_d}\,E(\lambda)}{\rho_{01}(\lambda+n)(\lambda+n^*)} - \frac{\mathrm{i}A}{\lambda-\tau_0^+}\left[1 - \frac{(\tau_0^++n)(\tau_0^++n^*)K^+(\lambda)\sqrt{\lambda-M_d}}{(\lambda+n)(\lambda+n^*)K^+(\tau_0^+)\sqrt{\tau_0^+-M_d}}\right] \tag{3.50}$$

$$U^-(\lambda) = \frac{-\mathrm{i}A\rho_{01}}{\beta(1+\mathrm{i}\eta)K^-(\lambda)\sqrt{\lambda-M_u}}\,\frac{(\tau_0^++n)(\tau_0^++n^*)}{(\lambda-\tau_0^+)K^+(\tau_0^+)\sqrt{\tau_0^+-M_d}} - \frac{E(\lambda)}{\beta(1+\mathrm{i}\eta)K^-(\lambda)\sqrt{\lambda-M_u}}. \tag{3.51}$$

Finally, we must determine the entire function $E(\lambda)$. This function is determined with the aid of Liouville's theorem (see for example Carrier *et al.*, 1983), which states

that an entire function that is bounded at infinity must be a constant. In a more general setting, entire functions which grow no faster than some power of $|\lambda|$ must be a polynomial. Thus, we anticipate that $E(\lambda)$ will have the form of a polynomial in λ. Next, assuming that $u(x)$ and $v(x)$ are smooth functions, it can be shown that if $u(x) \propto (-x)^a$ as $x \to 0_-$ and $v(x) \propto x^b$ as $x \to 0_+$, then $U^-(\lambda) \propto \lambda^{-a-1}$ as $\lambda \to \infty$ in the lower half-plane and $V^+(\lambda) \propto \lambda^{-b-1}$ as $\lambda \to \infty$ in the upper half-plane. Therefore, the rates of growth of the functions $U^-(\lambda)$ and $V^+(\lambda)$ as $\lambda \to \infty$ are related to the strengths of the singularities of the functions $u(x)$ and $v(x)$ as $x \to 0_\mp$. The admissible singularity strength is generally limited by physical considerations related to the behavior of the flow field near the origin; these are the so-called 'edge conditions.'

For the choice $E(\lambda) = 0$, $U^-(\lambda) \propto \lambda^{-3/2}$ and $V^+(\lambda) \propto \lambda^{-1}$ as $\lambda \to \infty$ in their respective half-planes, we find that $u(x) \propto (-x)^{1/2}$ and $v(x)$ approaches a constant as $x \to 0_\mp$.

In contrast, if $E(\lambda)$ is a non-zero constant then $U^-(\lambda) \propto \lambda^{-1/2}$ as $\lambda \to \infty$, leading to the more singular behavior $u(x) \propto (-x)^{-1/2}$ in the vicinity of the origin. This singularity is inconsistent with the unsteady Kutta condition (Crighton, 1985). Choices of $E(\lambda)$ involving powers of λ lead to even more singular behavior near the origin in the physical plane and must be ruled out. Therefore, we conclude that the choice that produces the least behavior is $E(\lambda) = 0$ (often, when using Wiener-Hopf analysis, the physically appropriate solution is the least singular solution). Substituting $E(\lambda) = 0$ into (3.50) and (3.51), we have

$$V^+(\lambda) = -\frac{\mathrm{i}A}{\lambda - \tau_0^+}\left[1 - \frac{(\tau_0^+ + n)(\tau_0^+ + n^*)K^+(\lambda)\sqrt{\lambda - M_d}}{(\lambda + n)(\lambda + n^*)K^+(\tau_0^+)\sqrt{\tau_0^+ - M_d}}\right] \tag{3.52}$$

$$U^-(\lambda) = -\frac{\mathrm{i}A\rho_{01}}{\beta(1 + \mathrm{i}\eta)K^-(\lambda)\sqrt{\lambda - M_u}}\,\frac{(\tau_0^+ + n)(\tau_0^+ + n^*)}{(\lambda - \tau_0^+)K^+(\tau_0^+)\sqrt{\tau_0^+ - M_d}}. \tag{3.53}$$

Having found expressions for $U^-(\lambda)$ and $V^+(\lambda)$, we can now solve for $B_1(\lambda)$ and $B_2(\lambda)$. To examine the scattered field in the upstream region, we need expressions

that expose the singularities in the upper half-plane. Substituting $B_2(\lambda)$ in (3.38) and replacing in (3.40), expressions for $B_1(\lambda)$ and $B_2(\lambda)$ involving $K^+(\lambda)$ are found. After substituting these expressions into (3.41), we obtain the following expressions for the inverse Fourier transforms in the upstream region ($x < 0$):

$$\phi_1(x,y) = \frac{-\mathrm{i}\,\mu_2(\tau_0^+)\tanh(\mu_2(\tau_0^+)d)\,(\tau_0^+ + n)(\tau_0^+ + n^*)}{2\pi\beta(1+\mathrm{i}\eta)K^+(\tau_0^+)\sqrt{\tau_0^+ - M_d}} \int_{-\infty}^{\infty} \frac{[(1+\mathrm{i}\eta)+\lambda]K^+(\lambda)\,\mathrm{e}^{-\mu_1(\lambda)y}}{(\lambda+n)(\lambda+n^*)\sqrt{\lambda - M_u}(\lambda - \tau_0^+)} \mathrm{e}^{-\mathrm{i}\lambda x} d\lambda, \tag{3.54}$$

$$\phi_2(x,y) = \frac{\mathrm{i}\,\mu_2(\tau_0^+)\tanh(\mu_2(\tau_0^+)d)\,(\tau_0^+ + n)(\tau_0^+ + n^*)}{2\pi K^+(\tau_0^+)\sqrt{\tau_0^+ - M_d}} \int_{-\infty}^{\infty} \frac{K^+(\lambda)\sqrt{\lambda - M_d}\cosh(\mu_2(\lambda)(y+d))}{(\lambda+n)(\lambda+n^*)\mu_2(\lambda)\sinh(\mu_2(\lambda)d)(\lambda - \tau_0^+)} \mathrm{e}^{-\mathrm{i}\lambda x} d\lambda. \tag{3.55}$$

The scattered field in the upstream region is then obtained by closing the inversion contour in the upper half-plane. Contributions are produced by the singularities of the integrand in the upper half-plane. The function $K^+(\lambda)$ is analytic in the upper half-plane, and the poles at $\lambda = -n$ and $\lambda = -n^*$ lie in the lower half-plane.

The integrand of (3.54) has a pole at τ_0^+, whose residue contribution is $-\phi_{i1}^{\mathcal{U}}$, i.e. cancels the incident field. Another contribution comes from the branch cut emanating from the branch point at $\lambda = M_u$. The integral arising from deformation of the contour around this branch cut corresponds to the continuous spectrum components of the solution. The contribution from this branch cut is the upstream external acoustic field. However, since the present study is focused on the acoustic field within the cavity, the acoustic field in the flow region upstream of the cavity ($x < 0$, $y > 0$) is of little interest and (3.54) will not be evaluated further.

For (3.55), note that the function $\cosh(\mu_2(\lambda)(y+d))$ is an entire function. Thus the solution in the 'duct region' ($x < 0$, $y < 0$) consists of the residue contributions arising from the poles associated with the zeros of the denominator. The pole contribution

from $\lambda = \tau_0^+$ in (3.55) cancels the incident upstream-propagating cavity mode field in the duct region. The other contributions come from the zeros in the upper half-plane of the function $\mu_2(\lambda)\sinh(\mu_2(\lambda)d)$ at $\lambda = \sigma_j^+,\ j = 0, 1, 2, ..., \infty$, which correspond to upstream duct modes. Evaluating the residue contributions of (3.55) in the upper half-plane, we obtain

$$\phi_2(x,y) = \sum_{j=0}^{\infty} D_j^{\mathcal{U}} \cos(\frac{j\pi}{d}y)\, \mathrm{e}^{-\mathrm{i}\sigma_j^+ x} \ - \phi_{i2}^{\mathcal{U}}(x,y), \tag{3.56}$$

where $\phi_{i2}^{\mathcal{U}}$ is given by (3.27), and the complex amplitudes of the upstream-propagating duct modes are given by

$$D_j^{\mathcal{U}} = -\frac{A(\tau_0^+ + n)(\tau_0^+ + n^*)}{K^+(\tau_0^+)\sqrt{\tau_0^+ - M_d}\ d}\ \frac{\epsilon_j K^+(\sigma_j^+)\sqrt{\sigma_j^+ - M_d}}{(\sigma_j^+ - \tau_0^+)(\sigma_j^+ + n)(\sigma_j^+ + n^*)\sigma_j^+}, \tag{3.57}$$

where

$$\epsilon_j = \begin{cases} \frac{1}{2} & j = 0, \\ 1 & j = 1, 2, \ldots \end{cases} \tag{3.58}$$

The superscript $(\cdot)^{\mathcal{U}}$ on $D_j^{\mathcal{U}}$ indicates that this contribution is generated by the impingement of the upstream cavity mode $\mathcal{U}$ on the overhanging lip. Note that the first factor in (3.57) is independent of j.

For the case of a semi-infinite overhanging lip, these acoustic modes simply propagate to upstream infinity and have no influence on the receptivity level. However, for a finite-length overhanging lip, these upstream-propagating duct modes reflect off the upstream end wall of the cavity, producing downstream-propagating duct modes which then interact with the edge of the overhanging lip, generating additional contributions to the receptivity level.

To examine the scattered field in the downstream region ($x > 0$), a more convenient form of the solution is obtained by replacing $K^+(\lambda)$ with $K(\lambda)/K^-(\lambda)$ (with $K(\lambda)$ given by (3.44)), in order to display singularities in the lower half-plane. We

obtain

$$\phi_1(x,y) = \frac{-\mathrm{i}\rho_{01}\,\mu_2(\tau_0^+)\tanh(\mu_2(\tau_0^+)d)\,(\tau_0^+ + n)(\tau_0^+ + n^*)}{2\pi\beta(1+\mathrm{i}\eta)K^+(\tau_0^+)\sqrt{\tau_0^+ - M_d}} \int_{-\infty}^{\infty} \frac{[(1+\mathrm{i}\eta)+\lambda]\mu_2(\lambda)\sinh(\mu_2(\lambda)d)}{K^-(\lambda)\sqrt{\lambda - M_u}(\lambda - \tau_0^+)\Delta(\lambda)} \mathrm{e}^{-\mu_1(\lambda)y}\,\mathrm{e}^{-\mathrm{i}\lambda x} d\lambda, \tag{3.59}$$

$$\phi_2(x,y) = \frac{\mathrm{i}\rho_{01}\,\mu_2(\tau_0^+)\tanh(\mu_2(\tau_0^+)d)\,(\tau_0^+ + n)(\tau_0^+ + n^*)}{2\pi K^+(\tau_0^+)\sqrt{\tau_0^+ - M_d}} \int_{-\infty}^{\infty} \frac{\sqrt{\lambda - M_d}\cosh(\mu_2(\lambda)(y+d))}{K^-(\lambda)(\lambda - \tau_0^+)\Delta(\lambda)} \mathrm{e}^{-\mathrm{i}\lambda x} d\lambda. \tag{3.60}$$

The inversion contour is then closed in the lower half-plane. Note that (3.59) and (3.60) have pole contributions arising from the zeros of $\Delta(\lambda)$ that lie in the lower half-plane. The residues of the poles at $\lambda = \tau_j^-$ produce the downstream-propagating cavity modes, while the pole of $\lambda = -n$ produce the instability wave, and the pole at $\lambda = -n^*$ produces its exponentially decaying counterpart. There is also a contribution coming from the branch cut emanating from $\lambda = M_d$.

The scattered fields in the stream region ($y > 0$) and cavity region ($y < 0$), for the downstream region ($x > 0$) are then given respectively by

$$\phi_1(x,y) = \sum_{j=0}^{\infty} C_j^{\mathcal{U}}\, m_1(\tau_j^-, y)\mathrm{e}^{-\mathrm{i}\tau_j^- x} + S^{\mathcal{U}}\, m_1(-n,y)\mathrm{e}^{\mathrm{i}nx} + S_*^{\mathcal{U}}\, m_1(-n^*,y)\mathrm{e}^{\mathrm{i}n^* x} + E_1^{\mathcal{U}}(x,y)\,\mathrm{e}^{-\mathrm{i}M_d x}, \tag{3.61}$$

$$\phi_2(x,y) = \sum_{j=0}^{\infty} C_j^{\mathcal{U}}\, m_2(\tau_j^-, y)\mathrm{e}^{-\mathrm{i}\tau_j^- x} + S^{\mathcal{U}}\, m_2(-n,y)\mathrm{e}^{\mathrm{i}nx} + S_*^{\mathcal{U}}\, m_2(-n,y)\mathrm{e}^{\mathrm{i}n^* x} + E_2^{\mathcal{U}}(x,y)\,\mathrm{e}^{-\mathrm{i}M_d x}, \tag{3.62}$$

where

$$m_1(\lambda,y) = -\frac{[(1+\mathrm{i}\eta)+\lambda]\mu_2(\lambda)\sinh(\mu_2(\lambda)d)\,\mathrm{e}^{-\mu_1(\lambda)y}}{(1+\mathrm{i}\eta)\mu_1(\lambda)} \tag{3.63}$$

and

$$m_2(\lambda,y) = \cosh(\mu_2(\lambda)(y+d)). \tag{3.64}$$

The complex amplitudes of the cavity modes and the shear-layer instability wave are given by

$$C_j^{\mathcal{U}} = \frac{\rho_{01}\,\mu_2(\tau_0^+)\tanh(\mu_2(\tau_0^+)d)\,(\tau_0^+ + n)(\tau_0^+ + n^*)}{K^+(\tau_0^+)\sqrt{\tau_0^+ - M_d}} \frac{\sqrt{\tau_j^- - M_d}}{K^-(\tau_j^-)(\tau_j^- - \tau_0^+)\Delta'(\tau_j^-)} \quad (3.65)$$

and

$$S^{\mathcal{U}} = \frac{\rho_{01}\,\mu_2(\tau_0^+)\tanh(\mu_2(\tau_0^+)d)\,(\tau_0^+ + n)(\tau_0^+ + n^*)}{K^+(\tau_0^+)\sqrt{\tau_0^+ - M_d}} \frac{\sqrt{-n - M_d}}{K^-(-n)(-n - \tau_0^+)\Delta'(-n)}, \quad (3.66)$$

where $\Delta'(\lambda) = d\Delta/d\lambda$ and $S_*^{\mathcal{U}}$ is obtained by substituting n by n^* in the second term of the right hand side of (3.66). $E_1^{\mathcal{U}}(x,y)$ is the complex amplitude (for each x and y) of the external acoustic field in the stream region ($y > 0$), and $E_2^{\mathcal{U}}(x,y)$ is the complex amplitude (for each x and y) of this same external acoustic field, in the cavity region ($y < 0$). The external field arises from the contribution of the branch cut emanating from $\lambda = -M_d$.

In this dissertation we focus on the behavior of the field for $O(1)$ values of y. The behavior in the stream at large distances ($x \gg 1$) is most naturally approached by applying the method of steepest descents, in which the integration contour for (3.59) and (3.60) is deformed to pass through the saddle point of the exponent. The external field generated by the interaction of the upstream cavity mode $\mathcal{U}$ with the edge of the upstream overhanging lip, far from the upstream end of the cavity is given by

$$E_1^{\mathcal{U}}(x,y) \approx \frac{-\mathcal{C}_1[(1+\mathrm{i}\eta) + M_d]\mu_2(M_d)\sinh(\mu_2(M_d)d)}{\beta(1+\mathrm{i}\eta)\sqrt{M_d - M_u}} \left(\frac{\beta \mathrm{e}^{\mathrm{i}3\pi/4}\sqrt{M_d - M_u}}{a_1}\, y - \frac{b_1}{a_1^2} \right) \frac{\Gamma(3/2)}{x^{3/2}}, \quad (3.67)$$

$$E_2^{\mathcal{U}}(x,y) \approx \mathcal{C}_1\, \mathrm{e}^{\mathrm{i}3\pi/4}\, \frac{\cosh(\mu_2(M_d)(y+d))}{a_1}\, \frac{\Gamma(3/2)}{x^{3/2}}, \quad (3.68)$$

where

$$\mathcal{C}_1 = \frac{\rho_{01}\,\mu_2(\tau_0^+)\tanh(\mu_2(\tau_0^+)d)\,(\tau_0^+ + n)(\tau_0^+ + n^*)}{\pi K^+(\tau_0^+)\sqrt{\tau_0^+ - M_d}K^-(M_d)(M_d - \tau_0^+)}, \quad (3.69)$$

$$a_1 = \rho_{01}[(1+\mathrm{i}\eta) + M_d]^2\mu_2(M_d)\sinh(\mu_2(M_d)d), \quad (3.70)$$

and

$$b_1 = \rho_{02} \mathrm{e}^{\mathrm{i}3\pi/4} \beta (1+\mathrm{i}\eta)^2 \sqrt{M_d - M_u} \cosh(\mu_2(M_d) d). \tag{3.71}$$

A general procedure to obtain the external fields and their expansions for large values of x is given in Appendix C.

3.2.2 Impingement of a Downstream Duct Mode

In order to analyze the receptivity for the case of a finite-length overhanging upstream lip or a square (90°) upstream corner, it is necessary to determine the response of a semi-infinite overhanging upstream lip to the impingement of a downstream duct mode. The incident field then takes the form of the k-th duct mode

$$\phi_{i1} = 0, \tag{3.72}$$

$$\phi_{i2} = \cos(\frac{k\pi}{d} y)\, \mathrm{e}^{-\mathrm{i}\sigma_k^- x}, \tag{3.73}$$

where σ_k^-, $k = 0, 1, 2, ..., \infty$, is the pole location corresponding to the k-th downstream-propagating duct mode (see figure 3.2), and is defined as

$$\sigma_k^{\pm} = \begin{cases} \pm\sqrt{M_2^2(1+\mathrm{i}\eta)^2 - \left(\frac{k\pi}{d}\right)^2} & k < \frac{M_2 d}{\pi} \\ \pm\mathrm{i}\sqrt{\left(\frac{k\pi}{d}\right)^2 - M_2^2(1+\mathrm{i}\eta)^2} & k > \frac{M_2 d}{\pi}. \end{cases} \tag{3.74}$$

The total field is again written as the sum (3.17) of the incident and scattered fields, but with (3.72) and (3.73) replacing (3.26) and (3.27). The incident fields (3.72) and (3.73) satisfy the reduced wave equations (3.18) and (3.19) respectively, so that the scattered field ϕ_1 and ϕ_2 satisfies these equations as well. The incident field satisfies the no-penetration condition (3.20) on the cavity bottom, and the no-penetration conditions (3.21) and (3.22) on the inner and outer surfaces of the overhanging lip, so that the scattered field also satisfies (3.21) and (3.22) on the cavity lip ($x < 0$) and (3.20) for all values of x.

In the region $x > 0$, the total field satisfies the vortex-sheet matching conditions (3.23) and (3.24) across $y = 0$. Since the incident field (3.72, 3.73) does not satisfy

the continuity of pressure across the vortex sheet, the scattered field satisfies an inhomogeneous form of the pressure matching conditions for $x > 0$,

$$\rho_{01}\left[(1+\mathrm{i}\eta)+\mathrm{i}\frac{\partial}{\partial x}\right]\phi_1|_{y=0^+} - \rho_{02}(1+\mathrm{i}\eta)\phi_2|_{y=0^-} = \rho_{02}(1+\mathrm{i}\eta)\mathrm{e}^{-\mathrm{i}\sigma_k^- x}. \tag{3.75}$$

The transverse velocity for the incident field (3.72, 3.73) vanishes at $y = 0$, so the scattered field satisfies the homogeneous form of (3.24), the continuity of particle displacement across the vortex sheet. The boundary conditions (3.21) and (3.22) on the upstream lip imply that the continuity of particle displacement is satisfied for $x < 0$ as well, so that (3.24) applies over the full range $-\infty < x < \infty$. As in previous section, the solutions to the reduced wave equations (3.18, 3.19) in Fourier transform space are again given by (3.31, 3.35).

To determine $B_1(\lambda)$ and $B_2(\lambda)$ using the Wiener-Hopf technique (Noble, 1988), we extend the no-penetration boundary condition (3.22) on the inner surface of overhanging lip by setting

$$\frac{\partial \phi_2}{\partial y}|_{y=0^-} = \begin{cases} 0 & x < 0, \\ v(x) & x > 0, \end{cases} \tag{3.76}$$

where $v(x) = 0$ for $x < 0$. Taking the Fourier transform and using (3.31 , 3.35), we have

$$B_2(\lambda)\mu_2(\lambda)\tanh(\mu_2(\lambda)d) = V^+(\lambda). \tag{3.77}$$

Extending the vortex-sheet pressure matching condition (3.75) in a similar way, we have

$$\rho_{01}\left[(1+\mathrm{i}\eta)+\mathrm{i}\frac{\partial}{\partial x}\right]\phi_1|_{y=0^+} - \rho_{02}(1+\mathrm{i}\eta)\phi_2|_{y=0^-} = \begin{cases} u(x), & x < 0 \\ B\mathrm{e}^{-\mathrm{i}\sigma_k^- x} & x > 0, \end{cases} \tag{3.78}$$

where $u(x) = 0$ for $x > 0$ and $B = \rho_{02}(1+\mathrm{i}\eta)$. Taking the Fourier transform and using (3.31) and (3.35), we obtain

$$\rho_{01}\left[(1+\mathrm{i}\eta)+\lambda\right]B_1(\lambda) - \rho_{02}(1+\mathrm{i}\eta)B_2(\lambda) = U^-(\lambda) + \frac{B\mathrm{i}}{\lambda - \sigma_k^-}. \tag{3.79}$$

The Fourier transform of the continuity of particle displacement again yields (3.41). Solving for $B_2(\lambda)$ in (3.77) and substituting into (3.79), we obtain

$$B_1(\lambda) = \frac{-[(1+\mathrm{i}\eta)+\lambda]V^+(\lambda)}{(1+\mathrm{i}\eta)\mu_1(\lambda)}. \tag{3.80}$$

Then, substituting the expressions for $B_1(\lambda)$ and $B_2(\lambda)$ into (3.41), we obtain

$$\frac{-V^+(\lambda)\rho_{01}(\lambda+n)(\lambda+n^*)}{(1+\mathrm{i}\eta)\mu_1(\lambda)K(\lambda)} = U^-(\lambda) + \frac{\mathrm{i}B}{\lambda-\sigma_k^-}, \tag{3.81}$$

where $K(\lambda)$ is given by (3.44).

Substituting $K(\lambda) = K^+(\lambda)K^-(\lambda)$ and multiplying both sides by $K^-(\lambda)\sqrt{\lambda - M_u}$, we obtain

$$\frac{-V^+(\lambda)\rho_{01}(\lambda+n)(\lambda+n^*)}{\beta(1+\mathrm{i}\eta)K^+(\lambda)\sqrt{\lambda-M_d}} = U^-(\lambda)K^-(\lambda)\sqrt{\lambda-M_u} + \frac{\mathrm{i}BK^-(\lambda)\sqrt{\lambda-M_u}}{\lambda-\sigma_k^-}. \tag{3.82}$$

The left-hand side of (3.82) is analytic in the upper half-plane, while the first term on the right-hand side is analytic in the lower half-plane. The second term on the right-hand side has singularities in both half-planes and is therefore a mixed function. However, since the only singularity of the mixed function in the lower half-plane is a pole at $\lambda = \sigma_k^-$, an additive split of this mixed function is easily obtained by subtracting off the pole contribution,

$$\begin{aligned}\frac{\mathrm{i}BK^-(\lambda)\sqrt{\lambda-M_u}}{\lambda-\sigma_k^-} = &\left[\frac{\mathrm{i}BK^-(\lambda)\sqrt{\lambda-M_u}}{\lambda-\sigma_k^-} - \frac{\mathrm{i}BK^-(\sigma_k^-)\sqrt{\sigma_k^- - M_u}}{\lambda-\sigma_k^-}\right] \\ &+ \frac{\mathrm{i}BK^-(\sigma_k^-)\sqrt{\sigma_k^- - M_u}}{\lambda-\sigma_k^-},\end{aligned} \tag{3.83}$$

Substituting the above equation into (3.82) and taking the minus functions to the left-hand side of the equation, we have

$$\begin{aligned}&U^-(\lambda)K^-(\lambda)\sqrt{\lambda-M_u} + \frac{\mathrm{i}B}{\lambda-\sigma_k^-}\left[K^-(\lambda)\sqrt{\lambda-M_u} - K^-(\sigma_k^-)\sqrt{\sigma_k^- - M_u}\right] \\ &\quad = \frac{-V^+(\lambda)\rho_{01}(\lambda+n)(\lambda+n^*)}{\beta(1+\mathrm{i}\eta)K^+(\lambda)\sqrt{\lambda-M_d}} - \frac{\mathrm{i}BK^-(\sigma_k^-)\sqrt{\sigma_k^- - M_u}}{\lambda-\sigma_k^-} = E(\lambda).\end{aligned} \tag{3.84}$$

The left-hand side of (3.84) is a minus function, while the right-hand side is a plus function. The two functions are equal on the strip of overlap, and by analytic continuation define an entire function $E(\lambda)$. Setting each side of (3.84) equal to $E(\lambda)$, we obtain

$$V^+(\lambda) = \frac{-\beta(1+\mathrm{i}\eta)K^+(\lambda)\sqrt{\lambda - M_d}E(\lambda)}{\rho_{01}(\lambda+n)(\lambda+n*)} - \frac{\mathrm{i}\beta(1+\mathrm{i}\eta)B\sqrt{\sigma_k^- - M_u}K^-(\sigma_k^-)K^+(\lambda)\sqrt{\lambda - M_d}}{\rho_{01}(\lambda-\sigma_k^-)(\lambda+n)(\lambda+n^*)}, \tag{3.85}$$

$$U^-(\lambda) = \frac{E(\lambda)}{K^-(\lambda)\sqrt{\lambda - M_u}} - \frac{\mathrm{i}B}{\lambda - \sigma_k^-}\left[1 - \frac{K^-(\sigma_k^-)\sqrt{\sigma_k^- - M_u}}{K^-(\lambda)\sqrt{\lambda - M_u}}\right]. \tag{3.86}$$

As before, the entire function $E(\lambda)$ is determined by examining the behavior of the physical field in the vicinity of the origin, i.e. $E(\lambda)$ is chosen to give the least singular behavior. For the choice $E(\lambda) = 0$, $U^-(\lambda) \propto \lambda^{-3/2}$ and $V^+(\lambda) \propto \lambda^{-1}$ as $\lambda \to \infty$ in their respective half-planes, so, as in the previous section, $u(x) \propto (-x)^{1/2}$ and $v(x)$ approaches a constant as $x \to 0_\mp$. Any other choice of $E(\lambda)$ leads to more singular behaviors in the vicinity of the lip edge, making this choice inconsistent with the unsteady Kutta condition (Crighton, 1985). Therefore,

$$U^-(\lambda) = \frac{-\mathrm{i}B}{\lambda - \sigma_k^-}\left[1 - \frac{K^-(\sigma_k^-)\sqrt{\sigma_k^- - M_u}}{K^-(\lambda)\sqrt{\lambda - M_u}}\right], \tag{3.87}$$

and

$$V^+(\lambda) = \frac{-\mathrm{i}\beta(1+\mathrm{i}\eta)B\sqrt{\sigma_k^- - M_u}K^-(\sigma_k^-)K^+(\lambda)\sqrt{\lambda - M_d}}{\rho_{01}(\lambda-\sigma_k^-)(\lambda+n)(\lambda+n^*)}. \tag{3.88}$$

Having found expressions for $U^-(\lambda)$ and $V^+(\lambda)$, we can now solve for $B_1(\lambda)$ and $B_2(\lambda)$. To obtain the scattered field in the upstream region, we need expressions for $B_1(\lambda)$ and $B_2(\lambda)$ that expose singularities in the upper half-plane. Solving for $B_2(\lambda)$ in (3.77) and substituting into (3.79), expressions for $B_1(\lambda)$ and $B_2(\lambda)$ involving $K^+(\lambda)$

are found and substitute into (3.41), yielding

$$\phi_1(x,y) = \frac{\mathrm{i}\,\rho_{02}(1+\mathrm{i}\eta)K^-(\sigma_k^-)\sqrt{\sigma_k^- - M_u}}{2\pi\rho_{01}} \int_{-\infty}^{\infty} \frac{[(1+\mathrm{i}\eta)+\lambda]K^+(\lambda)\mathrm{e}^{-\mu_1(\lambda)y}\mathrm{e}^{-\mathrm{i}\lambda x}}{(\lambda-\sigma_k^-)(\lambda+n)(\lambda+n^*)\sqrt{\lambda-M_u}}\,d\lambda, \tag{3.89}$$

$$\phi_2(x,y) = \frac{-\mathrm{i}\,\beta\,\rho_{02}(1+\mathrm{i}\eta)^2K^-(\sigma_k^-)\sqrt{\sigma_k^- - M_u}}{2\pi\rho_{01}} \int_{-\infty}^{\infty} \frac{K^+(\lambda)\sqrt{\lambda-M_d}\,\cosh(\mu_2(\lambda)(y+d))}{(\lambda-\sigma_k^-)(\lambda+n)(\lambda+n^*)\mu_2(\lambda)\sinh(\mu_2(\lambda)d)}\,\mathrm{e}^{-\mathrm{i}\lambda x}d\lambda. \tag{3.90}$$

The integration contour of (3.89) and (3.90) is closed in the upper half-plane. The only singularity in the upper half-plane for the integrand of (3.89) is the branch point at $\lambda = M_u$ and its corresponding branch cut extending into the upper half-plane. The contribution from this branch cut is the upstream-propagating external acoustic field. Since we are interested in the acoustic fields within the cavity, (3.89) will not be evaluated further. The only singularities in the upper half-plane for the integrand of (3.90) are the zeros of the function $\mu_2(\lambda)\sinh(\mu_2(\lambda)d)$, i.e. the poles at $\lambda = \sigma_j^+,\ j = 0,1,2,...,\infty$. The residues of these poles are upstream-propagating duct modes generated by the interaction at the edge of the overhanging upstream lip. Thus, within the cavity in the upstream region we have

$$\phi_2(x,y) = \sum_{j=0}^{\infty} D_j^{d,k}\cos(\frac{j\pi}{d}y)\mathrm{e}^{-\mathrm{i}\sigma_j^+ x}, \tag{3.91}$$

where the complex amplitudes of the duct mode coefficients are given by

$$D_j^{d,k} = \frac{\beta\,\rho_{02}(1+\mathrm{i}\eta)^2K^-(\sigma_k^-)\sqrt{\sigma_k^- - M_u}}{\rho_{01}\,d} \frac{\epsilon_j\,K^+(\sigma_j^+)\sqrt{\sigma_j^+ - M_d}}{(\sigma_j^+-\sigma_k^-)(\sigma_j^+ + n)(\sigma_j^+ + n^*)\sigma_j^+}, \tag{3.92}$$

where ϵ_j is defined in (3.58). The superscript $(\cdot)^{d,k}$ on $D_j^{d,k}$ indicates that this contribution is generated by the interaction of the k-th downstream duct mode with the overhanging lip. Note that the first factor in (3.92) is independent of j.

To examine the scattered field in the downstream region ($x > 0$), we replace $K^+(\lambda)$ in (3.89) and (3.90) with $K(\lambda)/K^-(\lambda)$, in order to display singularities in the

lower half-plane. Thus we obtain

$$\phi_1(x,y) = \frac{\mathrm{i}\,\rho_{02}(1+\mathrm{i}\eta)K^-(\sigma_k^-)\sqrt{\sigma_k^- - M_u}}{2\pi}\int_{-\infty}^{\infty}\frac{[(1+\mathrm{i}\eta)+\lambda]\mu_2(\lambda)\sinh(\mu_2(\lambda)d)\mathrm{e}^{-\mu_1(\lambda)y}}{(\lambda-\sigma_k^-)K^-(\lambda)\sqrt{\lambda-M_u}\Delta(\lambda)}\,\mathrm{e}^{-\mathrm{i}\lambda x}d\lambda, \tag{3.93}$$

$$\phi_2(x,y) = \frac{-\mathrm{i}\,\beta\,\rho_{02}(1+\mathrm{i}\eta)^2K^-(\sigma_k^-)\sqrt{\sigma_k^- - M_u}}{2\pi}\int_{-\infty}^{\infty}\frac{\sqrt{\lambda-M_d}\cosh(\mu_2(\lambda)(y+d))}{(\lambda-\sigma_k^-)K^-(\lambda)\Delta(\lambda)}\,\mathrm{e}^{-\mathrm{i}\lambda x}d\lambda. \tag{3.94}$$

The integration contour of (3.93) and (3.94) is closed in the lower half-plane. Singularities in the lower half-plane are poles at $\lambda = \tau_j^-,\ j = 0,1,2,...,\infty$, $\lambda = -n$ and $\lambda = -n^*$, whose residue contributions are, respectively, the downstream propagating cavity modes, the shear-layer instability wave and its exponentially decreasing counterpart. Also, (3.93) and (3.94) have a branch point at $\lambda = M_d$, with the corresponding branch cut extending into the lower half-plane; the contribution arising from this singularity is the downstream-propagating external acoustic field. Note that there is no pole contribution from $\lambda = \sigma_k^-$ in (3.93), while the pole contribution from $\lambda = \sigma_k^-$ in (3.94) cancels the incident field $\phi_{i2}(x,y)$. Hence in the downstream region $(x > 0)$ we have,

$$\phi_1(x,y) = \sum_{j=0}^{\infty} C_j^{d,k} m_1(\tau_j^-,y)\mathrm{e}^{-\mathrm{i}\tau_j^- x} + S^{d,k} m_1(-n,y)\mathrm{e}^{\mathrm{i}nx} + S_*^{d,k} m_1(-n^*,y)\mathrm{e}^{\mathrm{i}n^* x} + E_1^{d,k}(x,y)\,\mathrm{e}^{-\mathrm{i}M_d x}, \tag{3.95}$$

$$\phi_2(x,y) = \sum_{j=0}^{\infty} C_j^{d,k} m_2(\tau_j^-,y)\mathrm{e}^{-\mathrm{i}\tau_j^- x} + S^{d,k} m_2(-n,y)\mathrm{e}^{\mathrm{i}nx} + S_*^{d,k} m_2(-n^*,y)\mathrm{e}^{\mathrm{i}n^* x} + E_2^{d,k}(x,y)\mathrm{e}^{-\mathrm{i}M_d x} - \phi_{i2}, \tag{3.96}$$

where m_1 and m_2 are given by (3.63) and (3.64), respectively. The complex amplitudes of the cavity modes coefficients are given by

$$C_j^{d,k} = \frac{-\beta\,\rho_{02}(1+\mathrm{i}\eta)^2K^-(\sigma_k^-)\sqrt{\sigma_k^- - M_u}\sqrt{\tau_j^- - M_d}}{(\tau_j^- - \sigma_k^-)K^-(\tau_j^-)\Delta'(\tau_j^-)}, \tag{3.97}$$

$$S^{d,k} = \frac{-\beta\,\rho_{02}(1+\mathrm{i}\eta)^2K^-(\sigma_k^-)\sqrt{\sigma_k^- - M_u}\sqrt{-n - M_d}}{(-n - \sigma_k^-)K^-(-n)\Delta'(-n)}, \tag{3.98}$$

and $S_*^{d,k}$ is obtained by substituting n by n^* in the (3.98). $E_1^{d,k}(x,y)$ and $E_2^{d,k}(x,y)$ represent the complex amplitudes (at (x,y)) of the external acoustic field in the flow region ($y>0$) and cavity region ($y<0$) respectively.

In this dissertation we focus on the behavior of the field for $O(1)$ values of y. The behavior in the stream at large distances ($x \gg 1$) is most naturally approached by applying the method of steepest descents, in which the integration contour for (3.93) and (3.94) is deformed to pass through the saddle point of the exponent. The far field contribution of the external field generated by the interaction of the k-th downstream duct mode with the edge of the upstream overhanging lip is given by

$$E_1^{d,k}(x,y) \approx \frac{-\mathcal{C}_2[(1+\mathrm{i}\eta)+M_d]\mu_2(M_d)\sinh(\mu_2(M_d)d)}{\sqrt{M_d-M_u}}\left(\frac{\beta \mathrm{e}^{\mathrm{i}3\pi/4}\sqrt{M_d-M_u}}{a_1}\,y-\frac{b_1}{a_1^2}\right)\frac{\Gamma(3/2)}{x^{3/2}}, \tag{3.99}$$

$$E_2^{d,k}(x,y) \approx \mathcal{C}_2\,\mathrm{e}^{\mathrm{i}3\pi/4}\,\frac{\beta(1+\mathrm{i}\eta)\cosh(\mu_2(M_d)(y+d))}{a_1}\,\frac{\Gamma(3/2)}{x^{3/2}}, \tag{3.100}$$

where

$$\mathcal{C}_2 = \frac{\rho_{02}(1+\mathrm{i}\eta)K^-(\sigma_k^-)\sqrt{\sigma_k^- - M_u}}{\pi(M_d-\sigma_k^-)K^-(M_d)} \tag{3.101}$$

and a_1, b_1 are given by (3.70) and (3.71), respectively. A general procedure to obtain the external fields and their expansion for large values of x is given in Appendix C.

3.3 Analysis for a Finite-length Overhanging Lip or a Square Corner

In this section we develop an analysis of the scattering process for the impingement of an upstream cavity mode on an upstream overhanging lip of finite length, for $\eta = 0$. The geometry of the upstream end of the cavity consists of a vertical end wall at $x = -b$ and an infinitely thin overhanging lip extending from $x = -b$ to $x = 0$, as illustrated in figure 3.1b . The cavity is assumed sufficiently long that, in analyzing the interaction at the upstream end, the downstream end of the cavity can be neglected. Thus, for the purpose of the analysis, the cavity is assumed to extend

to upstream infinity. The generalized Wiener-Hopf technique is used to develop a solution for the case of a finite overhang length. Results for the case of a square (90°) upstream corner are then obtained by considering the limit $b \to 0$.

The generalized Wiener-Hopf technique is applicable to situations where a region exists in which the field contains only a finite number of 'cut-on' modes, which propagate either with no attenuation or weak attenuation. The rest of the infinite set of modes are 'cut-off,' i.e., they suffer strong attenuation in propagating a distance of the order of the cavity depth d. A typical application was presented by Koch (1977). The geometry typically involves reflected fields, so that both upstream-propagating modes (with amplitude D_q) and downstream-propagating modes (with amplitude E_q) are present. An infinite-dimensional matrix equation is developed for the modal amplitudes D_q and E_q. However, since only a finite number of modes are cut-on (say $q = 0, 1, ..., q^*$), while the rest exhibit exponential decay, entries in the matrix equation are very small for entries $q \gg q^*$. Thus, an accurate description of the field can be obtained by solving a truncated form of the infinite-dimensional matrix equation, which includes only a portion of the cut-off modes. To further improve accuracy, extrapolation techniques could be employed to account for the neglected modes, though this is seldom necessary due to the exponential decay with respect to mode order.

For the present, we assume a finite value for the cavity overhang length b and concentrate on the field in the region $-d < y < 0$ and $-b < x < 0$. In this region, the field $\phi_2(x, y)$ is a combination of upstream and downstream duct modes of unknown amplitudes D_q and E_q, respectively, thus

$$\phi_2 = \sum_{q=0}^{\infty} \left[E_q \cos(q\pi y/d) \mathrm{e}^{-\mathrm{i}\sigma_q^- x} + D_q \cos(q\pi y/d) \mathrm{e}^{-\mathrm{i}\sigma_q^+ x} \right]. \tag{3.102}$$

Expressions for the x-wavenumbers σ_q^+ and σ_q^- are given in (3.74). Since the acoustic propagation characteristics do not depend on the direction of propagation, we have $\sigma_q^- = -\sigma_q^+$. For the cut-on modes ($q \leq M_2 d/\pi$, for $\eta = 0$), σ_q^+ is real and positive, so

that these modes propagate without attenuation. For the cut-off modes ($q \geq M_2 d/\pi$, for $\eta = 0$), σ_q^+ is positive imaginary and $O(q)$ for large q. Hence these modes decay exponentially with distance in the direction of propagation, the decay rate increasing as the mode order increases.

When considering the impingement of the k-th downstream-propagating duct mode in section 3.2.2, the overhanging lip was assumed to extend to upstream infinity and the presence of the cavity end wall at $x = -b$ was neglected. Consider the influence of the upstream end wall of the cavity at $x = -b$. This end-wall reflects the upstream-propagating duct modes, producing an infinite set of downstream-propagating duct modes in the region $-b < x < 0$. Applying the no-penetration boundary condition on the vertical end wall (3.25) to (3.102), and noting that the duct modes are an orthogonal set, we obtain

$$E_q = D_q \mathrm{e}^{\mathrm{i}\sigma_q^+ 2b}, \tag{3.103}$$

where we have used the fact that $\sigma_q^- = -\sigma_q^+$. Since the end wall is a uniform surface, which is normal to the 'duct axis', each mode of the upstream-propagating field is reflected in phase as a downstream-propagating mode of the same order. For the cut-on modes ($q \leq M_2 d/\pi$, , for $\eta = 0$), σ_q^+ is real and positive and E_q differs from D_q by a simple phase shift, corresponding to the time delay required for propagation upstream to the end wall at $x = -b$, reflection in phase, and propagation back downstream to $x = 0$. For the cut-off modes ($q \geq M_2 d/\pi$), σ_q^+ is positive imaginary and $O(q)$ for large q, so that D_q is exponentially small compared to E_q. Thus, as the mode order increases in the cut-off range, the influence of reflection by the upstream end wall becomes insignificant.

Returning to the scattering of the $\mathcal{U}$ cavity mode at the upstream end of the cavity, the solution can be constructed from the solutions of sections 3.2.1 and 3.2.2, as follows.

First, the impingement of the upstream-propagating cavity mode $\mathcal{U}$ on the edge

of the overhanging lip generates a set of upstream duct modes of amplitude $D_j^{\mathcal{U}}$, $j = 0, 1, 2, ..., \infty$. Next, additional contributions to the upstream duct modes are generated by the impingement of the downstream duct modes on the edge of the overhanging lip. For a downstream-propagating duct mode of order k and amplitude E_k, the scattering at the lip edge produces contributions to the amplitudes of the upstream duct modes with amplitude $E_k D_j^{d,k}$, $j = 0, 1, 2, ..., \infty$. Thus, the amplitudes D_q of the total upstream mode field in the portion of the cavity under the overhanging lip are given by

$$D_q = D_j^{\mathcal{U}} \delta_{qj} + \sum_{k=0}^{\infty} E_k D_j^{d,k} \delta_{qj}, \quad q = 0, 1, 2, \ldots, \tag{3.104}$$

where $\delta_{qj} = 1$ when $q = j$, and $\delta_{qj} = 0$ when $q \neq j$. The $D_j^{\mathcal{U}}$ are given by (3.57) and $D_j^{d,k}$ by (3.92), while the amplitudes D_k are presently unknown.

Next, we use (3.103) to express the amplitudes E_k of the downstream duct modes in terms of the amplitudes of the upstream duct modes D_k. Employing the properties of the substitution tensor to eliminate the index q, we obtain

$$D_j - \sum_{k=0}^{\infty} D_k D_j^{d,k} \mathrm{e}^{\mathrm{i}\sigma_k^+ 2b} = D_j^{\mathcal{U}}, \quad j = 0, 1, 2..., \infty. \tag{3.105}$$

This is an inhomogeneous matrix equation of the form

$$\tilde{A}\bar{D} = \bar{D}^{\mathcal{U}} \tag{3.106}$$

for the vector $\bar{E} = [D_0, D_1, ..., D_\infty]^T$, where the superscript $(\cdot)^T$ indicates the transpose. Also, $\bar{D}^{\mathcal{U}} = \left[D_0^{\mathcal{U}}, D_1^{\mathcal{U}}, ..., D_\infty^{\mathcal{U}}\right]^T$ and the matrix $\tilde{A}$ has the components

$$\tilde{A}_{jk} = \delta_{jk} - D_j^{d,k} \mathrm{e}^{\mathrm{i}\sigma_k^+ 2b}. \tag{3.107}$$

The matrix equation (3.106) is infinite dimensional, but the influence of the higher-order cut-off modes is exponentially small so that accurate results can be obtained from a suitably truncated system; we prove this below.

To understand the behavior of the matrix equation (3.106), note that the coefficient matrix $\tilde{A}$ is the sum of the identity matrix $\tilde{I}$ and a matrix $\tilde{A}'$, with entries

$-D_j^{d,k} \mathrm{e}^{\mathrm{i}\sigma_k^+ 2b}$. We consider the properties of $\tilde{A}'$ for large j and k. The $D_j^{d,k}$ are given by (3.92). To determine the behavior for large j and k, note from Appendix A that $\sigma_j^+ \sim \mathrm{i}j\pi/d$ and $K^+(\sigma_j^+) \to 1$ for large j, while $\sigma_k^- \sim -\mathrm{i}k\pi/d$ and $K^-(\sigma_k^-) \to 1$ for large k. Thus, we see that $D_j^{d,k} = O(j^{-7/2})$ for $j \gg 1$ and $k = O(1)$, $D_j^{d,k} = O(k^{-1/2})$ for $k \gg 1$ and $j = O(1)$ and $D_j^{d,k} = O(j^{-3})$, when j and k are large and of the same order. Secondly, note that the σ_k^+ are purely real for the cut-on modes ($k \leq M_2 d/\pi$) , while σ_k^+ is purely imaginary and positive for the cut-off modes($k \geq M_2 d/\pi$), so that for non-zero values of b the factor $\mathrm{e}^{\mathrm{i}\sigma_k^+ 2b}$ decreases exponentially with index k in the cut-off range. Therefore, the entries of the matrix $\tilde{A}'$ decrease algebraically as the $7/2$ inverse power of the row index j, for large j, and more importantly, for non zero values of b, the entries decrease exponentially with k as the column index k increases in the cut-off range. Thus the entries $\tilde{A}_{jk}$, corresponding to sufficiently large values of j and k, differ only slightly from those of the identity matrix.

The behavior of the solution $\bar{D}$ depends both on the behavior of the coefficients of the matrix $\tilde{A}$ and on the behavior of the vector $\bar{D}^{\mathcal{U}}$ on the right-hand side. The entries $D_j^{\mathcal{U}}$ of this vector are given by (3.57). For large values of the index j, the entries of $\bar{D}^{\mathcal{U}}$ decrease algebraically as $j^{-7/2}$. Since the entries of $\tilde{A}_{jk}$ corresponding to sufficiently large values of j and k differ slightly from those of the identity matrix, the entries D_k of the solution $\bar{D}$ must also decrease algebraically as $k^{-7/2}$ for large k.

Thus, we solve a truncated version of the matrix equation (3.106),

$$\widetilde{A}\overline{D} = \overline{D}^{\mathcal{U}}, \tag{3.108}$$

in which all elements have been neglected for j and k greater than some $k_{\max}$. Wide tildes have been used to denote the truncated version of the matrix equation. We assume that b is non-zero and that $k_{\max}$ extends some distance into the cut-off range, i.e. $k_{\max} > M_2 d/\pi$. The error introduced by truncation can be investigated by examining the relative size of the neglected terms. Consider the row j of the coefficient matrix $\widetilde{A}$. This row has one entry $\widetilde{A}_{jj}$ whose value is near one. In contrast, the

entries in the row which has been neglected contain the factor $e^{i\sigma_k^+ 2b}$, which decreases exponentially with k when $k > M_2 d/\pi$. The size of the neglected coefficients in the j row of $\widetilde{A}$ is further decreased by the factor $D_j^{d,k}$, which decays as $k^{-1/2}$ for large k. In addition, these coefficients multiply the unknowns D_k which themselves decay as $k^{-7/2}$ for large k. Thus, it is clear that little error is introduced by neglecting the terms $k > k_{\max}$. This has been verified numerically by Cain *et al.* (2001).

Once the amplitudes D_k are determined from the truncated matrix equation, the amplitudes of the downstream cavity modes generated by the interaction of the upstream-propagating cavity mode $\mathcal{U}$ with the finite-length overhanging lip and the end wall are given by

$$C_j = C_j^{\mathcal{U}} + \sum_{k=0}^{\infty} D_k C_j^{d,k} e^{i\sigma_k^+ 2b}, \tag{3.109}$$

where $j = 0, 1, 2....$ Note that C_0 is the scattering coefficient $C_{\mathcal{DU}}$ of the global model, discussed in Chapter 2.

Analogously, the amplitude of the instability wave generated by the receptivity process for the finite-length overhanging lip is given by,

$$S = S^{\mathcal{U}} + \sum_{k=0}^{\infty} D_k S^{d,k} e^{i\sigma_k^+ 2b}, \tag{3.110}$$

where we have again made use of (3.103). Note that S is the receptivity coefficient $C_{\mathcal{SU}}$ discussed in Chapter 2. Thus, the receptivity level for the overhanging lip of finite length b is a sum of the element $S^{\mathcal{U}}$ for the direct interaction of an upstream propagating cavity mode with a semi-infinite lip and the levels $D_k S^{d,k}$ produced by the interaction of each of the downstream duct modes with the semi-infinite lip. For finite values of b, the factor $e^{i\sigma_k^+ 2b}$ decreases exponentially with k, for $k > M_2 d/\pi$, so that the contribution from the cut-off modes is exponentially small. However, the reflection of the cut-on modes by the upstream end wall can lead to a significant increase in the receptivity coefficient.

Similarly, the downstream-propagating external field generated by the scattering of the cavity mode $\mathcal{U}$, at the upstream end of the cavity, is given by

$$E_{1\mathcal{U}}(x,y) = E_1^{\mathcal{U}}(x,y) + \sum_{k=0}^{\infty} D_k E_1^{d,k}(x,y) \mathrm{e}^{\mathrm{i}\sigma_k^+ 2b}, \quad \text{for } y > 0 \tag{3.111}$$

$$E_{2\mathcal{U}}(x,y) = E_2^{\mathcal{U}}(x,y) + \sum_{k=0}^{\infty} D_k E_2^{d,k}(x,y) \mathrm{e}^{\mathrm{i}\sigma_k^+ 2b}, \quad \text{for } y < 0. \tag{3.112}$$

Note that $E_{2\mathcal{U}}(0,0)$ is the scattering coefficient $C_{\mathcal{E}_d\mathcal{U}}$, discussed in Chapter 2.

4. NUMERICAL RESULTS AND DISCUSSION FOR THE SCATTERING PROBLEM AT THE UPSTREAM END

Numerical results for the unsteady field generated by scattering of the upstream cavity mode $\mathcal{U}$ at the upstream edge of the cavity are presented in this section. The geometries illustrated in figure 3.1 are considered. The numerical results were obtained using *Mathematica*5 (Wolfram 2003) on a Pentium Computer. Results are presented for the cases $M_1 = M_2 = M = 0.35$ and $M = 0.85$, with $\omega d'/U = d = 1.5$ and $c_1 = c_2$. For a cavity with length to depth ratio $L/d = 5$, the non-dimensional frequencies for the first four Rossiter modes at $M = 0.35$ lie in the range $0.3 < d < 5.7$; while at $M = 0.85$ they lie in the range $0.26 < d < 4.5$. Thus, the case $d = 1.5$ is roughly centered in the frequency range of interest. Results for the case $\eta = 0$ are presented in this chapter, the influence of non zero η is discussed in Chapter 7.

4.1 Mode Wavenumbers

The x-wavenumbers of the first eight upstream and downstream cavity modes and duct modes for the case $M = 0.35$ are listed below in table 4.1, while the corresponding results for $M = 0.85$ are listed in table 4.2. The location of the wavenumbers in the complex plane, for $M = 0.35$, are illustrated in figure 3.2.

The wavenumbers σ_j^+ of the upstream duct modes (denoted by circles in figure 3.2) lie in the upper half of the complex λ plane, while the wavenumbers σ_j^- of downstream duct modes (denoted also by circles in figure 3.2) lie in the lower half of the complex λ plane. In the 'duct' region, the propagation characteristics are invariant under change of sign of x; hence $\sigma_j^- = -\sigma_j^+$. The x-wavenumber corresponding to the $j = 0$ mode ($\sigma_0^+ = M$) lies on the real axis; this mode is a plane wave which propagates at the speed of sound without damping (attenuation). The wavenumbers σ_j^+, $j \geq 1$ lie

j	τ_j^+	τ_j^-	σ_j^+	σ_j^-
0	$0.42204 + 0.11687\,\mathrm{i}$	$-0.26224 + 0.00000\,\mathrm{i}$	0.35000	-0.35000
1	$-0.07807 + 1.95289\,\mathrm{i}$	$0.06059 - 2.15638\,\mathrm{i}$	$2.06494\,\mathrm{i}$	$-2.06494\,\mathrm{i}$
2	$-0.03037 + 4.15786\,\mathrm{i}$	$0.02933 - 4.19076\,\mathrm{i}$	$4.17414\,\mathrm{i}$	$-4.17414\,\mathrm{i}$
3	$-0.01469 + 6.26833\,\mathrm{i}$	$0.01457 - 6.27863\,\mathrm{i}$	$6.27343\,\mathrm{i}$	$-6.27343\,\mathrm{i}$
4	$-0.00853 + 8.36807\,\mathrm{i}$	$0.00850 - 8.37250\,\mathrm{i}$	$8.37027\,\mathrm{i}$	$-8.37027\,\mathrm{i}$
5	$-0.00554 + 10.46500\,\mathrm{i}$	$0.00553 - 10.46730\,\mathrm{i}$	$10.46610\,\mathrm{i}$	$-10.46610\,\mathrm{i}$
6	$-0.00388 + 12.56080\,\mathrm{i}$	$0.00388 - 12.56220\,\mathrm{i}$	$12.56150\,\mathrm{i}$	$-12.56150\,\mathrm{i}$

Table 4.1 *Wavenumbers of the upstream and downstream cavity modes and duct modes, for* $M = 0.35$.

j	τ_j^+	τ_j^-	σ_j^+	σ_j^-
0	$0.85258 + 0.15183\,\mathrm{i}$	$-0.50441 + 0.00000\,\mathrm{i}$	0.85000	-0.85000
1	$-0.00525 + 1.75699\,\mathrm{i}$	$0.01597 - 2.03123\,\mathrm{i}$	$1.91416\,\mathrm{i}$	$-1.91416\,\mathrm{i}$
2	$-0.01648 + 4.08132\,\mathrm{i}$	$0.01583 - 4.12160\,\mathrm{i}$	$4.10164\,\mathrm{i}$	$-4.10164\,\mathrm{i}$
3	$-0.00822 + 6.21919\,\mathrm{i}$	$0.00814 - 6.23166\,\mathrm{i}$	$6.22543\,\mathrm{i}$	$-6.22543\,\mathrm{i}$
4	$-0.00479 + 8.33167\,\mathrm{i}$	$0.00478 - 8.33703\,\mathrm{i}$	$8.33435\,\mathrm{i}$	$-8.33435\,\mathrm{i}$
5	$-0.00312 + 10.43600\,\mathrm{i}$	$0.00311 - 10.43880\,\mathrm{i}$	$10.43740\,\mathrm{i}$	$-10.43740\,\mathrm{i}$
6	$-0.00218 + 12.53680\,\mathrm{i}$	$0.00218 - 12.53840\,\mathrm{i}$	$12.53760\,\mathrm{i}$	$-12.53760\,\mathrm{i}$

Table 4.2 *Wavenumbers of the upstream and downstream cavity modes and duct modes, for* $M = 0.85$.

on the positive imaginary axis; these modes are cut-off, i.e., they suffer exponential attenuation with distance upstream. The attenuation rate increases as j increases. The family σ_j^- has the same behavior, except that the cut-off modes decay with distance downstream. Therefore, the cut-off modes for both families are important only near the point at which they originate.

The x-wavenumbers of the cavity modes for $M = 0.35$ are plotted by diamonds in figure 3.2. The first upstream cavity mode, τ_0^+, has a real part larger than $\sigma_0^+ = 0.35$ but less than $M_u = 0.538$, the wavenumber of the upstream external acoustic field. Therefore, the τ_0^+ mode propagates at a subsonic speed relative to the speed of sound

in the cavity, and at a supersonic speed relative to the stream. Since τ_0^+ has a small positive imaginary part (0.116), this mode exhibits weak attenuation with distance upstream. This attenuation comes from the radiation of acoustic energy into the stream, which occurs because the phase speed of this mode is supersonic relative to the stream ($c_{\text{ph,rel}} = -1.18c_1$). In contrast, the wavenumbers for the higher-order upstream cavity modes have $O(1)$ positive imaginary parts. Therefore, these modes are strongly damped with upstream distance, the attenuation rate increasing with the mode index j. Note also that, as j increases, the wavenumbers of the upstream cavity modes approach the corresponding wavenumbers of the upstream duct modes. This implies that for the higher-order cavity modes, the vortex sheet presents an impedance boundary condition which differs slightly from a rigid surface.

Next consider the downstream cavity modes. The wavenumber $\tau_0^- = -0.262$, for the lowest order mode, is purely real. Hence this mode propagates downstream without attenuation. The absence of attenuation for the $j = 0$ downstream cavity mode is related to the fact that the phase speed of this mode relative to the stream is slightly subsonic ($c_{\text{ph,rel}} = \frac{M}{\tau_0^-} - M = 0.98c_1$). This can also be seen from the fact that that τ_0^- is very close to, but slightly to the left of, the wavenumber for the downstream external acoustic field ($M_d = -0.259$), see figure 3.2. Therefore, this mode produces an evanescent field in the stream, which decays exponentially with increasing y and radiates no acoustic energy. The wavenumbers of the higher-order downstream cavity modes have $O(1)$ negative imaginary parts, corresponding to strong exponential decay. The values of τ_j^- for $j \geq 1$ lie very close to the corresponding duct mode wavenumbers σ_j^-, $j \geq 1$.

The x-wavenumber for the shear-layer instability wave is $-n = -1.037 + 0.955\text{i}$ and is plotted as a triangle in figure 3.2. Thus, the shear-layer travels downstream with a phase speed $c_{\text{ph}} = 0.175c_1$ and $O(1)$ exponential growth rate. Relative to the stream, the instability wave appears as a disturbance traveling upstream at subsonic speed $c_{\text{ph,rel}} = -0.175c_1$. Hence the instability wave produces only evanescent waves

that decay exponentially in the stream. For comparison, the x-wavenumber for a shear layer instability wave in the absence of the cavity bottom wall ($d \to \infty$) is $-n = -1.0297 + 0.9996\mathrm{i}$; with phase speed $c_{\mathrm{ph}} = 0.175 c_1$. Hence, the presence of the cavity bottom produces an increase in the exponential growth rate.

For $M = 0.85$, the first seven cavity and duct modes are given in table 4.2. As can be seen, this case shows some important differences with the case $M = 0.35$. The first upstream cavity mode τ_0^+ for this case has a real part slightly larger than $M = 0.85$, but significantly smaller than $M_u = 5.67$. Therefore, the τ_0^+ mode propagates at a sonic speed relative to the speed of sound in the cavity, and at a greater supersonic speed relative to the stream; therefore the attenuation rate of the mode τ_0^+, for $M = 0.85$ is slightly larger than that of $M = 0.35$. The first downstream cavity mode τ_0^- for the case $M = 0.85$, exhibits, as in the case $M = 0.35$, no attenuation with downstream distance.

From tables 4.1 and 4.2, we see that the higher-order cavity modes are cut off, i.e. the imaginary part of the wavenumbers τ_j^+, $j = 1, 2, ..., \infty$, is of $O(1)$ and positive and the imaginary part of the wavenumbers τ_j^-, $j = 1, 2, ..., \infty$ of $O(1)$ and negative. Therefore these modes decay to negligible amplitudes within a distance from the upstream or downstream lip respectively. For the length to depth aspect ratios of interest (say $3 < L/d < 8$), it is only the $j = 0$ upstream/downstream cavity mode that provides the acoustic feedback to the downstream/upstream lip. However, the higher-order modes contribute to the local unsteady pressure levels near the upstream/downstream end of the cavity.

4.2 Mode Shapes

The mode shapes for the different disturbances are plotted in figures 4.1-4.5. The quantity plotted is the nondimensional pressure, p_1 for $y > 0$ and p_2 for $y < 0$. For the figures throughout this section, the bottom of the cavity is at $y = -1.5$ and

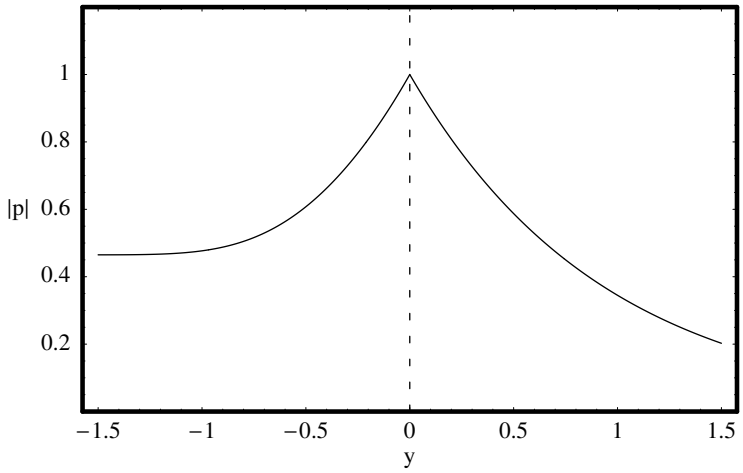

Figure 4.1 *Mode shape for the shear-layer instability wave, for* $M = 0.35$.

the vortex sheet at $y = 0$. The mode shape for the shear-layer instability wave, for $M = 0.35$ is plotted in figure 4.1. This mode decays exponentially out into the stream ($y > 0$), as expected due to its subsonic phase speed relative to the stream. In the cavity region ($y < 0$) (see figure 4.1), the instability wave amplitude decays exponentially away from the vortex sheet. The exponential decay is modified near the cavity bottom by the no-penetration boundary condition, which requires $\frac{\partial p_2}{\partial y} = 0$ at $y = -d$. The mode shape of the instability wave for $M = 0.85$ is similar.

The pressure mode shapes for the first three upstream cavity modes for $M = 0.35$ and $M = 0.85$ are plotted in figures 4.2 and 4.3, respectively. For Mach numbers 0.35 and 0.85, the pressure field of the $j = 0$ cavity mode is nearly uniform across the cavity region ($y < 0$). In the stream ($y > 0$), these two cases exhibit somewhat different behavior. For $M = 0.35$, the $j = 0$ cavity mode exhibits a slow exponential growth in y (see figure 4.2), while for $M = 0.85$, it has a slow exponential decay (see figure 4.3). This transition is in agreement with previous results obtained for the supersonic case by Cain *et al.* (2001).

For the $j = 1$ cavity mode and Mach numbers 0.35 and 0.85, the pressure amplitude has a shape that is close to the $|\cos(\pi y/d)|$ shape for the $j = 1$ duct mode. How-

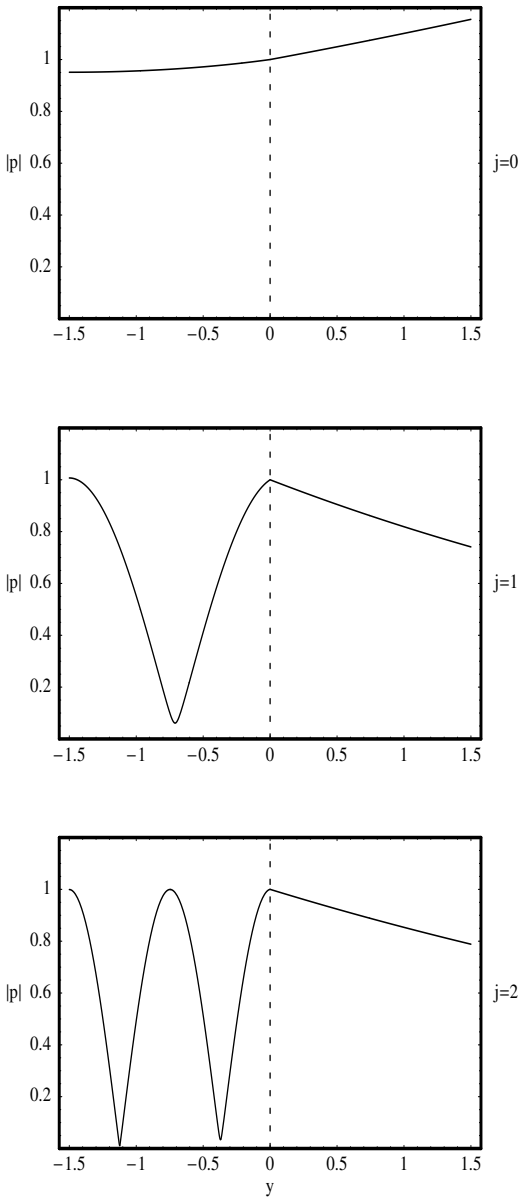

Figure 4.2 *Mode shapes for the first three upstream cavity modes for* $M = 0.35$.

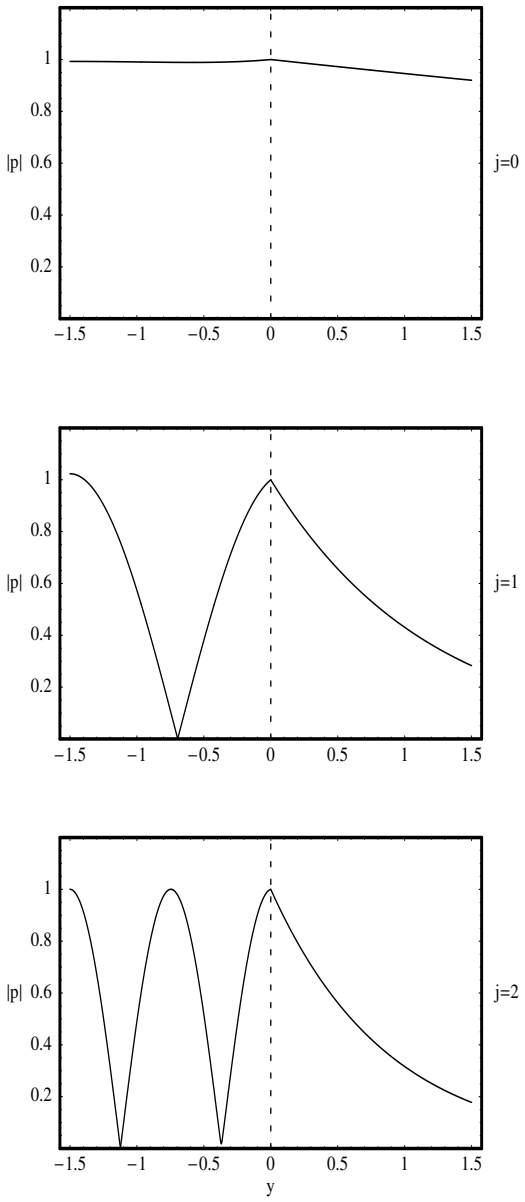

Figure 4.3 *Mode shapes for the first three upstream cavity modes for* $M = 0.85$.

ever, the pressure for the $j = 1$ cavity mode does not quite reach zero at $y = -0.75$, as it would for the corresponding duct mode. The exponential decay out in the stream for the $j = 1$ cavity mode is much faster than that of the $j = 0$ cavity mode, and the

decaying rate increases with Mach number. For the $j = 2$ cavity mode, the pressure amplitude in the cavity ($y < 0$) has a shape which is very close to the $|\cos(2\pi y/d)|$ shape for the $j = 2$ duct mode. The exponential decay of the $j = 2$ cavity mode is slower than that of the $j = 1$ cavity mode for Mach number 0.35, and is faster for Mach number 0.85 (see figures 4.2 and 4.3).

To understand the behavior of the upstream cavity modes, some mathematical and physical observations must be made. First, the similarity of the upstream cavity mode fields within the cavity region to the corresponding duct mode fields is explained mathematically by the fact that the cavity mode wave numbers τ_j^+ are quite close to the corresponding duct mode wavenumbers σ_j^+, and the differences become smaller as j increases. Physically, these higher-order cavity modes produce less deflection of the stream, so the vortex sheet behaves more like a rigid surface.

Second, for the $j = 0$ upstream cavity modes, for both Mach numbers considered, the speed is supersonic relative to the stream; but for $M = 0.35$, the mode grows exponentially out in the stream, and for $M = 0.85$; it decays exponentially. So, why does the $j = 0$ cavity mode for $M = 0.35$ appear to grow exponentially? The answer has to do with our choice of branch cuts. The disposition in the complex plane chosen for both branch cuts, allows us to apply the steepest descents method. In figure 3.2, we see that the wavenumber for the $j = 0$ upstream cavity mode, τ_0^+ for $M = 0.35$ is very close to the branch cut at M_u. Therefore the far field contribution for this mode becomes effective only for angles close to $\theta = \pi$, i.e. for small values of y. Thus in the far field, the exponential decay in the x direction overturns the exponential growth for the small range of y values. More details of our choice of branch cuts can be found in Appendix D.

The higher-order modes, for both Mach numbers, exhibit exponential decay in the stream ($y > 0$). The decay rate increases with Mach number. Contrary to what happens for Mach number 0.85 (see figures 4.2 and 4.3). This behavior is related to the values of the function $\mu_1(\lambda)$, at τ_j^+ for $j \geq 1$.

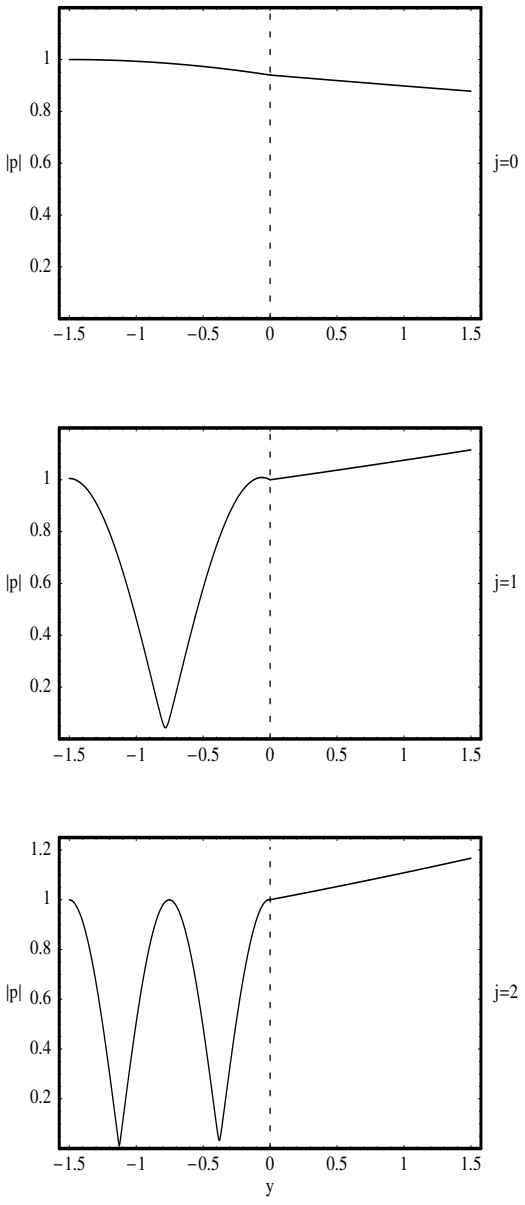

Figure 4.4 *Mode shapes for the first three downstream cavity modes for Mach number 0.35.*

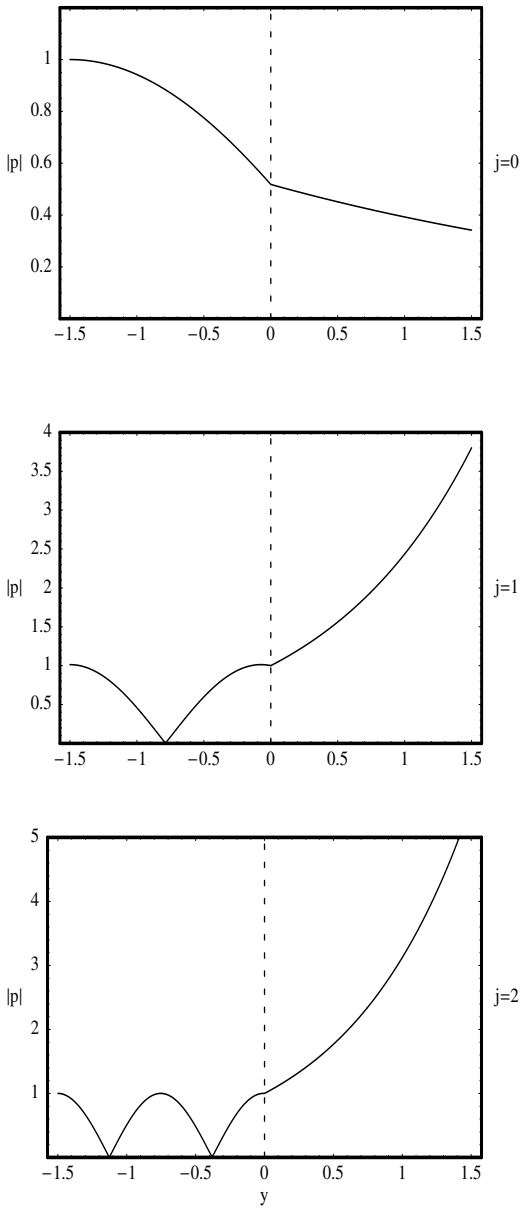

Figure 4.5 *Mode shapes for the first three downstream cavity modes for Mach number 0.85.*

The pressure mode shapes of the first three downstream cavity modes for Mach numbers 0.35 and 0.85 are plotted in figures 4.4 and 4.5, respectively. The pressure field for the $j = 0$ downstream cavity mode in the cavity region ($y < 0$) for $M = 0.35$

(figure 4.4) exhibits a small variation in amplitude which increases with Mach number (see figure 4.5). This last behavior differs significantly from that of the $j = 0$ upstream cavity mode for both Mach numbers considered (see figures 4.2 and 4.3), which has a nearly uniform pressure amplitude within the cavity. Mathematically, this difference in mode shape is related to the fact that the wavenumber τ_0^- for the $j = 0$ downstream cavity mode and $M = 0.85$ differs significantly from the corresponding duct mode wavenumber σ_0^-. In contrast, the wavenumbers τ_0^- and σ_0^- for the case $M = 0.35$ and the wavenumbers τ_0^+ and σ_0^+ for the upstream propagating cavity and duct modes differ only slightly (see figure 3.2 and tables 4.1 and 4.2). Physically, the increasing variation across the cavity region of the pressure amplitude of the $j = 0$ downstream cavity mode is due to the fact that with increasing Mach number the phase speed of the mode increases, i.e. the mode becomes 'more supersonic' in the cavity, increasing the obliqueness of the wavefronts.

For the higher-order downstream cavity modes ($j \geq 1$), the mode shapes for $y < 0$ are quite similar to that of the corresponding duct modes, since the cavity mode wavenumbers τ_1^- and τ_2^- differ slightly from the corresponding duct-mode wavenumbers σ_1^- and σ_2^-. As the mode order increases, the difference between the shape of the downstream cavity mode, for $y < 0$, and the corresponding duct mode, becomes smaller.

More interesting, in the stream region ($y > 0$), all three downstream cavity modes exhibit exponential growth. Although this may be counter intuitive (their phase speeds correspond to downstream propagation at speeds that are subsonic relative to the stream), it is explained by our choice of branch cuts in the complex λ plane. The disposition of both branch cuts emanating form M_u and M_d in the complex plane (see figure 3.2) enables us to use the method of steepest descents. When using this method, the residue contribution from these poles appears when they are crossed by the steepest descent path. This will happen for observation angles θ close to π. For these shallow angles of propagation, the y value is small, therefore the exponential

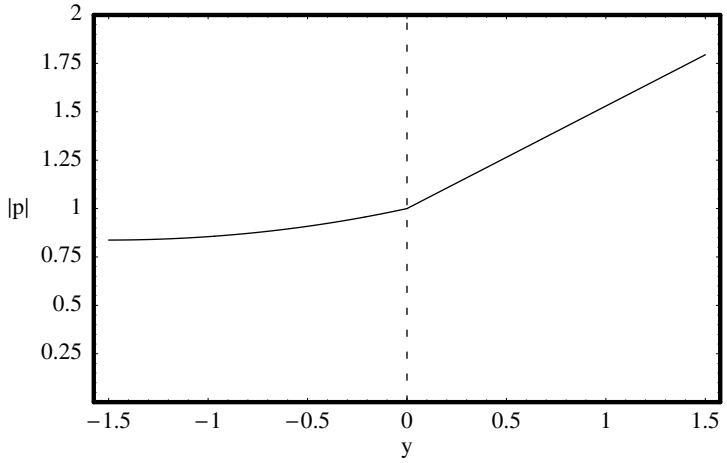

Figure 4.6 *Mode shape for the upstream external acoustic field, for* $M = 0.35$.

growth in y is overturned by the exponential decay in the x-direction. A more detailed explanation is given in Appendix D

Finally, the mode shapes in the far field of the upstream and downstream external acoustic fields for $M = 0.35$ are plotted in figures 4.6 and 4.7. The upstream external field E_u for Mach number $M = 0.35$ has a wavenumber $M_u = \frac{M}{1-M} = 0.538$, so its speed is sonic relative to the stream. The downstream external acoustic field E_D has a wavenumber $M_d = \frac{-M}{1+M} = 0.259$, so its speed is also sonic relative to the stream. Under conditions of no shear layer, the external acoustic fields E_u and E_d have a cylindrical propagation front, with a $r^{-1/2}$ decay, away from the point of origin. However, in the presence of a shear layer, the external fields experience a $x^{-3/2}$ decay for large values of x.

Basically, the wave field in the stream causes a deflection of the vortex sheet, thereby producing a field in the cavity (a 'tail' of the field in the stream); the properties of this field are different for both external fields. For the upstream external field, the phase speed relative to the stream is sonic, but subsonic ($c_{ph} = c_1(1-M)$) relative to the fluid in the cavity. Therefore, the external field produces an evanescent field in the cavity, i.e. the waves are not oblique. For the downstream external field, the

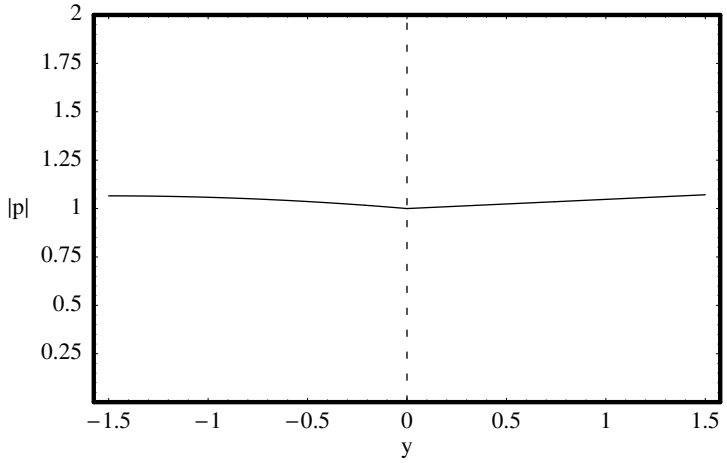

Figure 4.7 *Mode shape for the downstream external acoustic field, for* $M = 0.35$.

phase speed relative to the stream is sonic, but supersonic ($c_{ph} = c_1(1+M)$) relative to the fluid in the cavity. Therefore, it produces a Mach wave field, hence the wave fronts are oblique.

4.3 Results for a Semi-infinite Overhanging Lip

4.3.1 Impingement of the Upstream Cavity Mode $\mathcal{U}$

First, consider the interaction of the upstream-propagating cavity mode $\mathcal{U}$ with a semi-infinite overhanging lip. This interaction was analyzed in section 3.2.1. The geometry is illustrated in figure 3.1(c), and the incident field is given by (3.26, 3.27). The solution for the scattered field in the upstream region ($x < 0$) is given in integral form by (3.54, 3.55), and in the downstream region ($x > 0$) by (3.59, 3.60).

To examine the receptivity process for a semi-infinite overhanging lip, we need to consider only the downstream instability wave (5.33, 5.34) generated by the interaction, which corresponds to the residue for the pole at $\lambda = -n$ in (3.59, 3.60). The complex amplitude of this instability wave field in the downstream region ($x < 0$), $S^{\mathcal{U}}$, is given by (3.66).

For the cases $M = 0.35$ and $M = 0.85$, with $d = 1.5$, the receptivity coefficient

for the impingement of the upstream cavity mode $\mathcal{U}$ on the edge of a semi-infinite overhanging lip are given, respectively, by

$$S^{\mathcal{U}} = 0.03628 - 0.02302\mathrm{i} = 0.042\mathrm{e}^{\mathrm{i}0.565}, \text{ for } M = 0.35, \tag{4.1}$$

$$S^{\mathcal{U}} = 0.07556 + 0.04195\mathrm{i} = 0.086\mathrm{e}^{\mathrm{i}0.507}, \text{ for } M = 0.85 \tag{4.2}$$

The receptivity coefficient $S^{\mathcal{U}}$ is the complex amplitude of the shear-layer instablity wave, relative to the incident cavity mode. The magnitude of this coefficient $\left|S^{\mathcal{U}}\right|$ is the ratio of the amplitude of the perturbation pressure for the instability wave (extrapolated back to the lip edge) to the amplitude of the perturbation pressure for the upstream cavity mode $\mathcal{U}$ (also at the lip edge). From (4.1), we see that the amplitude of the instability wave is only 4.2% of that for the incident cavity mode for $M = 0.35$, while for $M = 0.85$ it is 8.6%. This relatively small value of the receptivity coefficient can be explained by noticing that the pressure field for the incident cavity mode is continuous across $y = 0$. Thus the receptivity is produced only by the impingement of the transverse velocity field of the cavity mode on the upstream overhanging lip. But the transverse velocity field is small since the wavefronts of the cavity mode have only a small obliqueness to the x-direction. The quantity $\mathrm{Arg}[S^{\mathcal{U}}]$ is the relative phase between the pressure fields for the instability wave and the incident cavity mode. For positive values of $\mathrm{Arg}[S^{\mathcal{U}}]$, the phase of the instability wave lags the phase of the incident cavity mode. From (4.1) and (4.2) we see that in the case for $M = 0.35$, the phase lag is about 32.4°, and for $M = 0.85$, the phase lag is 29°.

The impingement of an upstream cavity mode on the edge of an overhanging lip also generates an infinite set of duct modes that propagate upstream under the overhanging lip ($y < 0$, $x < 0$), an upstream external field (continuous spectrum component) above the lip ($y > 0$, $x < 0$), and cavity modes, which propagate downstream ($x > 0$). For the case of a semi-infinite overhanging lip, these disturbances propagate out to infinity. However, in order to analyze the receptivity for a finite-length overhanging lip or a square (90°) corner, we must calculate the amplitudes of

the upstream duct modes generated by the impingement of the upstream cavity mode $\mathcal{U}$ on the semi-infinite overhanging lip. These amplitudes are obtained by evaluating the residues corresponding to the poles of (3.55) at $\lambda = \sigma_j^+$, $j = 1, 2, ..., \infty$. The complex amplitudes $D_j^{\mathcal{U}}$ of the upstream duct modes are given by (3.57). This expression involves factors containing the wavenumber σ_j^+ of the upstream duct modes, as expected. In order to determine possible influence from secondary loops, we must calculate the amplitudes of the downstream propagating cavity modes.

The amplitudes $|D_j^{\mathcal{U}}|$ and phases $\arg[D_j^{\mathcal{U}}]$ of the first seven upstream duct mode fields generated by the interaction of the upstream cavity mode $\mathcal{U}$ field with a semi-infinite overhanging lip, are presented in the first two columns the tables 4.3 (for $M = 0.35$) and 4.4 (for $M = 0.85$), respectively. The quantity $|D_j^{\mathcal{U}}|$ is the ratio of the amplitude of the perturbation pressure for the j-th scattered upstream duct mode to that of the upstream cavity mode $\mathcal{U}$, with both pressures measured at $(0, 0)$. The quantity $\mathrm{Arg}[D_j^{\mathcal{U}}]$ is the phase of the j-th upstream duct mode relative to the phase of the incident upstream cavity mode, again with both phases measured at $(0, 0)$. From table 4.3, we see that for $M = 0.35$ the amplitude for the $j = 0$ duct mode is $|D_0^{\mathcal{U}}| = 1.15$ and its phase lags the incident $k = 0$ cavity mode by approximately $4.3°$. Similarily, from table 4.4, we see that for $M = 0.85$, $|D_0^{\mathcal{U}}| = 0.99$ and its phase leads the incident cavity mode by $0.31°$. The close-to-perfect match in amplitude and phase for the scattered $j = 0$ duct mode and the incident cavity mode (for both Mach numbers) can be understood by noting the similarity in the characteristics of these two modes. The $j = 0$ duct mode is a plane wave, closely matching the nearly uniform pressure field of the incident cavity $\mathcal{U}$ mode, and the phase speeds of the two modes are very close ($\tau_0^+ \approx \sigma_0^+ = M$). There is only weak scattering of the incident cavity mode into the other upstream duct modes; the $j = 1$ duct mode has an amplitude smaller than 0.1, and the amplitudes of the higher-order modes decrease rapidly with mode order. It is important to note that the close match between the characteristics of the scattered $j = 0$ duct mode and the incident cavity also contributes to the

j	$\lvert D_j^{\mathcal{U}}\rvert$	$\arg[D_j^{\mathcal{U}}]$	$\lvert C_j^{\mathcal{U}}\rvert$	$\arg[C_j^{\mathcal{U}}]$
0	1.15256	0.07529	0.00527	3.11398
1	0.02236	−0.22332	0.01648	3.07275
2	0.00215	−0.60789	0.00204	0.27170
3	0.00052	−0.72387	0.00051	−2.74169
4	0.00019	−0.77960	0.00019	0.46048
5	0.00009	−0.81251	0.00009	−2.64605
6	0.00005	−0.83429	0.00005	0.51841

Table 4.3 *Amplitudes and phases of the upstream duct modes and downstream cavity modes generated by the interaction of the upstream cavity mode* $\mathcal{U}$ *with a semi-infinite overhanging lip, for* $M = 0.35$ *and* $d = 1.5$.

j	$\lvert D_j^{\mathcal{U}}\rvert$	$\arg[D_j^{\mathcal{U}}]$	$\lvert C_j^{\mathcal{U}}\rvert$	$\arg[C_j^{\mathcal{U}}]$
0	0.99964	−0.00537	0.06604	3.08004
1	0.07172	−0.32556	0.04411	−2.80214
2	0.00596	−0.61696	0.00519	0.50583
3	0.00140	−0.69523	0.00129	−2.55377
4	0.00050	−0.73144	0.00048	0.62712
5	0.00023	−0.75251	0.00022	−2.49170
6	0.00012	−0.76638	0.00012	0.66474

Table 4.4 *Amplitudes and phases of the upstream duct modes and downstream cavity modes generated by the interaction of the upstream cavity mode* $\mathcal{U}$ *with a semi-infinite overhanging lip, for* $M = 0.85$ *and* $d = 1.5$.

relatively weak receptivity given by (4.1) and (4.2).

The downstream cavity modes generated by the interaction of an upstream cavity mode with a semi-infinite overhanging lip are given in tables 4.3 (for $M = 0.35$) and 4.4 (for $M = 0.85$). The largest amplitudes are $|C_0^{\mathcal{U}}| = 0.005$, for $M = 0.35$ and $|C_0^{\mathcal{U}}| = 0.06$ for $M = 0.85$. The amplitudes $C_j^{\mathcal{U}}$ decrease as the mode order j increases.

A downstream external acoustic field $E^{\mathcal{U}}(x, y)$ is also generated by the interaction. This external field, propagating in the downstream direction, has a magnitude at the lip edge of $|E^{\mathcal{U}}(0, 0)| = 0.24$. This magnitude, although higher than that of the $j = 0$ downstream cavity mode generated by the same interaction, experiences algebraic

decay in the order of $x^{-3/2}$ with downstream distance, whereas the $j = 0$ downstream cavity mode experiences no attenuation. The unsteady pressure field on the cavity bottom that is produced by the impingement of the upstream cavity mode $\mathcal{U}$ with an overhanging lip is presented in figure 4.8. In the downstream region, $x > 0$, the total field is the sum of the incident upstream cavity mode (3.27) and the scattered field (3.62). The scattered field contains the downstream instability wave, its exponentially decaying counter part, and cavity modes (whose amplitudes are given by 3.66). It also contains the scattered downstream external acoustic field (with amplitude $E^{\mathcal{U}}(x, y)$). In the upstream region, $x < 0$, the total field contains only the series of upstream propagating duct modes (3.56). The series have been evaluated using the first eight modes. Despite the finite term truncation of these series, the amplitude and phases for $x \to 0_-$ and $x \to 0_+$ agree to within 0.01%. Furthermore, accelerating convergence techniques (Shanks transformation, Bender & Orszag, 1999) made the amplitude and phases agree to within 0.001%.

In the downstream region, $0 < x < 2$, the amplitude of the total pressure field exhibits a rapid exponential decay due to the interference from higher-order cavity modes ($j \geq 1$) and the external acoustic field. For $x > 2$, the total pressure field exhibits exponential growth. In this region, the total pressure field is basically the instability wave field, so that the amplitude of the $j = 0$ downstream cavity mode, $|C_0^{\mathcal{U}}| = 0.005$, becomes negligible compared to that of the instablity wave. Hence for $x > 2$, the pressure field in this region grows with downstream distance at a rate set by $\mathrm{Im}[-n]$.

In the upstream region ($x < 0$), the only mode with a significant amplitude (and a non-decaying one) is the $j = 0$ upstream duct mode. Thus, the pressure level becomes constant at $|p| = 1.15$.

The phase of the total pressure field is also shown in figure 4.8. For $x > 4$, the phase of the total pressure field corresponds to that of the the instability wave. For $x < -1$, the phase of the total pressure field corresponds to upstream propagation of

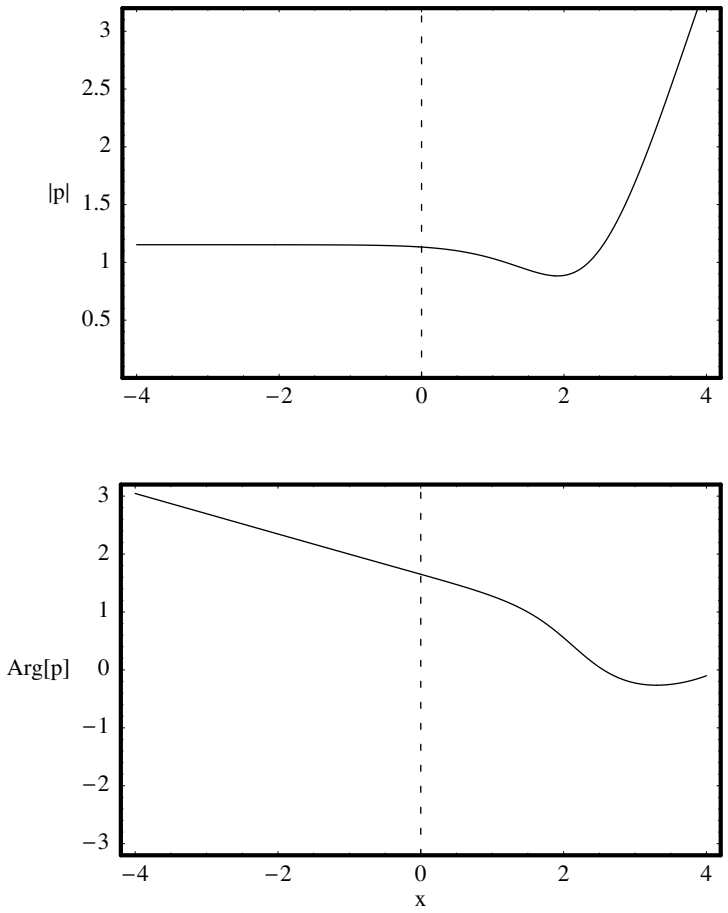

Figure 4.8 *Amplitude and phase of the pressure field on the cavity bottom for the interaction of the upstream cavity mode $\mathcal{U}$ with an overhanging lip, for $M = 0.35$.*

the $j = 0$ duct mode. In the region $-1 < x < 1$, the phase is dominated by upstream convection/propagation, while the phase variation in the region $1 < x < 4$ results from the constructive/destructive interference of the instability wave and the $j = 0$ upstream cavity mode.

4.3.2 Impingement of a Downstream Duct Mode

For the case of a finite-length overhanging lip, the upstream duct modes discussed in the previous section reflect off the upstream end wall of the cavity, producing

downstream duct modes which then interact with the edge of the overhanging lip. Thus, we must also consider the receptivity produced by the interaction of the k-th downstream duct mode with a semi-infinite overhanging lip. This interaction was analyzed in section 3.2.2. The incident field is given by (3.72, 3.73). The solution for the scattered field is given in the integral forms (3.89, 3.90) for the upstream region ($x < 0$) and by (3.93, 3.94) for the downstream region ($x > 0$).

The complex amplitudes of the receptivity ceofficients $S^{d,k}$ are given by (3.98). The magnitudes and phases of the receptivity coefficients for the impingement of the first seven downstream duct modes on a semi-infinite lip, are given in tables 4.5 (for $M = 0.35$) and 4.6 (for $M = 0.85$). For $M = 0.35$, the receptivity coefficient for the $k = 0$ downstream duct mode has a magnitude $|S^{d,0}| = 0.11$, and $|S^{d,0}| = 0.22$ for $M = 0.85$. These values are nearly three times the corresponding values $|S^{\mathcal{U}}| = 0.04$ and $|S^{\mathcal{U}}| = 0.09$ for the impingement of the upstream cavity mode $\mathcal{U}$, for $M = 0.35$ and $M = 0.85$, respectively. The much higher receptivity level for the $k = 0$ downstream duct mode is due to the discontinuity in pressure across $y = 0$ associated with the incident field (3.72, 3.73). When this duct mode propagates past the edge of the upstream lip, the pressure imbalance creates a significant transverse acceleration of the vortex sheet, which leads to a stronger excitation of the instability wave. In contrast, the pressure field for the incident upstream-propagting cavity mode is continuous across $y = 0$, so the instability wave is excited only by the weaker transverse velocity field corresponding to this mode. This behavior is consistent with results obtained for the supersonic case studied by Cain *et al.* (2001).

The impingement of the higher-order downstream duct modes on a semi-infinite overhanging lip produces lower receptivity levels. The receptivity coefficient $S^{d,1}$ associated with the impingement of the $k = 1$ downstream duct mode, has an amplitude of $|S^{d,1}| = 0.059$ (for $M = 0.35$) and $|S^{d,1}| = 0.061$ (for $M = 0.85$). The magnitudes of the remaining receptivity coeficients reduce with mode order.

The downstream cavity modes generated by the interaction of a downstream duct

k	$\lvert S^{d,k}\rvert$	$\arg[S^{d,k}]$
0	0.10549	0.87644
1	0.058696	2.06341
2	0.05194	2.27504
3	0.04605	2.35935
4	0.04161	2.40489
5	0.03819	2.43342
6	0.03547	2.45298

Table 4.5 *Receptivity coefficients for the interaction of the $k = 0$ downstream duct mode, with a semi-infinite overhanging lip, for $M = 0.35$.*

k	$\lvert S^{d,k}\rvert$	$\arg[S^{d,k}]$
0	0.21853	1.38631
1	0.06117	1.49886
2	0.03986	2.00069
3	0.03127	2.10881
4	0.02660	2.18223
5	0.02361	2.23487
6	0.02149	2.27425

Table 4.6 *Receptivity coefficients for the interaction of the $k = 0$ downstream duct mode, with a semi-infinite overhanging lip, for $M = 0.85$.*

j	$k=0$	1	2	3	4	5	6
0	0.07157	0.00456	0.00329	0.00271	0.00236	0.00212	0.00194
1	0.02965	0.89650	0.07067	0.04287	0.03298	0.02766	0.02426
2	0.00361	0.01080	0.98775	0.01978	0.01145	0.00855	0.00704
3	0.00090	0.00204	0.00592	0.99736	0.00857	0.00480	0.00351
4	0.00033	0.00067	0.00145	0.00360	0.99914	0.00471	0.00258
5	0.00015	0.00029	0.00056	0.00103	0.00240	0.99965	0.00296
6	0.00081	0.00015	0.00027	0.00044	0.00076	0.00171	0.99983

Table 4.7 *Amplitudes, $\lvert C_j^{d,k}\rvert$, of the downstream cavity modes generated by the interaction of the k-th downstream duct mode with a semi-infinite overhanging lip, for Mach number 0.35*

mode with a semi-infinite overhanging lip are given by (3.97). The amplitudes $|C_j^{d,k}|$ of the first seven scattered downstream cavity modes, for $M = 0.35$, are given in table 4.7. First note that, for $k \geq 1$, the diagonal elements are near one. This shows that for the impingement of the higher-order duct modes, little energy is scattered into the cavity modes of different order, i.e. the corresponding downstream scattered cavity mode is a nearly perfect continuation of the upstream incident duct.

Thus, the behavior of the receptivity coefficients as a function of the mode order k has a physical explanation. As the mode order k increases, the wavenumber τ_k^- of the k-th downstream cavity mode approaches the wavenumber σ_k^- of the incident downstream duct mode. This leads to a close similarity in the mode shapes and

j	$k=0$	1	2	3	4	5	6
0	0.0268	−0.7768	−0.6329	−0.5847	−0.5605	−0.5459	−0.5361
1	2.6121	3.1085	0.6625	0.6745	0.6833	0.6892	0.6932
2	−0.0243	0.9457	−0.0155	−2.0604	−2.0537	−2.0477	−2.0433
3	−2.9781	−2.0300	−1.9532	3.1360	1.2433	1.2482	1.2526
4	0.2542	1.1892	1.2688	1.2940	−0.0025	−1.8173	−1.8138
5	−2.8341	−1.9073	−1.8272	−1.8004	−1.7879	3.1402	1.3729
6	0.3425	1.2638	1.3440	1.3711	1.3846	1.3920	−0.0008

Table 4.8 *Phases,* $\arg[C_j^{d,k}]$*, of the downstream cavity modes generated by the interaction of the k-th downstream duct mode with a semi-infinite overhanging lip, for* $M = 0.35$

propagation characteristics of the two modes. Thus, the continuation of each higher-order duct mode into the cavity is dominated by the corresponding cavity mode, with little scattering into other modes.

For the $k = 0$, $j = 0$ we see that $|C_j^{d,0}| = 0.07$. Note that even though the magnitude is small compared to the higher-order modes ($k = j > 0$), this mode experiences no attenuation, $\mathrm{Im}[\tau_0^-] = 0$, when traveling across the length of the cavity so its influence will be much higher at the downstream end of the cavity than that of the higher-order modes, see figure 3.2.

Now consider the phase $\arg[C_j^{d,k}]$ of the scattered downstream cavity modes. The phases of the first seven cavity modes are given in table 4.8. Note that the diagonal entries ($j = k$) are close to zero when j is even and close to π when j is odd. Note also that for even values of j, the cavity mode $\cosh(\mu_2(\tau_j^-)(y+d))$ has a phase which is almost identical to that of the corresponding duct mode $\cos(\frac{j\pi}{d}y)$, while for odd values of j the cavity mode has a phase which differs from that of the corresponding duct mode by approximately π. Therefore, for an incident k-th downstream duct mode, the phase of the scattered k-th downstream cavity mode is such that to provide a nearly perfect continuation of the phase of the incident pressure field.

In the upstream region, $x < 0$, we have an infinite set of upstream duct modes generated by the interaction of the k-th downstream duct mode with a semi-infinite

j	$k=0$	1	2	3	4	5	6
0	0.38774	0.19581	0.14202	0.11715	0.10201	0.09155	0.08377
1	0.03651	0.02798	0.02686	0.02487	0.02307	0.02155	0.02028
2	0.00360	0.00365	0.00391	0.00391	0.00379	0.00364	0.00350
3	0.00088	0.00101	0.00116	0.00050	0.00120	0.00117	0.00115
4	0.00032	0.00039	0.00048	0.00025	0.00051	0.00051	0.00050
5	0.00015	0.00019	0.00023	0.00014	0.00026	0.00026	0.00026
6	0.00008	0.00010	0.00013	0.00009	0.00015	0.00015	0.00015

Table 4.9 *Amplitudes,* $|D_j^{d,k}|$*, of the upstream duct modes generated by the interaction of the k-th downstream duct mode with a semi-infinite overhanging lip, for* $M = 0.35$

overhanging lip. For the receptivity in the case of a semi-infinite overhanging lip, the upstream duct modes propagate to infinity and need not be considered any further. However, these upstream disturbances become important when we want to analyze the receptivity for a finite length overhanging lip or a square (90°) corner. The complex amplitudes of the upstream duct modes are given by (3.92). The amplitudes $|D_j^{d,k}|$ of the first seven reflected upstream duct modes, for Mach number 0.35, are presented in table 4.9, and their corresponding phases $\arg[D_j^{d,k}]$ are presented in table 4.10. From these tables we see that the $j = 0$ scattered duct modes have the largest amplitude among the scattered modes, with $|D_0^{d,0}| = 0.39$ having the largest amplitude and a phase lead of 124° relative to the incident downstream duct mode. The value of the amplitude is consistent with results from supersonic and no-flow cases studied by Cain *et al.* (2001). The amplitudes of the higher-order modes ($j \geq 1$) decrease dramatically with mode order. Furthermore, for the higher-order modes ($k, j \geq 1$), both the upstream and downstream duct modes are cut-off and decay exponentially with distance in the direction of propagation. Thus, the $k = j = 0$ incident downstream duct mode has a greater impact on the prediction of the resonant frequencies. The phases $\arg[D_j^{d,k}]$ show more variability, but since the amplitudes for all modes except $D_0^{d,0}$ are very small, they are of little importance.

The behavior of the scattering coefficients for $M = 0.85$ is similar to that of

j	$k=0$	1	2	3	4	5	6
0	−2.1626	−2.6720	−2.6760	−2.6766	−2.6768	−2.6768	−2.6768
1	0.0431	0.7688	0.8490	0.8763	0.8901	0.8984	0.9040
2	−0.5354	0.2745	0.3548	0.3820	0.3958	0.4042	0.4097
3	−0.7145	0.1233	0.2036	0.2309	0.2447	0.2530	0.2585
4	−0.8015	0.0502	0.1305	0.1578	0.1716	0.1799	0.1855
5	−0.8531	0.0070	0.0873	0.1145	0.1283	0.1366	0.1422
6	−0.8873	−0.0216	0.0586	0.0859	0.0997	0.1080	0.1136

Table 4.10 *Phases,* $\arg[D_j^{d,k}]$*, of the upstream cavity modes generated by the interaction of the k-th downstream duct mode with a semi-infinite overhanging lip, for* $M = 0.35$

$M = 0.35$. In this case, the $j = 0$ cavity mode coefficient has an amplitude $|C_0| = 0.3$, almost four times that of the same coefficient for $M = 0.35$. The $j = 0$ upstream duct mode has an amplitude $|D_0| = 0.1$, almost a fourth of the amplitude of the same coefficient for $M = 0.35$. This reduction in amplitude of the reflected coefficient and corresponding increase in the transmited coefficient has to do with the shear-layer behavior. For higher flow speeds, the cavity modes produce less deflection of the stream, so the vortex sheet behaves more like a rigid surface. Therefore the $j = 0$ downstream cavity mode is a natural continuation of the corresponding $j = 0$ downstream duct mode.

Returning to the case $M = 0.35$, we see that all the amplitudes of the scattered coefficients are still relatively small and none has a large enough value. So, where is most of the energy of the incident field going to? The answer is obtained by looking at the external acoustic field produced by this interaction, given by $E^{d,0}(0,0) = 0.5873 - 0.3070\mathrm{i} = 0.663\mathrm{e}^{-0.482\mathrm{i}}$. Hence the external acoustic field is an important element of the scattered field. This field has a phase lead of 27.6° with respect to the incident duct mode and experiences algebraic decay, as opposed to the exponential decay experienced by the higher-order cavity modes. Also, its amplitude for both interactions considered so far is considerably higher than that of the $k = j = 0$ cavity mode. Therefore, for shallow cavities with short aspect ratio L/d,

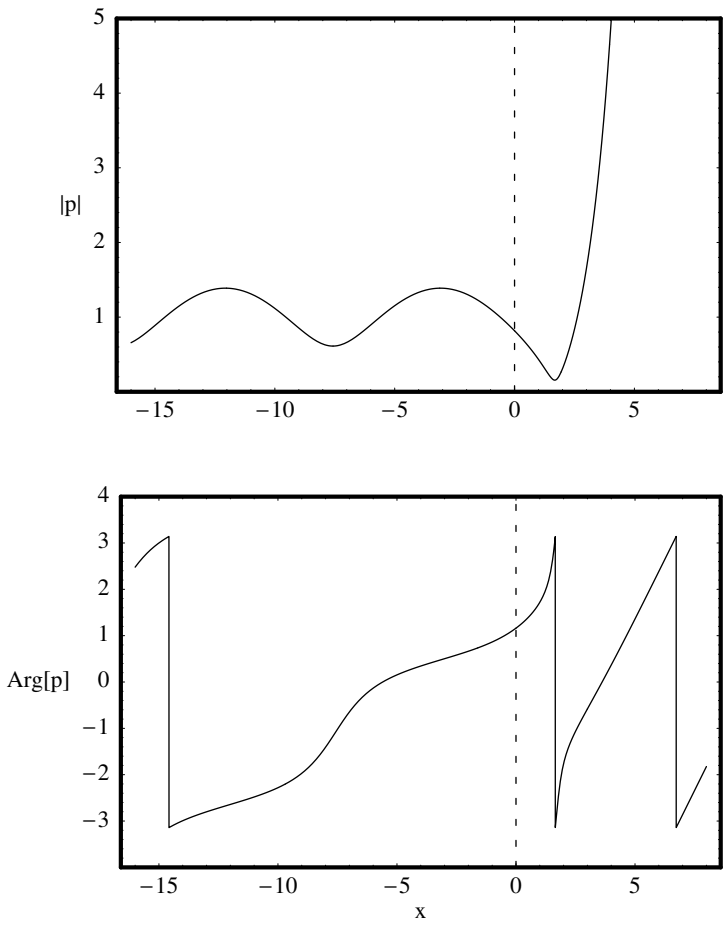

Figure 4.9 *Amplitude and phase of the pressure field on the cavity bottom for the interaction of the $k = 0$ downstream duct mode with an overhanging lip, for $M = 0.35$.*

the downstream external acoustic field may play a modest role when determining the total field reflected downstream.

The total pressure field on the cavity bottom for the interaction of the $k = 0$ downstream duct mode is presented in figure 4.9. In the downstream region, $x > 0$, the unsteady pressure field is given by the scattered field (3.96). This scattered field is the sum of the downstream instability wave (of amplitude $S^{d,0}$), its exponentially decaying counterpart (of amplitude $S_*^{d,0}$), the downstream propagating external acoustic field (with amplitude $E^{d,k}(x, y)$), and the series of downstream cavity modes (whose

amplitudes are given by 3.97). In the upstream region the unsteady pressure field is given by (3.91), is the sum of the incident downstream duct mode (3.73) and the series of reflected upstream duct modes (whose amplitude is given by (3.92)). The series have been evaluated numerically using the first eight modes. Despite the finite-term truncation of the series, the amplitude and phases for $x \to 0_-$ and $x \to 0_+$ agree to within 0.01% at the bottom of the cavity.

In the downstream region, $0 < x < 1.5$, the amplitude of the total pressure field exhibits a rapid exponential decay as the contributions from higher-order cavity modes ($j \geq 1$), which are cut-off modes, vanish and the contribution from the external acoustic field decays as $x^{-\frac{3}{2}}$. For $x > 1.5$, the total pressure field consists mainly of the contribution from the instability wave, that due to its growth counterbalances the low receptivity levels and becomes of $O(1)$. Hence for $x > 1.5$, the pressure field in this region grows with downstream distance at a rate set by $\mathrm{Im}[-n]$.

In the upstream region ($x < 0$), the field contains the incident downstream $k = 0$ duct mode of amplitude unity and the infinite set of scattered upstream duct modes. The higher-order modes are cut-off and can be neglected beyond a point, say $x = -2$. The maximum pressure amplitude on the cavity bottom is $|p| = 1.39$ at $x \approx -3.1$, a distance approximately twice the cavity depth d. Beyond the point $x = -2$ the amplitude of the pressure field exhibits a periodic oscillation, with a minimum value of $|p| = 0.61$, a maximum value of $|p| = 1.39$, and a wavelength equal to half the acoustic wavelength, $\frac{1}{2}\lambda_{ac} = \frac{\pi}{M} = 8.98$. This pattern results from the constructive/destructive interference between the incident $k = 0$ downstream duct mode of amplitude one and the scattered upstream $j = 0$ duct mode of amplitude $|D_j^{d,0}| = 0.39$.

The phase of the unsteady pressure field on the cavity bottom is also presented in figure 4.9. The behavior shown in this figure is consistent with the behavior explained in the previous paragraph. For $x > 2$, the phase of the pressure field corresponds to propagation of the instability wave at a phase speed of $0.175c_1$. In the region $-2 < x < 2$, the phase is dominated by upstream propagation. The phase variation

in the region $x < -2$ results from the previously mentioned constructive/destructive interference of the incident $k = 0$ downstream duct mode and the scattered upstream $j = 0$ duct mode.

4.4 Results for a Finite-length Overhanging Lip or a Square Corner

In this section, we present results for the interaction of an upstream cavity mode with a finite-length overhanging lip or a square (90°) corner, for Mach number $M = 0.35$ and $d = 1.5$. This interaction was analyzed in section 3.3. The geometry for an overhanging lip of length b is illustrated in figure 3.1(b) and the square corner geometry, which corresponds to the limit $b \to 0$, is illustrated in figure 3.1(a).

To determine the instability wave receptivity coefficient (the $C_{S\mathcal{U}}$ complex coefficient discussed in Chapter 2) and the scattering coefficient of the unsteady pressure field (the $C_{\mathcal{DU}}$ complex coefficient discussed in Chapter 2) generated by this interaction, we first have to solve the truncated version (3.108) of the infinite dimensional matrix equation (3.106) for the amplitudes $|D_k|$ of the upstream duct modes in the portion of the cavity under the overhanging lip ($-b < x < 0, \ -d < y < 0$). The entries $\tilde{A}_{jk}$ of the coefficient matrix $\tilde{A}$ are given by (3.107) and the entries $D_j^{\mathcal{U}}$ of the vector $\overline{D}^{\mathcal{U}}$ on the right-hand side by (3.57). The matrix equation involves three important physical effects: the generation of upstream duct modes by the impingement of the upstream cavity mode on the edge of the overhanging lip ($x = 0$), the generation of downstream duct modes by reflection of the upstream duct modes at the vertical end wall ($x = -b$), and the generation of upstream duct modes by impingement of the downstream duct modes on the edge of the overhanging lip ($x = 0$). Note that the reflections at the cavity end wall and the scatterings of the downstream duct modes into the upstream duct modes continue indefinitely and are accounted for in the matrix equation. The solution of the matrix equation is simplified by truncating the system at finite order. Accurate results are obtained even for truncations to a

j	$k=0$	1	2	3	4	5	6	7
0	1.25816	0.19582	0.14203	0.11715	0.10201	0.09155	0.08377	0.07769
1	0.03651	0.98009	0.02686	0.02487	0.02307	0.02155	0.02028	0.01919
2	0.00360	0.00365	0.99629	0.00392	0.00379	0.00364	0.00350	0.00336
3	0.00088	0.00101	0.00117	0.99883	0.00119	0.00117	0.00114	0.00111
4	0.00033	0.00039	4.76E-4	5.04E-4	0.99950	5.11E-4	5.05E-4	4.97E-4
5	0.00015	0.00019	2.34E-4	2.53E-4	2.62E-4	0.99974	2.63E-4	2.62E-4
6	7.92E-5	1.02E-4	1.30E-4	1.43E-4	1.50E-4	1.53E-4	0.99985	1.53E-4
7	4.62E-5	6.12E-5	7.89E-5	8.79E-5	9.27E-5	9.53E-5	9.66E-5	0.99990

Table 4.11 *Magnitudes $|A_{j,k}|$ of the entries of the matrix $\widetilde{A}$ for a square (90°) corner ($b=0$), for $M=0.35$*

system of small size.

4.4.1 Duct Mode Coefficients

We first consider the case $b=0$. Here the non-diagonal entries $|A_{jk}|$ decay algebraically as $k^{-\frac{1}{2}}$ for large k and fixed j, and as $j^{-\frac{7}{2}}$ for large j and fixed k. The diagonal entries decrease algebraically as k^{-3}. The magnitudes $|A_{jk}|$ of the entries of the coefficient matrix $\widetilde{A}$ for the case $b=0$ are presented in table 4.11, for values of j and k ranging from 0 to 7. The diagonally dominant character and the algebraic decay of the non-diagonal entries are easy to see. The slower decay in k than that in j is consistent with the analysis in section 3.3. Despite the lack of exponential decay with respect to k, the results in table 4.11 indicate that the solutions for the complex amplitudes D_k, can be obtained accurately by a finite-mode truncation of the matrix equation.

In table 4.12, the solutions for the complex amplitudes D_k are presented. Results are presented for both an eight mode truncation and a four mode truncation of the infinite dimensional system. The differences between the four-mode truncation and the eight-mode truncation are very small, despite the lack of exponential decay in k for the non diagonal elements of $\widetilde{A}$. The values $|D_3|$, obtained from the two truncations,

k	$\lvert D_k\rvert_{(8)}$	$\lvert D_k\rvert_{(4)}$	$\arg[D_k]_{(8)}$	$\arg[D_k]_{(4)}$
0	0.906702	0.906767	-0.185390	-0.185425
1	0.056746	0.056728	-0.153883	-0.153967
2	0.005591	0.005588	-0.647538	-0.647667
3	0.001372	0.001371	-0.798144	-0.798303
4	0.000504		-0.870735	
5	0.000232		-0.913755	
6	0.000123		-0.941887	
7	7.168E-5		-0.961999	

Table 4.12 *Amplitudes and phases of the downstream duct modes obtained as the solution of the matrix equation (3.108) for a square ($90°$) corner ($b = 0$). Results for an eight-mode truncation and a four-mode truncation, for $M = 0.35$, are listed.*

differ by less than 0.008%, the values $|D_2|$ differ by 0.05%, and the differences in the values$|D_1|$ and $|D_0|$ are even smaller. The phases, $\arg[D_k]$ obtained using four-mode and eight-mode truncation, differ by at most 0.05%. Therefore, highly accurate values for the amplitudes and phases of the total upstream duct mode field can be obtained by a low-order truncation of the system.

It is useful to consider the physical mechanism which determines the dependence of D_0 on b, and to develop an approximate closed-form expression for this quantity. The primary contribution to the $k = 0$ duct mode field comes from the interaction of the incident $k = 0$ upstream cavity mode with the edge of the overhanging lip. This interaction produces a $k = j = 0$ duct mode of amplitude $|D_0^{\mathcal{U}}| = 1.15$, which propagates upstream without attenuation and reflects off the cavity end wall at $x = -b$, producing a $k = j = 0$ downstream duct mode of the same amplitude. This downstream duct mode then interacts with the edge of the overhanging lip at $x = 0$, producing scattered upstream duct modes with amplitudes $|D_j^{d,0}|$, relative to the incident $k = j = 0$ downstream duct mode. The relative amplitude of the upstream duct mode produced by this interaction is $|D_0^{d,0}| = 0.39$, see table 4.9. Subsequent interactions at the cavity end wall at $x = -b$, and the interactions of the downstream duct modes with the edge of the overhanging lip, continue indefinitely. If the infinite-

dimensional system (3.106) is truncated to a single term in j and k, we obtain the following approximation for the amplitude D_0 of the $k = 0$ upstream duct mode,

$$D_0 = \frac{D_0^{\mathcal{U}}}{1 - D_0^{d,0} \mathrm{e}^{\mathrm{i}\sigma_0^+ 2b}}. \tag{4.3}$$

The above expression accounts for the infinite sequence of reflections and scatterings of the $k = j = 0$ upstream and downstream duct modes, but neglects the contributions to the $k = j = 0$ duct mode field which are produced by the scattering of the higher-order downstream duct modes. Note that the contributions of the higher-order modes are negligible, except for b small (they decay exponentially with downstream distance). Furthermore, the scattering coefficients $D_j^{d,k}$ for the higher-order modes ($j \geq 1$) are small compared to the scattering coefficients $D_0^{\mathcal{U}}$ and $D_0^{d,0}$ associated with the $k = 0$ upstream cavity mode and the $k = 0$ (plane-wave) duct mode, respectively. The accuracy of (4.3) is obtained by comparing its result with the result of the seven-mode truncation of the system (3.106). The largest error in the approximate closed-form expression of $|D_0|$ is only 1%, when $b = 0$, and this error decreases as b increases due to the exponential decay of the higher-order duct modes. Therefore (4.3) provides a remarkably accurate expression for the amplitude of the $k = 0$ duct mode.

4.4.2 Receptivity Coefficients

Once the complex amplitudes D_k of the upstream duct modes have been determined, the receptivity coefficient $C_{\mathcal{SU}}$ (discussed in Chapter 2) for the interaction of the upstream cavity mode $\mathcal{U}$ with a finite-length overhanging lip is given by (3.110). For an eight-mode and one-mode truncation for $b = 0$, the complex amplitudes are given in table 4.13. Note that the coefficient $\hat{S}$ in this table is the scattering coefficient $C_{\mathcal{SU}}$ in the global model presented in Chapter 2. Although the magnitude of this coefficient is relatively small, this disturbance grows with downstream distances.

$\lvert\hat{S}\rvert_{(8)}$	$\lvert\hat{S}\rvert_{(1)}$	$\arg[\hat{S}]_{(8)}$	$\arg[\hat{S}]_{(1)}$
0.139688	0.138393	0.674855	0.652133

Table 4.13 *Amplitudes and phases of the receptivity coefficients obtained from the matrix equation (3.110) for a square (90°) corner ($b = 0$), for $M = 0.35$. Results for an eight-mode truncation and a two-mode truncation are listed.*

The contribution from the $k = j = 0$ duct mode, for $M = 0.35$, has an amplitude near $|S^{d,0}| = 0.11$, since $|D_0| \approx 1$, while the contribution from the upstream cavity mode $\mathcal{U}$ has an amplitude $|S^{\mathcal{U}}| = 0.042$. In contrast, the contribution from the $k = 1$ duct mode has an amplitude of only $|D_1 S^{d,1}| = 0.003$, and the contributions from higher-order modes are even smaller. Thus, if we neglect the contribution from higher-order duct modes ($k \geq 1$), the receptivity coefficient for a finite-length overhanging lip can be approximated by

$$\hat{S} = S^{\mathcal{U}} + D_0 S^{d,0} \mathrm{e}^{\mathrm{i}\sigma_0^+ 2b}. \tag{4.4}$$

In addition, the amplitude D_0 of the $k = 0$ duct mode is approximated by (4.3), leading to

$$\hat{S} = S^{\mathcal{U}} + \frac{D_0^{\mathcal{U}} S^{d,0} \mathrm{e}^{\mathrm{i}\sigma_0^+ 2b}}{1 - D_0^{d,0} \mathrm{e}^{\mathrm{i}\sigma_0^+ 2b}}. \tag{4.5}$$

The above expression is very accurate for the case $b = 0$, the difference in amplitude for the one-mode and eight-mode truncations is less than 1%, and the phase difference is less than 3.7%, see table 4.13. Thus, only two terms, $S^{\mathcal{U}}$ and $S^{d,0}$, are important for the case of a finite-length overhanging lip or a square (90°) corner.

Thus we have shown that, for the present conditions ($M = 0.35$, $b = 0$, $d = 1.5$), the presence of the upstream wall increases the amplitude of the receptivity coefficient by a factor of 3.5, relative to that of a semi-infinite overhanging lip.

4.4.3 Other Coefficients

During the interactions of the $k = 0$ upstream cavity mode and the $k = 0$ upstream duct mode with an overhanging lip downstream cavity modes are also generated. The

k	$\lvert C_k\rvert_{(8)}$	$\lvert C_k\rvert_{(4)}$	$\arg[C_k]_{(8)}$	$\arg[C_k]_{(4)}$
0	0.059866	0.059870	−0.173511	−0.173516
1	0.090746	0.090760	2.825560	2.825510
2	0.010396	0.010401	−0.303204	−0.302768
3	0.002436	0.002440	2.853670	2.855270
4	0.000860		−0.284402	
5	0.000384		2.857660	
6	0.000199		−0.284260	
7	0.000114		2.856990	

Table 4.14 *Amplitudes and phases of the scattering coefficients for the downstream cavity modes; for a square (90°) corner ($b = 0$), for $M = 0.35$. Results for an eight-mode truncation and a four-mode truncation are listed.*

scattered coeffcient for the total acoustic cavity mode field propagating downstream, $\hat{\mathcal{D}}$ (discussed in Chapter 2), is given by (3.109). To obtain this field we need the already obtained complex amplitudes D_k and the cavity mode scattered coefficients generated at each of the interactions mentioned above. The scattered coefficients for the downstream cavity modes generated by the interaction of the $k = 0$ upstream cavity mode are listed in table 4.3. The amplitudes and phases of the scattered coefficients for the downstream cavity modes generated by the interaction of the $k = 0$ downstream-propagating duct mode are given in table 4.7 and 4.8, respectively.

Results for an eight-mode truncation and a four-mode truncation are shown in table 4.14. The maximum difference in amplitude and phase between the four-mode truncation and the eight-mode truncation is 0.2% and 0.07%, respectively, both for $|C_3|$. Also from table 4.14, we can see that the maximum amplitude of the scattered coefficients is $|C_0| = 0.06$, and it decreases with mode order. Hence the downstream cavity modes produced by the impingement of the upstream cavity mode $\mathcal{U}$ will not play a major role in the prediction of the resonant frequencies.

The C_0 coefficient is the scattering coefficient $C_{\mathcal{DU}}$ for the global model discussed in Chapter 2. Note that even if the magntidue $|C_1| = 0.09$ of the $j = 1$ downstream cavity mode is larger than $|C_0| = 0.06$, the $j = 0$ downstream cavity mode does

not exhibit exponential decay in the x-direction, whereas the $j = 1$ mode exhibits exponential decay with downstream distance ($\mathrm{Im}[\tau_1^+] > 1.5$), reaching the downstream end with a negligible magnitude.

5. SCATTERING PROCESS AT THE DOWNSTREAM END OF THE CAVITY

In this chapter, results for the scattering processes at the downstream end of the cavity are presented. The cavity is assumed large enough that the effects of the upstream end can be neglected. We assume harmonic time dependence, linearize the governing equations, and approximate the shear-layer by a vortex sheet.

At the downstream end, the primary incident field is the shear-layer instability wave $\mathcal{S}$ (discussed in section 2.1). The other downstream components ($\mathcal{D}$ and $\mathcal{E}_d$), as discussed in section 2.2, are secondary incident fields. In Section 5.1, we summarize the general formulation.

The scattering problems are solved using the generalized Wiener-Hopf technique (Noble, 1988). To do this, the downstream end of the cavity is substituted by a semi-infinite overhanging lip of zero thickness. A duct mode,as previously defined, is an acoustic field that propagates in the 'duct' formed by the cavity bottom and overhanging lip. It satisfies the no-penetration boundary conditions on the cavity bottom and inner surface of the overhanging lip.

In section 5.2.1 we consider the interaction of an upstream duct mode with the edge of the overhanging lip, and in section 5.2.2, the interaction of the shear-layer instability wave with the edge of the overhanging lip. The interaction of a downstream cavity mode with the edge of the downstream overhanging lip is summarized in section 5.2.3.

In section 5.3 a vertical end-wall is added under the overhanging lip, creating a finite-length overhanging lip of length b'. This problem is solved by solving a truncated matrix problem and then letting $b' \to 0$ to solve for a square ($90°$) upstream corner.

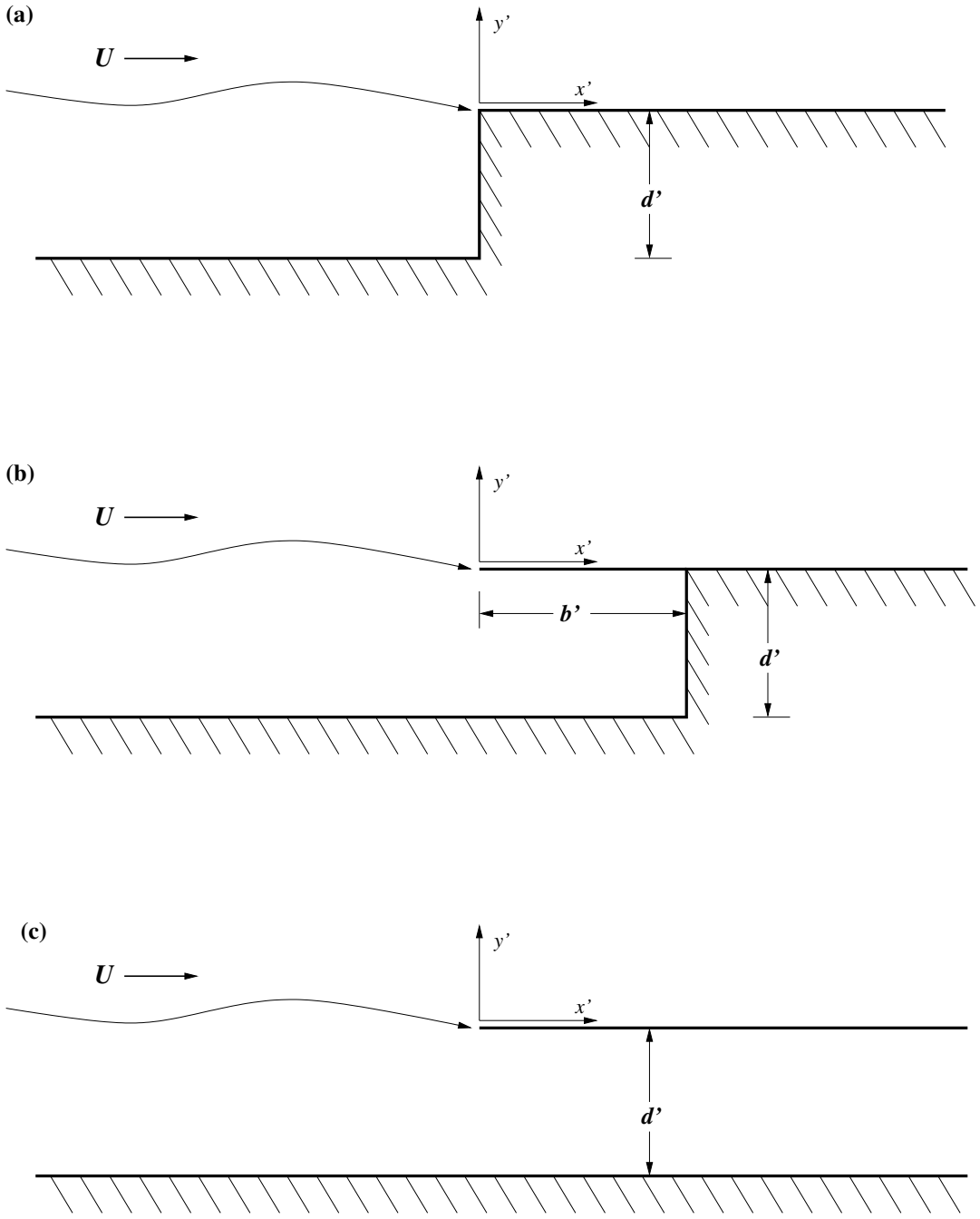

Figure 5.1 *Sketch of geometries for the interactions at the downstream end of the cavity: (a) square corner, (b) thin overhanging lip of finite length b, (c) semi-infinite overhanging lip.*

5.1 General Formulation at the Downstream End of the Cavity

The geometries and non-dimensional coordinate system for analysis of the unsteady flow in the vicinity of the downstream edge of a cavity are illustrated in figure 5.1. Three model geometries are illustrated. The case of a square (90°) corner is illustrated in figure 5.1(a), the case of a thin overhanging lip of finite length b' is illustrated in figure 5.1(b), and a semi-infinite overhanging lip with no end wall is illustrated in figure 5.1(c). The origin of the coordinate system is placed at the edge of the cavity lip. In analyzing the interaction at the downstream edge of the cavity, the cavity is assumed long enough that the presence of the upstream edge can be neglected.

Since the shear layer instabilities which are a crucial element of the cavity resonance phenomenon are primarily two-dimensional in nature, we shall assume that the geometry and flow field are two dimensional. In order to simplify the local analyses, the shear layer will be represented by a vortex sheet. This approximation is quite realistic for the upstream interaction, since the upstream boundary layer, which sets the initial thickness of the shear layer, is usually quite thin. The vortex-sheet approximation is less realistic for the interactions at the downstream end.

In the region $y' > 0$, a uniform flow of speed U and Mach Number $M = U/c < 1$ is present. There is no mean flow in the cavity region $y' < 0$. The shear layer spanning the open face of the cavity is represented by a vortex sheet. In the analysis of the local interaction at the downstream edge of the cavity, the cavity geometry and the vortex sheet are assumed to extend to infinity in the upstream direction. The cavity bottom at $y' = -d'$ is assumed to be rigid and impermeable, and to have infinite extent in the case illustrated in figure 5.1(c).

The development of the general theory at the downstream end is similar to that at the upstream end discussed in section 3.1. We place the origin at the upstream edge of the overhanging lip, as shown in figure 5.1. The governing equations (3.1 - 3.6) hold for the disturbance fields in the flow and cavity regions; the vortex sheet

matching conditions (3.7, 3.8) hold for $x' < 0$. The no-penetration boundary conditions (3.11, 3.10) at the inner and outer surfaces of the overhanging lip, in contrast to section 3.1, apply for $x' > 0$. The no-penetration boundary condition (3.9) at the cavity bottom remains the same, and the no-penetration condition (3.12) on the vertical end wall applies at $x = b'$.

The potential equations obtained after nondimensionalization have the same form as the equations in section 3.1. Governing equations (3.18 - 3.19) remain unchanged, as does the no-penetration boundary condition (3.20) on the cavity bottom. The no-penetration conditions (3.22, 3.21) apply for $x > 0$; the vortex sheet matching conditions (3.23, 3.24) for $x < 0$, and the no-penetration condition (3.25) applies at $x = b$.

5.2 Analysis for a Semi-infinite Overhanging Lip

In this section, we analyze unsteady interactions at the downstream lip of a cavity for the case of a semi-infinite overhanging lip. The geometry is illustrated in figure 5.1(c). This case is interesting in itself, and provides a building block for the analysis in section 5.3 of the downstream interaction for the case of a finite-length overhanging lip or a square (90°) corner. In section 5.2.1, we summarize the unsteady interaction of an upstream duct mode which has originated downstream of the edge of the cavity lip ($x > 0$). In section 5.2.2, we summarize the interaction of a shear-layer instability wave which has originated upstream of the edge of the cavity lip ($x < 0$). The results of these two sections are utilized in section 5.3 to study the case of a finite-length overhanging lip or a square (90°) corner.

5.2.1 Impingement of an Upstream Duct Mode

In this section, we analyze the unsteady field produced by the interaction of the k-th upstream acoustic duct mode with a semi-infinite overhanging downstream lip. The

incident field for this case has the form

$$\phi_{i1} = 0, \tag{5.1}$$

$$\phi_{i2} = \cos(\frac{k\pi}{d}y)e^{-\mathrm{i}\sigma_k^+ x}, \tag{5.2}$$

where σ_k^+ is the wavenumber for the k-th upstream duct mode. It is also the pole location corresponding to the k-th upstream propagating duct mode (see figure 3.2), and is defined by

$$\sigma_k^{\pm} = \begin{cases} \pm\sqrt{M_2^2(1+\mathrm{i}\eta)^2 - \left(\frac{k\pi}{d}\right)^2} & k < \frac{M_2 d}{\pi}, \\ \pm\mathrm{i}\sqrt{\left(\frac{k\pi}{d}\right)^2 - M_2^2(1+\mathrm{i}\eta)^2} & k > \frac{M_2 d}{\pi}. \end{cases} \tag{5.3}$$

The total field is again written as the sum (3.17) of the incident and scattered fields, but with (5.1) and (5.2) replacing (3.26) and (3.27). The incident field (5.1, 5.2) satisfy the reduced wave equations (3.18) and (3.19) respectively, so that the scattered field, ϕ_1 and ϕ_2, satisfies these equations as well. The incident field satisfies the no-penetration condition (3.20) on the cavity bottom, and the no-penetration conditions (3.21) and (3.22) on the inner and outer surfaces of the overhanging lip, so that the scattered field also satisfies (3.21) and (3.22) on the cavity lip ($x < 0$) and (3.20) for all values of x.

In the region $x < 0$, the total field satisfies the vortex-sheet matching conditions (3.23) and (3.24) across $y = 0$. The incident field (5.1, 5.2) does not satisfy continuity of pressure (3.23) across the vortex sheet, therefore the scattered field satisfies an inhomogeneous form of the pressure matching condition for $x < 0$,

$$\rho_{01}\left[(1+\mathrm{i}\eta) + \mathrm{i}\frac{\partial}{\partial x}\right]\phi_1|_{y=0^+} - \rho_{02}(1+\mathrm{i}\eta)\phi_2|_{y=0^-} = Ae^{-\mathrm{i}\sigma_k^+ x}, \tag{5.4}$$

where $A = \rho_{02}(1+\mathrm{i}\eta)$. The transverse velocity for the incident field (5.1, 5.2) vanishes at $y = 0_{\pm}$, so the scattered field satisfies the homogeneous form of the continuity of particle displacement (3.24) matching condition across the vortex sheet. The no-penetration boundary conditions (3.22) and (3.21) on the inner and outer surfaces of

the overhanging lip imply that (3.24) is satisfied as well for $x > 0$, so the continuity of particle displacement is satisfied over the full range $-\infty < x < \infty$. The solutions to the reduced wave equations (3.18 , 3.19) in Fourier transform space are again given by (3.31, 3.35).

To determine $B_1(\lambda)$ and $B_2(\lambda)$ using the Wiener-Hopf technique (Noble, 1988), we extend the no-penetration boundary condition (3.22) on the inner surface of the overhanging lip by setting

$$\frac{\partial \phi_2}{\partial y}|_{y=0^-} = \begin{cases} 0 & x > 0, \\ v(x) & x < 0, \end{cases} \tag{5.5}$$

where $v(x) = 0$ for $x > 0$. Taking the Fourier to the above equation and using (3.31) and (3.35), we obtain

$$B_2(\lambda)\mu_2(\lambda)\tanh(\mu_2(\lambda)d) = V^-(\lambda), \tag{5.6}$$

where $V^-(\lambda)$ is the Fourier transform of $v(x)$. The superscript $(\cdot)^-$ on $V(\lambda)$ denotes that this function is analytic in the lower half of the complex λ plane, a property which follows from the fact that $v(x) = 0$ for $x > 0$. In the Wiener-Hopf nomenclature, such functions are called 'minus' functions.

Extending the pressure continuity (3.23) matching condition in a similar way, we have

$$\rho_{01}\left[(1+\mathrm{i}\eta) + \mathrm{i}\frac{\partial}{\partial x}\right]\phi_1|_{y=0^+} - \rho_{02}(1+\mathrm{i}\eta)\phi_2|_{y=0^-} = \begin{cases} A\, e^{-\mathrm{i}\sigma_k^+ x} & x < 0, \\ u(x) & x > 0, \end{cases} \tag{5.7}$$

where $A = \rho_{02}(1+\mathrm{i}\eta)$ and $u(x) = 0$ for $x < 0$. In physical terms, the function $u(x)$ is related to the difference in perturbation pressure across the zero thickness plate that forms the downstream lip of the cavity. Taking the Fourier transform and using (3.31, 3.35), we have

$$\rho_{01}\left[(1+\mathrm{i}\eta) + \lambda\right] B_1(\lambda) - \rho_{02}(1+\mathrm{i}\eta)B_2(\lambda) = \frac{-\mathrm{i}A}{(\lambda - \sigma_k^+)} + U^+(\lambda), \tag{5.8}$$

where we have assumed that σ_k^+ has a small positive imaginary part, such that the transform converges as $x \to -\infty$ in this particular case ($\mathrm{Im}[\sigma_k^+] > 0$ for $k \neq 0$). The function $U^+(\lambda)$ is the Fourier transform of $u(x)$. The superscript $(\cdot)^+$ on $U(\lambda)$ denotes that this function is analytic in the upper half of the complex λ plane, a property which follows from the fact that $u(x) = 0$ for $x < 0$. In the Wiener-Hopf nomenclature, such functions are called 'plus' functions.

Now consider the continuity of particle displacement matching condition (3.24). This applies on the full range $-\infty < x < \infty$, hence we can apply Fourier transform directly, producing again (3.41).

In order to use the generalized Wiener-Hopf technique (Noble, 1988), we need an expression whose only unknowns are the two half-analytic functions, $U^+(\lambda)$ and $V^-(\lambda)$. To do this, we solve for $B_2(\lambda)$ in (5.6), and substituting into (5.8), we obtain

$$B_1(\lambda) = -\frac{[(1+\mathrm{i}\eta)+\lambda]}{(1+\mathrm{i}\eta)\mu_1(\lambda)} V^-(\lambda). \tag{5.9}$$

Then, substituting the obtained expression for $B_1(\lambda)$ and $B_2(\lambda)$ into (3.41), we obtain

$$-\mathrm{i}\frac{\rho_{01}(\lambda+n)(\lambda+n^*)}{(1+\mathrm{i}\eta)\mu_1(\lambda)K(\lambda)} V^-(\lambda) = \frac{A}{\lambda-\sigma_k^+} + \mathrm{i}U^+(\lambda), \tag{5.10}$$

where the Wiener-Hopf kernel function $K(\lambda)$ is given by (3.44).

Substituting $K(\lambda) = K^+(\lambda)K^-(\lambda)$ (expressions for $K^+(\lambda)$ and $K^-(\lambda)$ are given in Appendix A), and multiplying both sides by $\frac{K^+(\lambda)\sqrt{\lambda-M_d}}{(\lambda+n^*)}$, we obtain

$$\frac{-\mathrm{i}}{\beta(1+\mathrm{i}\eta)} \frac{(\lambda+n)V^-(\lambda)}{K^-(\lambda)\sqrt{\lambda-M_u}} = A\frac{K^+(\lambda)\sqrt{\lambda-M_d}}{(\lambda+n^*)(\lambda-\sigma_k^+)} + \mathrm{i}\frac{K^+(\lambda)U^+(\lambda)\sqrt{\lambda-M_d}}{(\lambda+n^*)}. \tag{5.11}$$

The left-hand side of (5.11) is analytic in the lower half-plane, while the second term on the right-hand side is analytic in the upper half-plane. The first term on the right-hand side has singularities in both half-planes and is therefore a mixed function. However, since the only singularity of the mixed function in the upper half-plane is a pole at $\lambda = \sigma_k^+$, an additive split of this mixed function is easily obtained by

subtracting off the pole contribution,

$$\frac{K^+(\lambda)\sqrt{\lambda - M_d}}{(\lambda + n^*)(\lambda - \sigma_k^+)} = \left[\frac{K^+(\lambda)\sqrt{\lambda - M_d}}{(\lambda + n^*)(\lambda - \sigma_k^+)} - \frac{K^+(\sigma_k^+)\sqrt{\sigma_k^+ - M_d}}{(\sigma_k^+ + n^*)(\lambda - \sigma_k^+)}\right] + \frac{K^+(\sigma_k^+)\sqrt{\sigma_k^+ - M_d}}{(\sigma_k^+ + n^*)(\lambda - \sigma_k^+)}. \tag{5.12}$$

Substituting the above equation into (5.11) and taking the minus function to the left-hand side of the equation, we obtain

$$\frac{-\mathrm{i}}{\beta(1+\mathrm{i}\eta)}\frac{(\lambda+n)V^-(\lambda)}{K^-(\lambda)\sqrt{\lambda - M_u}} - A\frac{K^+(\sigma_k^+)\sqrt{\sigma_k^+ - M_d}}{(\sigma_k^+ + n^*)(\lambda - \sigma_k^+)}$$
$$= A\left[\frac{K^+(\lambda)\sqrt{\lambda - M_d}}{(\lambda + n^*)(\lambda - \sigma_k^+)} - \frac{K^+(\sigma_k^+)\sqrt{\sigma_k^+ - M_d}}{(\sigma_k^+ + n^*)(\lambda - \sigma_k^+)}\right] + \mathrm{i}\frac{K^+(\lambda)U^+(\lambda)\sqrt{\lambda - M_d}}{(\lambda + n^*)} = E(\lambda). \tag{5.13}$$

The left-hand side of (5.13) is a minus function, while the right-hand side is a plus function. The two sides are equal in strip of overlap, and by analytic continuation define an entire function $E(\lambda)$. Setting each side of (5.13) equal to $E(\lambda)$, we can solve for $U^+(\lambda)$ and $V^-(\lambda)$, thus obtaining

$$V^-(\lambda) = \mathrm{i}\,A\beta\,(1+\mathrm{i}\eta)\frac{K^+(\sigma_k^+)\sqrt{\sigma_k^+ - M_d}}{(\sigma_k^+ + n^*)}\frac{K^-(\lambda)\sqrt{\lambda - M_u}}{(\lambda+n)(\lambda - \sigma_k^+)} + \mathrm{i}\beta\,(1+\mathrm{i}\eta)\frac{K^-(\lambda)\sqrt{\lambda - M_u}}{(\lambda+n)}E(\lambda), \tag{5.14}$$

$$U^+(\lambda) = \mathrm{i}\frac{A(\lambda+n^*)}{K^+(\lambda)\sqrt{\lambda - M_d}}\left[\frac{K^+(\lambda)\sqrt{\lambda - M_d}}{(\lambda + n^*)(\lambda - \sigma_k^+)} - \frac{K^+(\sigma_k^+)\sqrt{\sigma_k^+ - M_d}}{(\sigma_k^+ + n^*)(\lambda - \sigma_k^+)}\right] - \mathrm{i}\frac{(\lambda+n^*)E(\lambda)}{K^+(\lambda)\sqrt{\lambda - M_d}}. \tag{5.15}$$

As in Sections 3.2.1 and 3.2.2, we must determine the entire function $E(\lambda)$. This function will be determined with the aid of Liouville's theorem (see for example Carrier *et al.*, 1983), which states that an entire function that is bounded at infinity must be a constant. In a more general setting, entire functions that grow no faster

than some power of $|\lambda|$ must be polynomials. Thus, we anticipate that $E(\lambda)$ will have the form of a polynomial in λ.

First, consider the choice $E(\lambda) = 0$. In this case, $U^+(\lambda) \propto \lambda^{-1/2}$ and $V^-(\lambda) \propto \lambda^{-3/2}$ as $\lambda \to \infty$ in their respective half-planes, therefore $u(x) \propto x^{-1/2}$ and $v(x) \propto (-x)^{1/2}$. Generally, one anticipates more singular behavior in the vicinity of leading edges (like the downstream lip) than in the vicinity of trailing edges (upstream lip). For the interaction at the downstream lip, the choice $E(\lambda) = 0$ is unacceptable as $V^-(\lambda)$ has a pole at $\lambda = -n$, violating the requirement that this function be analytic in the extended 'lower' half-plane. The pole at $\lambda = -n$ of $V^-(\lambda)$ can be removed by setting $E(\lambda)$ equal to the constant

$$E(\lambda) = A\,\frac{K^+(\sigma_k^+)\sqrt{\sigma_k^+ - M_d}}{(\sigma_k^+ + n^*)(\sigma_k^+ + n)}, \tag{5.16}$$

leading to

$$V^-(\lambda) = \mathrm{i}A\,\beta(1+\mathrm{i}\eta)\frac{K^+(\sigma_k^+)\sqrt{\sigma_k^+ - M_d}}{(\sigma_k^+ + n)(\sigma_k^+ + n^*)(\lambda - \sigma_k^+)}K^-(\lambda)\sqrt{\lambda - M_u}, \tag{5.17}$$

and

$$U^+(\lambda) = \frac{\mathrm{i}A}{\lambda - \sigma_k^+}\left[1 - \frac{K^+(\sigma_k^+)\sqrt{\sigma_k^+ - M_d}(\lambda + n)(\lambda + n^*)}{K^+(\lambda)(\sigma_k^+ + n)(\sigma_k^+ + n^*)\sqrt{\lambda - M_d}}\right], \tag{5.18}$$

which imply that $u(x) \propto x^{-3/2}$ and $v(x) \propto (-x)^{-1/2}$ as $x \to 0_\pm$. Choices of $E(\lambda)$ involving powers of λ lead to even more singular behavior near the origin in the physical plane and must be ruled out. In our case the least singular solution is the one corresponding to equation (5.16).

Having found expressions for $U^-(\lambda)$ and $V^+(\lambda)$, we can now solve for $B_1(\lambda)$ and $B_2(\lambda)$. To obtain the scattered field in the upstream region, we need expressions for $B_1(\lambda)$ and $B_2(\lambda)$ that expose singularities in the upper half-plane. Solving for $B_2(\lambda)$ in (5.6) and substituting into (5.8), expressions for $B_1(\lambda)$ and $B_2(\lambda)$ involving $K^+(\lambda)$

are found. These expressions are then substituted into (3.41), yielding

$$\phi_1(x,y) = \frac{-\mathrm{i}\,\rho_{02}(1+\mathrm{i}\eta)K^+(\sigma_k^+)\sqrt{\sigma_k^+ - M_d}}{2\pi(\sigma_k^+ + n)(\sigma_k^+ + n^*)} \int_{-\infty}^{\infty} \frac{[(1+\mathrm{i}\eta)+\lambda]\,(\lambda+n)(\lambda+n^*)\mu_2(\lambda)\sinh(\mu_2(\lambda)d)\mathrm{e}^{-\mu_1(\lambda)y}}{K^+(\lambda)(\lambda-\sigma_k^+)\sqrt{\lambda - M_d}\Delta(\lambda)}\,\mathrm{e}^{-\mathrm{i}\lambda x}d\lambda, \tag{5.19}$$

$$\phi_2(x,y) = \frac{\mathrm{i}\,\rho_{02}\,\beta(1+\mathrm{i}\eta)^2K^+(\sigma_k^+)\sqrt{\sigma_k^+ - M_d}}{2\pi(\sigma_k^+ + n)(\sigma_k^+ + n^*)} \int_{-\infty}^{\infty} \frac{\sqrt{\lambda - M_u}\,(\lambda+n)(\lambda+n^*)\cosh(\mu_2(\lambda)(y+d))}{K^+(\lambda)(\lambda-\sigma_k^+)\Delta(\lambda)}\,\mathrm{e}^{-\mathrm{i}\lambda x}d\lambda. \tag{5.20}$$

The integration contour for (5.19) and (5.20) is closed in the upper half-plane. Singularities in the upper half-plane are poles at $\lambda = \tau_j^+,\ j = 0, 1, ..., \infty$, the contributions corresponding to these poles are the upstream cavity modes. Also, (5.19) and (5.20) have a branch point at $\lambda = M_u$, with the corresponding branch cut extending into the upper half-plane; the contribution arising from this singularity is the upstream external field. Note that the pole contribution from $\lambda = \sigma_k^+$ in (5.20) cancels the incident field (5.2). For (5.19), the function $\mu_2(\lambda)\sinh(\mu_2(\lambda)d)$ cancels the factor $(\lambda - \sigma_k^+)$ in the denominator. As expected, since the incident field (5.1) vanishes for $y > 0$, then in the upstream region we have,

$$\phi_1(x,y) = \sum_{j=0}^{\infty} C_j^{u,k} m_1(\tau_j^+, y)\mathrm{e}^{-\mathrm{i}\tau_j^+ x} + E_1^{u,k}(x,y)\,\mathrm{e}^{-\mathrm{i}M_u x}, \tag{5.21}$$

$$\phi_2(x,y) = \sum_{j=0}^{\infty} C_j^{u,k} m_2(\tau_j^+, y)\mathrm{e}^{-\mathrm{i}\tau_j^+ x} + E_2^{u,k}(x,y)\,\mathrm{e}^{-\mathrm{i}M_u x} - \phi_{i2}(x,y), \tag{5.22}$$

where $m_1(\lambda, y)$ and $m_2(\lambda, y)$ are given by (3.63) and (3.64), respectively. The complex amplitude cavity modes coefficients are given by

$$C_j^{u,k} = -\rho_{02}(1+\mathrm{i}\eta)\frac{K^+(\sigma_k^+)\sqrt{\sigma_k^+ - M_d}(\tau_j^+ + n)(\tau_j^+ + n^*)}{K^+(\tau_j^+)(\sigma_k^+ + n)(\sigma_k^+ + n^*)\sqrt{\tau_j^+ - M_d}}\frac{(1+\mathrm{i}\eta)\mu_1(\tau_j^+)}{(\tau_j^+ - \sigma_k^+)\Delta'(\tau_j^+)}, \tag{5.23}$$

where the superscript $(\cdot)^{u,k}$ indicates that this contribution is generated by the impingement of the k-th upstream duct mode on a semi-infinite overhanging lip.

$E_1^{u,k}(x,y)$ and $E_2^{u,k}(x,y)$ represent the complex amplitudes (for each x and y) of the external acoustic field in the stream region ($y > 0$) and cavity region ($y < 0$) respectively. We focus on the behavior of the field for $O(1)$ values of y. The behavior in the stream at large distances ($x \ll -1$) is most naturally approached by applying the method of steepest descents, in which the integration contour for (5.19) and (5.20) is deformed to pass through the saddle point of the exponent. The far field approximation of the external field generated by the interaction of the k-th upstream duct mode with the edge of the overhanging lip, is given by

$$E_1^{u,k}(x,y) \approx \frac{\mathcal{C}_3[(1+\mathrm{i}\eta)+M_u]\mu_2(M_u)\sinh(\mu_2(M_u)d)}{\sqrt{M_u-M_d}}\left(\frac{\beta \mathrm{e}^{-\mathrm{i}3\pi/4}\sqrt{M_u-M_d}}{a_2}\,y+\frac{b_2}{a_2^2}\right)\frac{\Gamma(3/2)}{x^{3/2}}, \tag{5.24}$$

$$E_2^{u,k}(x,y) \approx -\frac{\mathcal{C}_3\,\beta(1+\mathrm{i}\eta)\,\mathrm{e}^{-\mathrm{i}3\pi/4}\cosh(\mu_2(M_u)(y+d))}{a_2}\,\frac{\Gamma(3/2)}{x^{3/2}}, \tag{5.25}$$

where

$$\mathcal{C}_3 = \frac{\rho_{02}(1+\mathrm{i}\eta)K^+(\sigma_k^+)\sqrt{\sigma_k^+-M_d}(M_u+n)(M_u+n^*)}{\pi(\sigma_k^++n)(\sigma_k^++n^*)(M_u-\sigma_k^+)K^+(M_u)}, \tag{5.26}$$

$$a_2 = \rho_{01}[(1+\mathrm{i}\eta)+M_u]^2\mu_2(M_u)\sinh(\mu_2(M_u)d), \tag{5.27}$$

and

$$b_2 = \rho_{02}\mathrm{e}^{-\mathrm{i}3\pi/4}\beta(1+\mathrm{i}\eta)^2\sqrt{M_u-M_d}\cosh(\mu_2(M_u)d). \tag{5.28}$$

A general process to compute the external field and its expansion for large values of x is given in Appendix C.

To study the scattered field in the downstream region ($x > 0$), more convenient forms of solutions are obtained by replacing $K^+(\lambda)$ in (5.19) and (5.20) with $K(\lambda)/K^-(\lambda)$, in order to display singularities in the lower half-plane. Thus we obtain

$$\phi_1(x,y) = \frac{-\mathrm{i}\,\rho_{02}(1+\mathrm{i}\eta)}{2\pi}\frac{K^+(\sigma_k^+)\sqrt{\sigma_k^+-M_d}}{(\sigma_k^++n)(\sigma_k^++n^*)}\int_{-\infty}^{\infty}\frac{[(1+\mathrm{i}\eta)+\lambda]\,K^-(\lambda)\mathrm{e}^{-\mu_1(\lambda)y}}{(\lambda-\sigma_k^+)\sqrt{\lambda-M_d}}\mathrm{e}^{-\mathrm{i}\lambda x}d\lambda \tag{5.29}$$

$$\phi_2(x,y) = \frac{\mathrm{i}\,\beta\,\rho_{02}(1+\mathrm{i}\eta)^2}{2\pi}\frac{K^+(\sigma_k^+)\sqrt{\sigma_k^+-M_d}}{(\sigma_k^++n)(\sigma_k^++n^*)}\int_{-\infty}^{\infty}\frac{K^-(\lambda)\sqrt{\lambda-M_u}\cosh(\mu_2(\lambda)(y+d))}{(\lambda-\sigma_k^+)\mu_2(\lambda)\sinh(\mu_2(\lambda)d)}\mathrm{e}^{-\mathrm{i}\lambda x}d\lambda. \tag{5.30}$$

The inversion contour of (5.29) and (5.30) is closed in the lower half-plane. For (5.29) the only singularity in the lower half-plane comes from the branch point at $\lambda = M_d$ and its corresponding branch cut extending into the lower half-plane. The contribution from this branch cut is the downstream external acoustic field. Since we are interested in the acoustic field within the cavity, (5.29) will not be evaluated further. The only singularities in the lower half-plane for the integrand of (5.30) are the zeros of the function $\mu_2(\lambda)\sinh(\mu_2(\lambda)d)$, i.e. the poles at σ_j^-, $j = 0, 1, 2, ..., \infty$. The residues of these poles are the downstream duct modes; hence the scattered field in the 'duct region' is

$$\phi_2 = \sum_{j=0}^{\infty} D_j^{u,k} \cos(\frac{j\pi}{d}y)\mathrm{e}^{-\mathrm{i}\sigma_j^- x}, \tag{5.31}$$

where the complex amplitudes for the duct modes coefficients are given by

$$D_j^{u,k} = \beta\,\rho_{02}(1+\mathrm{i}\eta)^2 \frac{K^+(\sigma_k^+)\sqrt{\sigma_k^+ - M_d}}{(\sigma_k^+ + n)(\sigma_k^+ + n^*)\,d}\;\frac{\epsilon_j K^-(\sigma_j^-)\sqrt{\sigma_j^- - M_u}}{(\sigma_j^- - \sigma_k^+)\sigma_j^-}, \tag{5.32}$$

where ϵ_j is defined in (3.58).

For the case of a semi-infinite overhanging lip, these acoustic duct modes simply propagate to downstream infinity and have no influence on the acoustic field radiated back upstream in the cavity. However, for a finite-length overhanging lip, these duct modes reflect off the downstream end wall of the cavity, producing upstream duct modes which in turn interact with the edge of the overhanging lip, generating additional contributions to the acoustic field in the cavity, as analyzed in section 5.3.

In this dissertation we focus on the behavior of the field for $O(1)$ values of y. The behavior in the stream at large distances ($x \ll -1$) is most naturally approached by applying the method of steepest descents, in which the integration contour for (5.29) and (5.30) is deformed to pass through the saddle point of the exponent. For large distances, the dominant contribution to the integral is then localized about the saddle point, leading to a large distance asymptotic expansion for $\phi_1(x, y)$ and $\phi_2(x, y)$, respectively.

5.2.2 Impingement of a Shear-layer Instability Wave

In this section, we study the unsteady interaction of a shear-layer instability wave with a semi-infinite overhanging downstream lip. The incident field for this interaction has the form

$$\phi_{\mathcal{S}1} = \frac{\rho_{02}(1+\mathrm{i}\eta)}{\rho_{01}\left[(1+\mathrm{i}\eta)-n\right]}\mathrm{e}^{-\mu_1(-n)y+\mathrm{i}nx}, \tag{5.33}$$

$$\phi_{\mathcal{S}2} = \frac{\cosh(\mu_2(-n)(y+d))}{\cosh(\mu_2(-n)d)}\mathrm{e}^{\mathrm{i}nx}, \tag{5.34}$$

where $\lambda = -n$ is the zero of the vortex sheet dispersion relationship (3.45).

The total field is again written as the sum (3.17) of the incident and scattered fields, but with (5.33) and (5.34) replacing (3.26) and (3.27). The incident field (5.33, 5.34) satisfies the reduced wave equations (3.14) and (3.15), the no-penetration condition on the cavity bottom (3.20), and the vortex sheet matching conditions (3.23) and (3.24). However, the incident field does not satisfy the no-penetration boundary conditions on the outer and inner surfaces of the overhanging lip, (3.21) and (3.22).

In the outer and inner surfaces of the overhanging lip ($y = 0$, $x > 0$), the scattered field will satisfy inhomogeneous forms of (3.21) and (3.22)

$$\frac{\partial\phi_1}{\partial y}|_{y=0^+} = \frac{\rho_{02}\mu_1(-n)(1+\mathrm{i}\eta)}{\rho_{01}\left[(1+\mathrm{i}\eta)-n\right]}\mathrm{e}^{\mathrm{i}nx}, \tag{5.35}$$

$$\frac{\partial\phi_2}{\partial y}|_{y=0^-} = -B\,\mathrm{e}^{\mathrm{i}nx}, \tag{5.36}$$

where $B = \mu_2(-n)\tanh(\mu_2(-n)d)$. From (5.35), (5.36) and that $\Delta(-n) = 0$, it is easy to show that the scattered field satisfies the particle displacement conditions for $x > 0$. Therefore, the continuity of particle displacement matching condition is satisfied over the full range $-\infty < x < \infty$. The solutions to the reduced wave equations (3.18, 3.19) in Fourier transform space are again given by (3.31, 3.35).

As stated before, the conditions (3.21) and (3.22) are related through (3.24), so it suffices to apply the Fourier transform to (3.22). We extend the no-penetration

boundary condition (3.22) by setting

$$\frac{\partial \phi_2}{\partial y}|_{y=0^-} = \begin{cases} v(x) & x < 0, \\ -B\,\mathrm{e}^{\mathrm{i}nx} & x > 0, \end{cases} \tag{5.37}$$

where $v(x) = 0$ for $x > 0$. Taking the Fourier transform and using (3.35), we have

$$B_2(\lambda)\mu_2(\lambda)\tanh(\mu_2(\lambda)d) = V^-(\lambda) - \frac{\mathrm{i}B}{\lambda + n}, \tag{5.38}$$

where $V^-(\lambda)$ is the Fourier transform of $v(x)$ and superscript $(\cdot)^-$ on $V(\lambda)$ denotes that this function is analytic in the lower half of the complex λ plane.

Extending the vortex-sheet pressure matching condition (3.23) in a similar way, we have

$$\rho_{01}\left[(1+\mathrm{i}\eta) + \mathrm{i}\frac{\partial}{\partial x}\right]\phi_1|_{y=0^+} - \rho_{02}(1+\mathrm{i}\eta)\phi_2|_{y=0^-} = \begin{cases} 0 & x < 0, \\ u(x) & x > 0, \end{cases} \tag{5.39}$$

where $u(x) = 0$ for $x < 0$. Taking the Fourier transform and using (3.31) and (3.35), we have

$$\rho_{01}\left[(1+\mathrm{i}\eta) + \lambda\right]B_1(\lambda) - \rho_{02}(1+\mathrm{i}\eta)B_2(\lambda) = U^+(\lambda), \tag{5.40}$$

where the superscript $(\cdot)^+$ on $U(\lambda)$ denotes that this function is analytic in the upper half-plane. The Fourier transform of the continuity of particle displacement yields again (3.41).

Solving for $B_2(\lambda)$ in (5.38) and substituting into (3.41), we obtain

$$B_1(\lambda) = -\frac{\left[(1+\mathrm{i}\eta) + \lambda\right]}{(1+\mathrm{i}\eta)\mu_1(\lambda)}\left[V^-(\lambda) - \frac{\mathrm{i}B}{\lambda + n}\right]. \tag{5.41}$$

Then, substituting the expressions for $B_1(\lambda)$ and $B_2(\lambda)$ into (5.40), we obtain

$$-U^+(\lambda)\frac{(1+\mathrm{i}\eta)\mu_1(\lambda)K(\lambda)}{\rho_{01}(\lambda+n)(\lambda+n^*)} = V^-(\lambda) - \frac{\mathrm{i}B}{\lambda+n}, \tag{5.42}$$

where $K(\lambda)$ is given by (3.44). Substituting $K(\lambda) = K^+(\lambda)K^-(\lambda)$ and dividing both sides by $K^-(\lambda)\sqrt{\lambda - M_u}$, we obtain

$$\frac{-\beta(1+\mathrm{i}\eta)K^+(\lambda)U^+(\lambda)\sqrt{\lambda - M_d}}{\rho_{01}(\lambda+n)(\lambda+n^*)} = \frac{V^-(\lambda)}{K^-(\lambda)\sqrt{\lambda - M_u}} - \frac{\mathrm{i}B}{K^-(\lambda)(\lambda+n)\sqrt{\lambda - M_u}}. \tag{5.43}$$

The left-hand side of (5.43) is analytic in the upper half-plane, while the first term on the right-hand side is analytic in the lower half-plane. The second term on the right-hand side has singularities in both half-planes and is therefore a mixed function. However, since the only singularity of the mixed function in the lower half-plane is the pole at $\lambda = -n$, an additive split of this mixed function is easily obtained by subtracting off the pole contribution,

$$\left[\frac{-\mathrm{i}B}{K^-(\lambda)(\lambda+n)\sqrt{\lambda-M_u}} + \frac{\mathrm{i}B}{K^-(-n)(\lambda+n)\sqrt{-n-M_u}}\right] - \frac{\mathrm{i}B}{K^-(-n)(\lambda+n)\sqrt{-n-M_u}} \tag{5.44}$$

Substituting (5.44) into (5.43) and taking the minus functions to the left-hand side of the equation, we have

$$\frac{V^-(\lambda)}{K^-(\lambda)\sqrt{\lambda-M_u}} + \left[\frac{-\mathrm{i}B}{K^-(\lambda)(\lambda+n)\sqrt{\lambda-M_u}} + \frac{\mathrm{i}B}{K^-(-n)(\lambda+n)\sqrt{-n-M_u}}\right] = \frac{-\beta(1+\mathrm{i}\eta)K^+(\lambda)U^+(\lambda)\sqrt{\lambda-M_d}}{\rho_{01}(\lambda+n)(\lambda+n^*)} + \frac{\mathrm{i}B}{K^-(-n)(\lambda+n)\sqrt{-n-M_u}} = E(\lambda). \tag{5.45}$$

The left-hand side of (5.45) is a minus function, while the right hand side is a plus function. The two sides are equal in the strip of overlap, and by analytic continuation define an entire function $E(\lambda)$. Setting each side of (5.45) equal to $E(\lambda)$, we obtain

$$U^+(\lambda) = \mathrm{i}B\frac{\rho_{01}(\lambda+n^*)}{\beta(1+\mathrm{i}\eta)K^-(-n)\sqrt{-n-M_u}K^+(\lambda)\sqrt{\lambda-M_d}} - \frac{\rho_{01}(\lambda+n)(\lambda+n^*)}{\beta(1+\mathrm{i}\eta)K^+(\lambda)\sqrt{\lambda-M_d}}E(\lambda), \tag{5.46}$$

$$V^-(\lambda) = -\mathrm{i}B\frac{K^-(\lambda)\sqrt{\lambda-M_u}}{(\lambda+n)}\left[\frac{-1}{K^-(\lambda)\sqrt{\lambda-M_u}} + \frac{1}{K^-(-n)\sqrt{-n-M_u}}\right] + K^-(\lambda)\sqrt{\lambda-M_u}E(\lambda). \tag{5.47}$$

As before, the entire function $E(\lambda)$ is determined by examining the behavior of the physical field in the vicinity of the origin, i.e. $E(\lambda)$ is chosen to give the least singular behavior. For the choice $E(\lambda) = 0$, $u(x) \propto x^{-3/2}$ and $v(x) \propto (-x)^{-1/2}$ as $x \to 0_{\pm}$. Choices of $E(\lambda)$ involving powers of λ lead to even more singular behavior near the origin in the physical plane and must be ruled out. Thus, the physically appropriate solution is the one corresponding to $E(\lambda) = 0$. Therefore,

$$U^+(\lambda) = \frac{\mathrm{i}B}{\beta(1+\mathrm{i}\eta)} \frac{\rho_{01}(\lambda + n^*)}{K^-(-n)\sqrt{-n-M_u}K^+(\lambda)\sqrt{\lambda - M_d}}, \tag{5.48}$$

$$V^-(\lambda) = \frac{\mathrm{i}B}{(\lambda+n)} \left[1 - \frac{K^-(\lambda)\sqrt{\lambda - M_u}}{K^-(-n)\sqrt{-n-M_u}}\right]. \tag{5.49}$$

Having found expressions for $U^-(\lambda)$ and $V^+(\lambda)$, we can now solve for $B_1(\lambda)$ and $B_2(\lambda)$. To examine the scattered field in the upstream region, we find expressions for $B_1(\lambda)$ and $B_2(\lambda)$ that expose singularities in the upper half-plane. Solving for $B_2(\lambda)$ in (3.41) and substituting in (5.40), expressions for $B_1(\lambda)$ and $B_2(\lambda)$ involving $K^+(\lambda)$ are found, yielding the inverse transforms

$$\phi_1(x,y) = \frac{\mathrm{i}\,\rho_{01}\,\mu_2(-n)\tanh(\mu_2(-n)d)}{2\pi\beta(1+\mathrm{i}\eta)K^-(-n)\sqrt{-n-M_u}} \int_{-\infty}^{\infty} \frac{[(1+\mathrm{i}\eta)+\lambda](\lambda+n^*)\mu_2(\lambda)\sinh(\mu_2(\lambda)d)\mathrm{e}^{-\mu_1(\lambda)y}}{K^+(\lambda)\sqrt{\lambda - M_d}\,\Delta(\lambda)}\,\mathrm{e}^{-\mathrm{i}\lambda x}d\lambda, \tag{5.50}$$

$$\phi_2(x,y) = \frac{-\mathrm{i}\,\rho_{01}\,\mu_2(-n)\tanh(\mu_2(-n)d)}{2\pi K^-(-n)\sqrt{-n-M_u}} \int_{-\infty}^{\infty} \frac{\sqrt{\lambda - M_u}\,(\lambda+n^*)\cosh(\mu_2(\lambda)(y+d))}{K^+(\lambda)\Delta(\lambda)}\,\mathrm{e}^{-\mathrm{i}\lambda x}d\lambda. \tag{5.51}$$

The integration contour of (5.50) and (5.51) is closed in the upper half-plane. Singularities in the upper half-plane are poles at $\lambda = \tau_j^+$, $j = 0, 1, ..., \infty$. The residue contribution corresponding to these poles are the upstream cavity modes. Also, (5.50) and (5.51) have a singularity coming from the branch point at $\lambda = M_u$, with the corresponding branch cut extending into the upper half-plane; the contribution arising

from this singularity is the upstream external acoustic field. So in the upstream region ($x < 0$), we have

$$\phi_1(x,y) = \sum_{j=0}^{\infty} C_j^{\mathcal{S}} m_1(\tau_j^+, y)\, \mathrm{e}^{-\mathrm{i}\tau_j^+ x} + E_1^{\mathcal{S}}(x,y)\, \mathrm{e}^{-\mathrm{i}M_u x}, \tag{5.52}$$

$$\phi_2(x,y) = \sum_{j=0}^{\infty} C_j^{\mathcal{S}} m_2(\tau_j^+, y)\, \mathrm{e}^{-\mathrm{i}\tau_j^+ x} + E_2^{\mathcal{S}}(x,y)\, \mathrm{e}^{-\mathrm{i}M_u x}, \tag{5.53}$$

where m_1 and m_2 are given by (3.63) and (3.64), respectively. The complex amplitudes of the cavity modes coefficients are given by

$$C_j^{\mathcal{S}} = \frac{\rho_{01}\,\mu_2(-n)\tanh(\mu_2(-n)d)}{K^-(-n)\sqrt{-n-M_u}}\,\frac{\sqrt{\tau_j^+ - M_u}\,(\tau_j^+ + n^*)}{K^+(\tau_j^+)\Delta'(\tau_j^+)}, \tag{5.54}$$

where the superscript $(\cdot)^{\mathcal{S}}$ indicates that this contribution is generated by the impingement of the instability wave on a semi-infinite overhanging lip.

$E_1^{\mathcal{S}}(x,y)$ and $E_2^{\mathcal{S}}(x,y)$ are the complex amplitudes (for each x and y) of the external field in the flow region ($y > 0$) and cavity region ($y < 0$), respectively. The far field approximation of the external field generated by the interaction of the instability wave $\mathcal{S}$ with the edge of the overhanging lip is given by

$$E_1^{\mathcal{S}}(x,y) \approx \frac{-\mathcal{C}_4[(1+\mathrm{i}\eta)+M_u]\mu_2(M_u)\sinh(\mu_2(M_u)d)}{\beta(1+\mathrm{i}\eta)\sqrt{M_u-M_d}}\left(\frac{\beta \mathrm{e}^{-\mathrm{i}3\pi/4}\sqrt{M_u-M_d}}{a_2}\,y + \frac{b_2}{a_2^2}\right)\frac{\Gamma(3/2)}{x^{3/2}}, \tag{5.55}$$

$$E_2^{\mathcal{S}}(x,y) \approx \frac{\mathcal{C}_4\,\mathrm{e}^{-\mathrm{i}3\pi/4}\cosh(\mu_2(M_u)(y+d))}{a_2}\,\frac{\Gamma(3/2)}{x^{3/2}}, \tag{5.56}$$

where

$$\mathcal{C}_4 = \frac{\rho_{01}\,\mu_2(-n)\tanh(\mu_2(-n)d)\,(M_u+n^*)}{\pi K^-(-n)K^+(M_u)\sqrt{-n-M_u}}, \tag{5.57}$$

and a_2, b_2 are given by (5.27) and (5.28), respectively. A general calculation of the external field and its expansion for large values of x is given in Appendix C.

To examine the scattered field in the downstream region ($x > 0$), we replace $K^+(\lambda)$ in (5.50) and (5.51) with $K(\lambda)/K^-(\lambda)$, in order to display singularities in the

lower half-plane. Thus we obtain

$$\phi_1(x,y) = \frac{\mathrm{i}\,\mu_2(-n)\tanh(\mu_2(-n)d)}{2\pi\beta(1+\mathrm{i}\eta)K^-(-n)\sqrt{-n-M_u}}\int_{-\infty}^{\infty}\frac{[(1+\mathrm{i}\eta)+\lambda]\,K^-(\lambda)}{(\lambda+n)\sqrt{\lambda-M_d}}\mathrm{e}^{-\mu_1(\lambda)y}\mathrm{e}^{-\mathrm{i}\lambda x)}d\lambda, \tag{5.58}$$

$$\phi_2(x,y) = \frac{-\mathrm{i}\,\mu_2(-n)\tanh(\mu_2(-n)d)}{2\pi K^-(-n)\sqrt{-n-M_u}}\int_{-\infty}^{\infty}\frac{K^-(\lambda)\sqrt{\lambda-M_u}\cosh(\mu_2(\lambda)(y+d))}{(\lambda+n)\mu_2(\lambda)\sinh(\mu_2(\lambda)d)}\mathrm{e}^{-\mathrm{i}\lambda x}d\lambda. \tag{5.59}$$

The integration contour of (5.58) and (5.59) is closed in the lower half-plane. The only singularities in the lower half-plane for the integrand of (5.58) in the lower half-plane are a pole at $\lambda = -n$ and the branch cut emanating from $\lambda = M_d$ (see figure 3.2). The residue contribution corresponding to the pole $\lambda = -n$ is $-\phi_{\mathcal{S}1}$, i.e. it cancels the incident instability wave (5.33). The integral arising from the deformation of the contour around the branch cut (see Appendix C) corresponds to the continuous spectrum component of the solution. The contribution from this branch cut is the downstream external field. Since we are interested in the acoustic field within the cavity, this downstream external field in the flow region ($y > 0$) is of little interest and (5.58) will not be evaluated further.

The only singularities in the lower half-plane for the integrand of (5.59) are poles at $\lambda = -n$ and σ_j^-, $j = 0, 1, 2, ..., \infty$, associated with the zeros of the function $\mu_2(\lambda)\sinh(\mu_2(\lambda)d)$. The residue at $\lambda = -n$ cancels the incident field $\phi_{\mathcal{S}2}$, while the residue contribution of σ_j^-, $j = 0, 1, 2, ..., \infty$ are the downstream duct modes. Hence the scattered field in the cavity 'duct region' is

$$\phi_2 = \sum_{j=0}^{\infty} D_j^{\mathcal{S}}\cos(\frac{j\pi}{d}y)\exp(-\mathrm{i}\sigma_j^- x) \; - \phi_{\mathcal{S}2}, \tag{5.60}$$

where the complex amplitudes for the downstream duct modes are given by

$$D_j^{\mathcal{S}} = \frac{-\,\mu_2(-n)\tanh(\mu_2(-n)d)}{K^-(-n)\sqrt{-n-M_u}\,d}\;\frac{\epsilon_j K^-(\sigma_j^-)\sqrt{\sigma_j^- - M_u}}{(\sigma_j^- + n)\,\sigma_j^-}, \tag{5.61}$$

where ϵ_j is defined in (3.58).

5.2.3 Impingement of a Downstream Cavity Mode

In this section, we summarize the results for the interaction of a downstream cavity mode with a downstream overhanging lip. The incident field has the form

$$\phi_{i1}^{\mathcal{D}k} = \frac{\rho_{02}(1+\mathrm{i}\eta)}{\rho_{01}[(1+\mathrm{i}\eta)+\tau_k^-]}\mathrm{e}^{-\mathrm{i}\tau_k^- x}\mathrm{e}^{-\mu_1(\tau_k^-)y}, \tag{5.62}$$

$$\phi_{i2}^{\mathcal{D}k} = \mathrm{e}^{-\mathrm{i}\tau_k^- x}\frac{\cosh(\mu_2(\tau_k^-)(y+d))}{\cosh(\mu_2(\tau_k^-)d)}, \tag{5.63}$$

where τ_k^- is the wavenumber for the k-th downstream cavity mode and is also its pole location (see figure 3.2).

The total field is again written as the sum (3.17) of the incident and scattered fields, but with (5.62) and (5.63) replacing (3.26) and (3.27). The incident field satisfies the reduced wave equations (3.18) and (3.19), the no-penetration condition (3.20) on the cavity bottom, and the vortex sheet matching condition (3.23), but does not satisfy the no-penetration conditions (3.21) and (3.22) on the outer and inner surfaces of the overhanging lip.

Thus, the scattered field also satisfies the reduced wave equations (3.18) and (3.19) and the no-penetration boundary condition (3.20) on the cavity bottom. For $x < 0$, the scattered field satisfies the vortex-sheet matching conditions (3.23) and (3.24) across $y = 0$.

The scattered field satisfies the following inhomogeneous forms of the no-penetration boundary conditions (3.21) and (3.22) on the inner and outer surfaces of the lip,

$$\frac{\partial\phi_1}{\partial y}|_{y=0^+} = \frac{\rho_{02}(1+\mathrm{i}\eta)}{\rho_{01}[(1+\mathrm{i}\eta)+\tau_k^-]}\,\mu_1(\tau_k^-)\mathrm{e}^{-\mathrm{i}\tau_k^- x}, \tag{5.64}$$

$$\frac{\partial\phi_2}{\partial y}|_{y=0^-} = -R\,\mathrm{e}^{-\mathrm{i}\tau_k^- x}, \tag{5.65}$$

where $R = \mu_2(\tau_k^-)\tanh(\mu_2(\tau_k^-)d)$. From (5.64) and (5.65), and the fact that $\Delta(\tau_j^-) = 0$, it is easy to prove that the scattered field satisfies the homogeneous form of the continuity of particle displacement (3.24) for $x > 0$. Hence it is satisfied over the full

range $-\infty < x < \infty$. The solutions to the reduced wave equations (3.18, 3.19) in Fourier transform space are again given by (3.31, 3.35).

We recall from Chapter 3, and earlier in this chapter, that the conditions (3.21) and (3.22) are related through (3.24), so it suffices to apply the Fourier transform to (3.22). Extending the no-penetration boundary condition (3.22), we have

$$\frac{\partial \phi_2}{\partial y}|_{y=0^-} = \begin{cases} v(x) & x < 0, \\ -R\,\mathrm{e}^{-\mathrm{i}\tau_k^- x} & x > 0, \end{cases} \tag{5.66}$$

where $v(x) = 0$ for $x > 0$. Applying Fourier transform to the above equation and using (3.35),

$$B_2(\lambda)\mu_2(\lambda)\tanh(\mu_2(\lambda)d) = V^-(\lambda) - \frac{\mathrm{i}R}{\lambda - \tau_k^-} \tag{5.67}$$

where we have assumed that τ_0^- has a small negative imaginary part so that the transform converges as $x \to \infty$ in this particular case ($\mathrm{Im}[\tau_k^-] < 0$ for $k \neq 0$). The function $V^-(\lambda)$ is the Fourier transform of $v(x)$. The superscript $(\cdot)^-$ on $V(\lambda)$ denotes that this function is analytic in the lower half of the complex λ plane.

Extending the vortex-sheet pressure matching condition (3.23) in a similar way, we have

$$\rho_{01}\left[(1+\mathrm{i}\eta) + \mathrm{i}\frac{\partial}{\partial x}\right]\phi_1|_{y=0^+} - \rho_{02}(1+\mathrm{i}\eta)\phi_2|_{y=0^-} = \begin{cases} 0 & x < 0, \\ u(x) & x > 0 \end{cases} \tag{5.68}$$

where $u(x) = 0$ for $x < 0$. Taking the Fourier Transform and using (3.31) and (3.35), we obtain

$$\rho_{01}\left[(1+\mathrm{i}\eta) + \lambda\right]B_1(\lambda) - \rho_{02}(1+\mathrm{i}\eta)B_2(\lambda) = U^+(\lambda), \tag{5.69}$$

where the function $U^+(\lambda)$ is the Fourier transform of $u(x)$. The superscript $(\cdot)^+$ on $U(\lambda)$ denotes that this function is analytic in the upper half of the complex λ plane. The Fourier transform of the continuity of particle displacement yields again (3.41).

Solving for $B_2(\lambda)$ in (5.67) and substituting in (5.69), we have

$$B_1(\lambda) = \frac{U^+(\lambda)}{\rho_{01}[(1+\mathrm{i}\eta)+\lambda]} + \frac{\rho_{02}(1+\mathrm{i}\eta)}{\rho_{01}[(1+\mathrm{i}\eta)+\lambda]}\frac{1}{\mu_2(\lambda)\tanh(\mu_2(\lambda)d)}\left[V^-(\lambda) - \frac{\mathrm{i}R}{\lambda - \tau_k^-}\right]. \tag{5.70}$$

Substituting the expression obtained for $B_1(\lambda)$ and $B_2(\lambda)$ into (3.41), we obtain

$$-U^+(\lambda) = \frac{\rho_{01}(\lambda+n)(\lambda+n^*)}{(1+\mathrm{i}\eta)\mu_1(\lambda)K(\lambda)}\left[V^-(\lambda) - \frac{\mathrm{i}R}{\lambda-\tau_k^-}\right], \tag{5.71}$$

where $K(\lambda)$ is given by (3.44). Substituting $K(\lambda) = K^+(\lambda)K^-(\lambda)$ in (5.71) and multiplying both sides by $\frac{\beta(1+\mathrm{i}\eta)K^+(\lambda)\sqrt{\lambda-M_d}}{\rho_{01}(\lambda+n)(\lambda+n^*)}$, we obtain

$$\frac{-\beta(1+\mathrm{i}\eta)K^+(\lambda)U^+(\lambda)\sqrt{\lambda-M_d}}{\rho_{01}(\lambda+n)(\lambda+n^*)} = \frac{V^-(\lambda)}{K^-(\lambda)\sqrt{\lambda-M_u}} - \frac{\mathrm{i}R}{(\lambda-\tau_k^-)K^-(\lambda)\sqrt{\lambda-M_u}}. \tag{5.72}$$

The left-hand side of (5.72) is analytic in the upper half-plane, while the first term on the right-hand side is analytic in the lower half-plane. The second term on the right-hand side has singularities in both half-planes, and is therefore a mixed function. However, since the only singularity of the mixed function in the upper half-plane is a pole at $\lambda = \tau_k^-$, an additive split of this mixed function is easily obtained by subtracting off the pole contribution,

$$\begin{aligned}\frac{\mathrm{i}R}{(\lambda-\tau_k^-)K^-(\lambda)\sqrt{\lambda-M_u}} &= \frac{\mathrm{i}R}{(\lambda-\tau_k^-)K^-(\tau_k^-)\sqrt{\tau_k^- - M_u}} \\ &+ \mathrm{i}R\left[\frac{1}{(\lambda-\tau_k^-)K^-(\lambda)\sqrt{\lambda-M_u}} - \frac{1}{(\lambda-\tau_k^-)K^-(\tau_k^-)\sqrt{\tau_k^- - M_u}}\right]\end{aligned} \tag{5.73}$$

Substituting (5.73) into (5.72), and taking the plus functions to the left-hand side of the equation, we have

$$\begin{aligned}&\frac{-\beta(1+\mathrm{i}\eta)U^+(\lambda)K^+(\lambda)\sqrt{\lambda-M_d}}{\rho_{01}(\lambda+n)(\lambda+n^*)} + \frac{\mathrm{i}R}{(\lambda-\tau_k^-)K^-(\tau_k^-)\sqrt{\tau_k^- - M_u}} \\ &= \frac{V^-(\lambda)}{K^-(\lambda)\sqrt{\lambda-M_u}} - \frac{\mathrm{i}R}{(\lambda-\tau_k^-)}\left[\frac{1}{K^-(\lambda)\sqrt{\lambda-M_u}} - \frac{1}{K^-(\tau_k^-)\sqrt{\tau_k^- - M_u}}\right] \\ &= E(\lambda).\end{aligned} \tag{5.74}$$

The left-hand side of (5.74) is a plus function, while the right hand side is a minus function. The two sides are equal in the strip of overlap, and by analytic continuation

define an entire function $E(\lambda)$. Setting each side of (5.74) equal to $E(\lambda)$, we obtain

$$U^+(\lambda) = \frac{\mathrm{i}R}{\beta(1+\mathrm{i}\eta)K^-(\tau_k^-)\sqrt{\tau_k^- - M_u}} \frac{\rho_{01}(\lambda+n)(\lambda+n^*)}{(\lambda-\tau_k^-)K^+(\lambda)\sqrt{\lambda - M_d}} - \frac{E(\lambda)\rho_{01}(\lambda+n)(\lambda+n^*)}{\beta(1+\mathrm{i}\eta)K^+(\lambda)\sqrt{\lambda-M_d}}, \tag{5.75}$$

$$V^-(\lambda) = \frac{\mathrm{i}R}{\lambda-\tau_k^-}\left[1 - \frac{K^-(\lambda)\sqrt{\lambda-M_u}}{K^-(\tau_k^-)\sqrt{\tau_k^- - M_u}}\right] + E(\lambda)K^-(\lambda)\sqrt{\lambda - M_u}. \tag{5.76}$$

The entire function $E(\lambda)$ is determined by examining the behavior of the physical field in the vicinity of the origin, i.e. $E(\lambda)$ is chosen to give the least singular behavior. For the choice $E(\lambda) = 0$ we have that $u(x) \propto x^{-3/2}$ and $v(x) \propto (-x)^{-1/2}$ as $x \to 0_\pm$. Choices of $E(\lambda)$ involving powers of λ lead to even more singular behavior near the origin. Thus, the physically appropriate solution is the one corresponding to $E(\lambda) = 0$. Therefore,

$$U^+(\lambda) = \frac{\mathrm{i}R}{\beta(1+\mathrm{i}\eta)K^-(\tau_k^-)\sqrt{\tau_k^- - M_u}} \frac{\rho_{01}(\lambda+n)(\lambda+n^*)}{(\lambda-\tau_k^-)K^+(\lambda)\sqrt{\lambda - M_d}} \tag{5.77}$$

$$V^-(\lambda) = \frac{\mathrm{i}R}{\lambda-\tau_k^-}\left[1 - \frac{K^-(\lambda)\sqrt{\lambda-M_u}}{K^-(\tau_k^-)\sqrt{\tau_k^- - M_u}}\right]. \tag{5.78}$$

Having found expressions for $U^+(\lambda)$ and $V^-(\lambda)$, we can now solve for $B_1(\lambda)$ and $B_2(\lambda)$. To examine the scattered field in the upstream region ($x < 0$), we need expressions for $B_1(\lambda)$ and $B_2(\lambda)$ that expose singularities in the upper half-plane. Solving for $B_2(\lambda)$ in (3.41), replacing this expression in (5.69) and substituting the obtained expression into (5.67), we obtain

$$\phi_1(x,y) = \frac{\mathrm{i}\,\rho_{01}\,\mu_2(\tau_k^-)\tanh(\mu_2(\tau_k^-)d)}{2\pi\beta(1+\mathrm{i}\eta)K^-(\tau_k^-)\sqrt{\tau_k^- - M_u}} \int_{-\infty}^{\infty} \frac{[(1+\mathrm{i}\eta)+\lambda](\lambda+n)(\lambda+n^*)\mu_2(\lambda)\sinh(\mu_2(\lambda)d)\mathrm{e}^{-\mu_1(\lambda)y}}{(\lambda-\tau_k^-)K^+(\lambda)\sqrt{\lambda-M_d}\,\Delta(\lambda)}\,\mathrm{e}^{-\mathrm{i}\lambda x}d\lambda, \tag{5.79}$$

$$\phi_2(x,y) = \frac{-\mathrm{i}\,\rho_{01}\mu_2(\tau_k^-)\tanh(\mu_2(\tau_k^-)d)}{2\pi K^-(\tau_k^-)\sqrt{\tau_k^- - M_u}} \int_{-\infty}^{\infty} \frac{(\lambda+n)(\lambda+n^*)\sqrt{\lambda - M_u}\cosh(\mu_2(\lambda)(y+d))}{K^+(\lambda)(\lambda-\tau_k^-)\Delta(\lambda)} \mathrm{e}^{-\mathrm{i}\lambda x} d\lambda. \tag{5.80}$$

The integration contour of (5.79) and (5.80) is closed in the upper half-plane. Singularities in the upper half-plane are poles at $\lambda = \tau_j^+,\ j = 0, 1, ..., \infty$. The residue contributions corresponding to these poles are the upstream cavity modes. Also, (5.79) and (5.80) have a singularity coming from the branch point at $\lambda = M_u$, with the corresponding branch cut extending into the upper half-plane; the contribution arising from this singularity is the upstream external acoustic field. So in the upstream region ($x < 0$), we have

$$\phi_1(x,y) = \sum_{j=0}^{\infty} C_j^{\mathcal{D}k} m_1(\tau_j^+, y)\,\mathrm{e}^{(-\mathrm{i}\tau_j^+ x)} + E_1^{\mathcal{D},k}(x,y)\,\mathrm{e}^{-\mathrm{i}M_u x}, \tag{5.81}$$

$$\phi_2(x,y) = \sum_{j=0}^{\infty} C_j^{\mathcal{D}k} m_2(\tau_j^+, y)\,\mathrm{e}^{(-\mathrm{i}\tau_j^+ x)} + E_2^{\mathcal{D},k}(x,y)\,\mathrm{e}^{-\mathrm{i}M_u x}, \tag{5.82}$$

where $m_1(\lambda, y)$ and $m_2(\lambda, y)$ are given by (3.63) and (3.64), respectively. The complex amplitudes of the cavity modes coefficients are given by

$$C_j^{\mathcal{D}k} = \frac{\rho_{01}\,\mu_2(\tau_k^-)\tanh(\mu_2(\tau_k^-)d)}{K^-(\tau_k^-)\sqrt{\tau_k^- - M_u}} \frac{(\tau_j^+ + n)(\tau_j^+ + n^*)\sqrt{\tau_j^+ - M_u}}{(\tau_j^+ - \tau_k^-)K^+(\tau_j^+)\Delta'(\tau_j^+)}, \tag{5.83}$$

where $\Delta'(\lambda) = d\Delta/d\lambda$ and the superscript $(\cdot)^{\mathcal{D}k}$ indicates that this contribution is generated by the impingement of the k-th downstream duct mode on a semi-infinite overhanging lip.

$E_1^{\mathcal{D},k}(x,y)$ and $E_2^{\mathcal{D},k}(x,y)$ are the complex amplitudes (for each x and y) of the external acoustic fields in the flow region ($y > 0$) and cavity region ($y < 0$) respectively. The far field approximation of the external field generated by the interaction

of the downstream cavity mode $\mathcal{D}$ with the edge of the overhanging lip, is given by

$$E_1^{\mathcal{D},k}(x,y) \approx \frac{-\mathcal{C}_5[(1+\mathrm{i}\eta)+M_u]\mu_2(M_u)\sinh(\mu_2(M_u)d)}{\beta(1+\mathrm{i}\eta)\sqrt{M_u-M_d}}\left(\frac{\beta \mathrm{e}^{-\mathrm{i}3\pi/4}\sqrt{M_u-M_d}}{a_2}\,y+\frac{b_2}{a_2^2}\right)\frac{\Gamma(3/2)}{x^{3/2}},$$

(5.84)

$$E_2^{\mathcal{D},k}(x,y) \approx \frac{\mathcal{C}_5\,\mathrm{e}^{-\mathrm{i}3\pi/4}\cosh(\mu_2(M_u)(y+d))}{a_2}\,\frac{\Gamma(3/2)}{x^{3/2}}, \tag{5.85}$$

where

$$\mathcal{C}_5 = \frac{\rho_{01}\,\mu_2(\tau_k^-)\tanh(\mu_2(\tau_k^-)d)\,(M_u+n)(M_u+n^*)}{\pi K^-(\tau_k^-)K^+(M_u)(M_u-\tau_k^-)\sqrt{\tau_k^- - M_u}}, \tag{5.86}$$

and a_2, b_2 are given by (5.27) and (5.28), respectively. A general calculation of the external field and its expansion for large values of x is given in Appendix C.

To examine the scattered field in the downstream region ($x > 0$), we replace $K^+(\lambda)$ in (5.79) and (5.80) with $K(\lambda)/K^-(\lambda)$, in order to display singularities in the lower half-plane. Thus we obtain

$$\phi_1(x,y) = \frac{\mathrm{i}\,\rho_{01}\,\mu_2(\tau_k^-)\tanh(\mu_2(\tau_k^-)d)}{2\pi\beta(1+\mathrm{i}\eta)K^-(\tau_k^-)\sqrt{\tau_k^- - M_u}}\int_{-\infty}^{\infty}\frac{[(1+\mathrm{i}\eta)+\lambda]K^-(\lambda)\mathrm{e}^{-\mu_1(\lambda)y}}{(\lambda-\tau_k^-)\sqrt{\lambda-M_d}}\,\mathrm{e}^{-\mathrm{i}\lambda x}d\lambda, \tag{5.87}$$

$$\phi_2(x,y) = \frac{-\mathrm{i}\,\rho_{01}\,\mu_2(\tau_k^-)\tanh(\mu_2(\tau_k^-)d)}{2\pi K^-(\tau_k^-)\sqrt{\tau_k^- - M_u}}\int_{-\infty}^{\infty}\frac{K^-(\lambda)\sqrt{\lambda-M_u}\cosh(\mu_2(\lambda)(y+d))}{(\lambda-\tau_k^-)\mu_2(\lambda)\sinh(\mu_2(\lambda)d)}\,\mathrm{e}^{-\mathrm{i}\lambda x}d\lambda. \tag{5.88}$$

The inversion contour for (5.87) and (5.88) is closed in the lower half-plane. For (5.87), the only singularities in the lower half-plane are the pole at $\lambda = \tau_k^-$ and the branch cut emanating from $\lambda = M_d$ (see figure 3.2). The residue contribution corresponding to the pole $\lambda = \tau_k^-$ is $-\phi_{i1}^{\mathcal{D}k}$, i.e. it cancels the incident field (5.62). The integral arising from the deformation of the contour around the branch cut (see Appendix C) corresponds to the continuous spectrum component of the solution. The contribution from this branch cut is the downstream external field. Since we are interested in the acoustic field within the cavity, this downstream external field in the flow region ($y > 0$) is of little interest and (5.87) will not be evaluated further.

The residue contribution of (5.88) at $\lambda = \tau_k^-$ cancels the incident field (5.63). Note also that $\cosh(\mu_2(\lambda)(y+d))$ is an entire function, thus the solution in the 'duct region' ($y < 0, \;\; x > 0$) consists of residue contributions arising from the poles associated with the zeros of the function $\mu_2(\lambda)\sinh(\mu_2(\lambda)d)$. These poles are located at $\sigma_j^-, \;\; j = 0, 1, 2, ..., \infty$, and their contribution are the downstream duct modes. Hence the scattered field in the 'duct region' is

$$\phi_2(x,y) = \sum_{j=0}^{\infty} D_j^{\mathcal{D}k} \cos(\frac{j\pi}{d}y)\, \mathrm{e}^{-\mathrm{i}\sigma_j^- x} \; - \phi_{i2}^{\mathcal{D}k}(x,y), \tag{5.89}$$

where the complex amplitudes of the downstream duct modes are given by

$$D_j^{\mathcal{D}k} = \frac{-\mu_2(\tau_k^-)\tanh(\mu_2(\tau_k^-)d)}{K^-(\tau_k^-)\sqrt{\tau_k^- - M_u}\; d} \; \frac{\epsilon_j K^-(\sigma_j^-)\sqrt{\sigma_j^- - M_u}}{(\sigma_j^- - \tau_k^-)\sigma_j^-}, \tag{5.90}$$

and ϵ_j is defined in (3.58).

5.3 Analysis for a Finite-length Overhanging Lip or a Square Corner

In this section, we develop an analysis of the scattering process for the impingement of a shear-layer instability wave on a downstream overhanging lip of finite length, for $\eta = 0$. The analysis is similar to that of section 3.3. The geometry of the downstream end of the cavity consists of a vertical end wall at $x = b$ and an infinitely thin overhanging lip extending from $x = 0$ to $x = b$, as illustrated in figure 5.1b. The cavity is assumed sufficiently long that, in analyzing the interaction at the downstream end, the upstream end of the cavity can be neglected. Thus, for the purpose of the analysis, the cavity is assumed to extend to downstream infinity. The generalized Wiener-Hopf technique is used to develop a solution for the case of a finite overhang length. Results for the case of a square (90°) upstream corner are then obtained by considering the limit $b \to 0$. Results for the impingement of a downstream duct mode are presented at the end.

The generalized Wiener-Hopf technique is applicable to situations where a region exists in which the field contains only a finite number of 'cut-on' modes, which propagate either with no attenuation or weak attenuation. The rest of the infinite set of modes are 'cut-off', i.e. they suffer strong attenuation in propagating a distance of the order of the cavity depth d. A typical application of this technique was presented by Koch (1977). The geometry typically involves reflected fields, so that both upstream modes (with amplitude E_q) and downstream modes (with amplitude D_q) are present. An infinite-dimensional matrix equation is developed for the modal amplitudes D_q and E_q. However, since only a finite number of modes are cut-on (say $q = 0, 1, ..., q^*$), while the rest exhibit exponential decay, entries in the matrix equation are very small for entries $q \gg q^*$. Thus, an accurate description of the field can be obtained by solving a truncated form of the infinite-dimensional matrix equation, which includes only a portion of the cut-off modes. To further improve accuracy, extrapolation techniques could be employed to take account of the neglected modes, though this is seldom necessary due to the exponential decay with respect to mode order.

For the present, we assume a finite value for the cavity overhang length b and concentrate on the field in the region $-d < y < 0$ and $0 < x < b$. In this region, the field $\phi_2(x, y)$ is a combination of upstream and downstream duct modes of unknown amplitudes E_q and D_q respectively, thus

$$\phi_2 = \sum_{q=0}^{\infty} \left[D_q \cos(q\pi y/d) \mathrm{e}^{-\mathrm{i}\sigma_q^- x} + E_q \cos(q\pi y/d) \mathrm{e}^{-\mathrm{i}\sigma_q^+ x} \right]. \tag{5.91}$$

Expressions for the x-wavenumbers σ_q^+ and σ_q^- are given in Appendix C. Since the acoustic propagation characteristics do not depend on the direction of propagation, we have $\sigma_q^- = -\sigma_q^+$. For the cut-on modes ($q \leq M_2 d/\pi$, for $\eta = 0$), σ_q^+ is real and positive, so these modes propagate without attenuation. For the cut-off modes ($q \geq M_2 d/\pi$, for $\eta = 0$), σ_q^+ is positive imaginary and $O(q)$ for large q. Hence these modes decay exponentially with distance in the direction of propagation, the decay rate increasing as the mode order increases.

Consider the influence of the upstream end wall of the cavity at $x = b$. This end-wall reflects the upstream duct modes, producing an infinite set of downstream duct modes in the region $0 < x < b$. Applying the no-penetration boundary condition on the vertical end wall to (5.91), and noting that the duct modes are an orthogonal set, we obtain

$$E_q = D_q \mathrm{e}^{\mathrm{i}\sigma_q^+ 2b}. \tag{5.92}$$

Proceding in a similar fashion, as in section 3.3, the amplitudes D_q of the total downstream propagating mode field in the portion of the cavity under the overhanging lip are found to be

$$D_q = D_j^{\mathcal{S}} \delta_{qj} + \sum_{k=0}^{\infty} E_k D_j^{u,k} \delta_{qj}, \quad q = 0, 1, 2..., \infty, \tag{5.93}$$

where $\delta_{qj} = 1$ when $q = j$, and $\delta_{qj} = 0$ when $q \neq j$. The $D_j^{\mathcal{S}}$ term is given by (5.61), and $D_j^{u,k}$ by (5.32), while the amplitudes E_k are still unknown.

Equation (5.92) helps us express the amplitudes E_k of the upstream duct modes in terms of the amplitudes D_k of the downstream duct modes. Employing the properties of substitution tensor to eliminate the index q, (5.93) can then be written as

$$D_j - \sum_{k=0}^{\infty} D_k D_j^{u,k} \mathrm{e}^{\mathrm{i}\sigma_k^+ 2b} = D_j^{\mathcal{S}}, \quad j = 0, 1, 2..., \infty. \tag{5.94}$$

This is an inhomogeneous matrix equation of the form

$$\tilde{A}\bar{D} = \bar{D}^{\mathcal{S}} \tag{5.95}$$

for the vector $\bar{D} = [D_0, D_1, ..., D_\infty]^T$, where the superscript $(\cdot)^T$ indicates the transpose. Also, $\bar{D}^{\mathcal{S}} = \left[D_0^{\mathcal{S}}, D_1^{\mathcal{S}}, ..., D_\infty^{\mathcal{S}}\right]^T$, and the matrix $\tilde{A}$ has the components

$$\tilde{A}_{jk} = \delta_{jk} - D_j^{u,k} \mathrm{e}^{\mathrm{i}\sigma_k^+ 2b}. \tag{5.96}$$

The matrix equation (5.95) is infinite dimensional, but the influence of the higher-order cut-off modes is exponentially small, so accurate results can be obtained from a suitably truncated system, as proven in the following paragraphs.

To understand the behavior of the matrix equation (5.95), note that the coefficient matrix $\tilde{A}$ is the sum of the identity matrix $\tilde{I}$ and a matrix $\tilde{A}'$ with entries $-D_j^{u,k}\mathrm{e}^{\mathrm{i}\sigma_k^+ 2b}$. We consider the properties of $\tilde{A}'$ for large j and k. The $D_j^{u,k}$ are given by (5.32). To determine the behavior for large j and k, note from Appendix A that $\sigma_j^+ \sim \mathrm{i}j\pi/d$ and $K^+(\sigma_j^+) \to 1$ for large j, while $\sigma_k^- \sim -\mathrm{i}k\pi/d$ and $K^-(\sigma_k^-) \to 1$ for large k. Thus, we see that $D_j^{u,k} = O(j^{-3/2})$ for $j \gg 1$ and $k = O(1)$, $D_j^{u,k} = O(k^{-5/2})$ for $k \gg 1$ and $j = O(1)$, and $D_j^{u,k} = O(j^{-3})$ when j and k are large and of the same order. Secondly, note that the σ_k^+ are purely real for the cut-on modes ($k \leq M_2 d/\pi$), while σ_k^+ is purely imaginary and positive for the cut-off modes ($k \geq M_2 d/\pi$), so that for non-zero values of b the factor $\mathrm{e}^{\mathrm{i}\sigma_k^+ 2b}$ decreases exponentially with index k in the cut-off range. Therefore, the entries of the matrix $\tilde{A}'$ decrease algebraically as the $3/2$ inverse power of the row index j for large j and, more importantly, for non zero values of b, the entries decrease exponentially with k as the column index k increases in the cut-off range. Thus, the entries $\tilde{A}_{jk}$ corresponding to sufficiently large values of j and k differ only slightly from those of the identity matrix.

The behavior of the solution $\bar{D}$ depends both on the behavior of the coefficients of the matrix $\tilde{A}$ and on the behavior of the vector $\bar{D}^{\mathcal{S}}$ on the right-hand side. The entries $D_j^{\mathcal{S}}$ of this vector are given by (5.61). For large values of the index j, the entries of $\bar{D}^{\mathcal{S}}$ decrease algebraically as $j^{-3/2}$. Since the entries of $\tilde{A}_{jk}$ corresponding to sufficiently large values of j and k differ slightly from those of the identity matrix, the entries D_k of the solution $\bar{D}$ must also decrease algebraically as $k^{-7/2}$ for large k.

Thus, we solve a truncated version of the matrix equation (5.95),

$$\widetilde{A}\overline{D} = \overline{D}^{\mathcal{S}}. \tag{5.97}$$

The amplitudes D_k can be obtained, and from them the amplitudes of the upstream cavity modes generated by the interaction of the shear-layer instability wave with the

finite-length overhanging lip and a downstream end wall. Thus,

$$C_j = C_j^{\mathcal{S}} + \sum_{k=0}^{\infty} D_k C_j^{u,k} \mathrm{e}^{\mathrm{i}\sigma_k^+ 2b}.\ j = 0, 1, 2 \ldots, \infty. \tag{5.98}$$

Note that C_0 is the scattering coefficient $C_{\mathcal{US}}$ discussed in Chapter 2.

Similarly, for each x and y we can obtain the complex amplitudes of the external acoustic field at (x, y) arising from the branch cut contribution at $\lambda = M_u$,

$$E_{1\mathcal{S}}(x, y) = E_1^{\mathcal{S}}(x, y) + \sum_{k=0}^{\infty} D_k E_1^{u,k}(x, y) \mathrm{e}^{\mathrm{i}\sigma_k^+ 2b},\ \text{for } y > 0 \tag{5.99}$$

$$E_{2\mathcal{S}}(x, y) = E_2^{\mathcal{S}}(x, y) + \sum_{k=0}^{\infty} D_k E_2^{u,k}(x, y) \mathrm{e}^{\mathrm{i}\sigma_k^+ 2b} \text{ for } y < 0. \tag{5.100}$$

Note that $E_{2\mathcal{S}}(0, 0)$ is the scattering coefficient $C_{\mathcal{E}_u \mathcal{S}}$, discussed in Chapter 2.

Analogously, if we take the downstream cavity mode as the incident field, we follow the above procedure to obtain the matrix equation

$$\tilde{A}\bar{D} = \bar{D}^{\mathcal{D}k}, \tag{5.101}$$

where the matrix $\tilde{A}$ is defined in (5.96). As before, for nonzero overhang length b, the influence of the higher order cut-off modes is exponentially small, so that accurate results can be obtained from a suitably truncated system

$$\widetilde{A}\overline{D} = \overline{D}^{\mathcal{D}k}, \tag{5.102}$$

which, for the impingement of a downstream cavity mode, leads to the cavity mode amplitudes

$$C_j = C_j^{\mathcal{D}k} + \sum_{k=0}^{\infty} D_k C_j^{u,k} \mathrm{e}^{\mathrm{i}\sigma_k^+ 2b}. \tag{5.103}$$

Here C_0 is the scattering coefficient $C_{\mathcal{UD}}$, discussed in Chapter 2.

In a similar fashion, for each x and y, we obtain the complex amplitude of the external acoustic field at (x, y) generated by this interaction, namely

$$E_{1\mathcal{D}}(x,y) = E_1^{\mathcal{D}k}(x,y) + \sum_{k=0}^{\infty} D_k E_1^{u,k}(x,y) \mathrm{e}^{\mathrm{i}\sigma_k^+ 2b}, \text{ for } y > 0 \tag{5.104}$$

$$E_{2\mathcal{D}}(x,y) = E_2^{\mathcal{D}k}(x,y) + \sum_{k=0}^{\infty} D_k E_2^{u,k}(x,y) \mathrm{e}^{\mathrm{i}\sigma_k^+ 2b} \text{ for } y < 0. \tag{5.105}$$

Note that $E_{2\mathcal{D}}(0,0)$ is the scattering coefficient $C_{\mathcal{E}_u\mathcal{D}}$, discussed in Chapter 2.

6. NUMERICAL RESULTS AND DISCUSSION FOR THE SCATTERING PROBLEM AT THE DOWNSTREAM END

In this chapter, we present numerical results for the acoustic fields generated by the interactions of an instability wave and a downstream acoustic cavity mode with the downstream edge of the cavity. The geometries illustrated in figure 5.1 are considered. The numerical results were obtained using *Mathematica*5 (Wolfram 2003) on a Pentium Computer. Results are presented for the cases $M_1 = M_2 = M = 0.35$ and $M = 0.85$, with $\omega d'/U = d = 1.5$ and $c_1 = c_2$. For a cavity with length to depth ratio $L/d = 5$, the non-dimensional frequencies for the first four Rossiter modes at $M = 0.35$ lie in the range $0.3 < d < 5.7$; while at $M = 0.85$ they lie in the range $0.26 < d < 4.5$. Thus, the case $d = 1.5$ is roughly centered in the frequency range of interest. In these frequency ranges, the high order cavity modes are cut off, i.e. the imaginary part of the wavenumbers $\tau_j^+,\ j = 1, 2, ..., \infty$ is of $O(1)$ and positive and the imaginary part of the wavenumbers $\tau_j^-,\ j = 1, 2, ..., \infty$ is of $O(1)$ and negative. Therefore these modes decay to negligible amplitudes with upstream distance.

For the length to depth aspect ratios of interest (say $3 < L/d < 8$), it is only the upstream acoustic cavity mode $\mathcal{U}$ that provides acoustic feedback at the upstream lip. However, the higher-order modes contribute to the local unsteady pressure levels near the upstream end of the cavity. Results for the case $\eta = 0$ are presented in this chapter, the influence of non zero η is discussed in Chapter 7.

6.1 Results for a Semi-infinite Overhanging Lip

6.1.1 Impingement of an Instability Wave

First, lets consider the interaction of a shear-layer instability wave propagating in the downstream direction with an overhanging lip for Mach number $M = 0.35$. This in-

teraction was analyzed in section 5.2.2; the geometry is illustrated in figure 5.1(c),and the incident field is given by (5.33, 5.34). The solution for the scattered field in the upstream region ($x < 0$) is given in integral form by (5.50, 5.51) and in the downstream region ($x > 0$) by (5.58, 5.59).

In the upstream region ($x < 0$), the scattered field is given by (5.52, 5.53). It consists of an infinite series of upstream cavity modes with complex amplitudes $C_j^{\mathcal{S}}$ given by (5.54), and an upstream external acoustic field with complex amplitudes $E_1^{\mathcal{S}}(x, y)$ (for $y > 0$) and $E_2^{\mathcal{S}}(x, y)$ (for $y < 0$)). The amplitudes $|C_j^{\mathcal{S}}|$ and phases $\arg[C_j^{\mathcal{S}}]$ of the first seven upstream cavity modes generated by the interaction of a shear-layer instability wave with a semi-infinite overhanging lip, for Mach number 0.35, are shown in table 6.1. The $j = 0$ cavity mode has an amplitude $|C_0^{\mathcal{S}}| = 0.23$, while the $j = 1$ mode has an amplitude $|C_1^{\mathcal{S}}| = 0.39$. The amplitude of the $j = 2$ mode has an amplitude of only $|C_2^{\mathcal{S}}| = 0.1$, and the amplitudes of the higher-order cavity modes decay with mode order. Furthermore, the higher-order modes exhibit exponential decay in the x-direction. The decreasing rate increases with mode order, making these modes insignificant. The strong excitation of the $j = 1$ cavity mode is explained by noting that the scattered field is produced by a dipole acoustic source distribution on the inner surface of the overhanging lip. This dipole source distribution tends to excite transverse oscillations, which naturally couples the $j = 1$ cavity mode (see figures 4.1 and 4.2).

The interaction of a shear-layer instability wave with a semi-infinite overhanging lip, in the upstream region ($x < 0$), also produces an upstream external acoustic field. The amplitude of this field at the edge of the overhanging lip is $|E_2^{\mathcal{S}}(0, 0)| = 0.076$ and decays in the negative x-direction as $x^{-3/2}$. Hence, the upstream external acoustic field for this interaction, though important for the continuity of the pressure field at $x = 0$, will not play a major role in the prediction of the resonant frequencies.

In the duct region ($x > 0$, $y < 0$), the scattered field is given by (5.60) and consists of an infinite series of downstream duct modes, with complex amplitudes $D_j^{\mathcal{S}}$

j	$\lvert C_j^{\mathcal{S}}\rvert$	$\arg[C_j^{\mathcal{S}}]$	$\lvert D_j^{\mathcal{S}}\rvert$	$\arg[D_j^{\mathcal{S}}]$
0	0.22797	−0.69739	0.73921	0.28194
1	0.39351	−0.40967	0.13943	−0.10189
2	0.09929	2.31871	0.06104	0.10975
3	0.05011	−0.94202	0.03601	0.19404
4	0.03137	2.13947	0.02439	0.23959
5	0.02194	−1.07915	0.01790	0.26813
6	0.01643	2.04974	0.01385	0.28769

Table 6.1 *Amplitudes and phases of the upstream cavity modes and downstream duct modes generated by the interaction of a shear-layer instability wave with a semi-infinite overhanging lip, for* $M = 0.35$

given by (5.61). In the downstream flow region ($y > 0$), the scattered field consists of an upstream external acoustic field. The amplitudes $|D_j^{\mathcal{S}}|$ and phases $\arg[D_j^{\mathcal{S}}]$ of the first seven downstream duct modes are given in table 6.1. The $j = 0$ duct mode has an amplitude $|D_0^{\mathcal{S}}| = 0.74$, while $|D_1^{\mathcal{S}}| = 0.13$. The higher-order duct modes ($j \geq 2$) exhibit strong exponential decay; their amplitudes decay with mode order and are relatively insignificant. The strong dominance of the $j = 0$ duct mode in the downstream field is explained by noting that even though the pressure field of the incident instability wave varies across the cavity depth, its shape remains closer to the $j = 0$ (plane-wave) downstream duct mode than to any other ($j \geq 1$) duct mode, see figure 4.1. Hence the $j = 0$ duct mode is the natural continuation of the instability wave pressure field. The relatively small excitation of the $j = 1$ duct mode can be attributed to the deviation from uniform profile of the pressure field of the instability wave and to the acoustic dipole source distribution on the inner surface of the overhanging lip. The external acoustic field generated in the downstream region ($x > 0$, $y > 0$) propagates away from the cavity and has no influence on the resonant frequencies. It will not be consider any further. The behavior of the scattering coefficients $C_j^{\mathcal{S}}$ and $D_j^{\mathcal{S}}$ for $M = 0.85$ is similar to that obtained for $M = 0.35$.

The unsteady pressure field on the cavity bottom produced by the interaction of the shear-layer instability wave with a semi-infinite overhanging lip is shown in figure

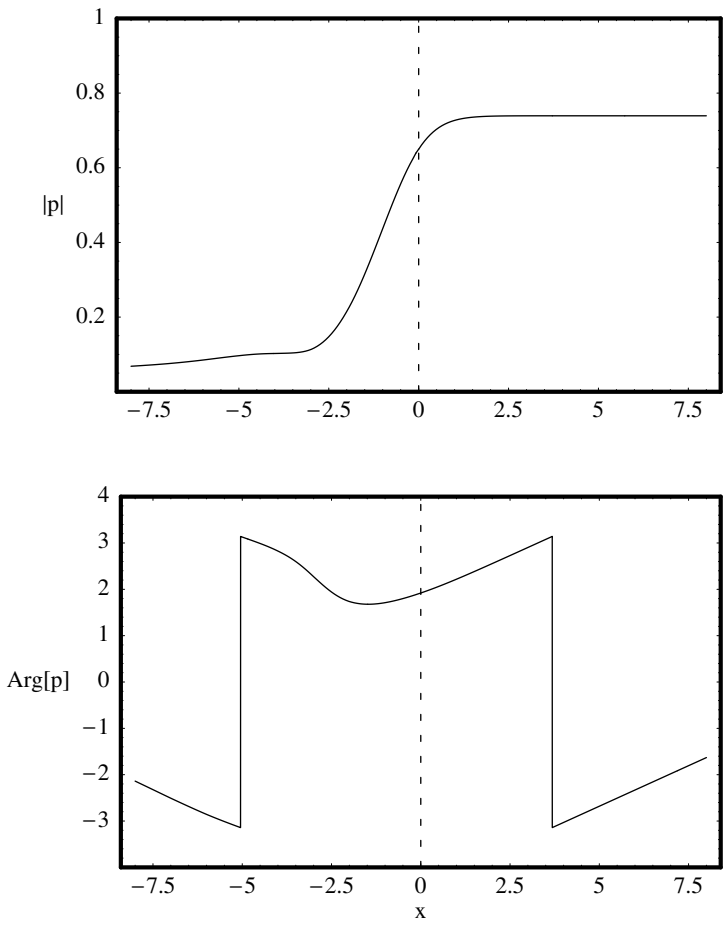

Figure 6.1 *Amplitude and phase of the pressure field on the cavity bottom for the interaction of a shear-layer instability wave with a semi-infinite overhanging lip, for* $M = 0.35$.

6.1. In the upstream region ($x < 0$), the total field on the bottom of the cavity is the sum of the incident instability wave (5.34), the upstream cavity mode series, and the upstream external acoustic field, as given by (5.53). In the duct region, the total field contains only the downstream duct mode series. Both series mentioned have been evaluated numerically using the first 8 modes. Despite the finite-term truncation of the series, the amplitude and phases for $x \to 0_-$ and $x \to 0_+$ agree to within 1% at the bottom of the cavity. Accelerating convergence techniques (Shanks transformation) make the amplitude and phases agree to within 0.01%.

The maximum pressure level at the bottom of the cavity is $|p| = 0.649$ at $x = 0$. For reference, the incident instability wave has a pressure amplitude $|p| = 1$ at the edge of the overhanging lip ($x = y = 0$) and an amplitude $|p| = 0.46$ at $x = 0$ on the bottom of the cavity. The pressure for $x < 0$ exhibits a rapid exponential decay as the contributions from the higher-order ($j \geq 1$) cavity modes (cut-off) vanish. The total pressure field for $-5 < x < -3$ is basically the sum of the shear-layer instability wave and the $j = 0$ upstream cavity mode. Due to the different phase characteristics of these components, the pressure amplitude in the region $-5 < x < -3$ exhibits small oscillations caused by the constructive/destructive interference of the instability wave and the $j = 0$ upstream cavity mode. For $x < -5$, the pressure field is dominated by the $j = 0$ cavity mode, so it decays with upstream distance at a rate set by $\mathrm{Im}[\tau_0^+]$.

In the duct region ($x > 0$), we see that for $0 < x < 2$ the pressure amplitude on the cavity bottom increases with x. This growth is due to the exponentially decaying interference of the higher-order ($j \geq 1$) downstream duct modes, which are cut-off in x. For $x > 2$, the only mode that contributes to the pressure amplitude is the $j = 0$ downstream duct mode (plane-wave), hence the pressure level becomes constant at $|p| = 0.74$.

The phase of the total pressure field is also shown in figure 6.1. For $x < -5$, the phase of the total pressure field corresponds to upstream propagation of the $j = 0$ cavity mode at the phase speed $0.83c_1$. For $x > 2$, the phase of the total pressure field corresponds to downstream propagation of the $j = 0$ duct mode at a phase speed $0.83c_1$. In the region $-5 < x < -1$, the phase behavior results from the constructive/destructive interference of the incident instability wave and the $j = 0$ upstream cavity mode. Finally, the phase behavior in the region $-1 < x < 2$ is dominated by downstream propagation.

6.1.2 Impingement of an Upstream Duct Mode

For the case of a finite-length overhanging lip, the downstream duct modes discussed in the previous section reflect off the upstream end wall of the cavity, producing upstream duct modes which interact with the edge of the overhanging lip. Thus, we must also consider the scattered field produced by the interaction of the k-th upstream duct mode with a semi-infinite overhanging lip. This interaction was analyzed in section 5.2.1, with the incident field is given by (5.1, 5.2). The solution for the scattered field is given in the integral forms (5.19, 5.20) for the upstream region ($x < 0$), and by (5.29, 5.30), for the downstream region ($x > 0$).

In the upstream region ($x < 0$), the scattered field is given by (5.21, 5.22). It consists of an infinite series of upstream cavity modes with amplitudes $C_j^{u,k}$, given by (5.23), and an upstream external acoustic field with complex amplitudes $E_1^{u,k}(x,y)$ (for $y > 0$) and $E_2^{u,k}(x,y)$ (for $y < 0$), whose far field approximations are given by (5.24) and (5.25), respectively. The amplitudes $|C_j^{u,k}|$ and phases $\arg[C_j^{u,k}]$ of the first seven upstream cavity modes generated by the interaction of the k-th upstream duct mode with a semi-infinite overhanging lip, for $M = 0.35$, are shown in tables 6.2 and 6.3.

Since the diagonal entries of table 6.2 are very close to one, we have that for an incident upstream duct mode of order k, the scattered field contains an order k cavity mode of amplitude almost identical to that of the incident duct mode. In contrast, the off-diagonal entries of table 6.2 are very small, the largest being $|C_1^{u,0}| = 0.09$. Therefore, in the interaction of an upstream duct mode, only a small amount of energy is scattered into upstream cavity modes of different order ($j \neq k$). This behavior can be explained by noting that the wavenumbers τ_j^+ of the upstream propagating cavity modes are almost identical to the wavenumbers σ_j^+ of the corresponding upstream duct mode (see figure 3.2). Also, the mode shapes of the upstream cavity modes are very similar to the mode shapes of the corresponding upstream duct modes (see

j	$k=0$	1	2	3	4	5	6
0	0.87251	0.04994	0.00974	0.00356	0.00174	0.00100	0.00063
1	0.08517	1.03615	0.02540	0.00723	0.00319	0.00173	0.00106
2	0.02495	0.04137	1.00225	0.00904	0.00297	0.00142	0.00082
3	0.01349	0.01675	0.01341	1.00055	0.00484	0.00174	0.00089
4	0.00876	0.00967	0.00580	0.00643	1.00019	0.00302	0.00115
5	0.00626	0.00649	0.00346	0.00287	0.00376	1.00008	0.00205
6	0.00476	0.00474	0.00236	0.00175	0.00171	0.00246	1.00004

Table 6.2 *Amplitudes* $|C_j^{u,k}|$ *of the upstream cavity modes generated by the interaction of the k-th upstream duct mode with a semi-infinite overhanging lip, for* $M = 0.35$

j	$k=0$	1	2	3	4	5	6
0	−0.5930	0.6792	0.2946	0.1786	0.1229	0.0900	0.0682
1	0.2533	3.1154	2.0478	1.8795	1.8005	1.7543	1.7238
2	−2.7166	2.5396	−0.0032	−1.2186	−1.2989	−1.3445	−1.3743
3	0.4533	−0.5958	−1.0936	3.1405	1.8377	1.7910	1.7612
4	−2.6809	2.5400	2.0451	1.8919	−0.0005	−1.3579	−1.3886
5	0.4633	−0.6071	−1.1016	−1.2532	−1.3276	3.1413	1.7474
6	−2.6771	2.5301	2.0357	1.8844	1.8110	1.7668	−1.5E-4

Table 6.3 *Phases* $\arg[C_j^{u,k}]$ *of the upstream cavity modes generated by the interaction of the k-th upstream duct mode with a semi-infinite overhanging lip, for* $M = 0.35$

figure 4.2). Hence, the k-th upstream cavity mode is nearly a perfect continuation corresponding upstream duct mode.

Consider now the phases $\arg[C_j^{u,k}]$ of the scattered upstream cavity modes, given in table 6.3. Note that the diagonal entries are close to zero when j is even, and close to π when j is odd. This behavior can be explained by noting that for even values of j, the cavity mode $\cosh(\mu_2(\tau_j^+)(y+d))$ has a phase which is almost identical to that of the corresponding duct mode $\cos(\frac{j\pi}{d}y)$; while for odd values of j, the cavity mode has a phase which differs by π from that of the corresponding duct mode. Hence, the phase of the k-th scattered upstream cavity mode is such as to provide a nearly perfect continuation of the phase of the incident duct mode.

The interaction of the k-th upstream duct mode with a semi-infinite overhanging

lip also produces an upstream external acoustic field in the upstream region ($x < 0$). The amplitude of this field at the edge of the overhanging lip is $|E^{u,d}(0,0)| = 0.11$ and decays in the negative x-direction as $x^{-3/2}$. Hence, the upstream external acoustic field for this interaction, though important for the continuity of the pressure field at $x = 0$, will not play a role in the prediction of the resonant frequencies.

For the duct region ($x > 0$, $y < 0$), the scattered field is given by (5.31), and consists of an infinite series of downstream duct modes with amplitude $D_j^{u,k}$ given by (5.32). The amplitudes $|D_j^{u,k}|$ and phases $\arg[D_j^{u,k}]$, for $M = 0.35$, of the first seven upstream cavity modes generated by the interaction of the k-th upstream duct mode with a semi-infinite overhanging lip are shown in tables 6.4 and 6.5.

From table 6.4, we see that the amplitudes of the scattered downstream duct modes are generally small. As expected, since the k-th upstream cavity mode provides an almost perfect continuation of the corresponding upstream incident duct mode. The exception is the amplitude for the $k = j = 0$ duct mode, which has a value $|D_0^{u,0}| = 0.39$ (recall $|C_0^{u,0}| = 0.87$). From table 6.5, we see that $\arg[D_0^{u,0}] = -2.16$, which corresponds to a phase lead of 65° for the scattered $j = 0$ downstream duct mode relative to the incident $k = 0$ upstream duct mode. The amplitude of this particular scattering coefficient is always the largest, but decreases with Mach number to an amplitude level very close to that of the rest of the scattered duct modes. For

j	$k=0$	1	2	3	4	5	6
0	0.38774	0.10770	0.02148	0.00793	0.00389	0.00223	0.00142
1	0.06638	0.02798	0.00739	0.00306	0.00160	0.00096	0.00063
2	0.02382	0.01329	0.00396	0.00175	0.00095	0.00059	0.00039
3	0.01307	0.00819	0.00261	0.00120	0.00067	0.00042	0.00029
4	0.00853	0.00569	0.00189	0.00090	0.00051	0.00033	0.00022
5	0.00612	0.00425	0.00145	0.00070	0.00041	0.00026	0.00018
6	0.00467	0.00333	0.00116	0.00057	0.00034	0.00022	0.00015

Table 6.4 *Amplitudes $|D_j^{u,k}|$ of the downstream duct modes generated by the interaction of the k-th upstream duct mode with a semi-infinite overhanging lip, for $M = 0.35$*

j	$k=0$	1	2	3	4	5	6
0	−2.1626	1.6139	1.0354	0.8563	0.7693	0.7177	0.6835
1	2.0404	0.7687	0.2745	0.1233	0.0502	0.0070	−0.0216
2	2.0364	0.8490	0.3548	0.2036	0.1305	0.0873	0.0586
3	2.0358	0.8763	0.3820	0.2309	0.1578	0.1145	0.0859
4	2.0356	0.8901	0.3958	0.2447	0.1716	0.1283	0.0997
5	2.0356	0.8984	0.4042	0.2530	0.1799	0.1366	0.1080
6	2.0356	0.9040	0.4097	0.2586	0.1855	0.1422	0.1136

Table 6.5 *Phases* $\arg[D_j^{u,k}]$ *of the downstream duct modes generated by the interaction of the k-th upstream duct mode with a semi-infinite overhanging lip, for* $M = 0.35$

example, for $M = 0.85$, we have $|C_0^{u,0}| = 1$ and $|D_0^{u,0}| = 0.10$; this can be explained from tables 4.1 and 4.2. Here we see that for $M = 0.85$, the distance $|\sigma_0^+ - \tau_0^+|$ is small compared to the same distance for $M = 0.35$. Thus, the relatively higher amplitude $|D_0^{u,0}|$ for lower Mach numbers is related to the mode shape of the corresponding $j = 0$ downstream cavity mode.

Also, from figures 4.2 and 4.3, we see that contrary to what happens for $M = 0.85$ and at supersonic speeds (see Cain *et al.*, 2001), the $j = 0$ downstream cavity mode for $M = 0.35$ exhibits growth in the stream region. Therefore, less energy is transmitted from the incident $k = 0$ (plane-wave) duct mode to the corresponding $j = 0$ cavity mode, while more energy is scattered to the $j = 0$ downstream duct mode.

The unsteady pressure field on the cavity bottom produced by the interaction of the $k = 0$ upstream duct mode is presented in figure 6.2. In the upstream region ($x < 0$), the total field is the sum of the upstream cavity mode series and the upstream external acoustic field, as given by (5.22). In the duct region, the total field contains the incident k-th upstream duct mode and downstream duct mode series, as given by (5.31). Both series mentioned have been evaluated numerically using the first 8 modes. Despite the finite-term truncation of the series, the amplitude and phases for $x \to 0_-$ and $x \to 0_+$ agree to within 0.2% and 0.5%, respectively, at the bottom of the cavity. Accelerating convergence techniques (Shanks transformation) make the

amplitude and phases agree to within 0.01%.

From figure 6.2, we see that the pressure amplitude on the cavity bottom decreases monotonically with upstream distance. This upstream field consists almost entirely of the $j = 0$ downstream cavity mode, as verified by the results on table 6.2. Furthermore, the wavenumbers τ_j^+ for the higher-order cavity modes ($j \geq 1$) have $O(1)$ imaginary parts, thus decay rapidly with upstream distance and become negligible beyond, say $x = -1$. Hence, the behavior of the total pressure field in the region $x < -1$ is dominated by the $j = 0$ upstream cavity and decays with upstream distance at a rate set by $\mathrm{Im}[\tau_0^+] = 0.12$.

In the downstream region ($x > 0$), the field contains the incident upstream $k = 0$ duct mode of amplitude unity and the infinite set of scattered downstream duct modes. The higher-order modes are cut-off and can be neglected beyond a point, say $x = 1$. The maximum pressure amplitude on the cavity bottom is $|p| = 1.39$ at $x \approx 3.1$, a distance approximately twice the cavity depth d. Beyond the point $x = -2$, the amplitude of the pressure field exhibits a periodic oscillation, with a minimum value of $|p| = 0.61$, a maximum value of $|p| = 1.39$, and a wavelength equal to half the acoustic wavelength, $\frac{1}{2}\lambda_{ac} = \frac{\pi}{M} = 8.98$. This pattern results from the constructive/destructive interference between the incident $k = 0$ upstream duct mode of amplitude one and the scattered downstream $j = 0$ duct mode of amplitude $|D_j^{u,k}| = 0.39$.

The phase of the unsteady pressure field on the cavity bottom is presented in figure 6.2. The behavior shown in this figure is consistent with the behavior explained on the previous paragraph. For $x < -1$, the phase of the pressure field corresponds to propagation of the upstream cavity mode at the phase speed $0.83c_1$. In the region $-1 < x < 1$, the phase is dominated by upstream propagation. The unusual behavior in the region $x > 1$ results from the previously mentioned constructive/destructive interference of the incident $k = 0$ upstream duct mode and the scattered downstream $j = 0$ duct mode.

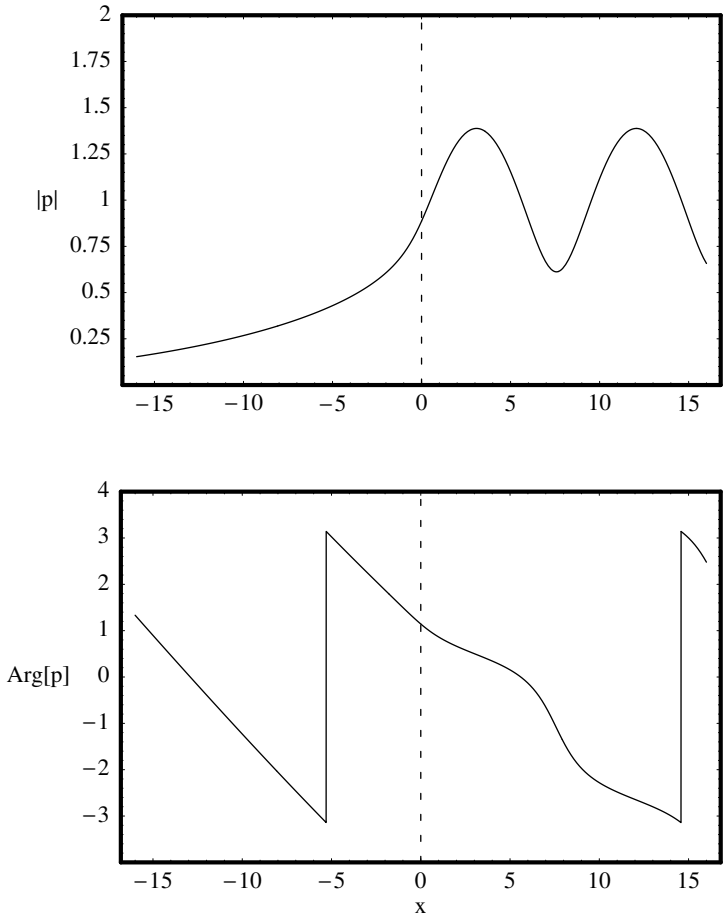

Figure 6.2 *Amplitude and phase of the pressure field on the cavity bottom for the interaction of the $k = 0$ upstream duct mode with a semi-infinite overhanging lip, for $M = 0.35$.*

6.1.3 Impingement of a Downstream Cavity Mode

Finally, we consider the interaction of the k-th downstream cavity mode with an overhanging lip, for $M = 0.35$. This interaction was analyzed in section 5.2.3; the geometry is illustrated in figure 5.1(c) and the incident field is given by (5.62 , 5.63). The scattered field in the upstream region ($x < 0$) is given in integral form by (5.79, 5.80) and in the downstream region ($x > 0$) by (5.87, 5.88).

In the upstream region ($x < 0$), the scattered field is given by (5.81, 5.82). It

consists of an infinite series of upstream cavity modes with complex amplitudes $C_j^{\mathcal{D}k}$, given by (5.83), and an upstream external acoustic field with complex amplitudes $E_1^{\mathcal{D}k}(x,y)$ (for $y > 0$) and $E_2^{\mathcal{D}k}(x,y)$ (for $y < 0$). The amplitudes $|C_j^{\mathcal{D}k}|$ and phases $\arg[C_j^{\mathcal{D}k}]$ of the first seven upstream cavity modes generated by this interaction, for $M = 0.35$, are shown in tables 6.6 and 6.7.

From table 6.6, we see that the largest amplitude is $|C_0^{\mathcal{D}0}| = 0.05$, with the amplitudes for higher-order modes ($k, j \geq 1$) decreasing with mode order. Therefore, in the interaction of a downstream cavity mode with an overhanging lip, only a small amount of energy is scattered into upstream cavity modes of other orders. The phases of the scattered upstream cavity modes, given in table 6.7, show more variability; as the amplitudes of these modes are very small, however, this feature is unimportant. Furthermore, for the parameter range of interest ($3 \leq \frac{L}{d} \geq 8$), this coefficient does not play an important role when determining the resonant frequencies.

The interaction of the k-th downstream cavity mode with a semi-infinite overhanging lip also produces an upstream external acoustic field in the upstream region ($x < 0$). The amplitude of this field at the edge of the overhanging lip is $|E_2^{\mathcal{D}k}(0,0)| = 0.014$, and decays in the negative x-direction as $x^{-3/2}$. Hence, the external acoustic field for this interaction, though important for the continuity of the pressure field at $x = 0$, will not play any role in the prediction of the resonant

j	$k=0$	1	2	3	4	5	6
0	0.05453	0.04221	0.00938	0.00352	0.00173	0.00100	0.00063
1	0.02743	0.03359	0.00938	0.00390	0.00203	0.00121	0.00079
2	0.00791	0.01338	0.00423	0.00188	0.00102	0.00063	0.00042
3	0.00427	0.00816	0.00274	0.00127	0.00071	0.00045	0.00030
4	0.00277	0.00565	0.00198	0.00094	0.00054	0.00034	0.00024
5	0.00198	0.00421	0.00151	0.00074	0.00043	0.00028	0.00019
6	0.00150	0.00330	0.00121	0.00060	0.00035	0.00023	0.00016

Table 6.6 *Amplitudes $|C_j^{\mathcal{D}k}|$ of the upstream cavity modes generated by the interaction of the k-th downstream cavity mode with a semi-infinite overhanging lip, for $M = 0.35$*

j	$k=0$	1	2	3	4	5	6
0	2.4457	0.8810	1.1934	1.3091	1.3660	1.3996	1.4218
1	2.7524	2.3040	2.6994	2.8486	2.9233	2.9679	2.9976
2	−0.3803	−0.7711	−0.3847	−0.2388	−0.1658	−0.1222	−0.0932
3	2.7403	2.3712	2.7551	2.8999	2.9725	3.0158	3.0446
4	−0.4184	−0.7759	−0.3932	−0.2488	−0.1764	−0.1332	−0.1045
5	2.7112	2.3607	2.7427	2.8869	2.9592	3.0024	3.0311
6	−0.4390	−0.7847	−0.4032	−0.2591	−0.1870	−0.1438	−0.1151

Table 6.7 *Phases* $\arg[C_j^{\mathcal{D}k}]$ *of the upstream cavity modes generated by the interaction of the k-th downstream cavity mode with a semi-infinite overhanging lip, for* $M = 0.35$

frequencies.

In the duct region ($x > 0$, $y < 0$), the scattered field is given by (5.89) and consists only of an infinite series of downstream cavity modes with amplitudes $D_j^{\mathcal{D}k}$, given by (5.90). The amplitudes of the first seven duct modes generated by this interaction, for $M = 0.35$, are given in table 6.8. Note that the diagonal entries are very near one, while the off-diagonal entries are relatively small, with $|D_0^{\mathcal{D}1}| = 0.1$ as the largest of these entries. This behavior is explained by the following two considerations. First, the x-wavenumber of the downstream cavity modes τ_j^- and the x-wavenumber of the corresponding downstream duct mode are very close to each other for higher-order modes ($j \geq 1$) (see figure 3.2). Second, the mode shapes of the downstream cavity modes are close to that of the corresponding duct mode (see figure 4.4). Hence, the k-th downstream duct mode provides a nearly perfect continuation of the corresponding incident downstream cavity mode.

Consider now the phases $\arg[D_j^{\mathcal{D}k}]$ of the scattered downstream cavity modes, given in table 6.7. Note that the diagonal entries are close to zero. When k is even, the cavity mode $\cosh(\mu_2(\tau_k^-)(y+d))$ has a phase which is almost identical to that of the corresponding duct mode $\cos(\frac{k\pi}{d}y)$, providing a nearly perfect phase continuation of the incident field. When k is odd, the phases of $\cosh(\mu_2(\tau_j^-)(y+d))$ and $\cos(\frac{j\pi}{d}y)$ differ by approximately π. So, contrary to what happens for the interaction of a duct

j	$k=0$	1	2	3	4	5	6
0	0.97729	0.10029	0.02184	0.00813	0.00398	0.00228	0.00145
1	0.02111	1.02797	0.02214	0.00622	0.00271	0.00146	0.00089
2	0.00754	0.04008	1.00201	0.00893	0.00292	0.00140	0.00080
3	0.00413	0.01618	0.01335	1.00039	0.00481	0.00173	0.00088
4	0.00270	0.00933	0.00579	0.00644	1.00012	0.00300	0.00114
5	0.00193	0.00626	0.00346	0.00288	0.00377	1.00005	0.00205
6	0.00148	0.00457	0.00237	0.00176	0.00172	0.00247	1.00002

Table 6.8 *Amplitudes* $|D_j^{\mathcal{D}k}|$ *of the downstream duct modes generated by the interaction of the k-th downstream cavity mode with a semi-infinite overhanging lip, for* $M = 0.35$

mode with an overhanging lip, when k is odd the phase of the scattered duct mode lags the phase of the incident cavity mode by approximately π. The off-diagonal entries show more variability, but since their amplitudes are very small, this feature is of little importance. Since higher-order $k \geq 1$ cavity modes exhibit exponential decay (cut-off), the only interaction that may play a role in determining the total field that propagates upstream is that of the $k = 0$ downstream cavity mode with the overhanging lip.

The unsteady pressure field on the cavity bottom produced by the interaction of the $k = 0$ downstream cavity mode is presented in figure 6.3. In the upstream region ($x < 0$), the total field is the sum of the incident $k = 0$ downstream cavity mode, the upstream cavity mode series, and the external acoustic field propagating in the

j	$k=0$	1	2	3	4	5	6
0	0.0268	1.0887	1.5657	1.7410	1.8280	1.8798	1.9142
1	−2.3476	0.0143	0.9650	1.1183	1.1922	1.2359	1.2648
2	−2.2038	−2.4317	0.0037	1.1951	1.2718	1.3159	1.3449
3	−2.1555	−2.4197	−2.0412	0.0012	1.2971	1.3428	1.3720
4	−2.1313	−2.4109	−2.0345	−1.8915	5.1E-4	1.3552	1.3855
5	−2.1167	−2.4050	−2.0285	−1.8867	−1.8143	2.6E-4	1.3929
6	−2.1069	−2.4009	−2.0241	−1.8822	−1.8108	−1.7672	1.5E-4

Table 6.9 *Phases* $\arg[D_j^{\mathcal{D}k}]$ *of the downstream duct modes generated by the interaction of the k-th downstream cavity mode with a semi-infinite overhanging lip, for* $M = 0.35$

upstream direction, as given by (5.82). In the duct region, the total field contains only the downstream duct mode series, as given by (5.89). Both series mentioned have been evaluated numerically using the first 8 modes. Despite the finite-term truncation of the series, the amplitude and phases for $x \to 0_-$ and $x \to 0_+$ agree to within 0.1% and 0.6%, respectively, at the bottom of the cavity. Accelerating convergence techniques (Shanks transformation) make the amplitude and phases agree to within 0.01%.

From figure 6.3, we see that the pressure amplitude on the cavity bottom increases with upstream distance up to a point, say $x = -1$, where the interference from higher-order modes and external acoustic field vanish. After this point, the upstream field consists almost entirely of the incident $j = 0$ downstream cavity mode, as can be verified by the results on table 6.6 and the fact that the incident field has amplitude one and does not exhibit decay in the x-direction.

The maximum pressure amplitude on the cavity bottom is $|p| = 1.09$ at $x \approx -5.1$, a distance approximately three times the cavity depth d. Beyond the point $x = -1$ the amplitude of the pressure field exhibits a periodic oscillation that dies with upstream distance, with a minimum value of $|p| = 1.04$, a maximum value of $|p| = 1.09$, and a wavelength equal to half the acoustic wavelength, $\frac{1}{2}\lambda_{ac} = \frac{\pi}{M} = 8.98$. This pattern results from the constructive/destructive interference between the incident $k = 0$ downstream cavity mode of amplitude one and the lightly damped scattered upstream $j = 0$ duct mode of amplitude $|C_j^{\mathcal{D}k}| = 0.05$. The oscillations die away as the $j = 0$ upstream cavity mode slowly decays and the remaining field consists entirely of the incident $k = 0$ downstream cavity mode.

In the downstream region ($x > 0$), the unsteady field contains only the infinite set of scattered downstream duct modes. For the first part of the duct region, say $0 < x < 1$, the scattered field decays as the contribution from higher-order (cut-off) duct modes disappear. For $x > 1$, the unsteady field consists entirely of the $j = 0$ (plane-wave) duct mode with amplitude $|D_0^{\mathcal{D}0}| = 0.98$, as can be seen from table 6.8.

The phase of the unsteady pressure field on the cavity bottom is also presented

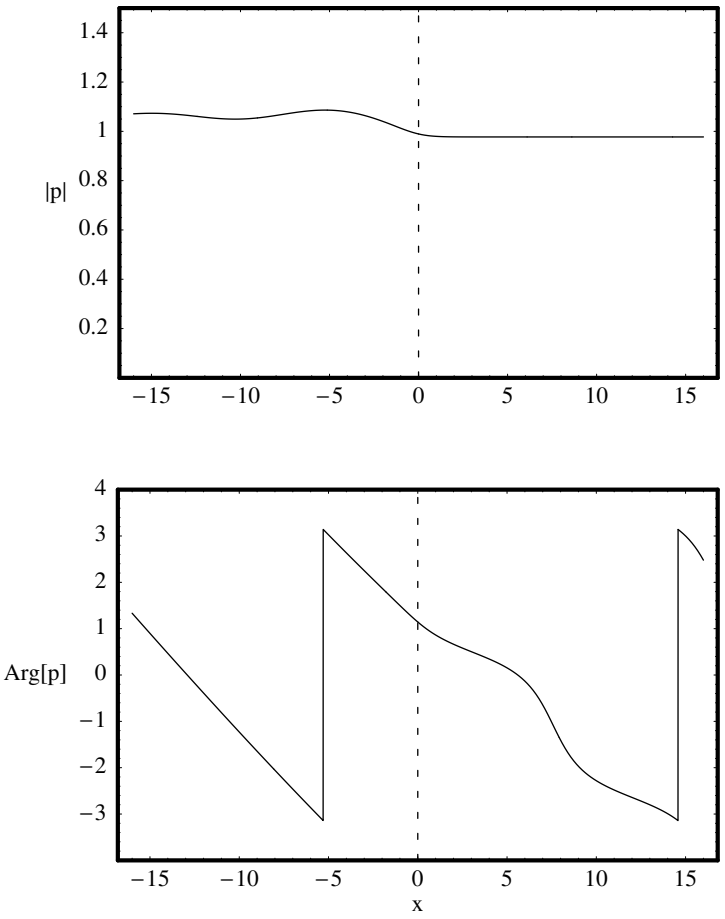

Figure 6.3 *Amplitude and phase of the pressure field on the cavity bottom for the interaction of the $k = 0$ downstream cavity mode with a semi-infinite overhanging lip, for $M = 0.35$.*

in figure 6.3. The behavior shown in this figure is consistent with the behavior explained in the previous paragraphs. For $x < -1$, the phase of the pressure field corresponds to propagation of the downstream cavity mode at the phase speed $1.33c_1$. In the region $-1 < x < 1$, the phase is dominated by downstream propagation. The phase variation in the region $0 < x < 9$ results from the previously mentioned constructive/destructive interference of the higher-order ($j \geq 1$) downstream duct modes with the $j = 0$ downstream duct mode. For $x > 9$, the phase of the pressure field corresponds to propagation of the $j = 0$ duct mode propagating in the upstream

direction.

6.2 Results for a Finite-length Overhanging Lip or a Square Corner

In this section, we present results for the interaction of a shear-layer instability wave with a finite-length overhanging lip or a square (90°) corner, for Mach number $M = 0.35$ and $d = 1.5$. This interaction was analyzed in section 5.3. The geometry for an overhanging lip of length b is illustrated in figure 5.1(b), and the square corner geometry, which corresponds to the limit $b \to 0$, is illustrated in figure 5.1(a).

To determine the unsteady pressure field generated by this interaction (the $\mathcal{U}$ complex coefficient discussed in Chapter 2), we first have to solve the truncated version (5.97) of the infinite dimensional matrix equation (5.95) for the amplitudes $|D_k|$ of the downstream duct modes in the portion of the cavity under the overhanging lip ($0 < x < b, \ -d < y < 0$). The entries $\tilde{A}_{jk}$ of the coefficient matrix $\tilde{A}$ are given by (5.96) and the entries $D_j^{\mathcal{S}}$ of the vector $\overline{D}^{\mathcal{S}}$ on the right-hand side by (5.61). The matrix equation involves three important physical aspects. (1) the generation of downstream duct modes by the impingement of the shear-layer instability wave on the edge of the overhanging lip ($x = 0$),(2) the generation of upstream duct modes by reflection of the downstream duct modes at the vertical end wall ($x = b$), (3) the generation of of downstream duct modes by impingement of the upstream duct modes on the edge of the overhanging lip ($x = 0$). Note that the reflections at the cavity end wall and the scatterings of the upstream duct modes into the downstream duct modes continue indefinitely and are accounted for in the matrix equation. The solution of the matrix equation is simplified by truncating the system at finite order. It will be shown that the effect of the truncation has negligible effects on the amplitude of the downstream disturbances generated at the upstream end of the cavity.

j	$k=0$	1	2	3	4	5	6	7
0	1.25816	0.10770	0.02148	0.00793	0.00389	0.00224	0.00142	9.68E-4
1	0.06638	0.98009	0.00739	0.00306	0.00160	9.57E-4	6.25E-4	4.35E-4
2	0.02382	0.01329	0.99629	0.00175	9.55E-4	5.88E-4	3.92E-4	2.77E-4
3	0.01307	0.00819	0.00261	0.99883	6.73E-4	4.23E-4	2.87E-4	2.05E-4
4	0.00853	0.00569	0.00189	8.96E-4	0.99950	3.27E-4	2.25E-4	1.62E-4
5	0.00612	0.00425	0.00145	7.03E-4	4.09E-4	0.99974	1.83E-4	1.33E-4
6	0.00467	0.00333	0.00116	5.71E-4	3.36E-4	2.20E-4	0.99985	1.13E-4
7	0.00371	0.00270	9.58E-4	4.77E-4	2.84E-4	1.87E-4	1.31E-4	0.99990

Table 6.10 *Magnitudes* $|A_{j,k}|$ *of the entries of the matrix* $\widetilde{A}$ *for a square (90°) corner* ($b=0$)*, for* $M=0.35$

6.2.1 Duct Mode Coefficients

In this case, the non-diagonal entries $|A_{jk}|$ decay algebraically as $k^{-\frac{1}{2}}$, for large k and fixed j, and as $j^{-\frac{7}{2}}$, for large j and fixed k. The diagonal elements decrease algebraically as j^{-3}. The magnitudes $|A_{jk}|$ of the entries of the coefficient matrix $\widetilde{A}$ for the case $b=0$ are presented in table 6.10 for values of j and k ranging from 0 to 7. The diagonally dominant character is present and the algebraic decay of the non-diagonal entries is easy to see. The slower decay in k than that of j is consistent with the analysis made in section 5.3. Despite the lack of exponential decay with respect to k, the results in table 6.10 indicate that the solutions for the complex amplitudes D_k can be obtained accurately by a finite-mode truncation of the matrix equation.

In table 6.11, the solutions for the complex amplitudes D_k are presented. Results are presented for both an eight-mode truncation and a four-mode truncation of the infinite dimensional system. The differences obtained by the four-mode truncation and the eight-mode truncation, even with the lack of exponential decay in k for the non-diagonal elements of $\widetilde{A}$, are very small. The values $|D_3|$ obtained from the two truncations differ by less than 0.08%; the values $|D_2|$ obtained by these truncations differ by 0.07%, and the differences for the values $|D_1|$ and $|D_0|$ are even smaller. The phases $\arg[D_1]$ for the two different truncations differ by less 0.5%; the phases

k	$\lvert D_k\rvert_{(8)}$	$\lvert D_k\rvert_{(4)}$	$\arg[D_k]_{(8)}$	$\arg[D_k]_{(4)}$
0	0.588847	0.588769	0.043354	0.043167
1	0.124189	0.124130	0.186763	0.186552
2	0.058665	0.058626	0.358148	0.357946
3	0.035445	0.035417	0.427727	0.427530
4	0.024291		0.465676	
5	0.017958		0.489585	
6	0.013964		0.506031	
7	0.011258		0.518037	

Table 6.11 *Amplitudes and phases of the downstream duct modes obtained as the solution of the matrix equation (5.97) for a square (90°) corner ($b = 0$). Results for an eight-mode truncation and a four-mode truncation, for $M = 0.35$,are listed.*

$\arg[D_k]$ for the higher-order modes ($k \geq 1$) differ by at most 0.05%. Therefore, highly accurate values for the amplitudes and phases of the total downstream duct mode field can be obtained by a low order truncation of the system.

It is useful to consider the physical mechanism which determines the dependence of D_0 on b, and to develop an approximate closed-form expression for this quantity. The primary contribution to the $k = 0$ duct mode field comes from the interaction of the incident shear-layer instability wave with the edge of the overhanging lip. This interaction produces a $k = j = 0$ duct mode of amplitude $|D_0^{\mathcal{S}0}| = 0.74$, which propagates downstream without attenuation and reflects off the cavity end wall at $x = b$, producing a $k = j = 0$ upstream duct mode of the same amplitude. This upstream duct mode then interacts with the edge of the overhanging lip at $x = 0$, producing scattered downstream duct modes with amplitudes $|D_j^{u,0}|$ relative to the incident $k = j = 0$ upstream duct mode. The relative amplitude of the downstream duct mode produced by this interaction is $|D_0^{u,0}| = 0.39$ (see table 6.4). Subsequent interactions at the cavity end wall at $x = b$ and the interactions of the upstream duct modes with the edge of the overhanging lip continue indefinitely. If the infinite-dimensional system (5.95) is truncated to a single term in j and k, we obtain the following approximations for the amplitude D_0 and D_1 of the $k = 0$ and $k = 1$

upstream duct modes:

$$D_0 = \frac{D_0^{\mathcal{S}}}{1 - D_0^{u,0} e^{i\sigma_0^+ 2b}}, \tag{6.1}$$

$$D_1 = \frac{D_1^{\mathcal{S}}}{1 - D_1^{u,0} e^{i\sigma_0^+ 2b}}. \tag{6.2}$$

The expression (6.1) accounts for the infinite sequence of reflections and scatterings of the $k = j = 0$ upstream and downstream duct modes, but neglects the contributions to the $k = j = 0$ duct mode field which are produced by the scattering of the higher-order downstream duct modes. Note that the contributions of these higher-order modes are negligible, except for b small, since the higher-order modes are cut-off and decay exponentially with distance downstream. Furthermore, the scattering coefficients $D_j^{u,k}$ for the higher-order modes ($j \geq 1$) are small compared to the scattering coefficients $D_0^{\mathcal{S}0}$ and $D_0^{u,0}$ associated with the shear-layer instability wave and the $k = 0$ (plane-wave) duct mode, respectively. The accuracy of (6.1) is verified by comparing its result with the result of the seven-mode truncation of the system (5.95). The largest error in the approximate closed-form expression of $|D_0|$ is only 0.2% when $b = 0$, and this error decreases as b increases due to the exponential decay of the higher-order duct modes. Therefore, (6.1) provides a remarkably accurate expression for the amplitude of the $k = 0$ duct mode. In a similar fashion, the error in $|D_1|$ produced by the expression (6.2) is approximately 8%, decreasing as b increases.

6.2.2 Cavity Mode Coefficients

Once the complex amplitudes D_k of the downstream duct modes have been found, the complex amplitudes C_j of the scattering coefficient for the total upstream propagating cavity mode $\mathcal{U}$ (discussed in Chapter 2) can be determined. For the interaction of the shear-layer instability wave with a finite-length overhanging lip, the scattered coefficients for the cavity modes are given by (5.98). For an eight-mode and one-mode truncation for $b = 0$, the complex amplitudes are given in table 6.12. The

k	$\lvert C_k\rvert_{(8)}$	$\lvert C_k\rvert_{(4)}$	$\arg[C_k]_{(8)}$	$\arg[C_k]_{(4)}$
0	0.740994	0.740902	−0.585721	−0.585951
1	0.323625	0.323781	−0.521997	−0.521993
2	0.093279	0.093374	1.897210	1.898060
3	0.053058	0.053183	−1.446860	−1.444640
4	0.035676		1.603010	
5	0.026137		−1.589860	
6	0.020217		1.519370	
7	0.016246		−1.644180	

Table 6.12 *Amplitudes and phases of the scattering coefficients for the upstream cavity modes; for a square (90°) corner ($b = 0$). Results for an eight-mode truncation and a four-mode truncation, for $M = 0.35$, are listed.*

maximum difference in amplitude between the four-mode truncation and the eight-mode truncation is 0.3% for $|C_3|$. The values fo the coefficients C_2, C_1 and C_0 are even smaller, with a difference of only 0.02% for C_0. The difference in phase is also very small, with the maximum difference being about 0.15% for C_3 and a minimum difference of 0.04% for C_0.

The amplitudes of the scattered coefficient of the upstream cavity modes for an eight-mode truncation are shown in table 6.12. As expected, the C_0 coefficient (corresponding to the $\mathcal{U}$ mode) has the highest amplitude $|C_0| = 0.74$. The amplitudes for the higher-order modes decrease with mode order. Interestingly in this case, the $j = 1$ has a relatively large amplitude $|C_1| = 0.32$. So, even though the $j = 1$ mode does exhibit exponential decay, it will have an important contribution to the acoustic field in the vicinity of the downstream end of the cavity. The $j = 0$ and $j = 1$ are obtained from (5.98), with only a few terms in the infinite series making significant contributions. If for $j = 0$ in (5.98), we neglect the terms $k \geq 1$, and substitute (6.1) into the equation, we obtain

$$C_0 = C_0^{\mathcal{S}} + \frac{D_0^{\mathcal{S}} C_0^{u,0} \mathrm{e}^{\mathrm{i}\sigma_k^+ 2b}}{1 - D_0^{u,0} \mathrm{e}^{\mathrm{i}\sigma_k^+ 2b}} \tag{6.3}$$

The accuracy of (6.3) for $b = 0$ can be evaluated by comparison with the results

from the eight-mode truncation, given in table 6.12. The difference in amplitude for the eight-mode truncation and (6.3) is only 0.23%, and the difference in phase is only 0.02 radians. Thus, (6.3) provides a remarkably accurate expression for the amplitude of the $j = 0$ upstream cavity mode. For most cavities of practical interest (say, $3 \leq L/d \leq 8$), the $j = 0$ upstream cavity mode is the only upstream acoustic field that is responsible for the receptivity process at the upstream edge. Hence, the importance of (6.3) for the modeling of cavity acoustic resonance is obvious.

From table 6.12, we see that in a small neighborhood of the downstream edge of the cavity, the C_1 contributes considerably to the total upstream acoustic field. Thus, an approximation for C_1 is of interest and can be obtained also by substituting $j = 1$ in (5.98), neglecting higher-order terms $k \geq 2$, and substituting (6.1) into the equation. We then obtain

$$C_1 = C_1^{\mathcal{S}} + \frac{D_0^{\mathcal{S}} C_1^{u,0} \mathrm{e}^{\mathrm{i}\sigma_k^+ 2b}}{1 - D_0^{u,0} \mathrm{e}^{\mathrm{i}\sigma_k^+ 2b}} + \frac{D_1^{\mathcal{S}} C_1^{u,1} \mathrm{e}^{\mathrm{i}\sigma_k^+ 2b}}{1 - D_1^{u,0} \mathrm{e}^{\mathrm{i}\sigma_0^+ 2b}}. \tag{6.4}$$

Again, the accuracy of (6.4) for $b = 0$ can be evaluated by comparison with the results from the eight-mode truncation, given in table 6.12. The difference in amplitude for the eight-mode truncation and (6.4) is 7.1%, and the difference in phase is only 0.07 radians. Thus, (6.4) provides an accurate expression for the amplitude of the $j = 1$ upstream cavity mode.

6.2.3 Other Interactions

Other interactions that occur at the downstream edge of the cavity, although less important, are interesting to mention. These include the impingement of a downstream propagating cavity mode with the downstream edge of the cavity. In particular, the interaction of the $j = 0$ cavity mode (the $\mathcal{D}$ mode discussed in Chapter 2) is worth summarizing. As we saw in section 4.4.3, this mode does not exhibit exponential decay. It has a magnitude of $|C_0| = 0.06$, as can be seen from table 4.14.

k	$\lvert C_k\rvert_{(8)}$	$\lvert C_k\rvert_{(4)}$	$\arg[C_k]_{(8)}$	$\arg[C_k]_{(4)}$
0	0.618827	0.618868	−0.841828	−0.841832
1	0.073182	0.073181	−0.362830	−0.362378
2	0.021058	0.021063	2.968070	2.96931
3	0.011376	0.011389	−0.141907	−0.138901
4	0.007387		3.008360	
5	0.005287		−0.129926	
6	0.004023		3.013290	
7	0.003194		−0.127126	

Table 6.13 *Amplitudes and phases of the scattering coefficients for the upstream cavity modes, for the impingement of the downstream cavity mode $\mathcal{D}$; for a square ($90°$) corner ($b = 0$). Results for an eight-mode truncation and a four-mode truncation, for $M = 0.35$, are listed.*

To determine the unsteady pressure field generated by this interaction, we first have to solve the truncated version (5.102) of the infinite dimensional matrix equation (5.101) for the amplitudes $|D_k|$ of the downstream duct modes in the portion of the cavity under the overhanging lip ($0 < x < b, \ -d < y < 0$). The entries $\tilde{A}_{jk}$ of the coefficient matrix $\tilde{A}$ are given by (5.96) and the entries $D_j^{\mathcal{D}k}$ of the vector $\overline{D}^{\mathcal{D}k}$ on the right-hand side by (5.90). The coefficient matrix $\widetilde{A}$ for the case $b = 0$ is the same one presented in section 6.2.1, whose entries for values of j and k varying from 0 to 7 are presented in table 6.10. The matrix equation (5.102) is easily solved and results for the amplitudes D_k are obtained.

Solutions for complex amplitudes C_k are given by (5.103). For an eight-mode and four-mode truncation for $b = 0$, the complex amplitudes are given in table 6.13. The maximum difference in amplitude between the four-mode truncation and the eight-mode truncation is 0.11% for $|C_3|$. The values for the coefficients C_2, C_1, and C_0 are even smaller. The difference in phase is also very small with the maximum difference being about 6.8% for C_3.

The $k = 0$ upstream cavity mode generated by this interaction has the maximum magnitude $|C_0| = 0.62$. Note that the coefficient C_0 corresponds to the scattering

coefficient $C_{\mathcal{UD}}$ discussed in Chapter 2. For the higher-order cavity modes ($k \geq 1$), the magnitude decreases with mode order and is at most one order of magnitude less than the magnitude of the $k = 0$ cavity mode. However, the $k = 0$ upstream cavity mode generated by the interaction of the $k = 0$ downstream cavity mode exhibits little decay while traveling across the cavity length. It interacts with the upstream end of the cavity and regenerates the $k = 0$ downstream cavity mode with a magnitude of 0.06 relative to that of the incident upstream cavity mode (see table 4.14). Thus, the secondary loop formed by only the upstream and downstream cavity modes will not have a significant influence on the prediction of the resonant frequencies.

7. RESULTS FOR GLOBAL MODEL

In this chapter, we present results calculated from our model. We concentrate mainly on results associated with the simplified feedback loop (2.8). Results for the scattering coefficients at the two ends of the cavity are presented in figures 7.1 and 7.2, propagation characteristics of the instability wave are presented in figures 7.4 and 7.5, and propagation characteristics of the upstream acoustic cavity mode are presented in figures 7.6 and 7.7. Finally, comparisons of our predictions with experimental data for resonance frequencies are presented in figure 7.8.

Scattering coefficients for the case of a cavity without overhanging lips ($b = 0$) were calculated for Mach numbers in the range $0.35 \leq M \leq 0.9$ and non-dimensional cavity depths $d = \omega d'/U = 1.0,\ 1.5,\ 2.0,\ 2.5$ and 3.0. (Note that the scattering coefficients for the cavity ends do not depend on the cavity length.) The scattering coefficient $C_{\mathcal{SU}}$ for the upstream end is presented in figure 7.1, while the scattering coefficient $C_{\mathcal{US}}$ for the downstream end is presented in figure 7.2. The scattering coefficients are based on the local amplitudes of the cavity acoustic mode and the shear-layer instability wave at the appropriate end of the cavity, $x = 0$ or $x = L$. In both figures, the magnitude of the scattering coefficient is plotted in part (a) and the phase of the scattering coefficient is plotted in part (b).

First consider the scattering coefficient $C_{\mathcal{SU}}$ for the upstream end, plotted in figure 7.1. Recall that $\hat{\mathcal{S}} = C_{\mathcal{SU}}\hat{\mathcal{U}}$, where $\hat{\mathcal{U}}$ is the amplitude of the incident upstream cavity mode, and $\hat{\mathcal{S}}$ is the amplitude of the scattered downstream instability wave. Thus, $C_{\mathcal{SU}}$ is the "receptivity coefficient" for the shear-layer instability wave. For the region of parameter space presented in figure 7.1, the magnitude of the receptivity coefficient lies in the range $0.05 \leq |C_{\mathcal{SU}}| \leq 0.35$. The magnitude $|C_{\mathcal{SU}}|$ is largest at small values of $d = \omega d'/U$ and decreases monotonically as d is increased. Thus, the receptivity process at the upstream end of the cavity is more efficient at low frequencies or small

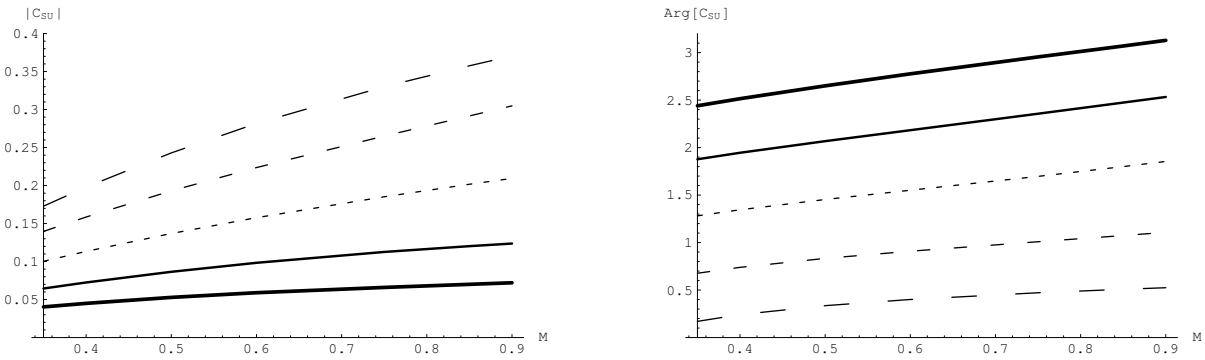

Figure 7.1 *Magnitude and phase of the scattering coefficient $C_{\mathcal{SU}}$ for the upstream end of the cavity, as a function of Mach number. (a) $|C_{\mathcal{SU}}|$; (b) $\arg[C_{\mathcal{SU}}]$. $d = 1$, long dashes; $d = 1.5$, medium dashes; $d = 2$, short dashes; $d = 2.5$, solid; $d = 3$, solid thick.*

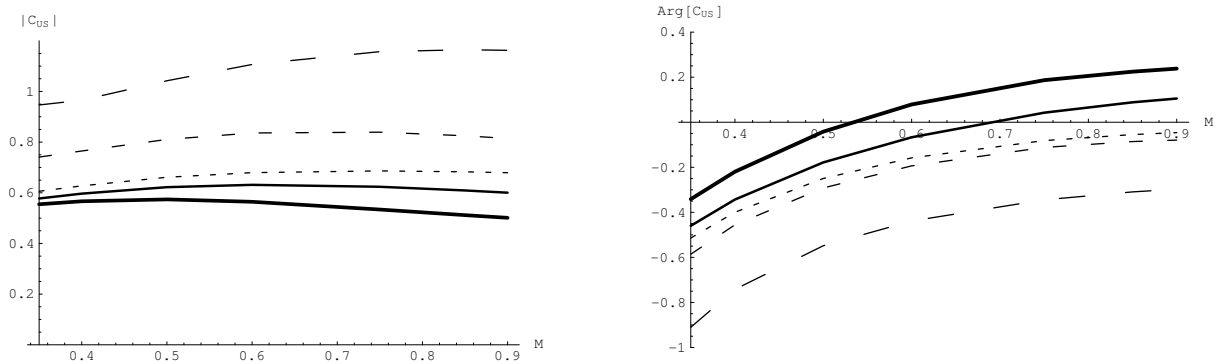

Figure 7.2 *Magnitude and phase of the scattering coefficient $C_{\mathcal{US}}$ for the downstream end of the cavity, as a function of Mach number. (a) $|C_{\mathcal{US}}|$; (b) $\arg[C_{\mathcal{US}}]$. $d = 1$, long dashes; $d = 1.5$, medium dashes; $d = 2$, short dashes; $d = 2.5$, solid; $d = 3$, solid thick.*

cavity depths. Essentially, as d increases, a greater fraction of the energy in the incident acoustic cavity mode $\mathcal{U}$ is transferred to the reflected acoustic cavity mode $\mathcal{D}$ (see below), causing less energy is transfer to the shear-layer instability wave $\mathcal{S}$. For a fixed value of d, $|C_{\mathcal{SU}}|$ increases with Mach number. The rate of increase of $|C_{\mathcal{SU}}|$ with M is larger for small values of d. For the largest value of d, shown in figure 7.1 ($d = 3$), $|C_{\mathcal{SU}}|$ is nearly independent of Mach number.

The phase $\arg[C_{\mathcal{SU}}]$ of the scattering coefficient for the upstream end is shown in figure 7.1(b). At a fixed Mach number, the phase increases significantly as the value of d increases, while at a fixed d, the phase exhibits a small increase as the Mach

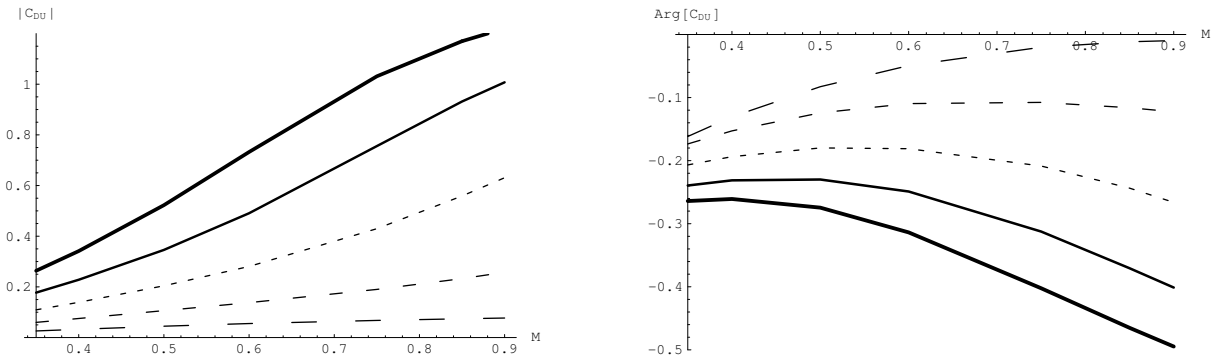

Figure 7.3 *Magnitude and phase of the scattering coefficient $C_{\mathcal{DU}}$ for the upstream end of the cavity, as a function of Mach number. (a) $|C_{\mathcal{DU}}|$; (b) $\arg[C_{\mathcal{DU}}]$. $d = 1$, long dashes; $d = 1.5$, medium dashes; $d = 2$, short dashes; $d = 2.5$, solid; $d = 3$, solid thick.*

number increases.

This behavior is consistent with the behavior of $|C_{\mathcal{DU}}|$ as a function of d, shown in figure 7.3, where we can see that, for a fixed Mach number, the amplitude of $C_{\mathcal{DU}}$ increases with cavity depth d. Note that $|C_{\mathcal{DU}}|$ exceeds one at large values of d for high subsonic Mach numbers. This is partially explained by the fact that $\mathrm{Re}[-\tau_0^-] < \mathrm{Re}[\tau_0^+]$, so that the pressure/velocity ratio is larger for $\mathcal{D}$ than for $\mathcal{U}$. Also, the rate of increase of $|C_{\mathcal{DU}}|$ with M is larger for large values of d. In contrast to what happens with $\arg[C_{\mathcal{SU}}]$, at a fixed Mach number, the phase $\arg[C_{\mathcal{DU}}]$ decreases as the value of d increases; the decrease in phase for $C_{\mathcal{DU}}$ is more dramatic for higher Mach numbers.

Next, consider the scattering coefficient $C_{\mathcal{US}}$ for the downstream end, plotted in figure 7.2. Recall that $\mathcal{U} = C_{\mathcal{US}}\mathcal{S}$, where $\mathcal{S}$ and $\mathcal{U}$ are the amplitudes of the incident shear-layer instability wave and the scattered upstream cavity mode, measured at the downstream end of the cavity. For the region of parameter space considered here, the magnitude $|C_{\mathcal{US}}|$ of the scattering coefficient for the downstream end lies in the range $0.5 \leq |C_{\mathcal{US}}| \leq 1.15$. These values are considerably higher than those for the scattering coefficient at the upstream end. The magnitude $|C_{\mathcal{US}}|$ exhibits only weak dependence on Mach number, but strong dependence on d. The dependence on d is related to

the 'penetration depth' of the instability wave into the cavity. The upstream cavity mode $\mathcal{U}$ is generated primarily as a response to the impingement of the axial velocity perturbation of the instability wave on the downstream end wall of the cavity. For small values of d, the axial velocity fluctuations of the instability wave extend across the full depth of the cavity, so that a fairly uniform velocity field impinges on the cavity end. However, as d increases, the exponential decay of the instability wave with distance from the shear layer comes into play, significantly reducing the integrated axial velocity fluctuation that impinges on the end wall of the cavity. This leads to a corresponding reduction in the amplitude of the upstream cavity mode, so that $|C_{\mathcal{US}}|$ decreases as d is increased.

The phase $\arg[C_{\mathcal{US}}]$ of the scattering coefficient for the downstream end is shown in figure 7.2(b). At a fixed Mach number, the phase $\arg[C_{\mathcal{US}}]$ increases as the value of d is increased, while at a fixed value of d, the phase increases with Mach number. The increase of the phase with Mach number for the scattering coefficient at the downstream end is stronger than that for the scattering coefficient at the upstream end. The sum of the phases of the scattering coefficients at the two ends, $\arg[C_{\mathcal{US}}] + \arg[C_{\mathcal{SU}}]$, enters into the expression (2.9) for the resonance frequencies.

Next, we present results by Yang & Tumin (2002) for the evolution of the shear-layer instability wave. The evolution of the instability wave depends on the cavity length and the initial thickness and subsequent downstream growth of the mean shear layer. Thus, details of the mean flow are required in order to make accurate predictions. We present results for two cases: (1) $M = 0.35$, $L' = 0.51$m, corresponding to the experiments Williams *et al.* (2002), and (2) $M = 0.85$, $L' = 8$in, corresponding to the geometry of Rossiter (1964). The magnitude and phase of the instability wave transfer function $\mathcal{S}/\widehat{\mathcal{S}}$, plotted as a function of frequency, is presented for the case $M = 0.35$ and $\eta = 0$ in figure 7.4. The maximum of $|\mathcal{S}/\widehat{\mathcal{S}}|$ is approximately 11. The phase based on Rossiter's empirical estimate of $0.57\,U$ for the propagation speed of the instability wave (shown as a dashed line) is seen to be in good agreement with our

theoretical predictions at this Mach number. The corresponding results for $M = 0.85$ are presented in figure 7.5. The maximum of $|\mathcal{S}/\widehat{\mathcal{S}}|$ is approximately 12 in this case, and the actual phase of the transfer function lies above Rossiter's empirical estimate, except at low frequencies.

The corresponding results for the evolution of the upstream acoustic cavity mode are presented in figures 7.6 and 7.7 for the cases $M = 0.35$ and 0.85, respectively. The magnitude $|\widehat{\mathcal{U}}/\mathcal{U}|$ of the transfer function decreases with frequency, falling to less than 0.4 at the upper end of the frequency range in each case. In Rossiter's original formula, the acoustic cavity mode was assumed to propagate at the speed of sound based on the free-stream static temperature. The phase $\arg[\widehat{\mathcal{U}}/\mathcal{U}]$, based on Rossiter's approximation, is plotted as a dashed line in figures 7.6 and 7.7. Rossiter's approximation is seen to be quite accurate at $M = 0.85$; whereas at $M = 0.35$, Rossiter's estimate for $\arg[\widehat{\mathcal{U}}/\mathcal{U}]$ is somewhat low, as the actual phase speed of the acoustic cavity mode is lower than the speed of sound. Note that modification of Rossiter's formula by Heller & Bliss (1975), which replaces the static temperature in the cavity by the stagnation temperature of the stream, would lie below the dashed line in figure 7.5 (b), and thus exhibit an even poorer agreement with our theoretical result.

The various elements of our global model were combined to predict the resonant frequencies for the cases $M = 0.35$ and $M = 0.85$, discussed above. Results for an intermediate case $M = 0.6$ were also obtained from Yang & Tumin (2002). In figure 7.8, our results are plotted on a figure taken from Heller & Bliss (1975). This figure contains experimental data from multiple experiments, as well as semi-empirical predictions (solid lines) based on their modified form of the Rossiter formula, in which the speed of sound in the cavity is based on free-stream stagnation temperature rather than static temperature.

First, consider our predictions for $M = 0.85$. The figure contains experimental data near $M = 0.8$ and 1.0. The Rossiter formula is in reasonable agreement with

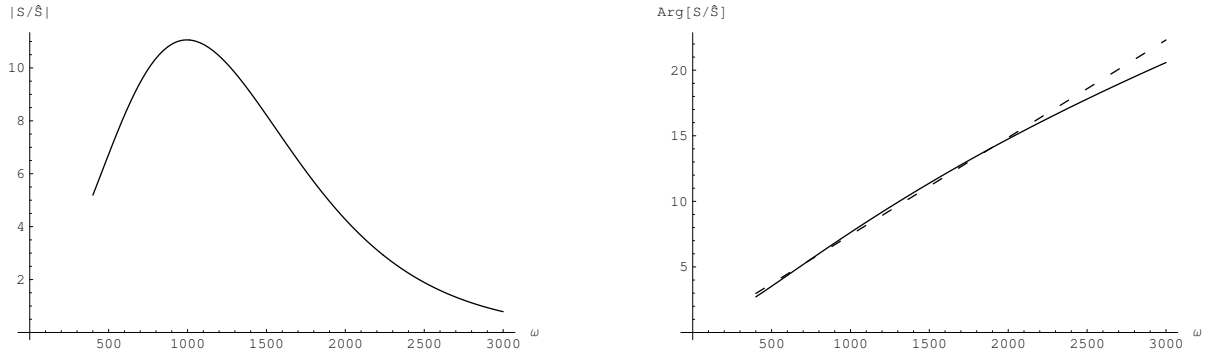

Figure 7.4 *Magnitude* $|\mathcal{S}/\widehat{\mathcal{S}}|$ *and phase* $\arg[\mathcal{S}/\widehat{\mathcal{S}}]$ *of the transfer functions for the instability wave for* $M = 0.35$*, results by Yang & Tumin (2002). Rossiter's empirical prediction for* $\arg[\mathcal{S}/\widehat{\mathcal{S}}]$ *is shown as a dotted line.*

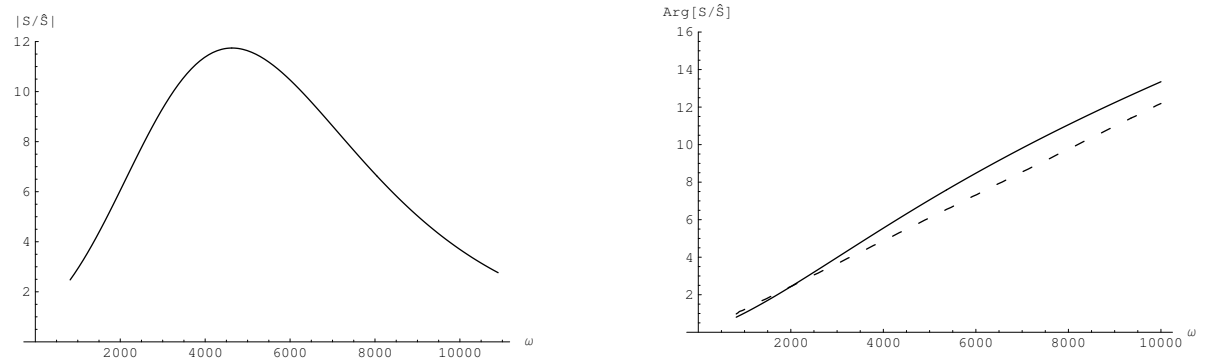

Figure 7.5 *Magnitude* $|\mathcal{S}/\widehat{\mathcal{S}}|$ *and phase* $\arg[\mathcal{S}/\widehat{\mathcal{S}}]$ *of the transfer function for the instability wave for* $M = 0.35$*, results by Yang & Tumin (2002). Rossiter's empirical prediction for* $\arg[\mathcal{S}/\widehat{\mathcal{S}}]$ *is shown as a dashed line.*

the data for the first three modes, but experimental data lie both below and above the Rossiter fourth-mode curve. Data below and above the Rossiter fourth-mode curve is also present at higher Mach numbers ($M = 1.5$ and 2.0). Our prediction for the first mode lies slightly above the data, while the predictions for the second and third modes are quite close to the data (and the Rossiter curves). However, our fourth and fifth modes lie below and above the Rossiter fourth-mode curve, quite near corresponding data points. This suggests that these data points may actually be two separate modes, rather than 'data scatter' associated with a single mode.

Next, consider our predictions for $M = 0.35$. The experimental data at low Mach

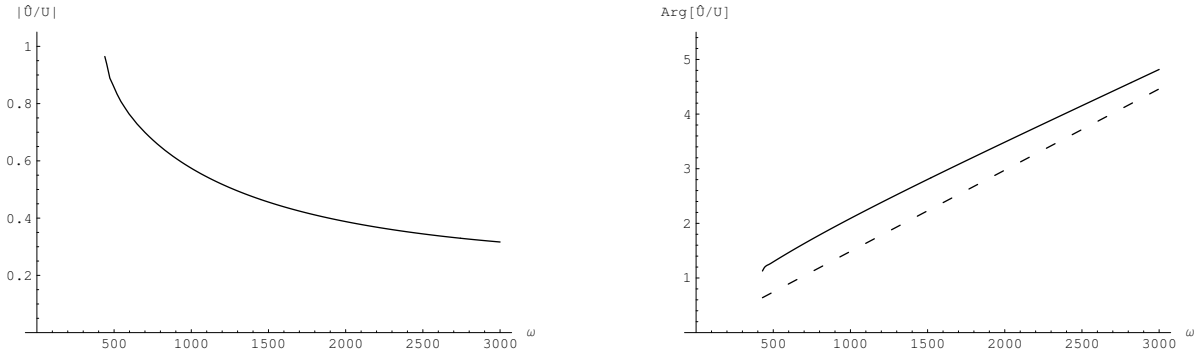

Figure 7.6 *Magnitude* $|\widehat{\mathcal{U}}/\mathcal{U}|$ *and phase* $\arg[\widehat{\mathcal{U}}/\mathcal{U}]$ *of the transfer function for the upstream cavity mode, for M=0.35. Rossiter's empirical prediction for* $\arg[\widehat{\mathcal{U}}/\mathcal{U}]$ *is shown as a dashed line.*

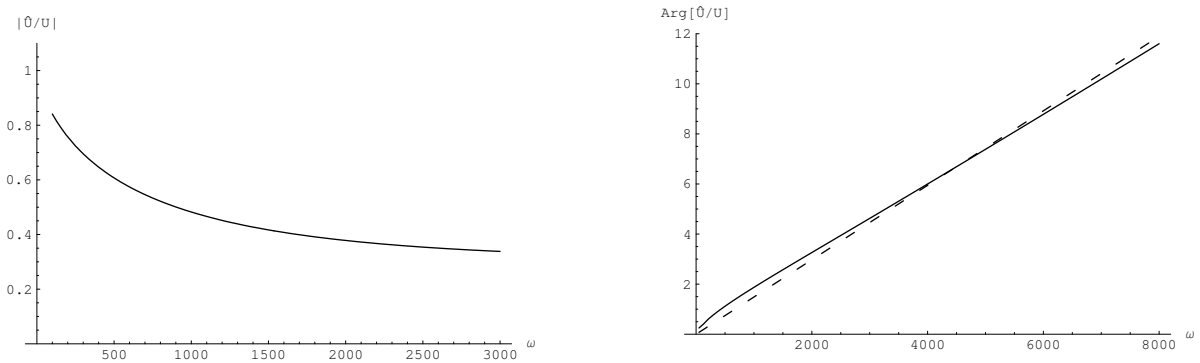

Figure 7.7 *Magnitude* $|\widehat{\mathcal{U}}/\mathcal{U}|$ *and phase* $\arg[\widehat{\mathcal{U}}/\mathcal{U}]$ *of the transfer function for the upstream cavity mode, for M=0.85. Rossiter's empirical prediction for* $\arg[\widehat{\mathcal{U}}/\mathcal{U}]$ *is shown as a dashed line.*

numbers lie consistently above the corresponding Rossiter curves. No data is shown for the first Rossiter mode. Possible explanations are that the first Rossiter mode is not unstable, or that the response is simply buried in the broadband noise floor, which has a higher amplitude at low frequencies. Our predictions for $M = 0.35$ also lie above the Rossiter curves, in close agreement with the experimental data. Also, the accuracy of our predicted frequencies for $M = 0.35$ increases with mode order.

Finally, predictions for $M = 0.6$ are also presented in figure 7.8. Our predictions for the first two modes are in excellent agreement with the experimental data, whereas the prediction for the third mode is slightly below the data. The frequencies

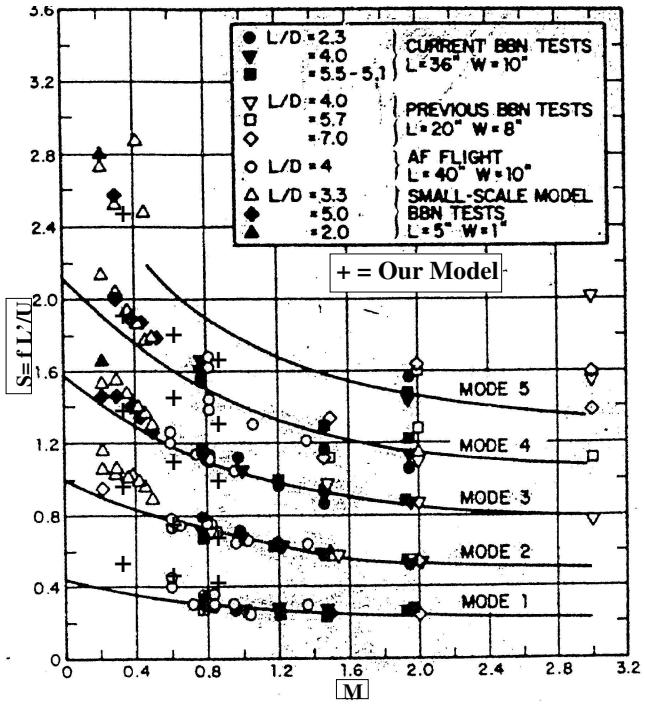

Figure 7.8 *Comparison of the predicted resonant frequencies with experimental data presented by Heller & Bliss (1975).*

corresponding to the fourth and fifth modes follow the pattern discussed above for $M = 0.85$.

The above discussion has focused on the oscillation frequencies ω of the global modes. The eigenvalue determined by our prediction method is the complex frequency $\omega_c = \omega(1 + i\eta)$. For $\mathrm{Im}[\omega_c] = \omega\eta > 0$, the mode is unstable and its amplitude grows with time; whereas for $\omega\eta < 0$, the mode is stable and its amplitude decays with time in the absence of a forcing mechanism. For $M = 0.85$, the first three modes were found to have a positive growth rate, while the higher-order modes were stable. For $M = 0.6$, the second mode was unstable, but the first mode was slightly damped and the third and higher modes were more strongly damped. For $M = 0.35$, the first mode was slightly unstable while the higher modes were damped.

The prediction of the stability boundary is influenced strongly by the amplification of the instability wave and the magnitudes of the scattering coefficients at the cavity

ends. The instability wave amplification is sensitive to the spreading rate of the mean shear layer, which is often not measured in cavity acoustic experiments. Thus, there is some uncertainty in the determination of growth (or decay) rates. A faster spreading of the mean shear layer reduces the total amplification of the instability wave in propagating from the upstream end to the downstream end. In fact, the increased spreading rate of the mean shear layer in the presence of strong instability wave motion may be one of the most important nonlinear mechanisms leading to saturation of the cavity mode amplitude.

Our prediction that the cavity modes are stable at low Mach numbers is consistent with recent experimental evidence from Rowley *et al.* (2002*b*). By examining phase portraits and probability density functions in their experiments, they concluded that cavity modes in the Mach number range $0.1 \leq M \leq 0.45$ were stable, the peaks in the spectrum corresponding to the forced response of a slightly stable system rather than limit cycle behavior of an unstable system. This is a remarkable and important discovery. Our results lend support to their conclusion.

The one exception in the low Mach number experiments performed by Rowley *et al.* (2002*b*) was the case $M = 0.34$, where the typical multiple Rossiter mode response was replaced by a single-frequency response of much higher amplitude. They ascribed this behavior to a coalescence of a Rossiter mode and a longitudinal resonance in the cavity. The longitudinal mode in the cavity would correspond to our $\mathcal{U}$–$\mathcal{D}$ secondary loop. A similar explanation was suggested by Ukeiley *et al.* (2003) for a strong single-frequency response they observed at $M = 0.75$. Results obtained for this secondary loop for $M = 0.35$ and $M = 0.85$ have very little influence on the resonant frequency. However, our results show that for higher subsonic Mach numbers, the $\mathcal{U}$–$\mathcal{D}$ loop may provide enough forcing to produce self-sustained oscillations.

Now lets consider the case $\eta \neq 0$. Common values of η oscillate between 0 and 0.25, so we consider the case $\eta = 0.1$, which is roughly a centered case. Comparisons of the first five (dimensionless) resonant frequencies (Rossiter modes), for $M = 0.85$,

Rossiter mode #	$\eta = 0$	$\eta = 0.1$
1	0.4151	0.4195
2	0.7239	0.7296
3	1.0224	1.0303
4	1.3274	1.3372
5	1.6444	1.6555

Table 7.1 *Comparison of the first five resonant frequencies (fL'/U) for $\eta = 0$ and $\eta = 0.1$. Results for $M = 0.85$.*

for $\eta = 0$ and $\eta = 0.1$, are shown in table 7.1. This data was obtained from (2.9). From table 7.1, we see that the resonant frequencies show weak dependance on η, with the largest difference being 1% for the first Rossiter mode.

The imaginary part of the resonant frequencies, given by (2.10), determines the stability of the tone. The boundary of the stability region for $\eta = 0$ suffers a slight shift for $\eta = 0.1$. Thus, for the case $M = 0.85$, some higher frequencies that were unstable for the case $\eta = 0$ may become stable for $\eta = 0.1$. This loss in growth due to the increase on the imaginary part of the frequency is consistent with previous results by Yang & Tumin (2002).

Hence, the case $\eta = 0$ provides a reasonable approximation for the resonant frequencies in (2.9). Also, the imaginary part (2.10) exhibits weak dependence on ω and η, and its behavior is monotonic with respect to η in the vicinity of $\eta = 0$. Thus, the stability or instability of a resonant frequency can be obtained by using results for real values of the frequency ($\eta = 0$) in (2.10).

8. CONCLUSIONS AND FUTURE WORK

8.1 Conclusions

We have developed a theoretical model for resonances in subsonic flow past a cavity. The model combines scattering analyses for the ends of the cavity with propagation analyses for the central region of the cavity, providing a global prediction method for the resonant modes. Both the frequencies and the growth (or decay) rates of the modes are predicted. Our predictions are in good agreement with experimental data.

Our model systematically incorporates the numerous feedback loops that are present in this flow geometry. In many situations, the simple feedback loop proposed by Rossiter appears to capture the dominant physics of the phenomenon. However, there is evidence that secondary loops may be important in certain situations involving the generation of particularly intense tones.

Finally, it appears that 'resonant tones' in shallow cavities at low Mach numbers may in fact be a forced response of a slightly stable system rather than a limit-cycle response of an unstable system. Our model could be extended to predict the cavity tones in this forced response regime by introducing an external forcing into the model, such as that due to boundary-layer turbulence passing over the upstream edge of the cavity. This appears to be a fruitful direction for future research.

8.2 Future Work

The present work predicted the resonant tones in a cavity under a subsonic flow in an unbounded setting. Work is being developed to extend our theory to a wind tunnel setting, i.e.bounded. Preliminary results presented by Alvarez & Kerschen (2005) show that in this case, the field external to the cavity has an important effect on the resonant behavior; dominant modes are also explained within this setting. Work has yet to be pursued, for cavities in wind tunnels under a supersonic flow.

Our theory may also be extended to the case of a self-excited jet or 'whistler-nozzle' (Hasan & Hussain, 1982). A whistler-nozzle is a passive control device that enhances mixing and produces self-sustained oscillation of controllable frequencies . Our theory may predict the frequencies of these self-sustained oscillations.

APPENDIX A: WIENER-HOPF KERNEL FUNCTION

The Wiener-Hopf kernel function is given by (3.44), repeated here for convenience,

$$K(\lambda) = \frac{(\lambda + n)(\lambda + n^*)\mu_2(\lambda)\sinh(\mu_2(\lambda)d)}{\Delta(\lambda)}, \tag{A.1}$$

with

$$\Delta(\lambda) = [(1 + \mathrm{i}\eta) + \lambda]^2 \mu_2(\lambda)\sinh(\mu_2(\lambda)d) + \frac{\rho_{02}}{\rho_{01}}(1 + \mathrm{i}\eta)^2\mu_1(\lambda)\cosh(\mu_2(\lambda)d) \tag{A.2}$$

The form of $K(\lambda)$ has been chosen so that $K \to 1$ as $\lambda \to \pm\infty$. We wish to split $K(\lambda)$ into multiplicative factors,

$$K(\lambda) = K^+(\lambda)K^-(\lambda), \tag{A.3}$$

where $K^+(\lambda)$ and $K^-(\lambda)$ are analytic and non-zero in the upper and lower halves of the complex λ plane, respectively. This multiplicative split is obtained by performing an additive split of the function

$$L(\lambda) = \log K(\lambda) = L^+(\lambda) + L^-(\lambda), \tag{A.4}$$

where $L^+(\lambda)$and $L^-(\lambda)$ are analytic in the upper and lower halves of the complex λ plane, respectively. These functions are defined by the integrals

$$L^+(\lambda) = \frac{1}{2\pi\mathrm{i}}\int_{-\infty}^{\infty}\frac{\log K(\alpha)}{\alpha - \lambda}\,\mathrm{d}\alpha, \tag{A.5}$$

$$L^-(\lambda) = \frac{-1}{2\pi\mathrm{i}}\int_{-\infty}^{\infty}\frac{\log K(\alpha)}{\alpha - \lambda}\,\mathrm{d}\alpha, \tag{A.6}$$

where the contours of integration lie in the strip of analyticity of $\log K(\alpha)$, formed by the overlap of the upper and lower half-planes of analyticity. Basically, in order to remain within the strip of analyticity, the integration contours must pass above all the branch points, poles and zeros of $K(\alpha)$ in the lower half-plane, and below all the branch points, poles and zeros of $K(\alpha)$ in the upper half-plane. The integration

contour in (A.5) passes below the pole at $\alpha = \lambda$, while the integration contour in (A.5) passes above the pole at $\alpha = \lambda$. Given $L^+(\lambda)$ and $L^-(\lambda)$, we then have

$$K^+(\lambda) = \exp(L^+(\lambda)), \qquad K^-(\lambda) = \exp(L^-(\lambda)). \tag{A.7}$$

In order to identify an appropriate integration contour for the evaluation of $L^+(\lambda)$ or $L^-(\lambda)$, we must consider the branch points, poles and zeros of $K(\alpha)$. These are sketched in figure 3.2 for a typical case, $M = 0.35$, $d = 1.5$. The presence of $\mu_1(\alpha)$ in $K(\alpha)$ leads to two branch points: one in the upper half plane at $\alpha = M_u$, extending upward to plus infinity. The other branch cut is in the lower half plane, at M_d, extending downward to minus infinity. The branch points of $\mu_2(\alpha)$ are not branch points of $K(\alpha)$, because this function enters $K(\alpha)$ only in the forms $\mu_2 \sinh(\mu_2 d)$ and $\cosh(\mu_2 d)$, both of which are even functions of μ_2. Thus, these branch points are shown as dashed lines in figure 3.2.

There is an infinite number of roots to $\Delta(\alpha) = 0$, which correspond to poles of $K(\alpha)$. The poles contain two infinite sets, at $\alpha = \tau_j^+$, $j = 0, 1, 2, \ldots, \infty$, in the upper half-plane and at $\alpha = \tau_j^-$, $j = 0, 1, 2, \ldots, \infty$, in the lower half-plane. The locations of these poles for the case $M = 0.35$, $d = 1.5$ are illustrated in figure 3.2. The poles in the upper half-plane, $\alpha = \tau_j^+$, $j = 0, 1, 2, \ldots, \infty$, correspond to the upstream-propagating acoustic cavity modes, which satisfy the vortex-sheet matching condition at $y = 0$ and the rigid-wall condition at $y = -d$. The upstream-propagating cavity modes suffer exponential attenuation with distance upstream ($\mathrm{Im}[\tau_j^+] > 0$) due to the acoustic energy which these modes radiate out into the stream.

The second set of poles, $\alpha = \tau_j^-$, $j = 0, 1, 2, \ldots, \infty$, lie in the lower half-plane and correspond to the downstream-propagating acoustic cavity modes. In the Mach number range $0.35 < M < 0.9$, only the $j = 0$ mode propagates without attenuation; the higher-order modes have $O(1)$ attenuation rates ($\mathrm{Im}[\tau_j^-] < 0$, $j = 1, 2, \ldots, \infty$). The roots $\tau_j^\pm$ must be found numerically; the wavenumbers $\sigma_j^\pm$ of the upstream- and downstream-propagating duct modes, which are given by (A.9), provide useful

initial estimates for a numerical root-finding scheme. The cavity-mode dispersion relationship $\Delta(\alpha) = 0$ also has two additional roots, $\alpha = -n$ and $-n^*$, which lie in the second and third quadrants, respectively. The root $\alpha = -n$ corresponds to the shear-layer instability wave which amplifies exponentially as it propagates downstream, while the root $\alpha = -n^*$ corresponds to its exponentially decaying counterpart. Note however, that $\alpha = -n$ and $\alpha = -n^*$ are not poles of $K(\alpha)$, since the factor $(\alpha + n)(\alpha + n^*)$ appears in the numerator of (A.1).

There are an infinite number of roots to

$$\mu_2(\alpha)\sinh(\mu_2(\alpha)d) = 0, \tag{A.8}$$

which correspond to zeros of $K(\alpha)$. These can also be separated into two sets, at $\alpha = \sigma_j^+$, $j = 0, 1, 2, \ldots, \infty$, in the upper half-plane and at $\alpha = \sigma_j^-$, $j = 0, 1, 2, \ldots, \infty$, in the lower half-plane. The σ_j^+ are the x-wavenumbers corresponding to the upstream-propagating duct modes, while the σ_j^- are the x-wavenumbers corresponding to downstream-propagating duct modes. In contrast to the cavity modes, closed-form expressions for the duct-mode wavenumbers can be obtained. The $\sigma_j^\pm$ are given by

$$\sigma_k^\pm = \begin{cases} \pm\sqrt{M_2^2(1+\mathrm{i}\eta)^2 - \left(\frac{k\pi}{d}\right)^2} & k < \frac{M_2 d}{\pi} \\ \pm\mathrm{i}\sqrt{\left(\frac{k\pi}{d}\right)^2 - M_2^2(1+\mathrm{i}\eta)^2} & k > \frac{M_2 d}{\pi} \end{cases} \tag{A.9}$$

where the index j starts at $j = 0$. For $\eta = 0$, the σ_j^+ in the first group ($j \leq M_2 d/\pi$) lie along the positive real axis in the range $0 \leq \alpha \leq M_2$ and correspond to upstream-propagating, cut-on duct modes, while the σ_j^+ in the second group lie along the positive imaginary axis of the α plane and correspond to cut-off duct modes which suffer exponential attenuation with distance upstream. The distinction between cut-on and cut-off modes is retained qualitatively for small non-zero values of η. The σ_j^- are the negative of the σ_j^+ and correspond to downstream-propagating duct modes. From figure 3.2, we note that the upstream-propagating cavity mode wavenumbers τ_j^+ lie fairly close to the σ_j^+, so that the σ_j^+ provide useful starting values for a numerical

scheme to determine the τ_j^+. Similarly, the downstream-propagating cavity mode wavenumbers τ_j^- lie close to the σ_j^-, except for τ_0^- which differs significantly from σ_0^-.

To determine the coefficients D_k of the downstream-propagating duct modes for a finite-length overhanging lip, we must calculate the scattering coefficients $D_j^{\mathcal{S}}$ and $D_j^{u,k}$ which contain the factors $K^+(\sigma_k^+)$, $K^-(\sigma_j^-)$ and $K^-(-n)$. Determination of the coefficients C_j of the upstream-propagating cavity modes requires the additional scattering coefficients $C_j^{\mathcal{S}}$ and $C_j^{u,k}$, which contain the additional factor $K^+(\tau_j^+)$. First consider the calculation of $K^+(\sigma_k^+)$ and $K^+(\tau_j^+)$. An appropriate integration contour for (A.5) is sketched in figure 3.2. Basically, we desire a path which does not pass too close to any of the branch points, zeros, or poles of $K(\alpha)$, and along which $K(\alpha)$ does not exhibit strong growth or rapid oscillation. Outside the region of singularities $-M_2 < \alpha < M_u$, the real-α axis is most attractive. In the central region, the contour must first be deformed upward to avoid the singularities on and near the negative real axis, then deformed downward to avoid the singularities on and near the positive real axis. Note also that the contour must pass below σ_k^+ or τ_j^+. The path in the complex plane used to calculate the results presented in this report consisted of straight line segments connecting the following points: $-\infty + 0\,\mathrm{i}$, $-4 + 0\,\mathrm{i}$, $-4 + 0.5\,\mathrm{i}$, $-0.5 + 0.5\,\mathrm{i}$, $0.5 - 0.5\,\mathrm{i}$, $4 - 0.5\,\mathrm{i}$, $4 + 0\,\mathrm{i}$ and $\infty + 0\,\mathrm{i}$. This path proved satisfactory for the case $M = 0.35$ and $d = 1.5$.

To calculate $K^-(\sigma_j^-)$, the integration contour for (A.6) must pass above σ_j^-. This integral was evaluated using the contour described in the previous paragraph. To calculate $K^-(-n)$ from (A.6), the integration contour must pass above $-n = -1.0370 + 0.9535\mathrm{i}$. This would require the use of a different contour than that described above. Therefore, we chose instead to first compute $K^+(-n)$ from (A.5) using the integration contour described above, and to then set $K^-(-n) = K(-n)/K^+(-n)$.

APPENDIX B: PROPAGATION ACROSS CAVITY LENGTH

The determination of cavity resonance frequencies requires accurate predictions of the phase evolution of the instability wave and the acoustic cavity mode as they propagate the length of the cavity, while accurate prediction of the resonance temporal growth (or decay) rate requires accurate predictions of the amplitude evolution of these disturbances as they propagate the length of the cavity. We first discuss calculation of the instability wave evolution, and then discuss calculation of the acoustic cavity mode evolution.

In order to accurately predict the evolution of the instability wave, we must account for both the non-parallel effects due to the streamwise development of the shear layer, and the influence of fine-grain turbulence on the instability wave. The instability wave evolution is calculated using the method of Yang & Tumin (2002). Their method utilizes the triple decomposition technique of Reynolds & Hussain (1972). In this technique, the flow field is decomposed into three components: a mean (time-averaged) flow, a coherent (phase-averaged) component, and random (turbulent) motion. The coherent component is the instability wave of interest for the cavity resonance. The influence of the random turbulent fluctuations on the large-scale coherent disturbance is approximated by the Newtonian eddy viscosity model. The governing equations for the coherent disturbances have the same form as in laminar flow, with substitution of the Reynolds number and the Prandtl number by their turbulent counterparts.

The solution for the (coherent) instability wave component is developed using the method of multiple scales. At leading order, an eigenvalue problem is found for the local value of the instability wavenumber at each x-station. The streamwise variation of the wavenumber is significant, due to the streamwise development of the mean shear layer. The amplitude equation which arises at second order accounts for non-parallel mean flow effects.

The evolution of the acoustic cavity mode as it propagates the length of the cavity can be analyzed very similarly. The governing equations are basically the same as those used for the instability wave development, except for changes in the boundary conditions. Again, the triple-decomposition method is applicable. However, in contrast to the instability wave, the acoustic cavity mode is not concentrated in the shear layer but rather extends across the full depth of the cavity. Therefore, the propagation of the acoustic cavity mode is influenced less by the details of the shear layer. Hence, the vortex-sheet approximation may provide sufficiently accurate results for the evolution of the acoustic cavity mode.

APPENDIX C: CALCULATION OF THE EXTERNAL FIELDS

The scattered fields have the general form

$$\phi_{1,2} = \int_{-\infty}^{\infty} I_{1,2}(\lambda, y)\, \mathrm{e}^{-\mathrm{i}\lambda x} d\lambda. \tag{C.1}$$

The external fields are calculated by deforming the integration contour around the appropriate branch cut.

For the downstream-propagating external field, we deform the integration contour around the branch cut emanating from $\lambda = M_d$. This branch point comes from the term $\sqrt{\lambda - M_d}$, in both numerator and denominator of the integrands. If we let γ be the distance from the branch point M_d, then the two paths that 'wrap' the branch cut are given by the following change of variables

$$\lambda = M_d + \gamma \mathrm{e}^{\mathrm{i}3\pi/2}, \quad \text{on LHS} \tag{C.2}$$

$$\lambda = M_d + \gamma \mathrm{e}^{-\mathrm{i}\pi/2}, \quad \text{on RHS} \tag{C.3}$$

Thus the branch cut contribution is given by

$$E^{\mathcal{U}}_{1,2} = -\mathrm{i} \int_0^{\infty} \left[I_{1,2}(M_d + \gamma \mathrm{e}^{-\mathrm{i}\pi/2}, y) - I_{1,2}(M_d + \gamma \mathrm{e}^{\mathrm{i}3\pi/2}, y) \right] \mathrm{e}^{-\gamma x} d\gamma, \tag{C.4}$$

where the phase factor $\mathrm{e}^{-\mathrm{i}M_d x}$ has been extracted.

For the branch cut contribution for $y = O(1)$ and $x \gg 1$, the main contribution comes from small values of γ, i.e. $\gamma \ll 1$. Also, the branch point $\gamma = 0$ in the integrands of (C.4) comes from the $\sqrt{\gamma}$. Therefore, when expanding the integrands around $\gamma = 0$ the main contribution will come from a $\sqrt{\gamma}$ term, as follows

$$E^{\mathcal{U}}_{1,2} \approx \int_0^{\infty} \sqrt{\gamma}\, \mathrm{e}^{-\mathrm{i}\gamma x} d\gamma, \tag{C.5}$$

where all constants outside of the integrand have been omitted.

Since we want to obtain the behavior for large values of x, we need to take x out of the integrand. We do this by making the change of variable $\rho = \gamma x$, thus we get

$$E_{1,2}^{\mathcal{S}} \approx \frac{1}{x^{3/2}} \int_0^\infty \sqrt{\rho}\, \mathrm{e}^{-\rho} d\rho = \frac{1}{x^{3/2}} \Gamma\left(\frac{3}{2}\right). \tag{C.6}$$

Hence for $x \gg 1$ and $y = O(1)$ the downstream external field decays as $x^{-3/2}$.

Similarly for the upstream-propagating external field, we deform the integration contour around the branch cut emanating from $\lambda = M_u$. This branch point comes from the term $\sqrt{\lambda - M_u}$, in both numerator and denominator of the integrands. If we let γ be the distance from the branch point M_u, then the two paths that 'wrap' the branch cut are given by the following change of variables

$$\lambda = M_u + \gamma \mathrm{e}^{-\mathrm{i}3\pi/2}, \quad \text{on LHS} \tag{C.7}$$

$$\lambda = M_u + \gamma \mathrm{e}^{\mathrm{i}\pi/2}, \quad \text{on RHS} \tag{C.8}$$

Thus the branch cut contribution is given by

$$E_{1,2}^{\mathcal{S}} = \mathrm{i} \int_0^\infty \left[I_{1,2}(M_u + \gamma \mathrm{e}^{-\mathrm{i}3\pi/2}, y) - I_{1,2}(M_u + \gamma \mathrm{e}^{\mathrm{i}\pi/2}, y) \right] \mathrm{e}^{-\gamma x} d\gamma, \tag{C.9}$$

where the phase factor $\mathrm{e}^{-\mathrm{i}M_u x}$ has been extracted.

For the branch cut contribution for $y = O(1)$ and $x \gg 1$, the main contribution comes from small values of γ, i.e. $\gamma \ll 1$. Also, the branch point $\gamma = 0$ in the integrands of (C.9) comes from the $\sqrt{\gamma}$. Therefore, when expanding the integrands around $\gamma = 0$ the main contribution will come from a $\sqrt{\gamma}$ term, as follows

$$E_{1,2}^{\mathcal{S}} \approx \int_0^\infty \sqrt{\gamma}\, \mathrm{e}^{-\mathrm{i}\gamma x} d\gamma, \tag{C.10}$$

where all constants outside of the integrand have been omitted.

Again, we make the change of variable $\rho = \gamma x$, thus

$$E_{1,2}^{\mathcal{S}} \approx \frac{1}{x^{3/2}} \int_0^\infty \sqrt{\rho}\, \mathrm{e}^{-\rho} d\rho = \frac{1}{x^{3/2}} \Gamma\left(\frac{3}{2}\right). \tag{C.11}$$

Hence for $x \gg 1$ and $y = O(1)$ the upstream external field decays as $x^{-3/2}$.

APPENDIX D: STEEPEST DESCENT AND CHOICE OF BRANCH CUTS

In section 4.2, we saw that some disturbances exhibit exponential growth in the stream region ($y > 0$). We argued that by the method of steepest descents, these disturbances actually decay in the far field, since the corresponding singularities in the complex plane are relevant only for shallow angles of propagation. Here we give more details for this explanation. The inverse transform in the stream region, for the different cases considered in Chapters 3 and 5, has the general form

$$\phi_1 = \frac{1}{2\pi}\int_{-\infty}^{\infty} B_1(\lambda) e^{-\mu_1(\lambda)y} \mathrm{e}^{-\mathrm{i}\lambda x} d\lambda, \tag{D.1}$$

where

$$\mu_1(\lambda) = \left[\lambda^2 - M_1^2(\lambda + (1+\mathrm{i}\eta))^2\right]^{\frac{1}{2}} \tag{D.2}$$

$$= \beta\left[(\lambda - M_u)(\lambda - M_d)\right]^{\frac{1}{2}} \tag{D.3}$$

In this appendix we explain in more detail the method of steepests descents and analyze the other choices of branch cuts we could have made.

Lets start with the method of steepest descents (Bender & Orszag, 1999) for our particular problem. This method deforms the integration contour into a contour (steepest descent path) where the function in the exponent has a constant imaginary part. To apply this method, we perform the change of variables $x = r\cos(\theta)$ and $y = r\sin(\theta)$, where $r = \sqrt{x^2 + y^2}$ and θ is the angle of observation. Then (D.1) becomes

$$\phi_1 = \frac{1}{2\pi}\int_{-\infty}^{\infty} B_1(\lambda)\ e^{-(\mu_1(\lambda)\sin(\theta) + \mathrm{i}\lambda\cos(\theta))r} d\lambda, \tag{D.4}$$

where the steepest descent path is determined by θ, thus the behavior of the integral is determined by the behavior of the integrand in the vicinity of the local maxima of the real part of the exponent function $f(\lambda) = \mu_1(\lambda)\sin(\theta) + \mathrm{i}\lambda\cos(\theta)$. If $f(\lambda)$ has a

local maximum at the point λ_0, then this point is called a saddle point. In our case the saddle point for $f(\lambda)$ is given by

$$\lambda_0 = \frac{(M_u + M_d)(\cos^2(\theta) + \beta^2 \sin^2(\theta)) - \cos(\theta)(M_u - M_d)\sqrt{1 - (\beta^2 - 1)\sin^2(\theta)}}{2(\cos^2(\theta) + \beta^2 \sin^2(\theta))}. \tag{D.5}$$

Note that the saddle point depends on θ. It is real and moves in the region between the two branch points M_d and M_u. Thus, $\lambda_0(0) = M_d$, $\lambda_0(\pi/2) = (M_u + M_d)/2$ and $\lambda_0(\pi) = M_u$. The steepest descent path is the contour that passes through the saddle point λ_0. Along this contour, $f(\lambda)$ has constant imaginary part, $\mathrm{Im}[f(\lambda)] = \mathrm{Im}[f(\lambda_0)]$, and the real part of $f(\lambda)$ decreases in the directions away from the saddle point.

Figure D.1 shows five steepest descent paths for five different angles of observation for $M = 0.35$ and $d = 1.5$. Notice that for $\theta = 0$ ($\lambda_0 = M_d$) and $\theta = \pi$ ($\lambda_0 = M_u$), the steepest descent path 'wraps' around the corresponding branch cut. For $\theta = 90°$, the steepest descent path goes to the horizontal asymptote $\mathrm{Im}[\lambda] = \pm\frac{\mathrm{Im}[f(\lambda_0)]}{\beta}$, and for $\theta = 45°$ and $\theta = 135°$, the paths have parabolic shape.

From the different paths in figure D.1, we see the evolution of the steepest descent path as we vary the angle of observation. In section 4.2, we saw that for $M = 0.35$ and $d = 1.5$, the $j = 0$ upstream cavity mode (which comes from the contribution of the the pole at $\lambda = \tau_0^+$), exhibits exponential growth in the stream region ($y > 0$). In this case, the steepest descent path will cross the pole at τ_0^+ for an angle of approximately 151°. For $151° < \theta < 180°$, the real part of the function $f(\lambda) = \mu_1(\lambda)\sin(\theta) + \mathrm{i}\lambda\cos(\theta)$ along the steepest descent path is positive, even for regions where $\mathrm{Re}[\mu_1(\lambda)] < 0$, hence the integrand of (D.4) exhibits exponential decay as $r \to \infty$.

Analogously, the contributions from the poles at $\lambda = \sigma_j^-$ $j = 1, 2, 3 \ldots \infty$ (the higher-order downstream cavity modes) will become apparent for $0° < \theta < 8°$. For these shallow angles, the real part of $f(\lambda)$ is again positive and y is small compared to x; therefore (D.4) exhibits exponential decay as $r \to \infty$ (see figure D.1). So even

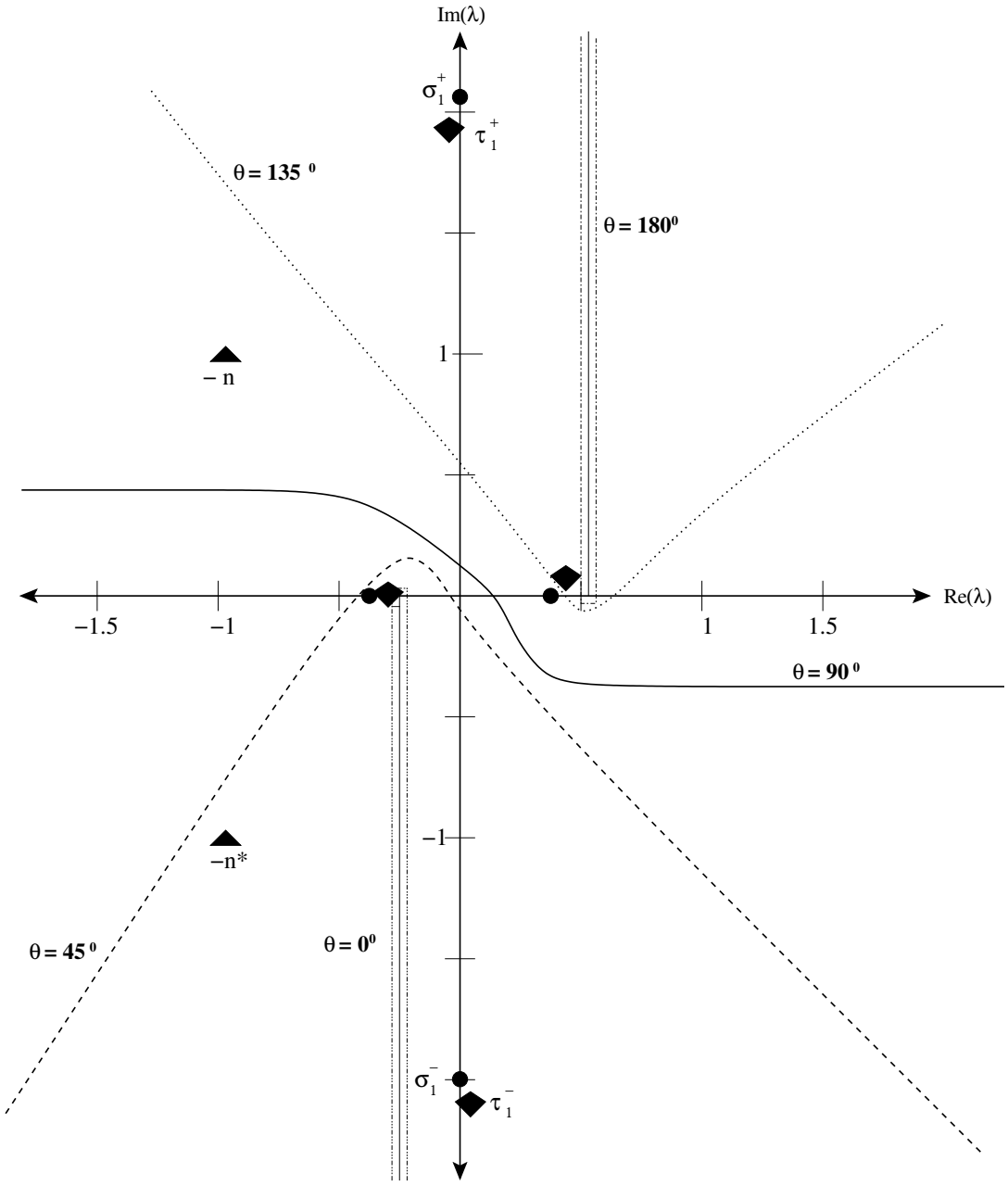

Figure D.1 *Path of steepest descents for different angles of observation*

if the disturbances show growth in y for $y = O(1)$, they decay in their respective directions of propagation, where the growth in y is overturned by the decay in x.

Now lets examine the other possible branch cuts we could have chosen. The two possible dispositions of the branch cuts, for $M = 0.35$ and $d = 1.5$, are shown in figure D.2.

First, we could have required that $\mathrm{Re}[\mu_1(\lambda)] > 0$ throughout the complex plane. This choice generates the dashed branch cuts in figure D.2. In this case, the pole at σ_0^+ lies on the branch cut and the poles at τ_0^+ and $\lambda = \tau_j^-$ $j = 1, 2, 3 \ldots \infty$ are shifted to the second Riemann sheet. Thus the effect of the upstream duct mode will get buried into the continuous spectrum and the contributions from τ_0^+ and $\lambda = \tau_j^-$ $j = 1, 2, 3 \ldots \infty$ will be lost. Hence this choice of branch cuts looses important contributions.

Second, we could have chosen branch cuts that do not interfere with the stationary phase inversion contours. This choice generates the dotted contour in figure D.2. In this case, the poles at $\lambda = \sigma_0^-$ and $\lambda = \tau_0^-$ lie on the branch cut and the pole at $-n^*$ is shifted to the second Riemann sheet. Thus the contribution from $\lambda = \sigma_0^-$ and $\lambda = \tau_0^-$ gets buried in the continuous spectrum and we loose the contribution from $-n^*$. Furthermore, the continuous spectrum would represent a non-decaying disturbance traveling at all possible subsonic speeds relative to the stream. This interpretation does not have a tangible meaning and obscures the physics of the continuous spectrum.

Therefore, the other possible choices of branch cuts do not produce growing disturbances in the stream, but important physical disturbances are lost, and the physical meaning of the continuous spectrum is obscured.

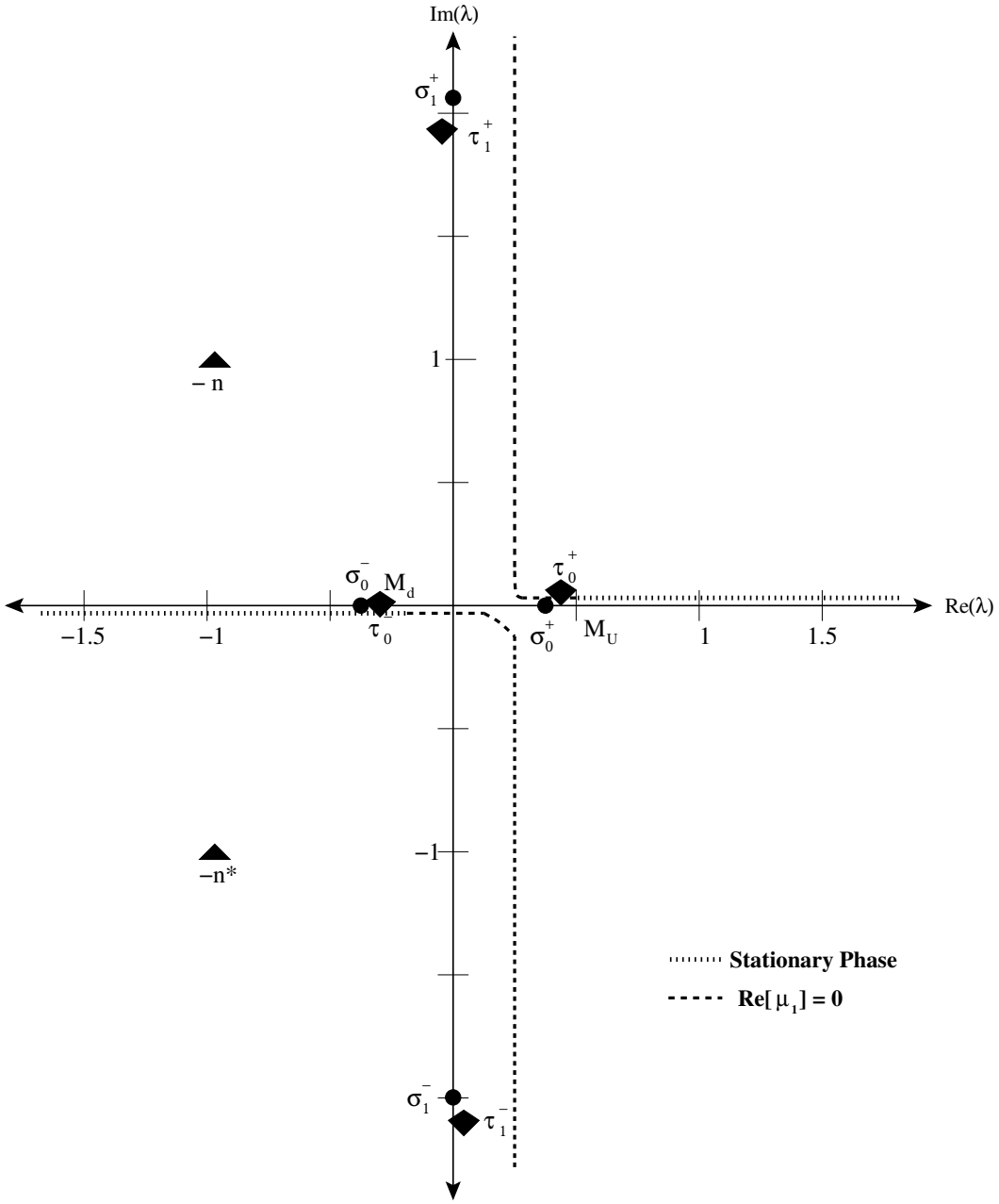

Figure D.2 *Other possible choices of branch cuts.*

REFERENCES

Alvarez, J. O. & Kerschen, E. J. 2005 Influence of wind tunnel walls on acoustic cavity resonances. *AIAA Paper* **2005-2804**.

Bender, C. M. & Orszag, S. A. 1999 *Advanced Mathematical Methods for Scientists and Engineers*. New York: Springer-Verlag.

Bers, A. 1975 Linear waves and instabilities. In *Plasma Physics* (ed. C. D. Wett & J. Pehraud), pp. 113–216. New York: Gordon and Breach.

Briggs, R. 1964 Electron-stream interaction with plasmas. In *Res. Monograms*, , vol. 29, chap. 2. Cambridge: MIT Press.

Cain, A. B., Kerschen, E. J., Cary, A. W. & Bower, W. W. 2001 Prediction and active control of weapons bay acoustics-phase 2. *Tech. Rep.* F33615-96-D-3011. Air Force Research Laboratory.

Cain, A. B., Rubio, A. D., Bortz, D. M., Banks, H. T. & Smith, R. C. 2000 Optimizing control of open bay acoustics. *AIAA Paper* **2000-1928**.

Carrier, G., Krook, M. & Pearson, C. 1983 *Functions of a complex Variable*. New York: Hod Books.

Cattafestta, L. I., Shukla, D., Garg, S. & Ross, J. 1999 Development of an adaptive weapons-bay suppression system. *AIAA Paper* **99-1901**.

Crighton, D. G. 1985 The kutta condition in unsteady flow. *Ann. Rev. Fluid Mech.* **17**, 411–445.

Debiasi, M., Yan, P., Little, J., Ozbay, H. & Samimy, M. 2004 An experimental study of subsonic cavity flow-physiscal understanding and control. *AIAA Paper* **2004-2123**.

Hasan, M. A. Z. & Hussain, A. K. M. F. 1982 The self-excited axisymmetric jet. *J. Fluid Mech.* **115**, 59–89.

Heller, H. H. & Bliss, D. B. 1975 The physical mechanism of flow induced pressure fluctuations in cavities and concepts for suppression. *AIAA Paper* **75-491**.

Kegerise, M., Cattafesta, L. N. & Ha, C. 2002 Adaptive identification and control of flow-induced cavity oscillation. *AIAA Paper* **2002-3158**.

Kerschen, E. J. & Tumin, A. 2003 A theoretical model of cavity acoustic resonances based on edge scattering processes. *AIAA Paper* **2003-0175**.

Koch, W. 1977 Attenuation of sound in multi-element acoustically lined rectangular ducts in the absence of mean flow. *J. Sound Vib.* **52**, 459–496.

Koch, W. 2004 Acoustic resonances in rectangular open cavities. *AIAA Paper* **2004-2843**.

Larcheveque, L., Sagaut, P. & Le, T. H. 2003 Large-eddy simulations of flows in weapon bays. *AIAA Paper* **2003-778**.

Noble, B. 1988 *Methods Based on the Wiener-Hopf Technique*. New York: Chelsea.

Raman, G., Raghu, S. & Beninc, T. 1999 Cavity resonance suppression using minature fluidic oscillators. *AIAA Paper* **99-1900**.

Reynolds, W. C. & Hussain, A. K. M. F. 1972 The mechanics of an organized wave in turbulent shear flow. part 3. theoretical models and comparisons with experiments. *J. Fluid Mech.* **54**, 263–288.

Rossiter, J. E. 1964 Wind tunnel experiments on the flow over rectangular cavities at subsonic and transonic speeds. *Tech. Rep.* 64307. Royal Aircraft Establishment.

Rowley, C. W., Colonius, T. & Basu, A. J. 2002*a* On self-sustained oscillations in two-dimensional compressible flow over rectangular cavities. *J. Fluid Mech.* **455**, 315–346.

Rowley, C. W., Williams, D. R., Colonius, T., Murray, R. M., MacMartin, D. G. & Fabris, D. 2002*b* Model-based control of cavity oscillations - part ii: System identification and analysis. *AIAA Paper* **2002-0972**.

Stanek, M. J., Raman, G., Kibens, V., Ross, J. A., Odedra, J. & Peto, J. W. 2000 Control of cavity resonance through very high frequency forcing. *AIAA Paper* **2000-1905**.

Tam, C. K. W. & Block, P. J. W. 1978 On the tones and pressure oscillations induced by flow over rectangular cavities, part 2. *J. Fluid Mech.* **89**, 373–399.

Ukeiley, L., Seiner, J., Ponton, M. & Jansen, B. 2003 Suppression of pressure loads in resonating cavities through blowing. *AIAA Paper* **2003-0181**.

Williams, D. R., Fabris, D. & Morrow, J. 2000 Experiments on controlling multiple acoustic modes in cavities. *AIAA Paper* **2000-1903**.

Williams, D. R., Rowley, C., Colonius, T., Murray, R., MacMartin, D., Fabris, D. & Albertson, J. 2002 Model-based control of cavity oscillations - part i: Experiments. *AIAA Paper* **2002-0971**.

YANG, H. & TUMIN, A. 2002 On harmonic perturbations in compressible mixing layers. *AIAA Paper* **2002-2854**.